Final Report to

Evaluation of Fracture Systems and Stress Fields Within the Marcellus Shale and Utica Shale and Characterization of Associated Water-Disposal Reservoirs: Appalachian Basin.

08122-55.Final

January 2013

Principal Investigator: Bob A. Hardage

Co-Authors: Engin Alkin, Milo M. Backus,
Michael V. DeAngelo, Diana Sava,
Donald Wagner, and Robert J. Graebner

Subcontractor: Bureau of Economic Geology

Subcontractor: The University of Texas at Austin

Telephone: 512-471-0300

http://www.beg.utexas.edu/

Email: bob.hardage@beg.utexas.edu

Evaluation of Fracture Systems and Stress Fields Within the Marcellus Shale and Utica Shale and Characterization of Associated Water-Disposal Reservoirs: Appalachian Basin

Final Report

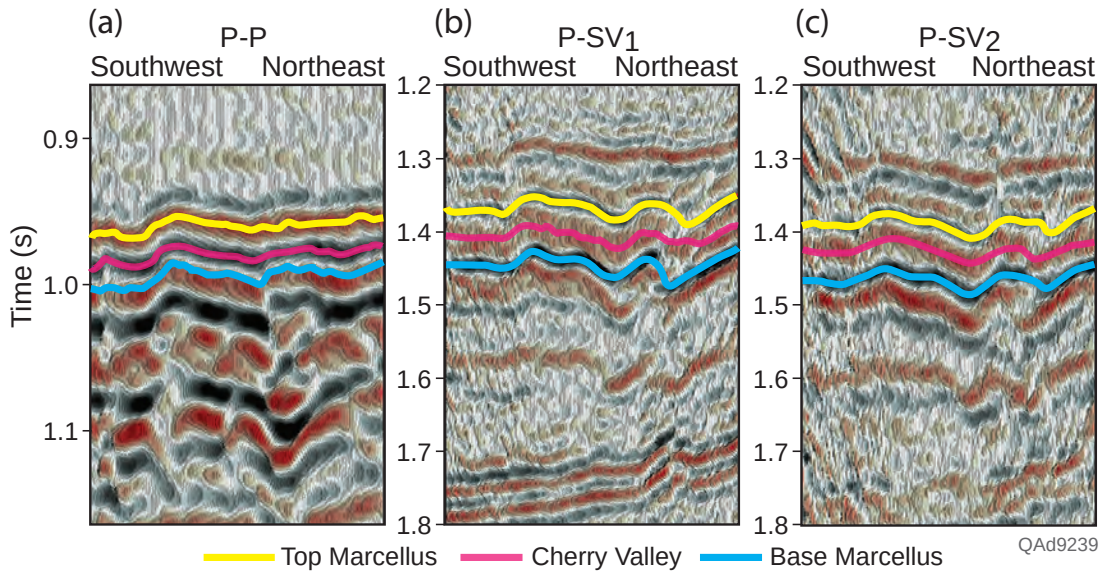

RPSEA Subcontract: 08122-55

Research period:	29 September 2009 through 31 January 2013
Report date:	January 2013
Submitting organization:	Bureau of Economic Geology The University of Texas at Austin
Research Team:	Bob A. Hardage (Principal Investigator), Engin Alkin, Milo M. Backus, Michael V. DeAngelo, Diana Sava, Donald Wagner, and Robert J. Graebner

Disclaimer

This report was prepared by the Bureau of Economic Geology as an account of work sponsored by the U.S. Department of Energy. The National Energy Technology Laboratory, the U.S. Department of Energy, nor any person acting on behalf of these entities:

- MAKES ANY WARRANTY OR REPRESENTATION, EXPRESS OR IMPLIED WITH RESPECT TO ACCURACY, COMPLETENESS, OR USEFULNESS OF THE INFORMATION CONTAINED IN THIS DOCUMENT, OR THAT THE USE OF ANY INFORMATION, APPARATUS, METHOD, OR PROCESS DISCLOSED IN THIS DOCUMENT MAY NOT INFRINGE PRIVATELY OWNED RIGHTS, OR

- ASSUMES ANY LIABILITY WITH RESPECT TO THE USE OF, OR FOR ANY AND ALL DAMAGES RESULTING FROM THE USE OF, ANY INFORMATION, APPARATUS, METHOD, OR PROCESS DISCLOSED IN THIS DOCUMENT.

This is a final report. The data, calculations, information, conclusions, and/or recommendations reported herein are the property of the U.S. Department of Energy.

Reference to trade names or specific commercial products, commodities, or services in this report does not represent or constitute an endorsement, recommendation, or favoring by DOE or its contractors of the specific commercial product, commodity, or service.

Bob A. Hardage

Principal Investigator: Bob A. Hardage

11 January 2013

Date: 11 January 2013

Abstract

The Exploration Geophysics Laboratory at the Bureau of Economic Geology partnered with Geokinetics, Geophysical Pursuit, and Chesapeake Energy to demonstrate the value of multicomponent seismic technology for evaluating the Marcellus Shale and associated water-storage reservoirs. Geokinetics and Geophysical Pursuit provided the multicomponent seismic data used in the study. Chesapeake drilled a Marcellus well inside the multicomponent seismic image space and provided well log data and vertical seismic profile data from this well that allowed P-wave and S-wave seismic attributes to be calibrated with rock properties across targeted stratigraphic intervals.

Two research findings stand out. First, the spatial resolution of converted-SV shear data (the P-SV mode) was shown to be significantly better than the spatial resolution of compressional-wave data (the P-P mode). As a result, geological information needed for optimal exploitation of the Marcellus Shale is defined in greater detail with P-SV seismic data than with P-P data. Yet P-P data continue to dominate the seismic data used by shale-gas operators across the Appalachian Basin. Second, when evaluating porous rock units as potential storage reservoirs for hydrofrac flow-back water, P-SV seismic attributes defined intra-reservoir anomalies within Devonian sandstone units that could not be seen with P-P seismic attributes. The improved definition of the internal architecture of porous, brine-filled Devonian reservoirs achieved with P-SV data will allow Appalachian Basin operators to better decide which rock units should be considered as potential storage reservoirs for flow-back waters produced when hydrofracing either the Marcellus Shale or the Utica Shale. The bottom-line conclusion provided by these two research findings is that multicomponent seismic technology is far more valuable than is conventional, single-component, P-P seismic technology for evaluating Marcellus Shale prospects and for selecting appropriate water-storage units that can support hydrofrac operations.

A seismic field test was done in the early phase of the study to compare P-wave and S-wave radiation patterns produced by each major type of vertical-force and horizontal-force source used by seismic contractors. This field test was a part of an ongoing multi-year research program performed by the Exploration Geophysics Laboratory that has the objective of demonstrating that full elastic wavefield data can be acquired using only vertical-force seismic sources. Analysis of these test data supported earlier investigations by showing that a rich amount of S-wave energy radiates directly from the point where a vertical-force source applies its force vector to the Earth. Documentation of this seismic source test is a major part of this report.

Table of Contents

Results and Discussions

Impact to Producers

Technology Transfer Efforts

Conclusions

Recommendations

List of Figures

Tables

Executive Summary

This research was proposed as a study that would illustrate the value of multicomponent seismic technology for evaluating the Marcellus Shale, the Utica Shale, and porous brine-filled rock units local to these shales. The reason that the study encompassed porous brine-filled rocks was that such rocks can be used as reservoirs for sequestering flow-back waters produced during hydrofracing operations. The Utica Shale part of the study was not done with great rigor because at our final study site, the Utica was far deeper than any available well log control. Our original industry partner was a small independent whose objectives were to acquire multicomponent seismic data and to drill a Utica Shale well in south-central New York. The difficulty of implementing shale-gas projects in the State of New York did not allow this operator to initiate these activities across their leased acreage.

As a result of this no-go situation in the State of New York, we switched to a new industry partner, Chesapeake Energy, and focused our study in Bradford County, Pennsylvania, where Chesapeake planned to drill a Marcellus Shale well inside an area where multicomponent seismic data were to be acquired by Geokinetics and Geophysical Pursuit. At this Pennsylvania location, the Marcellus Shale was 6,000 ft (1820 m) deep, and the Utica Shale was approximately twice as deep, with its depth being approximately 12,000 ft (3660 m). No operator in Bradford County, PA, or in neighboring counties, has yet drilled a Utica Shale well. As a result, there are no logs or seismic checkshot data to identify where the Utica Shale is positioned in seismic image space. Because no subsurface control in Bradford County extended an appreciable distance below the Marcellus Shale, we did only a simple analysis of “best guess” seismic data windows where we assumed the Utica Shale would be positioned. We then focused on the Marcellus Shale and its associated rock units that could be considered as potential water-storage reservoirs.

One important fact is demonstrated in this study that verifies multicomponent seismic data have greater value for exploiting the Marcellus Shale than do single-component P-wave seismic data, with the latter data (P-P data) being the most common seismic data used across the Appalachian Basin. Specifically, we show the converted-SV mode (the P-SV mode) provides better spatial resolution of Marcellus Shale stratigraphy than does its companion P-P mode. The difference in resolution is significant, with P-P wavelengths being longer than P-SV wavelengths by 40-percent to as much as 50-percent. In the twelve years our laboratory has concentrated on multicomponent seismic research, the Appalachian Basin data used in this study exhibit the most dramatic advantage of P-SV data over P-P data in terms of deep target resolution that we have seen. The improved resolution of P-SV data over P-P data is easy to document by making side-by-side displays of P-SV and P-P wiggle trace data over targeted depth intervals. Several such displays are

presented in Chapter 9 to emphasize that multicomponent seismic data provide better resolution of Marcellus Shale geology than do conventional, single-component P-P data.

A second important advantage of multicomponent seismic data was demonstrated in this study when sand-prone Devonian intervals were evaluated as potential reservoirs for storing flow-back water from hydrofrac operations. When the Devonian section immediately below the Tully Limestone was interpreted using both P-P and P-SV data, we found P-P data showed this interval to be rather uniform and homogeneous. In contrast, P-SV data showed an anomalous geobody of significant dimensions (at least 5 km long and approximately 0.5 km wide) resided within this targeted water-storage reservoir interval. Without subsurface control, it is not possible to know if this intra-reservoir heterogeneity will enhance or retard lateral fluid flow. However, it is important to know the heterogeneity exists when these porous rocks are considered as water-storage reservoirs. Without applying multicomponent seismic imaging, the presence of this Devonian intra-reservoir anomaly would not be known. This analysis is documented in Chapter 9.

This study was the first opportunity our research staff had to analyze the behavior of multicomponent seismic wavefield propagation in an orthorhombic medium. The Marcellus Shale is a textbook example of an orthorhombic medium because it has two orthogonal joint sets and is also thin layered. In past studies in which we have analyzed fractured targets having a single set of oriented fractures, our studies have consistently established that there is a powerful advantage of shear-wave (S-wave) data over single-component P-P seismic data. The advantage is that fractures cause an S wavefield to segregate into two modes called the fast-S mode and the slow-S mode. The fast-S mode is polarized with its displacement vector parallel to an oriented fracture set, and the slow-S mode is polarized with its displacement vector perpendicular to aligned fractures. Furthermore, the velocity of the slow-S mode decreases as fracture intensity increases. As a result, S-wave seismic data define fracture orientation and estimate fracture intensity. In contrast, neither of these fracture-sensitive behaviors (fracture orientation and fracture intensity) occurs with P-P seismic data, so there is an obvious advantage in using S-wave data (multicomponent data) when analyzing fractured rock systems.

This study shows some of these fracture-sensitive advantages of S-wave data over P-wave data do not apply when the fractured rock system is an orthorhombic medium with two orthogonal joint sets, such as is found in the Marcellus Shale. Because there is not a single, dominate system of aligned fractures within the Marcellus, but rather two orthogonal fracture sets, the result is that an S-wave behaves like a slow-S mode in every azimuth in which its displacement vector is oriented within the Marcellus, and there is no effective fast-S mode. A totally different rock physics model had to be developed to

describe S-wave propagation in the Marcellus Shale. The applicable rock physics theory is discussed and illustrated in Chapter 5.

Three conclusions related to S-waves and orthorhombic media were reached in this study. First, it does not seem possible to use S-wave data to determine the azimuth orientations of two orthogonal joint sets such as exist within the Marcellus Shale. This finding is in stark contrast to the physics of S-wave illumination of a fractured rock that has a single set of oriented fractures. Second, an S-wave that illuminates two sets of orthogonal joints does not segregate into a fast-S and slow-S mode unless one joint set has a fracture density significantly different than the fracture density of the companion joint set. This conclusion is essentially a restatement of the preceding conclusion, but uses a different logic to emphasize the principle. Third, joint density within the Marcellus Shale can still be estimated with S-wave data if it is possible to construct accurate S-wave interval velocities across the Marcellus Shale. Specifically, if joint density increases, the S-wave velocity (which is a slow-S velocity) across the Marcellus Shale will decrease. Conversely, if joint density decreases, S-wave velocity (slow-S velocity) across the Marcellus interval will increase. This is a different velocity analysis approach to fracture-intensity estimation than is the conventional approach of comparing fast-S and slow-S velocities.

The overarching conclusion reached in this study is that much more geologic, rock-specific, fluid-specific, and fracture-attribute information is provided by multicomponent seismic data than by single-component P-P seismic data. The evidence leading to this conclusion is spread throughout this report, but the principal data examples and interpretations are presented in Chapter 9.

A long, multi-year research effort at the Exploration Geophysics Laboratory has been to develop technology that will allow full elastic seismic wavefields to be acquired with simple vertical-force seismic sources that are widespread across the seismic contractor industry. If P and S data can be generated directly at a source station without deploying the horizontal-force sources (horizontal vibrators) that are now used to generate direct S waves, then multicomponent seismic technology will be available to a wide community of shale-gas operators. Included as Chapter 6 in this report is a description of a field test performed by the Exploration Geophysics Laboratory that verifies SV and SH shear-wave modes are produced directly at the point where a vertical force is applied to the Earth in addition to a P mode. So far, the only illuminating wavefield produced directly at a source station that is utilized when vertical-force sources are deployed for prospect evaluation is the P mode. By including these field test results in this report, more shale-gas operators should become aware of this simpler way to generate both direct-P and direct-S wavefields across shale-gas prospects

Experimental Methods

Chapter 1

Methodology Used in Study

Introduction

The overarching methodology used in this study was to demonstrate multicomponent seismic technology has greater value than conventional, single-component P-wave seismic technology for characterizing shale-gas systems and for evaluating porous units where flow-back water from fracing operations could be injected for long-term storage. Our study considered the Marcellus Shale, Utica Shale, and porous brine-filled sandstones and carbonates in an area of the Appalachian Basin in northeastern Pennsylvania. Concepts and principles documented in this study can be used in areas other than the Appalachian Basin and can be applied to rock facies other than those present at our research site.

To carry out the broad methodology of establishing the value of multicomponent seismic technology in shale-gas exploitation, several secondary research methods were embedded in our research tasks. The purposes of these secondary methods were to compile information and evidence describing the physics of compressional (P) and shear (S) wave propagation in Earth layering associated with shale-gas systems. Among these secondary research methods were seismic field tests that established: (1) cable-free seismic data-acquisition systems provide 3-component (3C) seismic data having quality equal to that of data acquired with conventional cable-based seismic recording systems, (2) data acquired with a cable-based recording system have signal spectra extending to frequencies approximately 10-percent higher than signal spectra of data acquired with cable-free systems, and (3) 3C geophones and 3C accelerometers provide equivalent-quality multicomponent seismic data, but accelerometers enhance low-frequency components of P and S wave modes slightly better than do typical 10-Hz geophones. Enhanced lower frequencies can be important for some seismic applications.

Field test data were also acquired to compare attributes of P and S wave modes produced by explosive, accelerated-weight impact, and vibratory energy sources and to document the relative merits of these sources for illuminating shale-gas targets and their associated stratigraphic units. These tests led to the most important principle documented in this study; that being that full-elastic wavefield data can be acquire with vertical-force seismic sources. This research finding eliminates the need to use both vertical-force and horizontal-force seismic sources to produce full-elastic wavefield data for many seismic applications and simplifies multicomponent seismic data acquisition.

The most common seismic source used to study shale-gas systems is a vertical-force source such as a vertical vibrator, a vertical impact, or a shot-hole explosive. When 3C seismic data are acquired with a vertical-force source, traditionally the only S-wave information that is utilized is the upgoing converted-SV mode (P-SV mode) created when downgoing P waves arrive at rock interfaces at incident angles different than zero (normal incidence) and create upgoing SV reflection events. One focus of our research was to demonstrate that valuable S-wave modes are produced directly at the point where a vertical-force source applies its force vector to the Earth, which allows S-wave modes other than P-SV data to be utilized in shale-gas studies. The recognition and use of these direct-S modes introduce new seismic imaging options into shale-gas studies and provide expanded suites of seismic attributes that can be used to infer rock and fluid properties across shale-gas prospects.

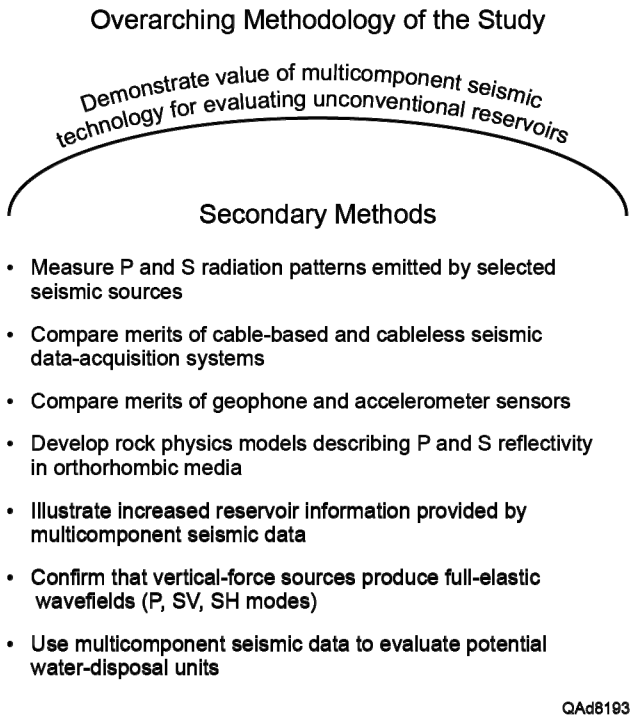

Figure 1.1. Experimental methods used in study. Numerous secondary experimental methods were implemented to achieve the basic, overarching methodology of demonstrating the value of multicomponent seismic technology for characterization shale-gas systems.

Broad Methodology: Demonstrate Value of Multicomponent Seismic Technology for Evaluating Unconventional Reservoirs

The fundamental experimental methodology used in this study was to demonstrate the value of multicomponent seismic data in shale-gas projects. The approach to implementing this methodology was to conduct the research effort using a series of smaller, secondary research activities that collectively allowed a rigorous documentation of the basic principles that need to be demonstrated. This research strategy is illustrated by the graphic exhibited as Figure 1.1.

Experimental Method 1: Measure P and S Radiation Patterns Emitted by Selected Sources

The most common type of energy source used to acquire exploration seismic data is a source that applies a vertical force vector to the Earth. Examples of such sources are vertical vibrators, vertical-impact weights, and shot-hole explosives. For decades, geophysicists have considered vertical-force sources to be only P-wave sources. One objective of this research was to demonstrate that full elastic wavefields, consisting of a P-wave mode, a radial-S mode, and a transverse-S mode, are produced by vertical-force sources. The implication of this principle is significant because, when proven to be true, it is no longer necessary to use horizontal-force sources (either horizontal vibrators or inclined-impact sources) to generate S-wave modes directly at a source station. Instead, simpler and more common vertical-force sources can be used to produce S waves directly at source stations, in addition to producing converted-SV waves at interfaces remote from a source station.

Vertical-force sources can be classified into three categories—vertical vibrators, vertical impacts, and shot-hole explosives. Test data were collected at the Devine Test Site operated by the Bureau of Economic Geology to evaluate each of these source types. Sources that were tested were:

- Vertical vibrator: An Input/Output Model AHV IV PLS 362 with a hold-down weight of 60,000 lb (27,733 kg).

- Explosive: One kilogram (2.2 lbs) of pentolite placed at a depth of 6 m (20 ft).

- Vertical impact: A VSX source manufactured by United Services Alliance—a 33,000-lb vehicle with a 1000-psi nitrogen-spring weight acceleration system that delivers impact energy of 22,276 ft-lb (30,202 joules) to its base plate.

The fundamental physics documented by these seismic-source tests was:

Research Finding 1

Vertical-force seismic sources produce full elastic wavefields having robust compressional (P), radial-shear (SR), and transverse-shear (ST) modes.

A conclusion reached in this study is that these full elastic wavefields are created directly at the point where each source applies its vertical force vector to the Earth. The data and methodology used to achieve this objective and to produce this research finding are described in Chapter 6.

This research finding adds additional confirmation to previous conclusions reached by our research laboratory, this being that full elastic wavefields can be acquired with simple vertical-force sources. The fact that three, independent, and orthogonal force vectors (vertical, inline horizontal, crossline horizontal) do not have to be applied at a source station to produce full elastic wavefields can have significant impact on lowering the cost of acquiring multicomponent seismic data.

Experimental Method 2: Compare Merits of Cable-Based and Cable-Free Seismic Data Recording Systems

Three seismic recording systems were used to collect multicomponent seismic test data at the Devine Test Site. One system was the popular Sercel 428 used by many seismic crews around the world. A Sercel 428 is a cable-based system, meaning data outputs from sensors deployed across a seismic prospect are transmitted to a central recorder and data storage unit by a series of interconnecting cables. If there are several thousand sensor stations distributed across a sizeable area, there is only one data recorder and one data storage unit, but there are many kilometers of interconnecting cable that interface this central recorder/storage system to all sensor stations distributed across the area.

The other two recording systems involved in the field tests were cable-free systems. Cable-free seismic data acquisition is a relatively new technology, with the first prototypes introduced less than 10 years ago. As is the case with many technologies, the reliability and versatility of cable-free equipment has increased on an annual basis, and today, cable-free systems appear to be fully competitive with standard cable-based systems. The attraction of cable-free seismic data acquisition is that by avoiding spread cables, a seismic contractor eliminates a huge amount of equipment (hundreds of kilometers of cable, hundreds of thousands of kilograms of weight, and several millions of dollars of capital investment), reduces the number of equipment-transport trucks, avoids expensive daily cable repair, and operates with fewer field personnel. Cable-free data-acquisition systems thus have economic appeal to seismic contractors.

However, skeptics still demand proof that cable-free systems provide seismic data of the same quality provided by cable-based systems that have been used for decades. This attitude is what caused the objective of comparing 3C seismic data acquired with cable-based and cable-free systems to be incorporated into this study.

In cable-free data acquisition, a small box is connected directly to the sensors at each receiver station. Data outputs from the sensors at a particular station are recorded only by the box deployed at that station. If there are several thousand 3C receiver stations across a sizeable area, there is an equivalent (or larger) number of data recorders and data-storage boxes (one 3-channel box, or three 1-channel boxes at each 3C station). The only cable required at each receiver station is a short length of less than a meter that connects the data-recorder box to the geophone string. There are no interconnecting spread cables; there is no central data recorder or central data storage unit. Instead at appropriate clock/calendar times, a replacement box is deployed at a receiver station while the box that was active at that station is transported to a local field office where data are downloaded onto the same digital media used by cable-based data acquisition systems.

The two cable-free systems utilized in our field tests were EUnite boxes provided by Sercel, and Sigma boxes provided by Seismic Source and iSeis. Photos of these cable-free boxes can be seen on Figure 6.4 of Chapter 6. Data acquired with the Sercel 428 cable-based system, and with EUnite and Sigma cable-free systems, are displayed and discussed throughout Chapter 6. The principal research finding developed from analyzing these data was:

Research Finding 2

There are negligible differences in the quality of multicomponent seismic data acquired with cable-free data-acquisition systems and data acquired with cable-based data-acquisition systems. Cable-based data had only slightly broader signal spectra than cable-free data in our tests.

This research finding is important in shale-gas programs because cable-free systems allow seismic data to be acquired in areas of high culture (houses, streets, roads, industrial plants, and so forth) more easily than can be done with cable-based systems. Shale-gas projects are often located in close proximity to high levels of human activity. Cable-free seismic data acquisition will be important for studying shale-gas prospects across urban, industrial, and heavy-use properties.

Experimental Method 3: Compare Merits of Geophone and Accelerometer Sensors

The standard sensor used to acquire seismic data for evaluating shale-gas targets is the moving-coil geophone that has been used by seismic contractors for more than 70 years. Approximately 10 years ago, solid state accelerometers called MEMS (micro-electronic mechanical systems) were introduced as seismic sensors. Today both sensor types—geophones and accelerometers—are used to acquire multicomponent seismic data. Several companies and groups have done tests to compare P and S data acquired with these two sensor types. Most of these tests are proprietary to the companies that did the tests. Publicly available comparisons of data recorded by geophones and accelerometers are limited. Thus an objective integrated into this research was to collect test data that allowed similarities and differences between geophone data and accelerometer data to be provided to the shale-gas community. These data should allow better informed decisions to be made when setting parameters and equipment standards for seismic data acquisition across shale-gas areas.

The 3C geophones deployed for testing at the Devine Test Site were Oyo Geospace Model 20DX, which had 10-Hz resonance suspension springs in their vertical and horizontal moving-coil elements. The 3C accelerometers were Sercel DSU3 MEMS. Surface spreads of these sensors used to collect test data are shown on the photographs displayed as Figure 6.4 of Chapter 6. Although other types of geophones with suspension springs having different resonances could have been utilized, the data collected in our field test with these 10-Hz geophones will be used to make generalized statements about attributes of P and S data acquired with geophones and accelerometers. Specifically, the research finding resulting from analyzing geophone and accelerometer data was:

Research Finding 3

Accelerometers provide better low-frequency data (frequencies less than 8 Hz) than do geophones. Otherwise geophone data and accelerometer data are equivalent.

This research finding can be important when it is important to acquire optimal-quality S-wave data because S-modes tend to be lower frequency than P-wave data. When S waves are critical to evaluating a shale-gas target, serious consideration should be given to using accelerometers. Geophone manufacturers counter with the argument that the frequency roll-off exhibited by geophones below their natural spring resonance can be removed during data processing because the amplitude and phase character of each type of geophone is documented by careful laboratory measurements for frequencies less than resonant frequency. This argument has merit, but in practice few geophysicists apply such numerical adjustments to geophone data. Geophone and accelerometer test data are displayed and discussed in Chapter 6.

Experimental Method 4: Develop Rock Physics Models Describing P and S Reflectivity in Orthorhombic Media

The log data, physical principles, and analysis procedures used to develop shale-gas and water-storage-unit rock physics models are discussed in Chapter 5. Regarding rock units considered for water-storage reservoirs, we found there was sufficient porosity (12 to 16 percent) in many brine-filled rock units across our study area in northeast Pennsylvania for those units to accept significant volumes of injected flow-back water from shale-gas hydrofracing operations. Regarding the Marcellus Shale, an orthorhombic rock system, our findings were:

Research Finding 4

S-wave splitting in an orthorhombic medium such as the Marcellus Shale is quite subdued unless there is a significant difference in the fracture densities of the two orthogonal joint sets J1 and J2 occurring within the Marcellus interval. When the fracture densities of joint sets J1 and J2 are similar, there is no measurable S-wave splitting, and all S-wave modes within the Marcellus are a slow mode.

Experimental Method 5: Illustrate Increased Reservoir Information Provided by Multicomponent Seismic Data

The geological information content of multicomponent seismic data is compared to the information content of single-component P-wave data in Chapter 9. Comments here will be limited to observations related to stratigraphic resolution and to detecting and characterizing faults. Additional comments related to seismic sequence and seismic facies are provided in the discussion of Objective 7. As documented in Chapter 9, we found the following advantage of multicomponent seismic technology which will be invaluable in evaluating shale-gas prospects.

Research Finding 5

Converted-shear (P-SV) seismic data provided better vertical resolution of strata related to shale-gas systems and also detected and resolved faults better than did P-wave seismic data.

In addition to these findings, the combination of fast-S and slow-S seismic modes estimated approximately the same magnitude of S-wave anisotropy as did local dipole sonic log data. Thus multicomponent seismic technology allows fracture densities inside targeted rock units to be estimated across broad areas of shale-gas systems.

Experimental Method 6: Confirm Vertical-Force Sources Produce Full Elastic Wavefields

Multicomponent wave modes propagating away from a source station can be best evaluated if they are captured by a vertical array of downhole receivers. Such data define the properties of all downgoing source-generated wavefields that illuminate geologic targets. Analyzing vertical-array data allows all P and S modes embedded in illuminating wavefields to be identified and quantified. Because of this insight, analyzing vertical-array data is the preferred way to evaluate seismic source performance and was the method used in this study. Analysis of vertical-array data acquired at the Devine Test Site showed:

Research Finding 6

Each tested vertical-force source generated radial-shear and transverse-shear modes directly at each source station in addition to the expected compressional-wave mode. The energy content and data quality of these S modes equaled or exceeded those of the P mode.

This research finding was further verified by recording reflected wavefields with horizontal arrays of 3C geophones and extracting P and S reflection events from single-fold data having low signal-to-noise ratios. These data processing results are illustrated and discussed in Chapter 6. In terms of fundamental seismic wavefield physics and the impact of these principles on future seismic data-acquisition projects, this research finding is perhaps the most important research result achieved in this study. Examples of direct S-wave modes extracted from 3C3D seismic data are discussed in Chapter 8.

Experimental Method 7: Use Multicomponent Seismic Data to Evaluate Potential Water-Disposal Units

Seismic data interpretation examples used to achieve this objective are discussed in Chapter 9. Interpretation results summarized here relate to seismic sequences and seismic facies observed in poststack P and S image volumes.

Research Finding 7

S-wave data revealed a reservoir compartmentalization feature in an interval dominated by transgressive Devonian sandstone that could not be seen with P-wave data.

Detecting depositional features such as documented in this example is critical for describing the internal architecture of potential water-disposal units. The implications of this finding are significant. Features such as the one documented in Chapter 9 can be either an enhancement to fluid flow or an impediment, depending on the lithological nature of the fill material. If only P-wave data were

used to evaluate this prospect, the existence of the internal reservoir-compartment feature would not be suspected. With the inclusion of S-wave data into the interpretation, the presence of the feature is known, and a different thought process has to be implemented as to the fluid-flow behavior that could be expected within this particular reservoir unit.

Conclusions

A broad spectrum of secondary experimental methods was implemented to create our principle research methodology of *demonstrating the value of multicomponent seismic technology for studying shale-gas systems*. Important research findings were documented as each secondary experimental method was completed. The cumulative effect of these research findings was definitive proof that multicomponent seismic data provide more information about geological sequences and facies, and allow better estimation of rock and fluid properties, than do single-component P-wave seismic data. These research findings need to be distributed among companies and individuals engaged in shale-gas projects so the advantages of multicomponent seismic technology are considered in future shale-gas projects.

Chapter 2

Methods Used to Select Study Site

Introduction

The fundamental objective of this research was to demonstrate the value of multicomponent seismic technology for evaluating shale-gas prospects. An early decision was that the study should focus on the Marcellus Shale play across the Appalachian Basin. As research plans matured, additional geologic targets were introduced into the study. Final study objectives encompassed not only the Marcellus, but also the Utica Shale, which is considerably deeper than the Marcellus Shale, as well as porous, brine-filled units local to Marcellus and Utica reservoirs that could serve as repositories for flow-back water produced during shale hydrofrac operations.

The most constraining criterion for selecting a research study site was the availability of appropriate multicomponent seismic data. More interest has risen in multicomponent seismic surveys across shale-gas prospect areas the past several years as companies have begun to appreciate that S-wave modes are more valuable than P-wave data for evaluating fracture systems embedded in shale-gas units. Because of this growing industry interest in applying multicomponent seismic technology to shale-gas exploitation, we were able to combine attractive shale-gas geology with the availability of modern multicomponent seismic data in northeast Pennsylvania. The result was an excellent study site located in Bradford County, Pennsylvania.

Selection Method 1—Availability of Multicomponent Seismic Data

An opportunity arose to utilize a high-quality, 3C3D seismic survey acquired by Geokinetics and Geophysical Pursuit for the purpose of multiclient leasing to companies wishing to develop Marcellus Shale prospects. Our research team succeeded in negotiating acceptable data-confidentiality terms that allowed us to use these data to demonstrate the value of multicomponent seismic data for evaluating the Marcellus and Utica Shales and porous water-storage reservoirs. The availability of these 3C3D seismic data was the dominant factor that determined the exact position of our study site. A map showing the generalized location of this multicomponent seismic survey is presented as Figure 2.1. An attraction of positioning the study area in this part of the Appalachian Basin is that the study site sits atop some of the thickest Devonian strata in the basin. The Marcellus Shale is Devonian age, as are several potential water-storage units that need to be evaluated. The value of this site was further enhanced by an operator drilling a Marcellus Shale well in the exact center of the 3C3D seismic grid and acquiring valuable geological calibration data in that well

consisting of a full suite of modern well logs and vertical seismic profile (VSP) data.

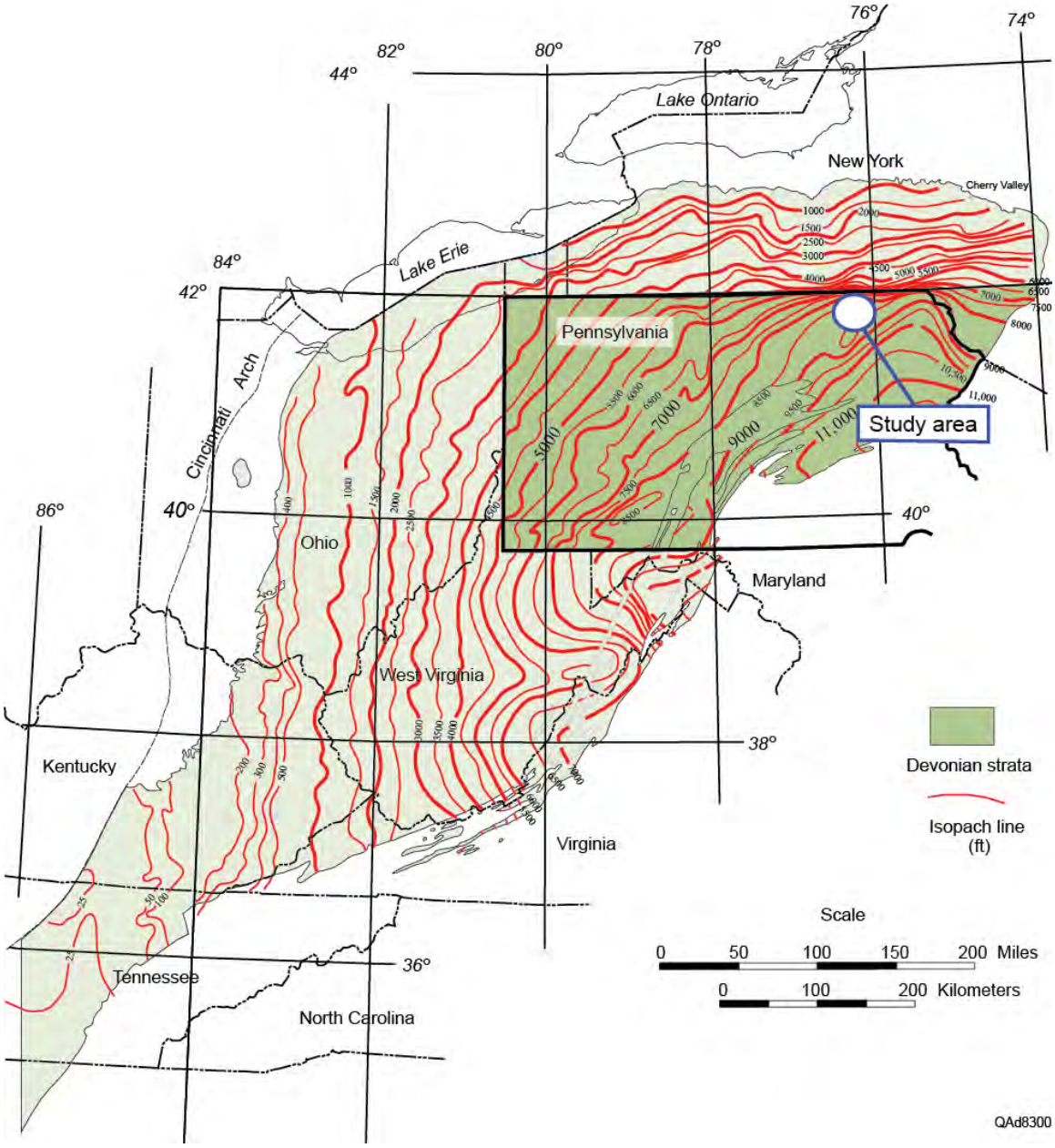

Figure 2.1. Location of the multicomponent seismic data used in this study relative to thickness of Devonian strata. The study area defined for this project was the area local to this seismic image space. An appeal of the study site is that it sits atop thick Devonian strata, which ensures there is a significant interval of Marcellus Shale and also enhances the possibility that several potential water-storage units are present. Modified from Milici and Swezey (2006).

Detailed maps showing the location of the study site on geological maps are illustrated and discussed in Chapter 3 (Geological Analysis). Additional maps showing the configuration of the seismic data-acquisition grid, the position of the central calibration well, and the locations of several local wells that provide additional calibration data are displayed and discussed in Chapter 4 (Research Database).

Selection Method 2—Presence of Potential Water Storage Units

An important part of this study was to evaluate rock units that could be used to store flow-back water from hydrofrac operations. Rock facies targeted for storage of flow-back water can be porous, brine-filled sandstones or carbonates. The confirmation that the study site shown on Figure 2.1 was appropriate for this aspect of the research was dictated by whether one or more porous, brine-filled rock facies acceptable for water storage, together with one or more impermeable sealing units above these potential sequestration targets, were present across the seismic image area.

After appropriate investigation, we decided the study area defined on Figure 2.1 was ideal for evaluating potential water-storage units. A generalized stratigraphic column of the northeast Appalachian Basin is displayed on Figure 2.2 to indicate the relative stratigraphic positions of potential water-storage sandstone targets local to our study site. A fifth sequestration target, the Catskill Sandstone, identified on this stratigraphic column may exist beneath the study site, which broadened the research opportunity.

Conclusions

The site selected for this study is in Bradford County, Pennsylvania, in the northeastern portion of the Appalachian Basin. The study area traverses attractive Marcellus Shale and Utica Shale geology and also numerous brine-filled sandstones and carbonates that are potential water-storage targets. Most importantly, a modern (Year 2009) 3C3D seismic survey spans the site, and an exploratory well was drilled in Year 2009 at the center point of this 3D seismic image space. Invaluable seismic-to-geology calibration data were acquired in this well and made available to the research team.

The multicomponent seismic data provided by Geopursuit and Geokinetics have allowed the research team to do innovative seismic data analysis to expand the number and type of P and S seismic attributes that can be used to define rock and fluid properties associated with shale-gas plays. Our seismic data-processing studies are discussed in Chapter 8 (Multicomponent Seismic Data Processing). These multicomponent seismic data also allowed elastic wavefield seismic stratigraphy to be practiced, which is a science based on the principles:

(1) S-wave seismic data provide seismic facies and seismic sequences that differ from P-wave seismic facies and seismic sequences, and

(2) P and S seismic facies and sequences have equal importance and must be treated as equals during seismic interpretation.

These principles of elastic wavefield seismic stratigraphy are emphasized in Chapter 9 (Multicomponent Seismic Interpretation).

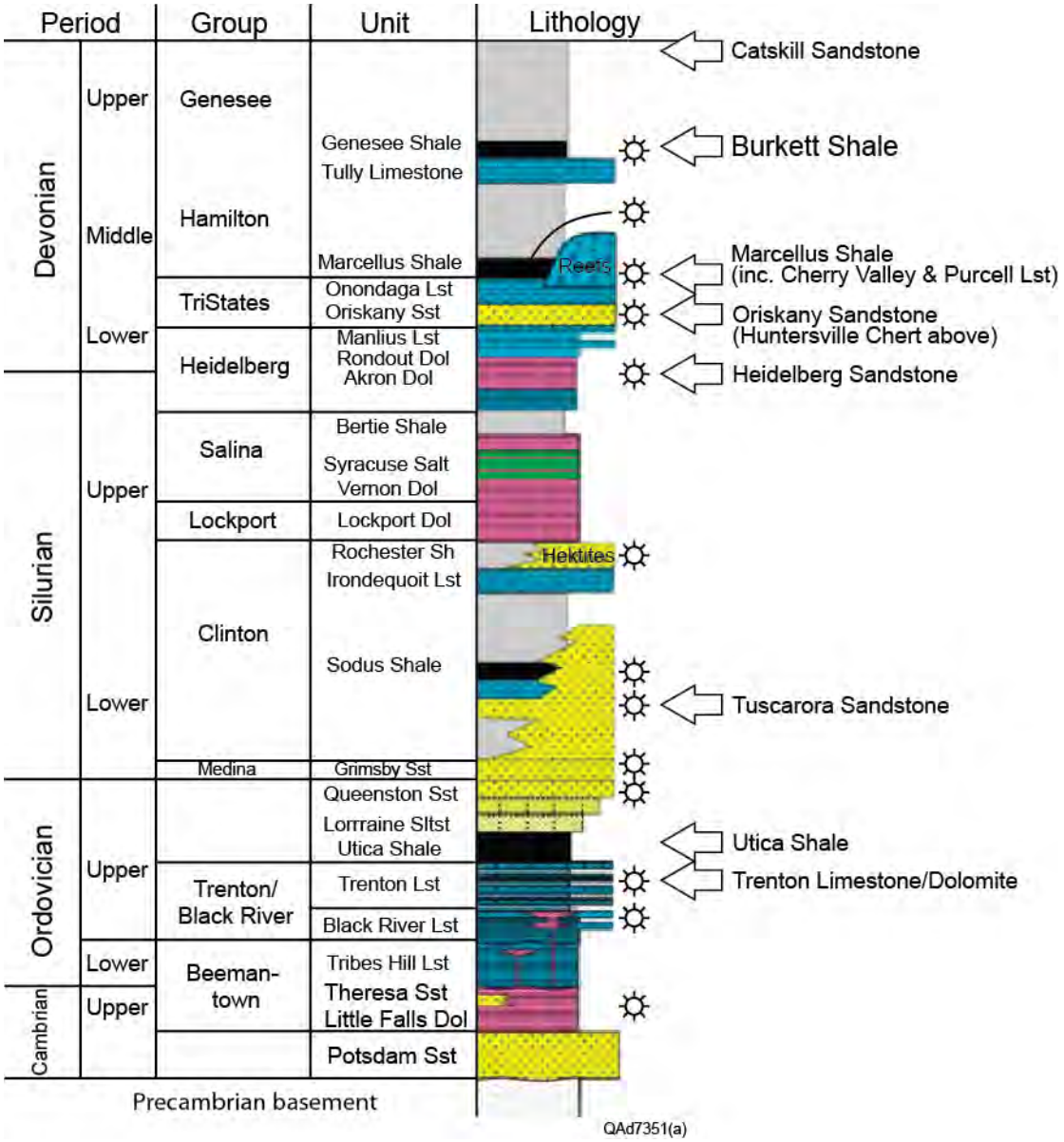

Figure 2.2. Stratigraphic column for the study area showing the stratigraphic position of the Marcellus Shale, Utica Shales, and brine sandstones (Catskill, Oriskany, and Tuscarora) that can be analyzed as water-disposal reservoirs. From Nyahay et al. (2007).

Results and Discussions

Chapter 3

Geology of Water-Storage Rock Units and the Marcellus Shale

Introduction

Numerous saline aquifers across the Appalachian Basin are candidates for sequestering flow-back water produced during hydrofrac operations. This chapter presents an overview of the geology of the northeastern portion of the Appalachian Basin where our study site was located in Bradford County, Pennsylvania. The primary focus of our geological analysis was to describe porous brine-filled units throughout the entire stratigraphic column to ensure all possible water storage targets were considered local to Bradford County. Geological descriptions start with Lower Devonian sequestration candidates and proceed to deeper Basal Cambrian sandstones.

Any rock unit considered for CO_2 sequestration is also a potential reservoir for injecting hydrofrac flow-back water. Thus geological studies published by researchers investigating CO_2 sequestration targets across the Appalachian Basin are a rich source of information for shale-gas operators who wish to understand water-storage possibilities local to prospect areas.

Because of the recent, intense focus by the gas industry on the Marcellus Shale, much geological information about Marcellus Shale geology has been published. Our objectives in this chapter are to only summarize key aspects of this growing body of papers describing Marcellus geology, and to create a reasonable number of references that provide readers more geological detail than we include in this short treatise.

Geological Overview

Bradford County, Pennsylvania, lies in the northeastern part of the asymmetric Appalachian foreland basin. The preserved elongate axis of the Appalachian Basin extends southwest-northeast across the western half of Pennsylvania. The eastern margin of the basin is overthrust by the Appalachian Mountains, and the western margin extends into Ohio and Kentucky. Appalachian sedimentation is controlled by repetition of passive margin environments, basin deepening and sediment starvation, and advances of immature siliciclastic units in a general east-to-west direction.

Delineating deep subsurface geology across Pennsylvania is largely controlled by hydrocarbon exploration. Recent exploration for tight-gas sand plays and post-2005 seismic-based exploration for Marcellus Shale and other

shale-gas plays have provided new geological information. There are few penetrations of the sub-Oriskany interval in Pennsylvania. As of 2009, only 170 sub-Oriskany well had been drilled in central and eastern Pennsylvania (DCNR, 2009a). Much of the reconstruction of deep geology comes from projections of trends outside of Bradford County compiled by the Pennsylvania Geologic Survey (Harper, 1990; Harper, 2008), the West Virginia Geologic Survey (Roen and Walker, 1996), and the U.S. Geological Survey (Milici and Swezey, 2006).

The stratigraphy and basin structure of northern Pennsylvania reflect Precambrian rifting and sediment deposition in a passive margin setting during most of the Cambrian through Early/Middle Ordovician (Fig. 3.1). Structural features EC, RR, RS, RT, and RW shown on Figure 3.1 are elements of the Precambrian Rome Trough. The RT arm of the Rome Trough extending across Pennsylvania is offset by several regional faults and passes in the immediate vicinity of our study site. Late Cambrian events included plate movement of the present-day Appalachian area into the evaporative subtropical trade winds belt (Fig. 3.2) where it remained until late Mississippian time (Miall and Blakely, 2009).

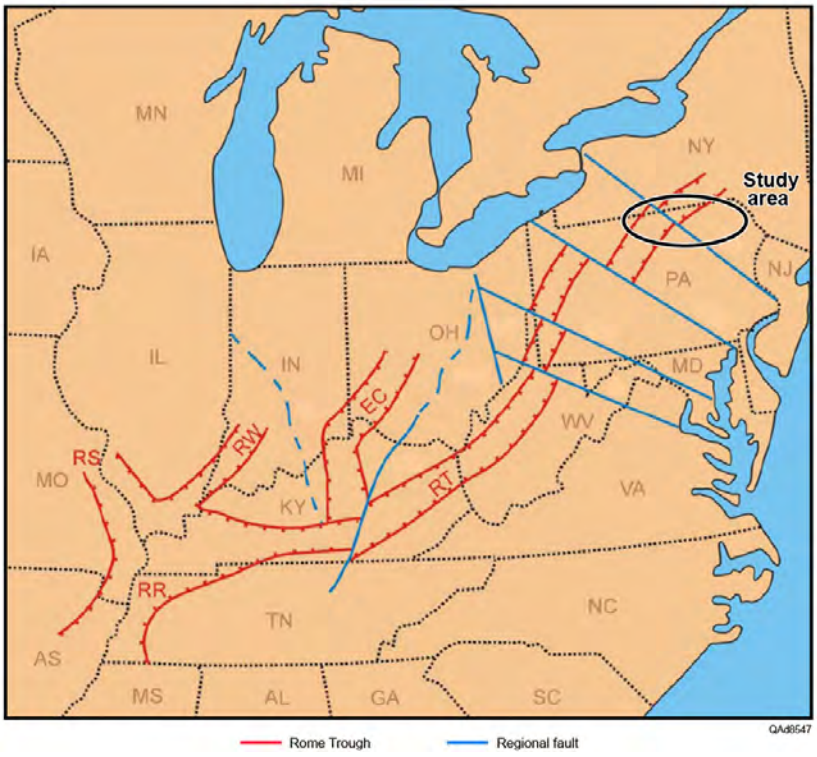

Figure 3.1. Red outline shows segments of the Precambrian Rome Trough (RR, RS, RW, RT, EC) and their offsets by later strike-slip faults (blue). After Harper (2005). Our study site in Bradford County, Pennsylvania is at the northern terminus of the Rome Trough.

Overprinted on this early depositional setting are the effects of continental collisions and tectonic movements that produced various uplifts, downwarps, foreland basin formation and fill, and burial by prograding clastic wedges during Late Ordovician/Early Silurian Taconic, Devonian Acadian, and Pennsylvanian Alleghenian orogenies. The Alleghenian collision resulted in late-stage, warm (110° C), reactive basinal fluids being flushed toward the Cincinnati Arch (Fig. 3.2), resulting in vugular porosity development in some Cambrian–Ordovician carbonates (Rowan et al., 2008). Of importance to our study, collision dynamics caused both thick-skin and thin-skin fault developments that include décollement surfaces associated with the Silurian Salina evaporite beds (Harper, 1990; Harper and Patchen, 1996; Fig. 3.3). This thin-skin faulting is well documented in northern Pennsylvania and across Bradford County, the location of our study site. Line drawings are shown on Figure 3.4 of the configurations of faulted and deformed Salina evaporates observed on two regional seismic lines.

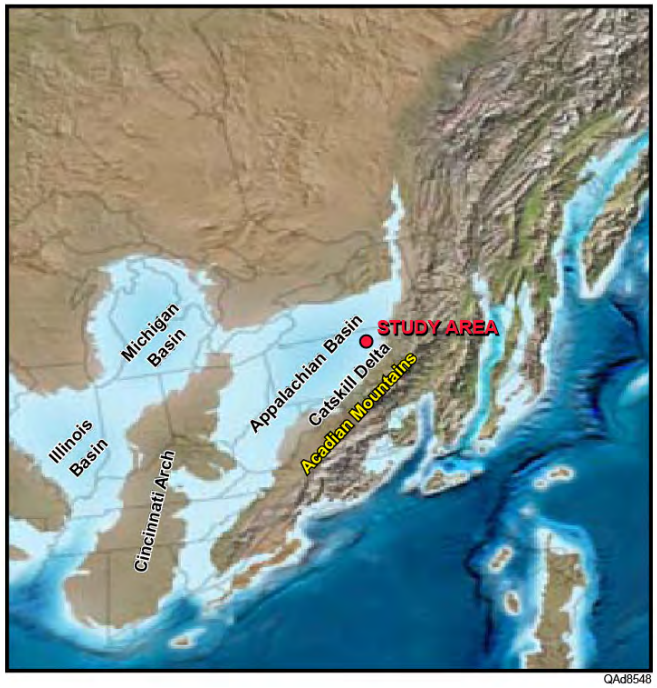

Figure 3.2. Middle Devonian paleo-reconstruction of Laurentia showing location of our study site in Bradford County, Pennsylvania. Our study area was proximal to the Acadian Mountains, the Catskill clastic wedge/delta, and the subsequent Alleghenian front (not labeled). Modified from Harper and Kostelnik (2010).

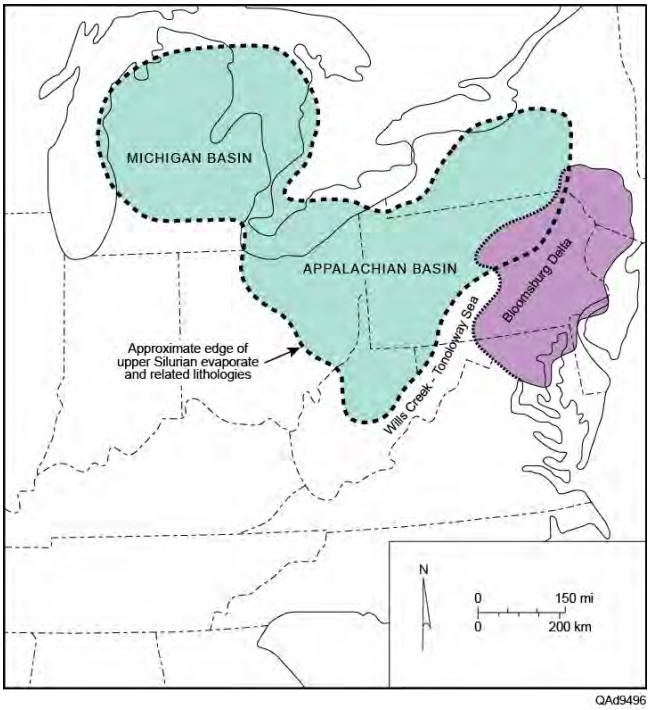

Figure 3.3. Depocenters for Silurian evaporites. Thick, deformed evaporite layers are present in some seismic profiles from Bradford County, Pennsylvania. The Bloomsburg Delta is contemporaneous with the lower part of the Salina evaporites (after DCNR, 2009a).

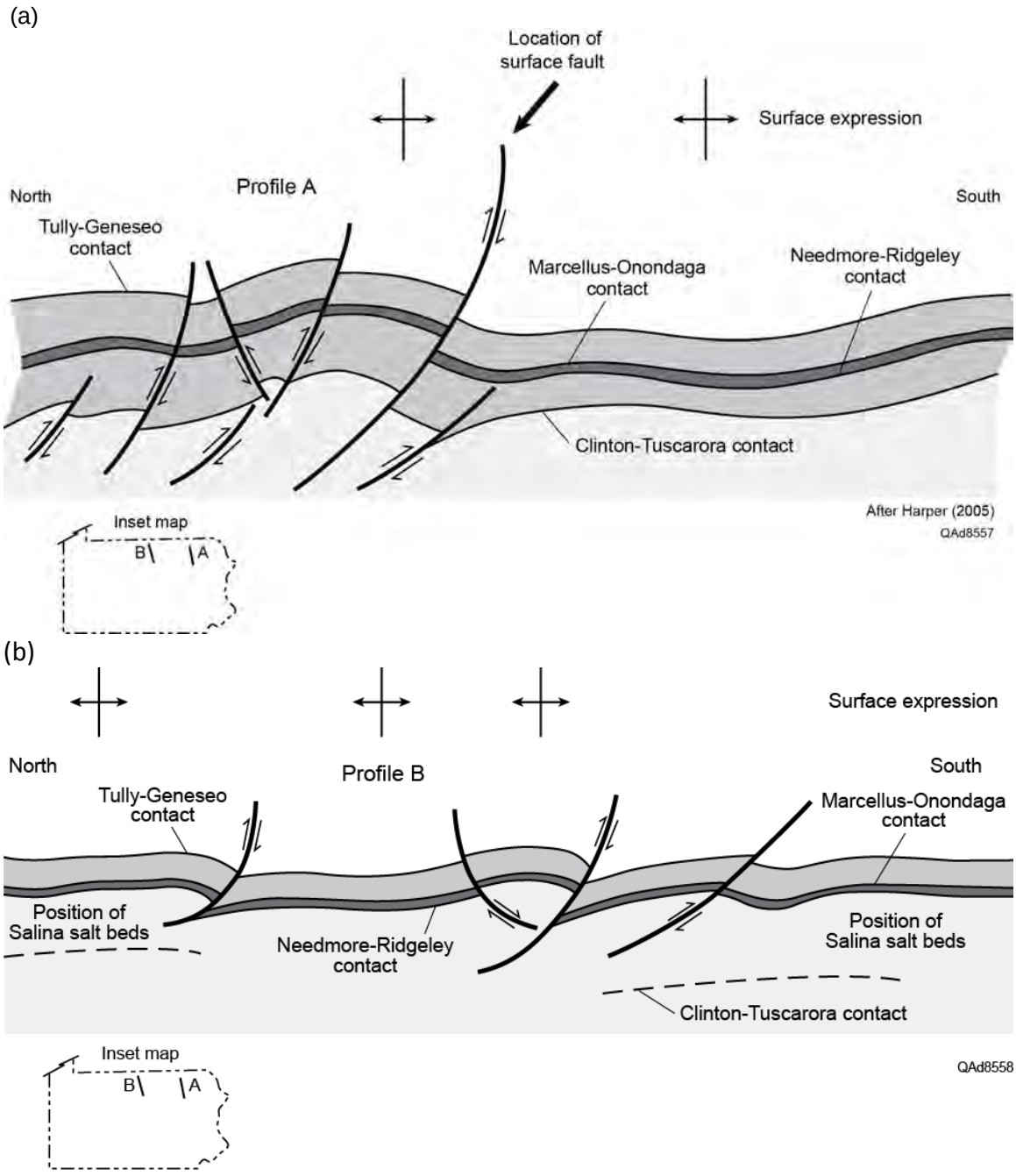

Figure 3.4. Thin-skinned, evaporite-soled faults interpreted on two seismic lines in northern Pennsylvania. These exhibits are line drawings of interpreted seismic horizons (after Harper, 1990).

Water Storage Units

Water-storage reservoir targets across the Appalachian Basin are most attractive when they demonstrate large storage capacity and injectivity and have no transmissive faults or fracture zones. Reservoir targets include deep saline reservoirs and downdip ‘water legs” of known hydrocarbon bearing zones.

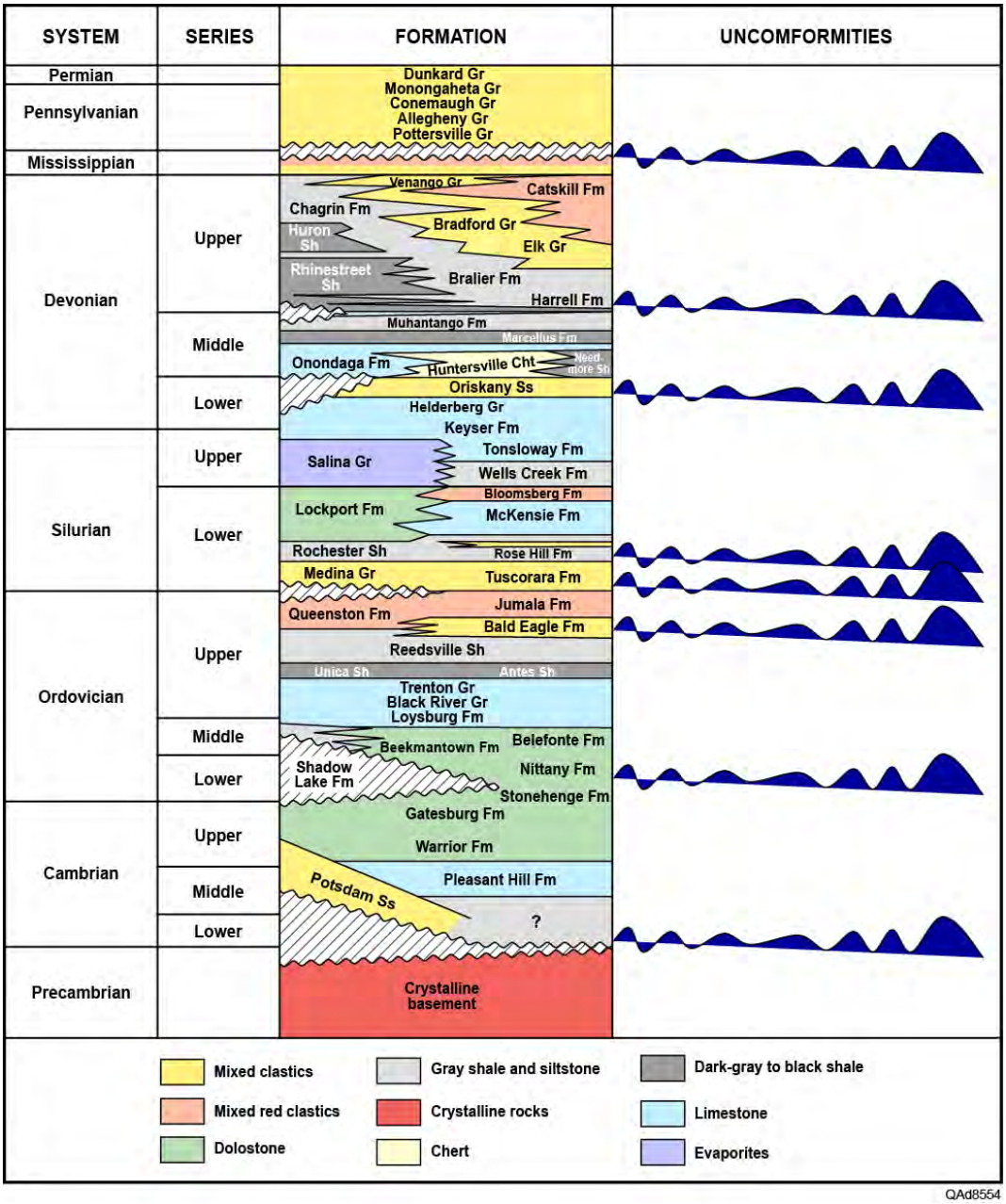

Figure 3.5. The most prospective water-storage reservoirs in Pennsylvania are sandstones and carbonates associated with unconformities. Porous transgressive sandstones often occur above unconformities, and porous carbonates often are created below unconformities by dissolution and dolomitization processes. Numerous unconformity surfaces are present across the Appalachian Basin, as shown (modified from DCNR 2009a).

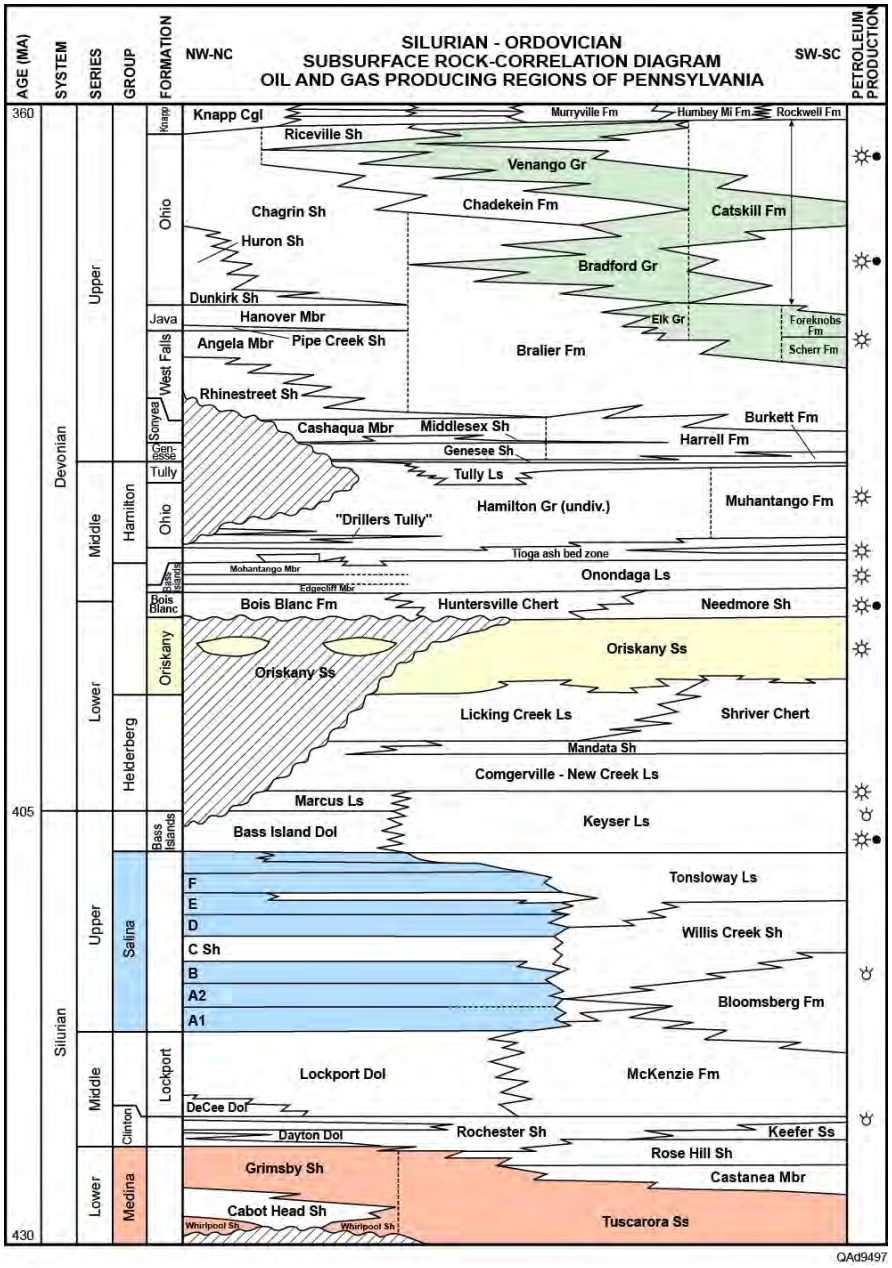

Figure 3.6. Four potential Silurian—Devonian water-storage targets in Pennsylvania are: (1) the Upper Devonian Venango-Bradford-Lock Haven/Elk clastic wedge, (2) Lower Devonian Oriskany sandstones, (3) Upper Silurian Salina evaporites, and (4) the Lower Silurian Tuscarora Formation (after DCNR, 2009a).

Most of the units in the stratigraphic column of Pennsylvania can be considered as confining zones or seals. In general, the best regional porosity development in the Appalachian Basin is associated with laterally extensive unconformities. Fortunately, several unconformities traverse the basin as documented on Figure 3.5. The most widespread sandstone reservoirs are transgressive sandstones developed immediately above, or between, regional

and local unconformities. These transgressive systems tend to grade upward into carbonates and shales. Sandstone porosity can develop locally in association with still stands or in association with tectonically forced regressions during progradations of clastic wedges. Such sandstone porosity development is observed in the Upper Devonian Venango and Lock Haven Groups (Fig. 3.6).

Porosity in carbonates may develop below unconformities as a result of karsting, dissolution, and dolomitization of grain-rich lithofacies. Dolomitization or leaching of carbonates can also result from contact with migrating basinal and hydrothermal fluids. Dolomitized reef rubble is reported to generate reservoir quality porosity in the Silurian Lockport Formation of Pennsylvania (Harper 2005).

In Pennsylvania, the most regionally prospective water-storage reservoirs are sandstones. Referring to Figures 3.5 and 3.6, these sandstone units are, from younger to older (Harper 2011; DCNR 2009a):

- Upper Devonian Venango and Elk/Lock Haven sandstones,
- Middle Devonian transgressive sandstones immediately below the Tully Limestone,
- Lower Devonian Oriskany (or Ridgeley), and
- Lower Silurian Tuscarora (Clinton/ Medina).

Although the Cambrian Potsdam Sandstone is likely present in the subsurface of eastern Pennsylvania, it has few penetrations and is probably too deeply buried to have retained porosity in that part of the State (DCNR 2009b). Cambrian and Lower Devonian sandstones were typically deposited as transgressive, shore-parallel sandstones. Middle Devonian and Lower Silurian siliciclastic depositional environments also include incised fluvial deposits. Upper Devonian reservoir-quality sandstones were deposited in a variety of fluvial, deltaic, and shallow marine environments. In general, fluvial sandstones in the Appalachian Basin are thought to be better able to retain porosity in the subsurface.

Petrophysical Properties of Water Storage Units

Within the western Pennsylvania area studied by Kostelnik and Carter (2009a), average porosities in Oriskany sandstones ranged from 1.4 to 14 percent. They report three main porosity types:

1. Primary intergranular porosity related to stratigraphic pinch-out zones near the Oriskany no-sand area and at the western limit of the Oriskany Sandstone,

2. Secondary dissolution of carbonate constituents that dominate combination stratigraphic/structural gas plays in western Pennsylvania, western West Virginia, and eastern Ohio, and

3. Fracture porosity that dominates gas plays in the central Appalachian Plateau Province and the Valley and Ridge Province**.**

Kostelnik and Carter (2009a) report permeability in the Oriskany ranges from 0.2 to 42.7 md, with stratigraphic pinch-outs at the northern and western edges of the basin having the highest permeabilities. In most of Pennsylvania, the development of secondary dissolution or fractures is important for developing permeability in the Oriskany.

Upper Devonian Water-Storage Sandstones

Prospective Upper Devonian sandstones in Pennsylvania belong to the Venango, Bradford, and Elk Groups (Fig. 3.6), which are associated with the Middle to Upper Devonian Catskill delta that formed in response to the Acadian orogeny (Fig. 3.2). Devonian strata are thickest in eastern Pennsylvania, where they reach a thickness of 12,000 ft (3658 m). Reservoir quality sandstones were deposited primarily in deltaic and turbidite environments associated with tectonically forced low stands of the progradational Devonian clastic wedge (Milici and Swezey, 2006).

The Venango group, including the Murrysville (Brea in part), Hundred-Foot Zone, and Gordon Formations, produces oil and gas in southwestern Pennsylvania (Sager, 2007) and has considerable potential for water storage in western Pennsylvania. In southwestern Pennsylvania where the Murrysville depositional environment is interpreted as a high-energy braid delta, porosity can exceed 20-percent, and permeability may exceed one Darcy (Smosna and Sager, 2008). When large pore volumes are found, porosity is retained or enhanced by coarse grain size, moderate compaction, leaching of unstable grains, lack of externally derived carbonate cement, and the presence of detrital and authigenic chlorite that inhibited quartz cement overgrowths (Sager, 2007). Unfortunately, the Venango Group sandstone lithofacies do not extend into eastern Pennsylvania where our study site is located.

The most important Upper Devonian target in Bradford County may be the Lock Haven sandstones of the Catskill clastic wedge that are hydrocarbon productive in north-central Pennsylvania's Centre and Clinton Counties. The Council Run field covers about 290 mi^2 (742 km^2) and has approximately 700 wells with a cumulative production of 56 Bcf as of 2001 and an estimated ultimate recovery of 250 Bcf (Laughery et al., 2004). The most prolific of the Council Run reservoirs are in the Lock Haven Formation and were deposited in deltaic and nearshore marine environments associated with a lowstand systems

tract of a third-order tectonically forced regression. Multicomponent seismic mapping of this or other Upper Devonian lowstands may allow similar reservoirs to be identified for water storage. At the Council Run Field, core porosity in lithic to feldspathic reservoir sandstones ranges up to 16-percent. Permeabilities are generally low and require hydraulic fracture stimulation. Original porosity has been reduced by diagenesis and compaction, enhanced by grain dissolution of deformable lithic fragments, and preserved, in part, by pore-lining clay cements and early hydrocarbon emplacement (Laughery et al., 2004). It is important to note that this mode of porosity formation and retention appears to be a regional phenomenon along the Alleghany structural front (Bruner and Smosna, 1994; Laughery et al., 2004).

Middle Devonian Water-Storage Sandstones

Middle Devonian sandstones are regionally less extensive, but include transgressive sandstones immediately below the Tully Limestone, a strong seismic marker at the top of the Hamilton Group or Mahantango Formation (Fig. 3.7). These transgressive units are interpreted as being coincident with the regional erosion of the Moscow Shale observed in upstate New York by Lash

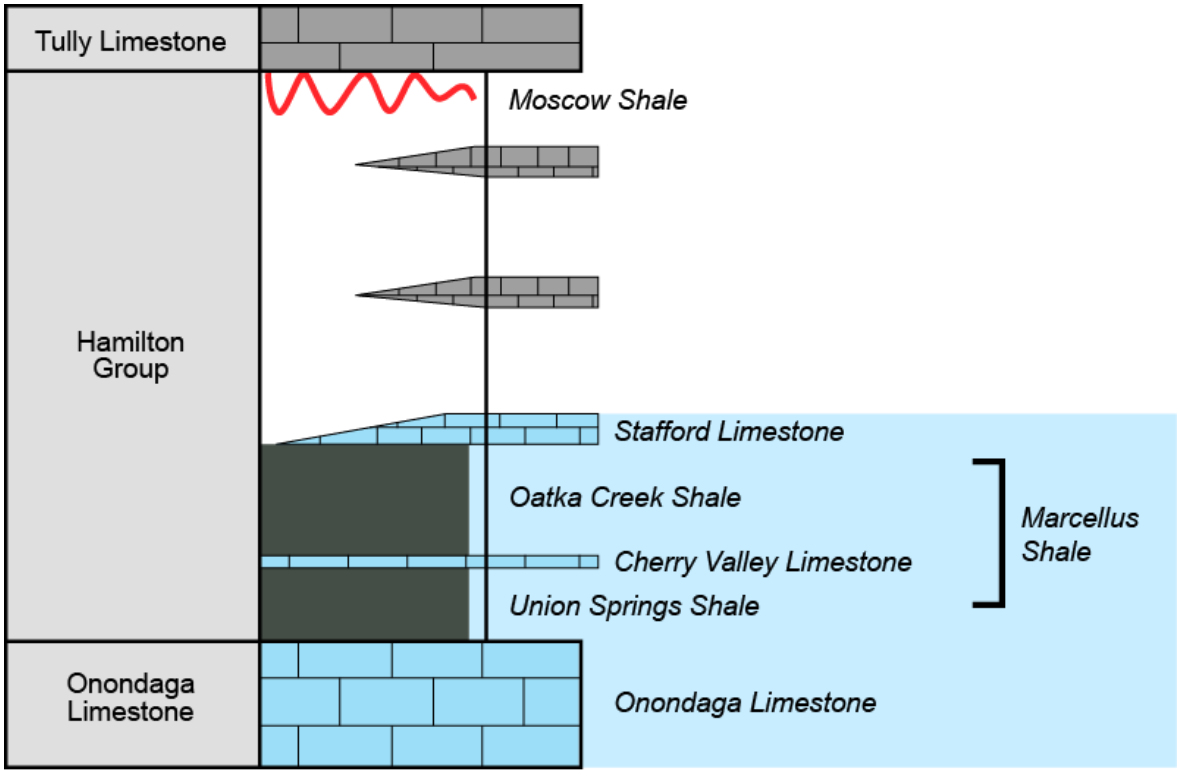

Figure 3.7. Middle Devonian stratigraphy in New York and Northern Pennsylvania. Unconformity related sandstones below the Tully Limestone may form potential water-storage reservoirs in Bradford County. Modified from Lash, 2007.

(2007). On regional seismic lines, these sandstones display channel-shaped morphologies, are quite likely incised into underlying shales, and might possibly develop reservoir quality porosity in Bradford County.

A striking example of such a channel-like morphology defined by our Bradford County seismic data is illustrated in Chapter 9. An intriguing aspect of this channel facies is that it is prominent in converted-shear data but is absent in conventional P-wave data, the latter being the primary seismic data used to evaluate water-storage targets. This study thus presents evidence that multicomponent seismic data should be used to evaluate water-storage reservoirs and their seals rather than having total reliance on P-wave data.

Lower Devonian Water-Storage Sandstones

The Oriskany (Ridgeley) Sandstone is considered the most promising siliciclastic saline reservoir in northeastern Pennsylvania (Skeen and Carr, 2009; Kostelnik and Carter, 2009b; DCNR, 2009a). The Oriskany Formation occurs across New York, Pennsylvania, Ohio, Maryland, West Virginia, Virginia, and Kentucky (Diecchio, 1985; Bruner and Smosna, 2008; Dilmore et al., 2008). As a facies, the Oriskany is a fossiliferous shallow-marine quartzarenite, variably cemented with calcite or quartz. Depositionally, the Oriskany is a transgressive sandstone that unconformably overlies the Helderberg Limestone or equivalents, and is overlain by more siliciclastic-poor lithologies of the Onondaga Limestone, Huntersville Chert, or Needmore Shale (Figs. 3.7 and 3.8). These units may locally be arenaceous (Diecchio, 1985; Skeen, 2010).

The Oriskany sandstone was generally deposited on an unconformity and in many places also has an erosional upper contact (Fig. 3.9). Locally in parts of central Pennsylvania, the Oriskany appears to be in conformable contact with the underlying Helderberg Group limestones and cherts (DCNR, 2009a). The Oriskany (Ridgeley) is an orthoquartzite that is locally conglomeratic and was deposited in a shallow marine environment. In central Pennsylvania, the Oriskany was deposited in a high-energy shoreface environment with shallow marine shoreline parallel bars, and tidally influenced sandstone bodies (Kostelnik and Carter, 2009a). Within our study area the Oriskany is estimated to have a thickness between 50 and 100 ft (15 and 30 m), as shown on Figure 3.10.

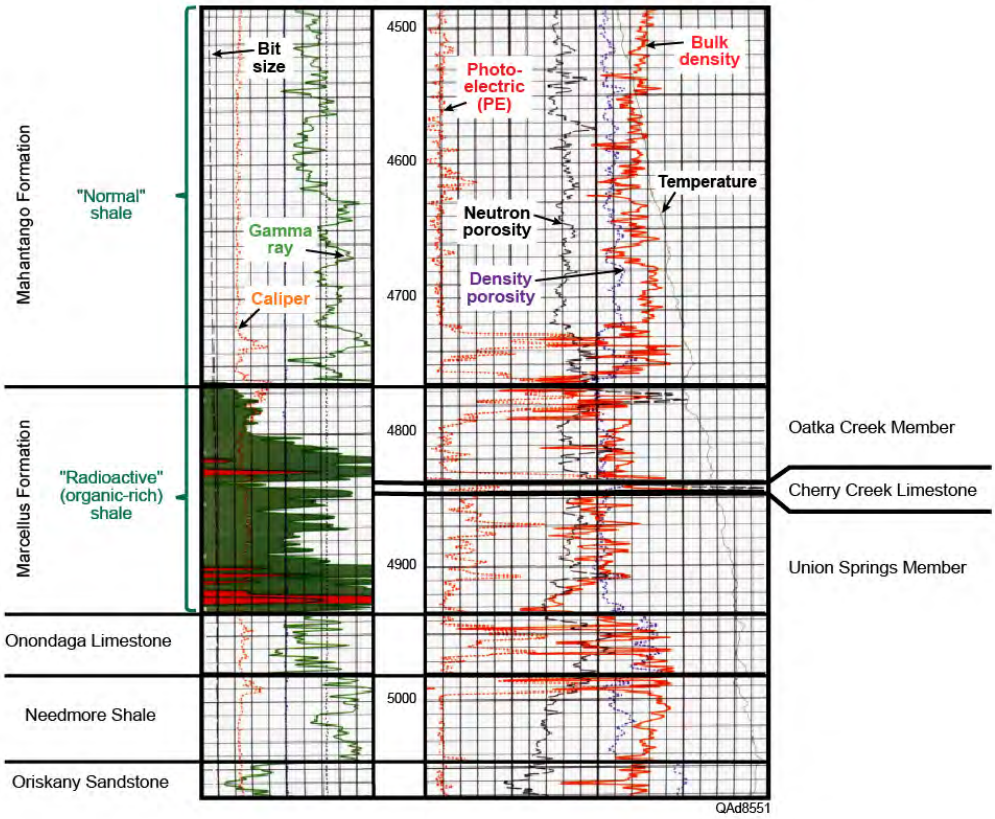

Figure 3.8. Type log for the Oriskany Sandstone in the Bradford County area. After Harper and Kostelnik (2010).

The Oriskany produces oil and gas from permeability pinch-outs in northwestern and north-central Pennsylvania and from fractured reservoirs in southwestern Pennsylvania (Opritza, 1996; Patchen and Harper, 1996; Kostelnik and Carter, 2009a). Depth of the Oriskany in these areas is generally between 1700 and 3100 ft (518 and 945 m). Some Oriskany gas fields in the central Appalachian Basin coincide with the boundary of higher and lower salinities and appear to reflect geologic-scale basinal fluid flow (Skeen 2010). In addition to being hydrocarbon productive, the Oriskany has been used for injection of industrial wastes. There are 32 Oriskany gas storage fields with a cumulative total of over one Tcf storage capacity (Skeen, 2010). The primary risk for Oriskany water storage in Bradford County, and elsewhere parallel to the Alleghany structural front, is the presence of fractured and leaky caprock (Kostelnik and Carter 2009b). Seismic detection of faults and fracture systems is therefore critical to evaluating the non-hydrocarbon bearing Oriskany for water storage potential.

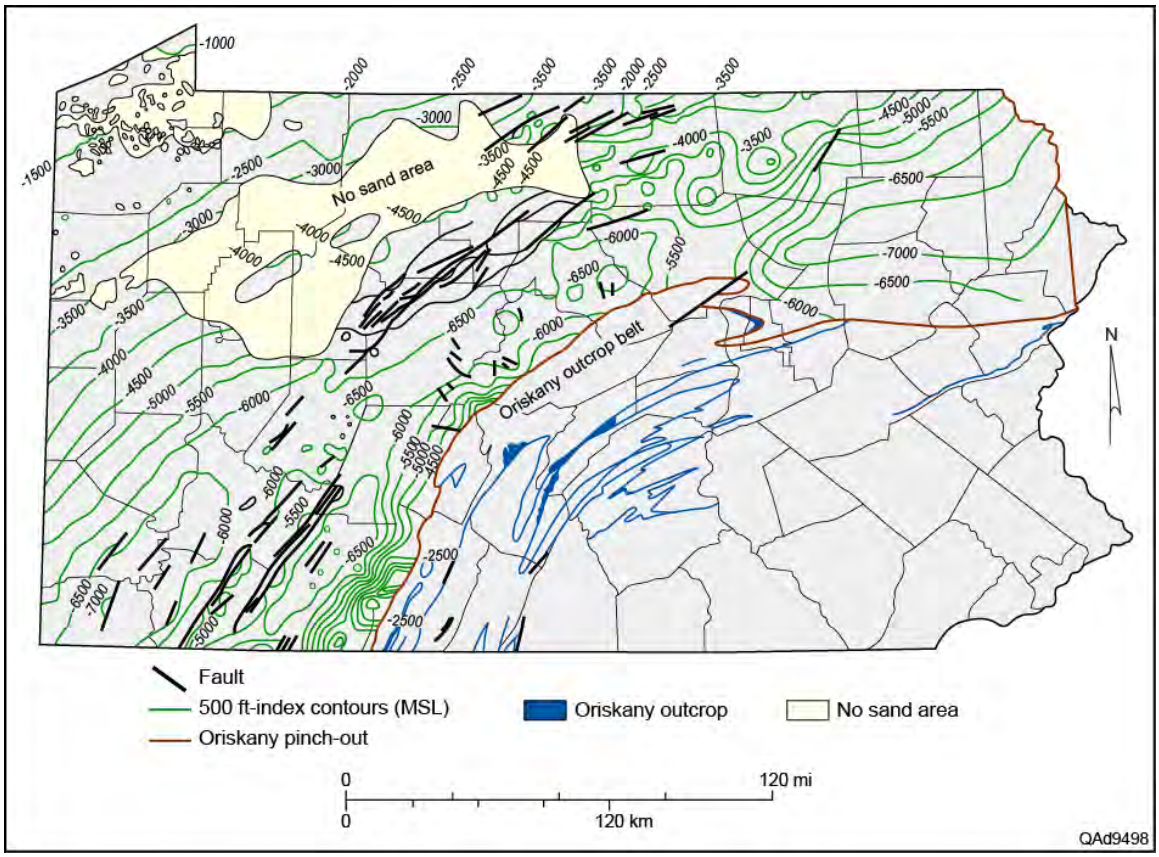

Figure 3.9. Structure on top of the Oriskany. Depths are subsea. Note the areas of nondeposition in northwestern Pennsylvania. The depth of the Oriskany changes rapidly local to our study area. (After DCNR 2009a)

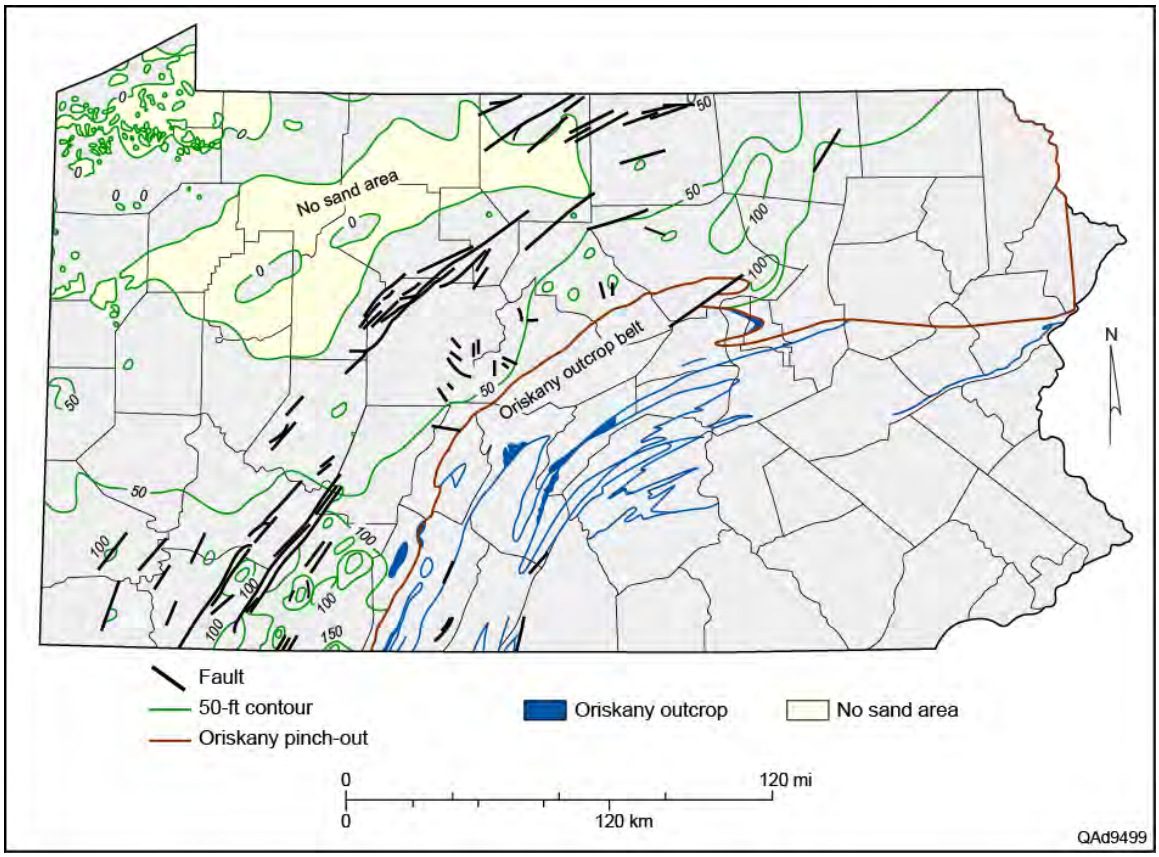

Figure 3.10. Thickness of the Oriskany sandstone. The Oriskany can be expected to be between 50 and 100 feet thick across Bradford County. After DCNR 2009a.

Lower Silurian Medina Group/Tuscarora Sandstone Water-Storage Units

Within a sequence stratigraphic framework, Medina Group sandstones of northwestern Pennsylvania and Tuscarora sandstones of northeastern Pennsylvania unconformably overlie the Upper Ordovician Queenston Shale to the west and the time-equivalent siliciclastics of the Juniata Formation to the east (Fig. 3.5). The Tuscarora is correlative to the Shawangunk Formation in eastern Pennsylvania (DCNR 2009b). Tuscarora sandstones are derived from the Taconic highlands to the east. Lithologies include fine-grained to coarse-grained quartz arenite, subgraywacke, siltstone with occasional thin shales, and conglomerates. Deposition of these sandstones occurred near the end of the Taconic orogeny, and depositional environments ranged from fluvial to shallow marine. Depositional processes commonly produced shoreline-parallel sand bodies. Of six lithofacies identified by Castle and Byrnes (2005) in the Lower Silurian sandstones of the Appalachian basin, those associated with incised fluvial channels had the highest porosities and permeabilities. Lithofacies of the Medina and Tuscarora sandstones in Northern Pennsylvania have variable lithologies, low porosity, and burial depths of 7,000–10,000 ft (2,134–3,048 m) subsea (Fig. 3.11) across Bradford County (DCNR, 2009a).

Although Medina Group sandstones (including the Clinton) are relatively thick and form oil and gas reservoirs in Crawford and Erie counties, Pennsylvania, their north-central and northeastern Pennsylvania equivalents are thin, tight, have variable lithologies, and are less attractive as water-storage units. The Tuscarora Formation can be expected to be between 150 and 200 ft (46 and 61 m) thick in Bradford County. For comparison, sandstone lithologies across the state generally range from 3–50 ft (1–15 m) with an average of about 23 ft (7 m) as shown on Figure 3.12 (DCNR, 2009a).

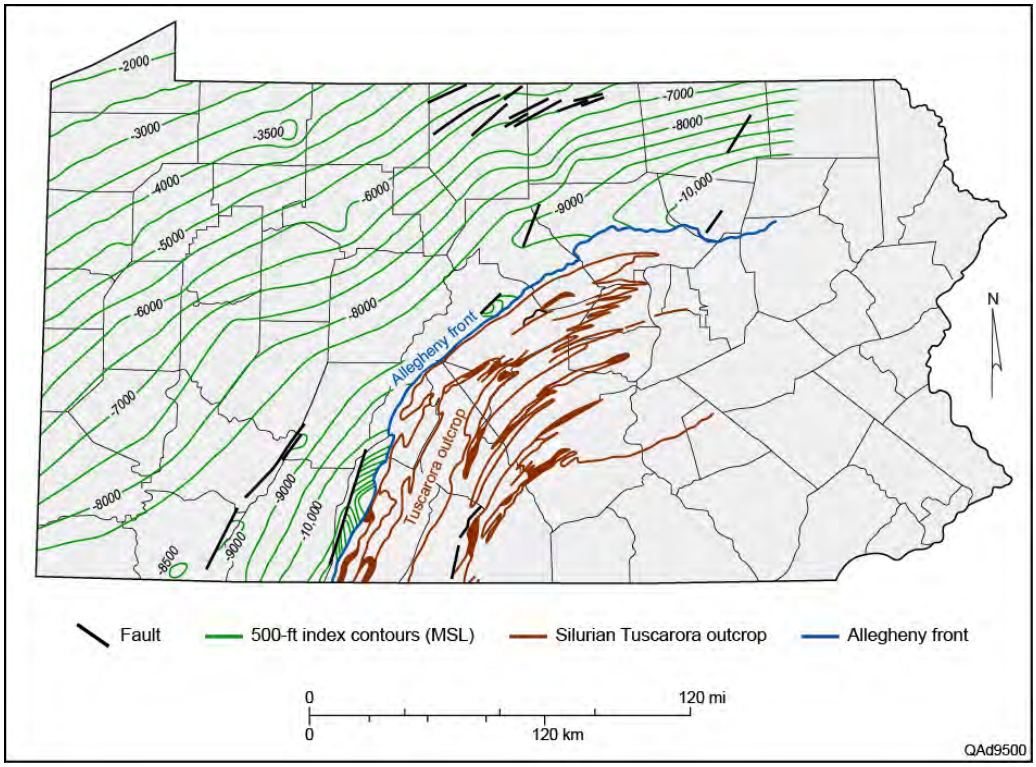

Figure 3.11. Structure across top of Silurian Tuscarora in Pennsylvania. Depths are subsea (after DNRC, 2009a).

Ordovician Water-Storage Reservoirs

The greatest number of siliciclastics in the Ordovician section is associated with unconformities and sea-level stillstands of the Upper Ordovician Queenston clastic wedge (Fig. 3.5). These include sandstones of the Juniata and Bald Eagle Formations. In Juniata County, the Bald Eagle Formation comprises fine to coarse sandstones with some cross-stratification, and some conglomeratic intervals. The sandstones of the overlying Juniata formation also include siltstones and some shale.

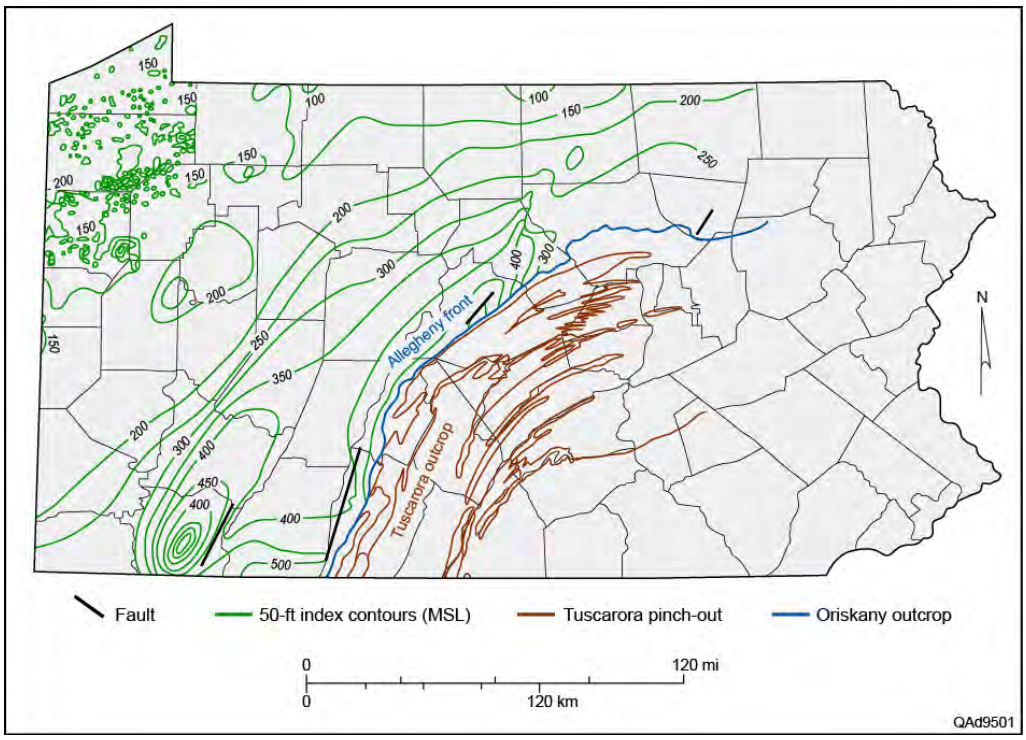

Figure 3.12.Gross thickness of the Silurian Tuscarora Formation. Actual sandstone lithology thickness averages less than 30 ft (9 m) (after DCNR 2009a).

Cambrian Water-Storage Sandstones

During the Cambrian, the North American landmass of Laurentia, containing Pennsylvania, was at the equator and rotated about 90 degrees clockwise of its present position. The collision of the passive margin of Laurentia with the Taconic island arc initiated during mid-Cambrian (Miall and Blakely, 2009) and culminated in the Ordovician, forming the Appalachian foreland basin and causing subaerial karstification of carbonates across of much of the craton.

In Pennsylvania, transgressive Cambrian sandstones are considered to have greater sequestration potential than Cambrian carbonates. Because of increasing depth of burial and lack of penetrations in northeastern Pennsylvania, the Midwestern Regional Sequestration Partnership (MRCSP) and the Department of Conservation and Natural Resources (DCNR) have assessed only Cambrian sandstones in the western part of Pennsylvania. Seismic surveys acquired in conjunction with shale-gas exploration are providing important new information on depth and porosity retention in the deeper part of the Appalachian Basin.

Gatesburg Water-Storage Sandstone

Cambrian sandstones in Pennsylvania include the Upper Cambrian Gatesburg and the transgressive basal sandstones of the Potsdam (Fig. 3.5). The Upper Sandy member of the Gatesburg is correlative to Rose Run sandstones, which produce hydrocarbons in eastern Ohio (Riley et al., 1993), especially where they subcrop beneath the Knox unconformity. Depositional environments of these sandstones in eastern Ohio include tidal channels, bays, estuaries, and shallow marine shelf (Riley et al., 1993, Nwaodua, 2008).

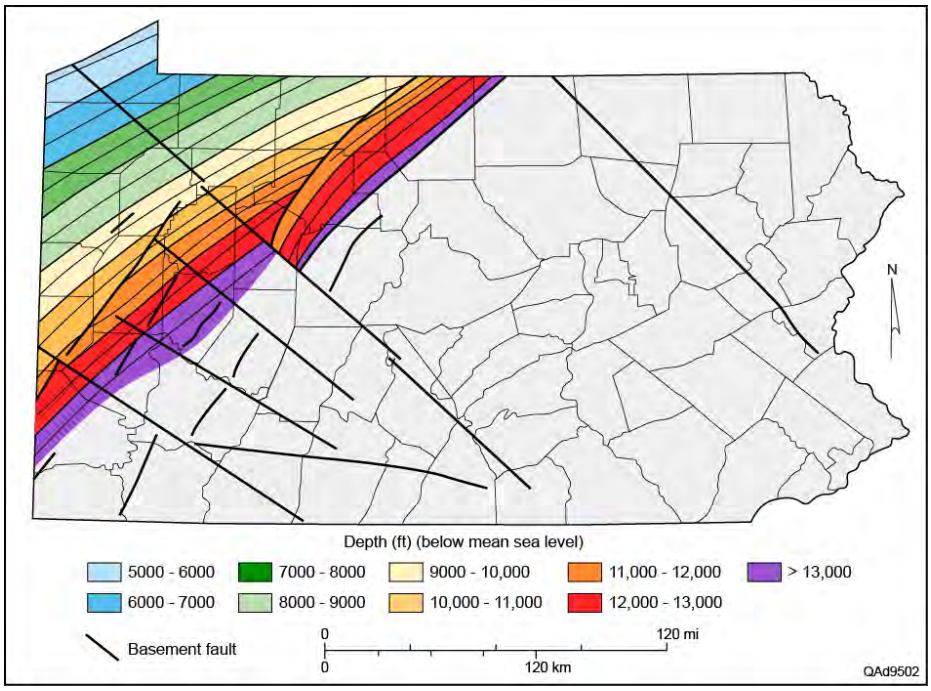

Figure 3.13. Structure on the Potsdam Sandstone. Increased acquisition of 3D seismic data should allow mapping to extend into northeastern Pennsylvania (after MRCSP, 2005, and DCNR, 2009b).

Structure and isopach maps of Cambrian sandstone across western Pennsylvania are shown on Figures 3.13 and 3.14, respectively, to illustrate the water-storage potential of these deep rocks. One Gatesburg brine disposal well in northwest Pennsylvania demonstrates reservoir potential (DCNR, 2009b). Both Gatesburg and Potsdam sandstones are expected to be present in northern Pennsylvania, including Bradford County, but there are few well penetrations to provide evaluation data. The Rose Run Formation in Ohio and West Virginia includes dolomites as well as sandstones, and although the overall thickness of the correlative Upper Sandy Member increases into the deeper Appalachian Basin, the sandstone facies may decrease.

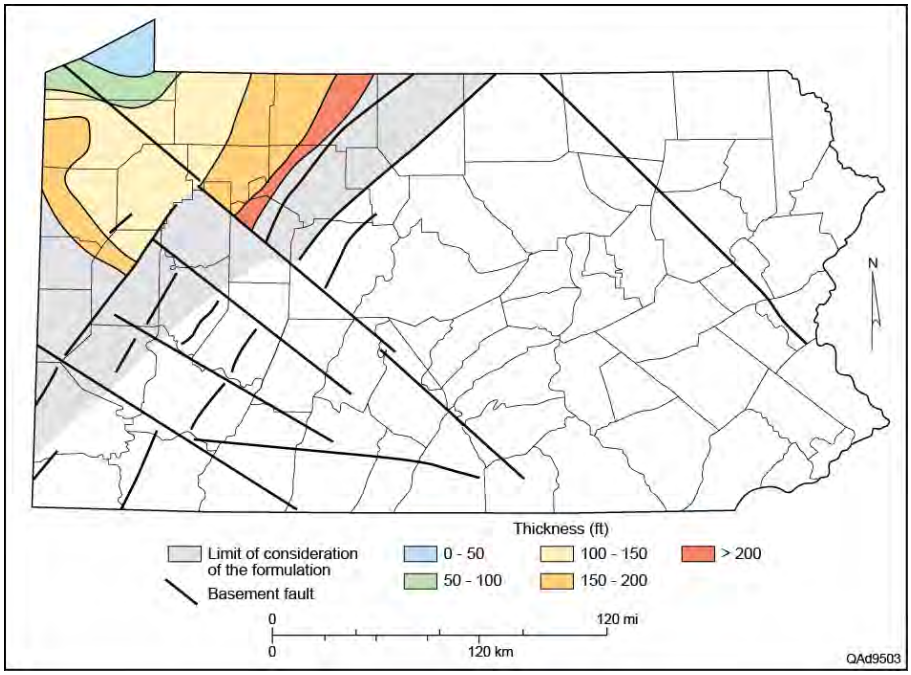

Figure 3.14. Thickness map of the Potsdam Sandstone (after MRCSP, 2005, and DCNR, 2009b).

Basal Cambrian Water-Storage Sandstones

Basal Cambrian sandstones directly and unconformably overlie Precambrian non-sedimentary basement. These include dolomitic sandstones of the Conasauga Group of the Rome Trough that extends into western Pennsylvania, and the stratigraphically older, but unnamed transgressive sandstones of both the Rome Trough and the eastern proto-Appalachian Basin of Pennsylvania (DCNR 2009b). These sandstones are expected to be 50 to 150 ft (15 to 45 m) thick.

Cap rock for the basal Cambrian sandstones includes the Queenston Shale and relatively thick, continuous, low-permeability Trenton and Black River limestones. Although the expected low porosities and depths of 10,000 ft (3,048 m) or greater generally make Cambrian sandstones less attractive as sequestration targets, paleotopographic and structural highs are strong controls on reservoir development. New 3D seismic data acquired in Bradford and other northeastern Pennsylvanian counties should identify structural highs and define porosity-sensitive seismic attributes.

Geological Overview of the Marcellus Shale

The Middle Devonian Marcellus Shale spans a distance of 600 mi (960 km), six states, and two countries. It extends into the Finger Lakes region of New York, beneath Lake Erie into southern Ontario, across Pennsylvania, eastern Ohio, western Maryland, West Virginia, extreme western New Jersey, and into Kentucky and Tennessee (Fig. 3.15). The limit of the play is defined to the north, south, and east by the Marcellus outcrop belt and to the west by stratigraphic pinch-out or by erosional truncation beneath the mid-Devonian unconformity (Wrightstone 2009). The Marcellus is exposed in central New York and reaches depths of over 8,000 ft (2440 m) in southern Pennsylvania (Harper and Kostelnik, 2010.)

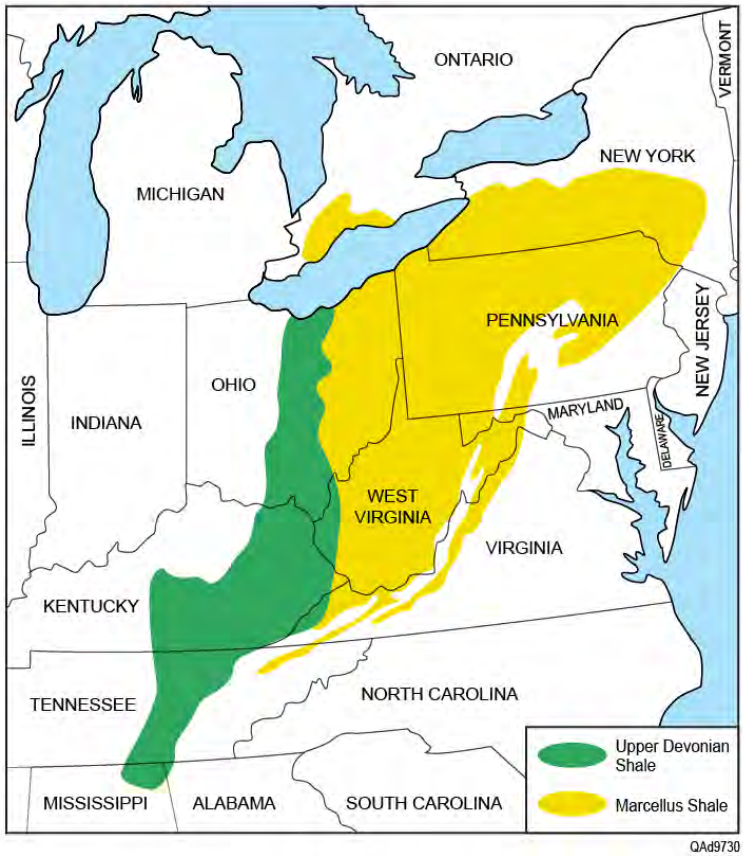

Figure 3.15. Distribution of Devonian organic-rich black shales in the Appalachian Basin (Modified from Harper and Kostelnik (2010.)

Gross thickness of the Marcellus ranges from more than 250 ft (76 m) in northeast Pennsylvanian and New Jersey to a zero isopach in eastern Ohio and western West Virginia (Wrightstone, 2009). Local irregularities in eroded underlying carbonates and extra accommodation space caused by down-dropped fault blocks locally alter the thickness (Lash, 2007).

Stratigraphy of the Marcellus

The Middle Devonian Marcellus Shale belongs to the Hamilton Group, which has various subdivisions across the Appalachian basin (Fig. 3.16). The Hamilton Group overlies the Onondaga Formation in New York, the Selinsgrove carbonate in western Pennsylvania, the Needmore shale in western Maryland and parts of north Virginia and West Virginia, and the Columbus Limestone in Ohio, where the Marcellus pinches out (USGS, 2006).

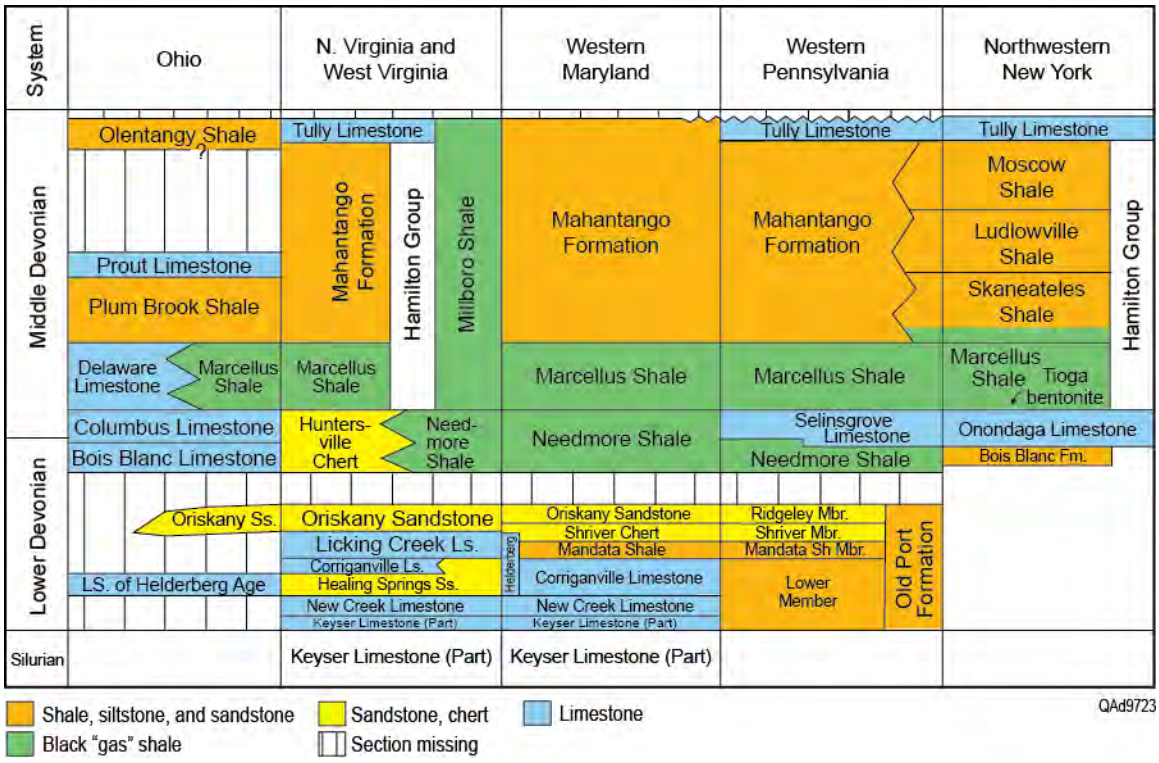

Figure 3.16. Stratigraphy of the Lower and Middle Devonian of the Appalachian Basin, with emphasis on the Hamilton Group. (Modified from USGS, 2006.)

In New York, the Marcellus Shale unconformably overlies the eroded Onondaga Limestone. In ascending order, the Marcellus consists of a basal black shale (the Union Springs), the Cherry Valley Limestone, and an upper black shale (the Oatka Creek). The Union Springs forms the Lower Marcellus, and the Oatka Creek is the Upper Marcellus (Fig. 3.17). Additional shale and limestone members are recognized above the Oatka Creek in New York; these units are equivalent to the Mahantango elsewhere. The Tully Limestone is the upper bounding formation of the Hamilton Group. The Union Springs Shale, Cherry Valley Limestone, and the lowermost part of Oatka Creek Shale pinch out to the west (Rickard, 1984, Lash, 2007; Smith 2011). In Ontario, the Hamilton

Group consists of the equivalent Bell Shale, Rockport Quarry Limestone, and the Arkona Shale (Rickard, 1984). In south central Pennsylvania, the Hamilton group includes in stratigraphic ascending order: the Marcellus, Fisher Ridge, Montebello sandstone, Sherman Ridge and the Tully Limestone (Pennsylvania State Geologic Survey, 1995).

Figure 3.17. Subdivisions of the Marcellus Shale in central New York. After Smith (2011).

Appalachian sedimentation from the Cambrian to Middle Ordovician is marked by passive margin deposition, whereas Late Ordovician to Late Devonian sedimentation reflects repeated tectonic-induced basin deepening and sediment starvation to the west, and an increasing advance of texturally and compositionally immature siliciclastics from the east (Fig. 3.6).

Marcellus Depositional Environment

The westward stepping nature of Devonian black shales can be explained in terms of four tectophases (Ettensohn, 2004) that link basin deformation, subsidence, and sedimentation. This depositional model includes an active orogenic highland that created a westward migrating foreland basin and an associated subaerially exposed peripheral forebulge on the western, craton side of the basin (Lash, 2007). The eroding orogenic fold-belt supplied siliciclastic

sediments, which become finer grained from east to west. Much of the mobile sediment was trapped in the foreland basin.

Figure 3.18 shows the eight organic-rich Devonian/ Mississippian shales assigned to four major tectonically controlled phases (Tectophases) of sediment deposition (Lash, 2007). The Marcellus Shale belongs to the second tectophase. Three of the regional black shales are underlain by carbonates that mark temporary basin tectonic quiescence. For the Marcellus Shale in central New York, the underlying limestone unit is the Lower Devonian Onondaga Limestone. Later thrust-loading, subsidence, and migration of the forebulge to the west are indicated by onlap of the Upper Devonian Geneseo black shale onto the eroded Tully limestone (Lash, 2007; Smith 2011).

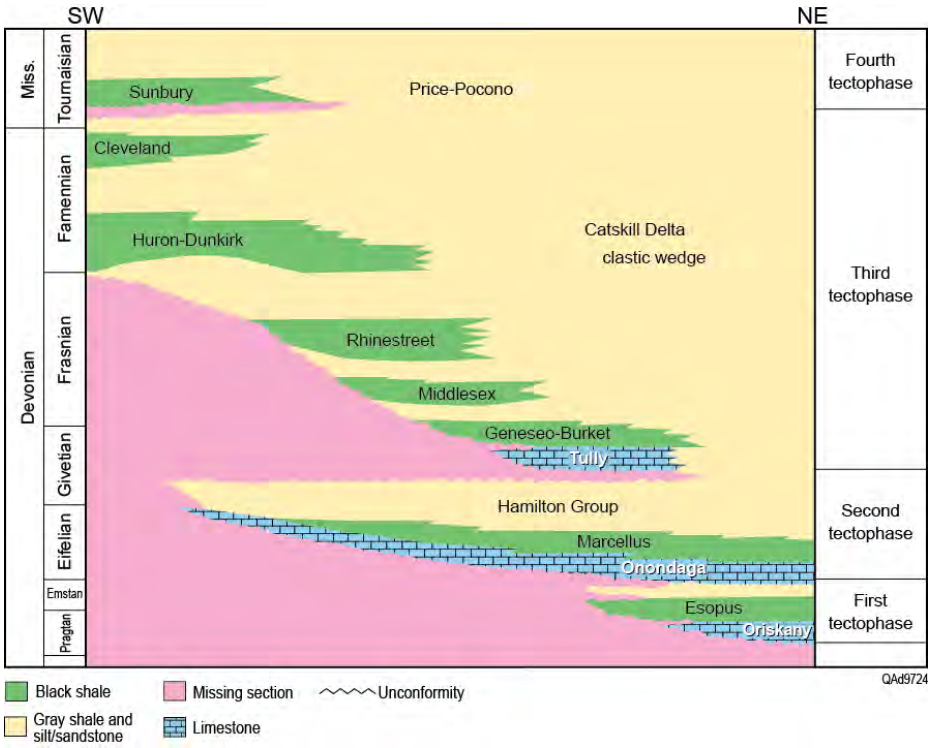

Figure 3.18. Eight Devonian organic-rich shales and their relation to four major tectonically controlled phases of sediment deposition. After Lash (2007).

The development of black shales west of the basin axis has caused a reinterpretation of depositional environments. Although organic-rich black shales have traditionally been interpreted as being the product of deep, sediment-starved basins (Fig.3.19), recent stratigraphic work across the Appalachian Basin indicates a shallow, low-oxygen environment for Devonian shales. In this depositional model, the Marcellus Shale was deposited during Devonian greenhouse conditions involving a tectonically forced, rather than an eustatic sea

level, transgression. These conditions are postulated by Smith and Leone (2010) to have been conducive to freshwater runoff from land and to the development of shallow anoxic conditions along the margin of newly developing tectonic peripheral forebulges (Fig. 3.20). Note that the lower three black shales in Figure 4 overlie carbonates, a situation which is consistent with the production of dissolved, rather than suspended, bedload during erosion.

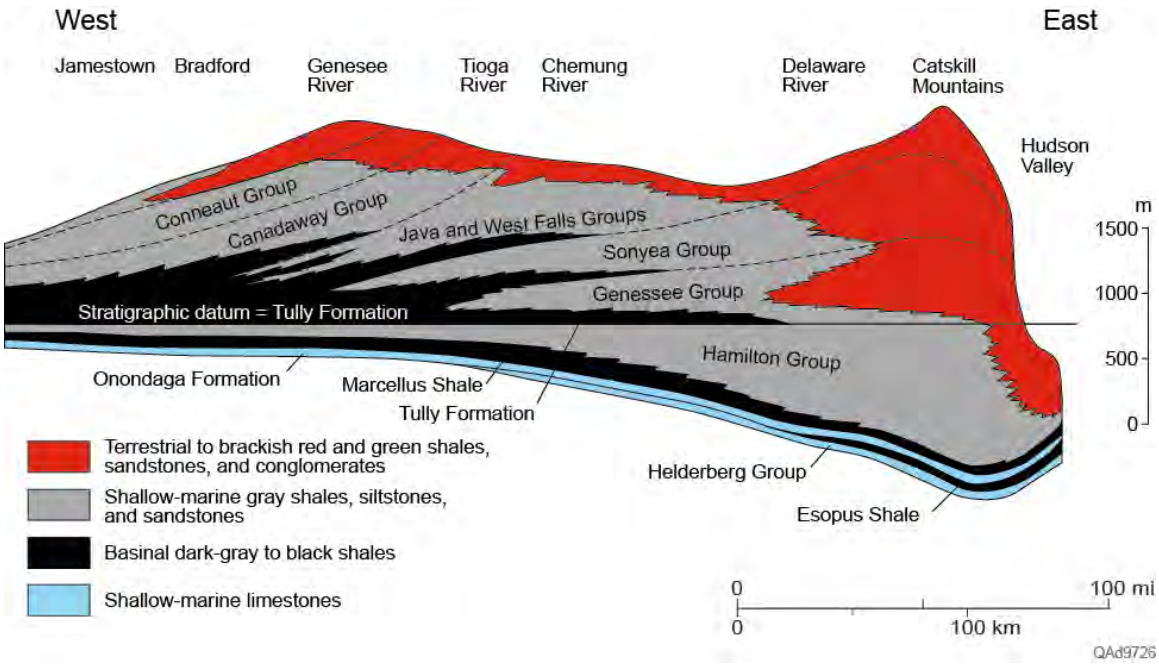

Figure 3.19. Older, deep-water, downlapping model of the Devonian black shales, shown for a cross-section across New York. After Smith and Leone (2010).

Details of the development of anoxic depositional environments under shallow-water conditions are shown on Figure 3.20. In this model, Devonian shales were probably deposited in 30 to150 ft (9 to 45 m) of water with the deeper foreland basin to the east being more fully oxygenated, and with siliciclastic input from the mountain front causing siltstones and gray shales to prograde from east to west as shown on Figure 3.21 (Smith and Leone, 2010).

(a)

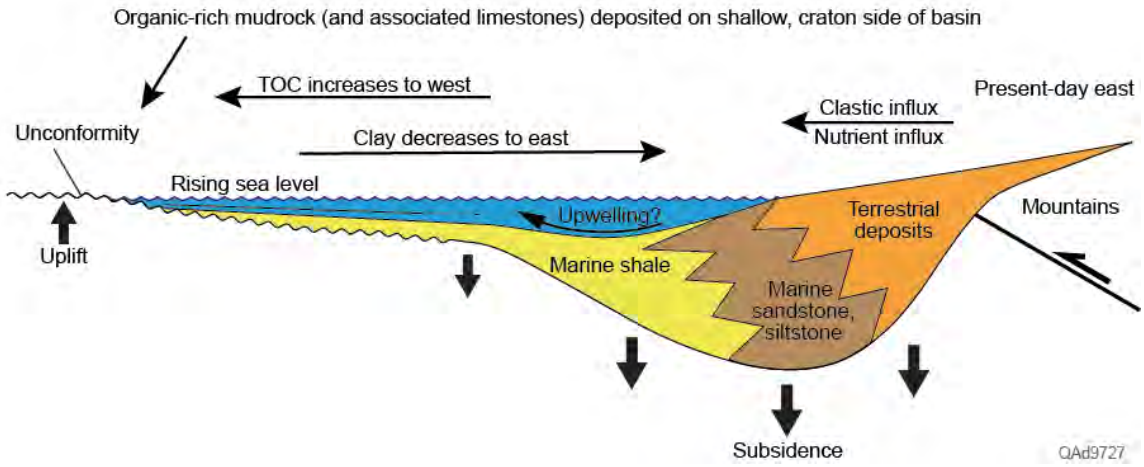

(b)

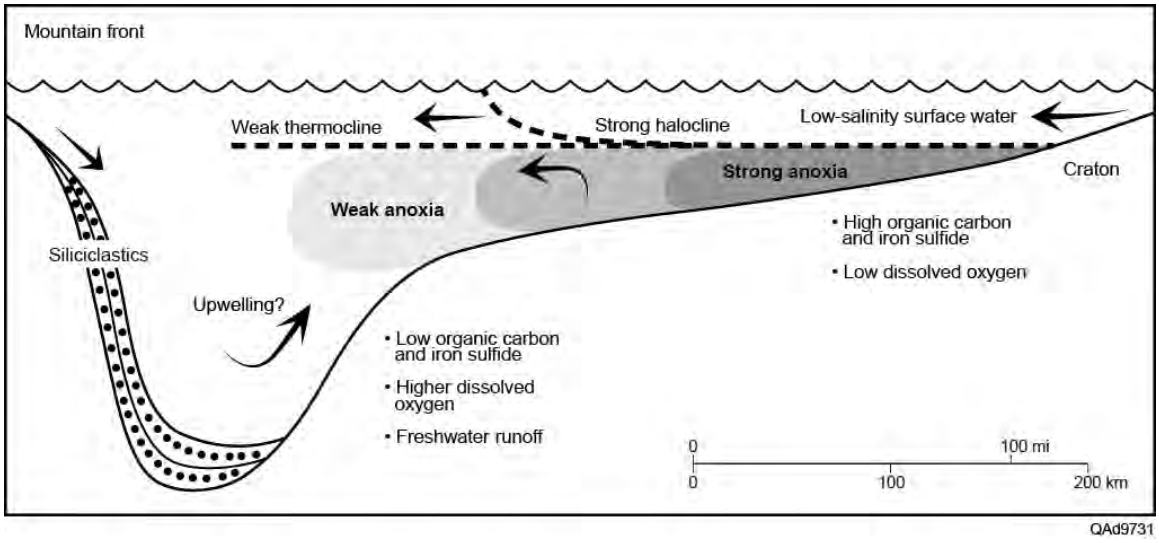

Figure 3.20. (a) Shallow water depositional model for Devonian organic-rich black shales of New York. (b) Hydrographic details of development of a shallow, sediment-starved anoxic marine depositional environment. Modified from Smith and Leone (2010).

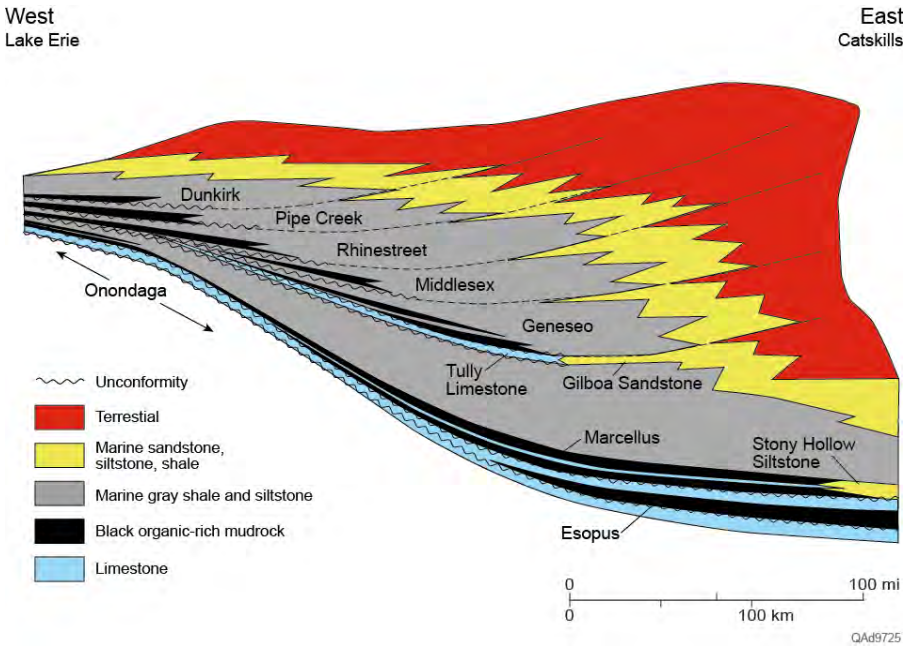

Figure 3.21. Shallow-water, cratonward onlapping model of Devonian black shales in New York. After Smith and Leone (2010).

Marcellus Source Rock Characteristics

Source rock characteristics such as total organic carbon (TOC), thermal maturity, and kerogen content determine whether a Devonian black shale contains economic quantities of gas. NETL (2009) reported that with an estimated depth of production for the Marcellus Shale of 4,000 to 8,500 ft (1220 to 2440 m), an area of 95,000 mi^2 (243,000 km^2), an average thickness of 50 to 200 ft (15 to 60 m), and a relative gas content of 60 scf/ton to 100 scf/ton, the original gas in-place estimate is as much as 1,500 Tcf. Using an average well spacing of 40 to 160 acres across the Marcellus, the technically recoverable resource was estimated to be 262 Tcf.

Total organic carbon [as indicated by laboratory analysis or by mapping of high radioactivity shales (Schmoker, 1981)], depth of burial, and shale thickness (Fig. 3.22) are important components in the development of economic gas reserves. Within the Marcellus Shale, TOC generally increases to the west onto the eroded craton and decreases to the east as it is diluted by siliciclastic sediment deposited in more oxygen-rich marine waters (Smith, 2011). TOC values appear to be higher above the Cherry Valley equivalent in the western part of the Marcellus play; and higher below the Cherry Valley to the east in New York and Pennsylvania This behavior is consistent with coeval westward migration of anoxic conditions and the tectonic peripheral bulge. Depth of burial increases from west to east and generally parallels the Appalachian tectonic front (Fig. 3.23). Thermal maturity (Fig. 3.24) and fracturing are additional overprints that influence or control production in the Marcellus Shale.

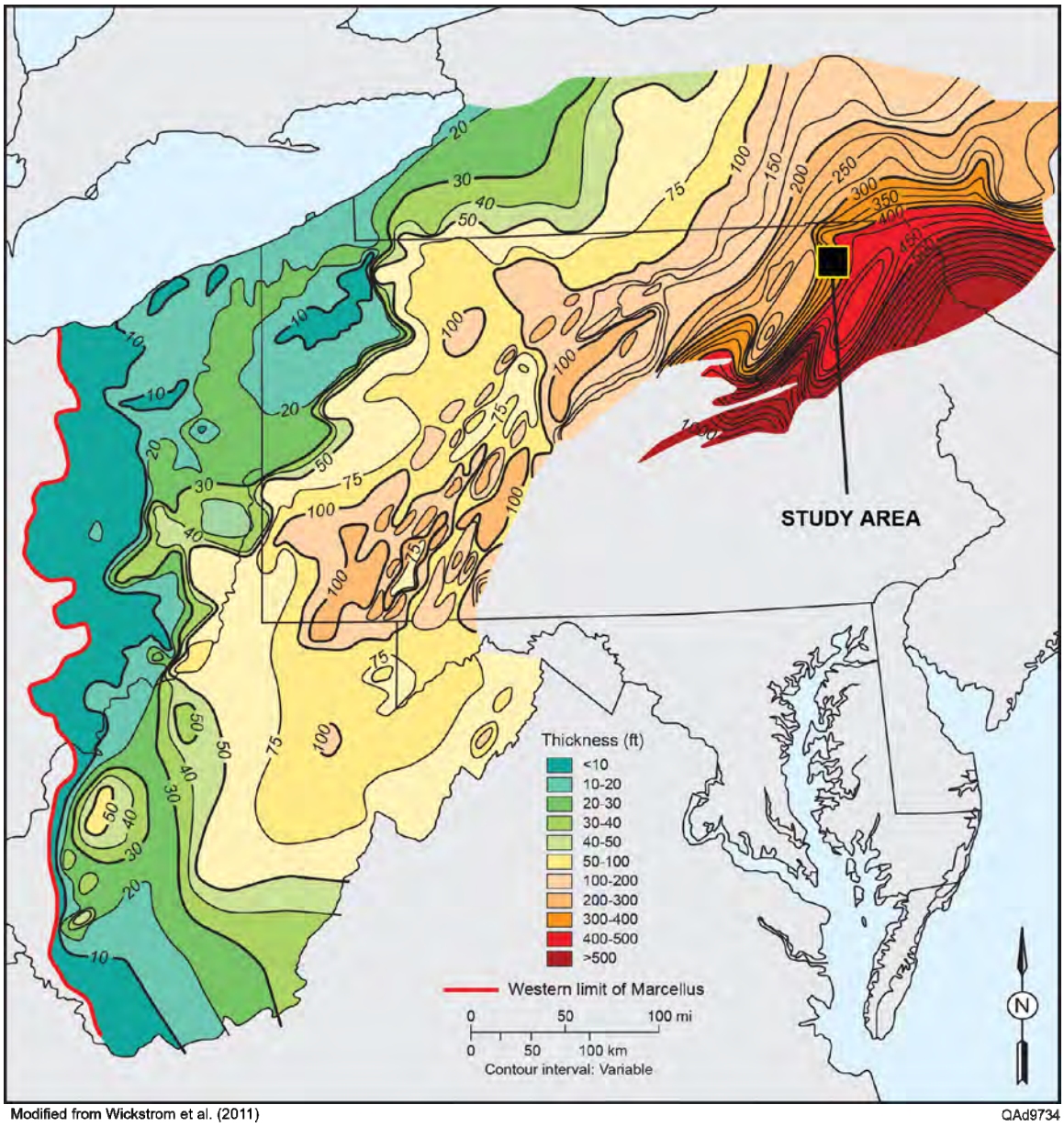

Figure 3.22. Thickness of the Marcellus Shale in the northern Appalachian Basin. After Wickstrom et al. (2011).

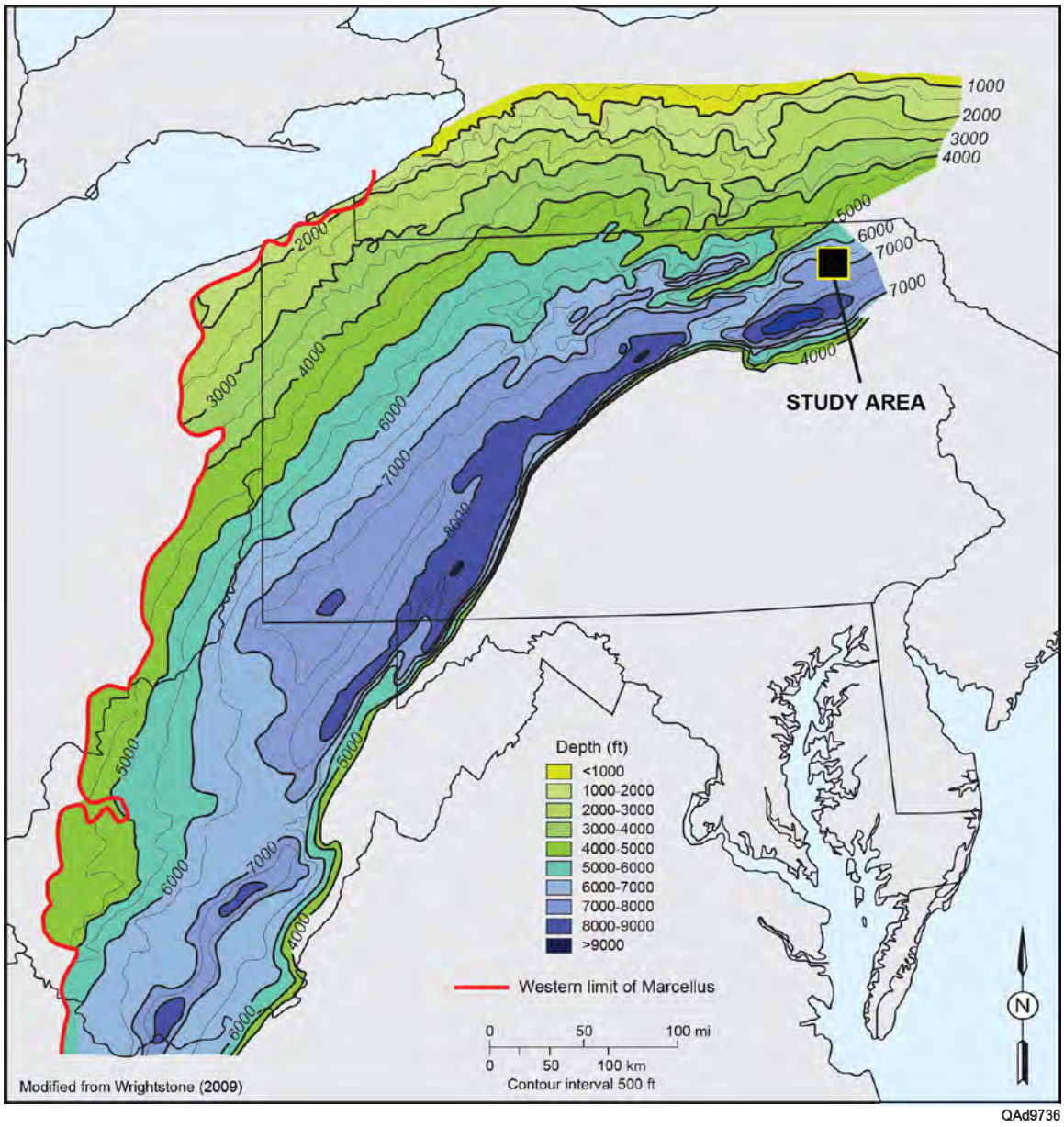

Figure 3.23. Depth in feet to the base of the Marcellus Shale. After Wrightstone (2009).

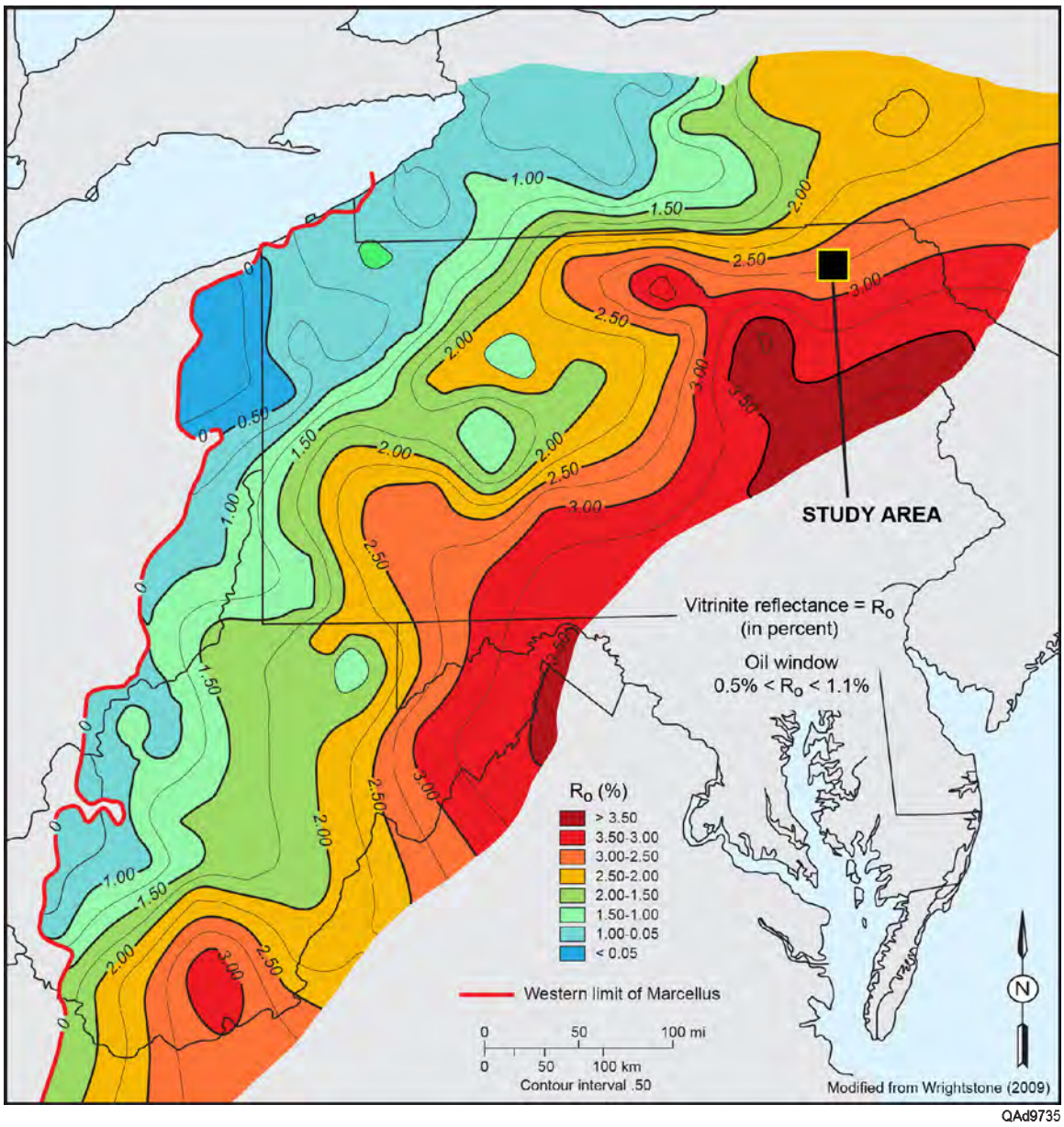

Figure 3.24. Thermal maturity of Devonian shales as measured by vitrinite reflectance. Shales with an Ro of less than 1.1 are thermally immature for gas. After Wrightstone (2009).

Marcellus Structural Aspects

Both tectonics and hydrocarbon maturation fracturing exert an important influence on shale gas production in the Appalachian Basin. Dominant basin configuration initiated with the collision of the passive margin of Laurentia with the Taconic island arc during mid-Cambrian (Miall and Blakely, 2009) and culminated in the Ordovician, forming the Cincinnati Arch and the Appalachian foreland basin. Devonian orogenic activity and reactivation of earlier Rome Trough faults (Figure 3.25) influenced tectonic development and erosion of migrating peripheral forebulges and the amount of sediment accommodation space (Lash 2007; Smith, 2011)

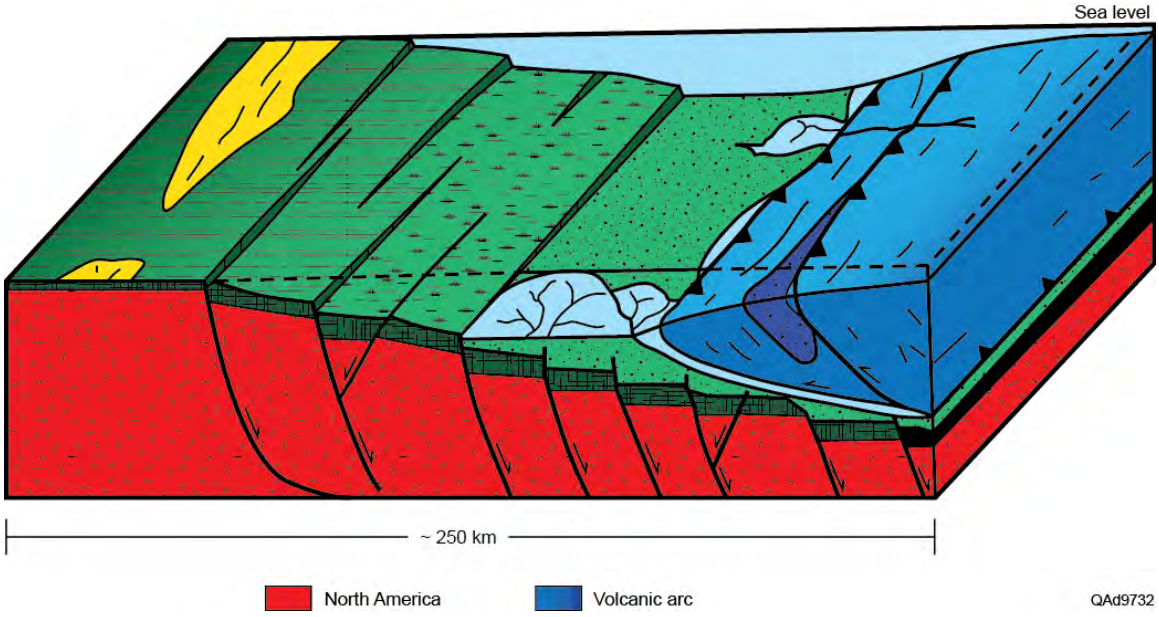

Figure 3.25. Diagrammatic view of the reactivation of Cambrian and older faults during the late Ordovician Taconic Orogeny. These faults were reactivated during the Devonian. After Smith and Leone (2010).

Although large-scale tectonics generated the basin configurations and dynamics that controlled deposition of Devonian black shales, post depositional burial and tectonics were important in the formation of local structural and thickness variations as well as tectonic fractures in the Marcellus Shale. Collision-related thick-skin and thin-skin faults (Figs. 3.3 and 3.4) that include décollement surfaces are associated with the distribution of the Silurian Salina evaporite beds (Harper, 1990; Harper and Patchen, 1996). Thin-skin faulting associated with presence of evaporites is well documented in northern Pennsylvania. Line drawings of faulted and deformed Salina evaporates observed on two regional seismic lines are shown on Figure 3.4.

Marcellus Joint Systems

Joint systems are important structural components of subsurface geology across the Appalachian Basin and play an important role in gas production from vertical and horizontal wells penetrating organic Devonian shales, particularly the Middle Devonian Marcellus Shale in Ohio, West Virginia, Pennsylvania, and New York (Boswell, 1996; Milici and Swezey, 2006; NETL, 2010). One remarkable aspect of the joint systems in Middle and Upper Devonian gas-producing shales across the basin is a common orientation of two joint sets that do not reflect regional tectonics as much as they indicate post-Devonian timing of thermal maturation of organic matter and the natural hydraulic fracturing induced by that process (Engelder, et al., 2009).

The two joint systems (termed J1 and J2) are typically orthogonal to each other and strike E-NE and W-NW, respectively. A photograph of a Marcellus Shale outcrop illustrating J1 and J2 joint sets is shown as Figure 3.26. The older J1 set is often more closely spaced and coincides with (but is not related to) the azimuth of current maximum horizontal regional stress (S_{Hmax}). The J1 set is bed-normal and postulated to have formed during maximum burial, early in the Alleghenian tectonic cycle. Outcrops and subsurface cores indicate that commonly J1, and less commonly J2, joints are open and unmineralized. Open J1 and J2 joints may have survived bed-parallel tectonic shortening because of the presence of methane in the fractures. Mineralized joints may represent water-filled joints (Engelder, et al., 2009).

The J2 set is younger than the J1 set, and the two sets are not always orthogonal (Fig. 3.27). Although J2 joints largely result from natural hydraulic fractures, they appear to be syntectonic and radiate from an oroclinal bend in the central Appalachian fold belt produced during the Alleghenian orogeny (Evans, 1994). A third set of regional joints (J3) is vertical, crosscuts structures, and is assumed to be late-formed, near-surface, and neotectonic in origin (Engelder, et al., 2009). Defining seismic attributes that detect these joint systems is important to hydrocarbon production, particularly production from the Marcellus Shale.

Figure 3.26. Two dominant joint systems in outcrops of the Oatka Creek Member of the Marcellus Shale. J1 joints cut front to back; the J2 joints cutting right to left. View is to the ENE. From Engelder (2011.)

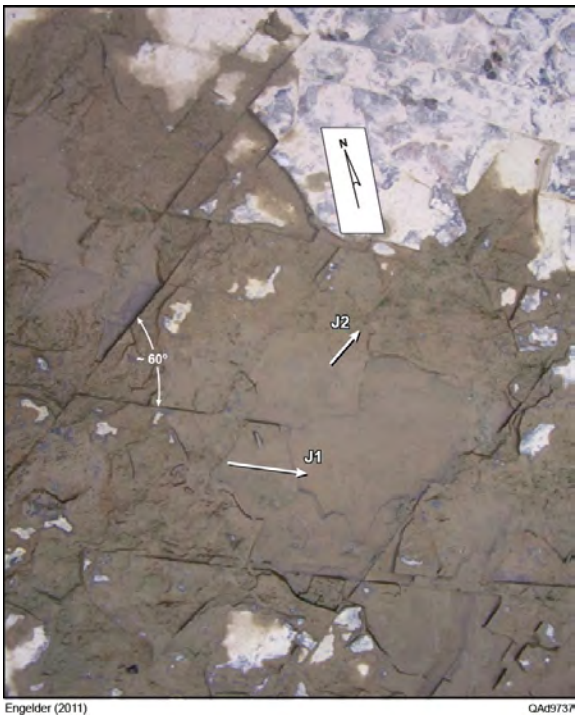

Figure 3.27. Nonorthogonal J1 and J2 joint sets in Marcellus outcrop on the Appalachian Plateau. The J1 joints maintain the same orientation around oroclinal bends, whereas J2 joints change orientation to remain orthogonal to the oroclinal bends. From Engelder (2011)

Conclusions

Numerous unconformities have been observed in sections spanning Cambrian to Devonian rocks across the Appalachian Basin. Any unconformity surface traversing Bradford County, Pennsylvania (our study site) has the potential of being an interval where water-storage reservoirs could be concentrated. Foremost among sequestration possibilities are porous, transgressive sandstone reservoirs deposited on unconformity surfaces during local subsidence. Other possibilities are porous carbonate units that have been exposed to dissolution processes and/or dolomitic replacement during uplift and surface exposure. Both of these conditions, commonly associated with unconformities, create rock units that could be attractive CO_2 storage reservoirs.

Almost no log data are available within and near Bradford County to evaluate porous rock units below the Marcellus Shale, which handicaps any analysis of reservoir targets older than Middle Devonian. Thus if seismic-based unconformities are observed below the Marcellus Shale, it is not possible to establish definitive relationships between P and S seismic attributes related to that unconformity and log-based porosity and rock type. Seismic characterization of pre-Marcellus water-storage reservoirs must therefore be based on petrophysical speculation and assumption. For this reason, data interpretation will focus on post-Marcellus rock units where log data allow some degree of seismic calibration to be done to establish links between seismic attributes and reservoir quality.

The description of potential water-storage reservoirs in this chapter spans what is thought to be the full geologic time period in which Appalachian Basin water-storage reservoir units could have been deposited. As deeper wells are drilled and more modern-log data become available, the documentation in this chapter can be extended to deeper and deeper seismic data.

Because of recent focus on Marcellus gas production, the general extent, structure, thickness, and depth of the Marcellus is well known across the Appalachian Basin. What remains to be defined in acceptable detail across the basin are specific factors, such as TOC, maturation, breeching faults, and fracture density, that affect Marcellus gas production across local prospects. Our study assists in developing seismic technology that address two of these specific factors—the detection of breeching faults and the quantification of fracture density.

For many years, it was assumed the Marcellus Shale was deposited in a deep-water, sediment-starved basin. A second environmental model is now proposed by people who have done recent studies; this being that the Marcellus was deposited in shallow-water, low-oxygen conditions. The older model is based on an interpretation that the transgressive movements associated with each Devonian black shale were caused by worldwide eustatic sea-level

changes. The newer model assumes these transgressive boundaries are the result of local tectonic movements. Our study will not provide information or technology that can contribute to which of these two Marcellus depositional models is the more appropriate.

Chapter 4

Research Database

Introduction

An extensive database was amassed to support this research. Key elements of the database were well logs that defined petrophysical properties of rock units and pore fluids across the study site, vertical seismic profile data that established depth registration of P and S reflection events, and surface-based 3C3D seismic data that imaged geological units with P and S wavefields. This chapter illustrates critical components of the database and discusses strengths and weaknesses of the data that were assembled for the study.

Vertical Seismic Profiles

Vertical seismic profile (VSP) data are essential for a rigorous interpretation of multicomponent seismic data. Because P and S wave modes propagate with different velocities, P-wave data position a targeted stratigraphic interval in an image-time window that is significantly different from the image-time window where S-wave data position that same stratigraphy. In addition, P-P reflectivities of interfaces associated with a stratigraphic target often differ in phase and amplitude from S-S and P-SV reflectivities of those same interfaces. Thus not only do P and S images depict a geologic target at different image-time coordinates, but the reflection character of the target may look quite different in P-wave image space than it does in S-wave image space. As a result, the greatest challenge in interpreting multicomponent seismic data is to depth register P and S wave modes so there is a rigorous correlation between a stratigraphic depth interval and its associated P-mode and S-mode image-time windows.

VSP data provide several critical pieces of information that allow interpreters to correctly position stratigraphic depth on P-wave or S-wave time-based data. Notably, VSP data permit the following actions steps to be taken.

1. P-wave image time can be defined as a function of depth.

2. S-wave image time can be defined as a function of depth.

3. The depth of each interface where a VSP P-P reflection occurs can be identified, and the phase and amplitude properties of reflection events from imaged interfaces are recorded.

4. The depth of each interface where a VSP S-S reflection occurs can be identified, and the phase and amplitude properties of reflection events from imaged interfaces are recorded.

5. The depth of each interface where a VSP P-SV or SV-P reflection occurs is identified, and the phase and amplitude properties of reflection events from imaged interfaces are recorded.

6. A P-P image can be constructed as a function of two-way P-wave time.

7. A P-P image can be expressed as a function of depth.

8. An S-S image can be created as a function of two-way S-wave time.

9. An S-S image can be expressed as a function of depth.

10. P-SV and SV-P images can be constructed as functions of image time.

11. P-SV and SV-P images can be expressed as functions of depth.

Collectively, these features of VSP data allow interpreters of multicomponent seismic data to create, analyze, and compare surface-based P and S seismic attributes in depth-equivalent windows that span specific geologic targets.

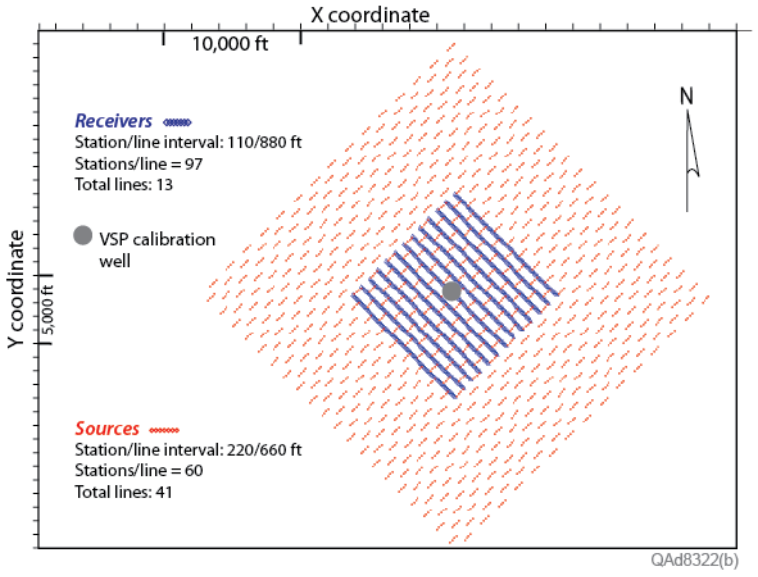

Figure 4.1. Map of study area showing location of VSP calibration well relative to planned positions of source and receiver stations used for the 3C3D seismic survey.

The VSP calibration data integrated into our database were acquired near the center of our 3C3D seismic study area as shown on Figure 4.1. The location of this calibration well was ideal for transferring VSP-based information into 3D seismic volumes for interpretation purposes. An extensive set of VSP data was acquired in this central-image well, consisting of:

- An outer walk-around survey involving 73 source stations that allowed P and S wave propagation to be analyzed at large offsets of 1 to 1.5 mi (1.6 to 2.4 km) in azimuth increments of approximately 5 degrees. Source stations occupied by this walk-around are shown by red station labels on Figure 4.2.

- An inner walk-around survey involving six source stations that allowed P and S velocities and images to be created at moderate offsets of 0.5 to to.75 mi (0.8 to 1.2 km) in azimuth increments of approximately 60 degrees. These inner walk-around source stations are shown as yellow flags on Figure 4.2.

- An 18-station walk-away profile extending southeast from the receiver well approximately 1.5 mi (2.4 km). Walk-away source stations are shown as blue station flags (Fig. 4.2).

- An orthogonal-azimuth source station pair positioned approximately 0.8 mi (1.3 km) from the receiver well (green station flags, Fig. 4.2).

- A conventional zero-offset VSP with a source positioned at the walk-away station closest to the well.

The source used to generate all of these VSP data was a vertical vibrator. Wavefields generated by the orthogonal-azimuth vibrator source pair (green flags on Figure 4.2) will be used to illustrate the quality of the VSP data acquired for this study. Data from the southwest vibrator source station are exhibited on Figure 4.3, and data from the southeast station are shown on Figure 4.4. The data are transformed to a rotated coordinate system that isolates P, radial-shear (labeled as SR or SV), and transverse-shear (labeled as SH or ST) wave modes on Figures 4.3b and 4.4b. These displays show the data exhibit high-quality P and S wavefields that can be used for imaging and for P-to-S depth registration. Several downgoing and upgoing events are labeled on the wavefields to illustrate different wave modes contained in the data (Figs. 4.3b and 4.4b).

Data having quality equivalent to that shown on Figures 4.3 and 4.4 were generated at all VSP source stations. As a result, the VSP calibration data integrated into the project database are ideal for depth registering P and S data, assisting interpretation of P and S geological images, and analyzing P and S wave propagation across our study site. Interpretation applications of these VSP data are illustrated and discussed in Chapter 9.

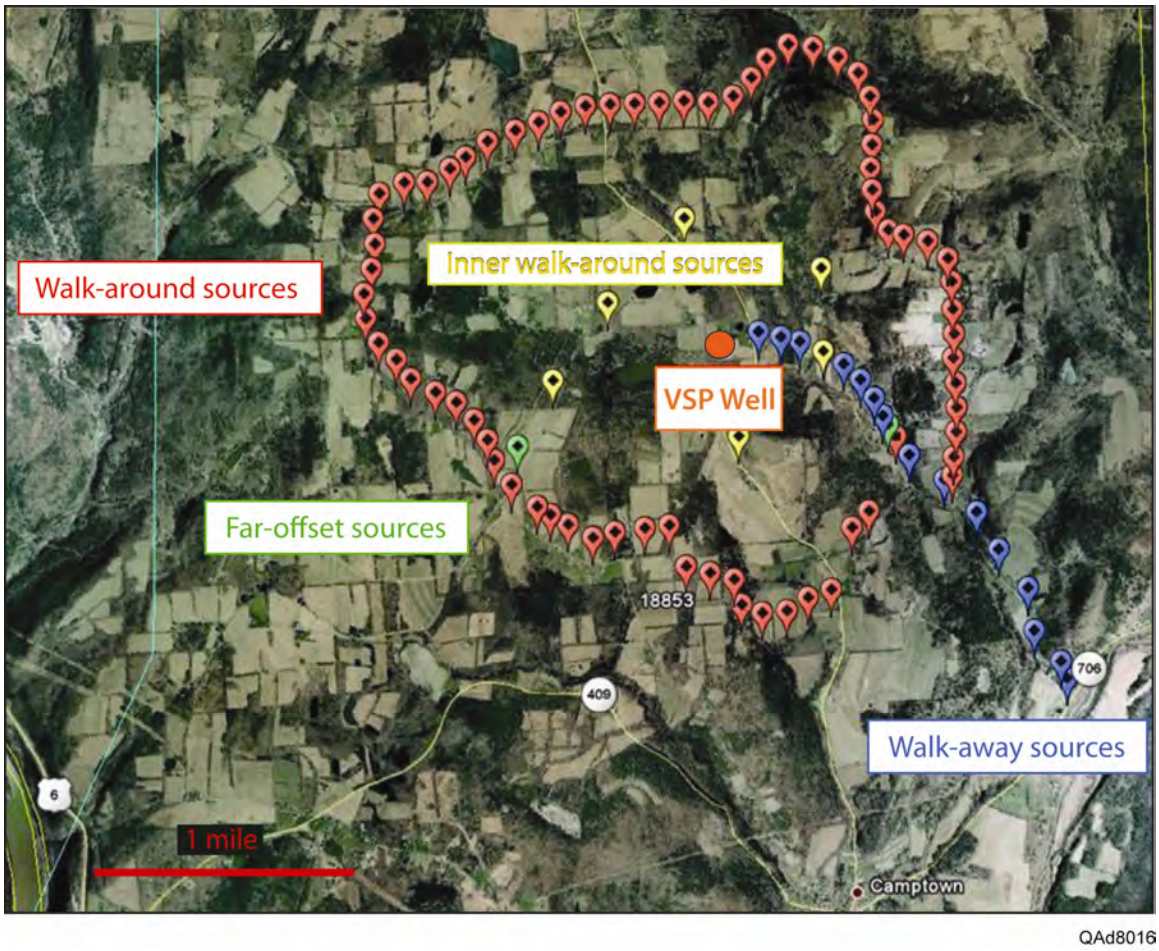

Figure 4.2. Source stations utilized in VSP data acquisition. Data acquisition included a 73-station outer walk-around (red stations), a 6-station inner walk-around (yellow stations), an 18-station walk-away (blue stations), a 2-station orthogonal-azimuth pair (green stations), and a zero-offset station (blue station closest to the well).

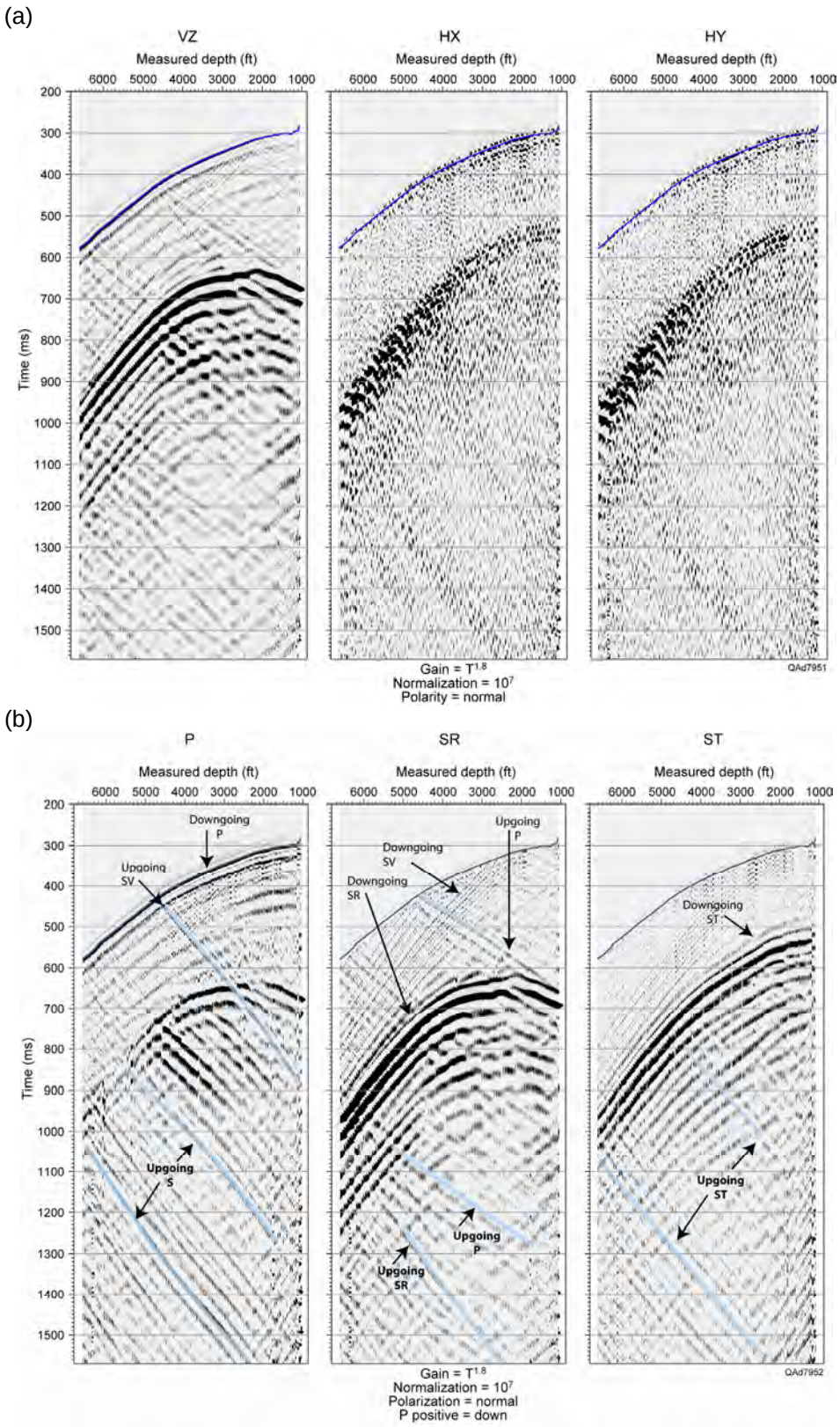

Figure 4.3. VSP data acquired when the source was at the green-flag station southwest of the receiver well. (a) Raw data as recorded. (b) Data after coordinate rotation to P, S-radial (labeled SR or SV), and S-transverse (labeled ST or SH) data space.

These vertical slices verify that targeted geology is presented as high-quality P-P and P-SV images. Specific examples of P and S definitions of faults, sequences, and facies are provided in Chapter 9.

Well Log Data

Log data acquired in the VSP calibration well at the center of the 3D seismic image space (Fig. 4.1) were an important part of the research database. These logs allowed direct correlations between rock and fluid properties and multicomponent seismic attributes that spanned the well position. The logged well was a horizontal exploration well targeting the Marcellus Shale, and drilling terminated when the well reached the Onondaga Limestone immediately below the Marcellus. The well was then kicked-out from its vertical track a short distance above the Marcellus and drilled laterally through the Marcellus interval. Because of this drilling strategy, petrophysical properties of the Utica Shale and potential water-storage reservoirs below the Oriskany Sandstone (a short distance below the Onondaga Limestone) were not logged.

Gamma-ray (GR) and velocity logs acquired in the central-image calibration well are displayed on Figure 4.8. The low-GR/high-velocity interval response between 4400 and 4500 ft (1341 and 1372 m) is the Tully Limestone. The high-GR/low-velocity interval response between 6100 and 6500 ft (1859 and 1981 m) is the Marcellus Shale. The GR response (Fig. 4.8a) reveals no thick, clean, high-porosity sandstones above the Marcellus, which would be ideal water-storage reservoirs for Marcellus operators. V_P and V_S velocities are also relatively high for the entire drilled interval, which is a second implication that porosity in all logged rock units is low to moderate. However, porosities in some intervals are still sufficient to justify evaluating those intervals for water-storage potential.

Fast-S and slow-S velocities calculated from dipole sonic log data by the well-log contractor (Halliburton) show only minor differences across the entire well depth (Fig. 4.8c). The anisotropy curve plotted on Figure 4.8d is a measure of the difference between slow-S velocity [V_S(slow)] and fast-S velocity [V_S(fast)] calculated as,

$$(4.1) \qquad \text{ANISO} = \{ [V_S(\text{fast}) - V_S(\text{slow})] \,/\, V_S(\text{slow}) \} \times 100.$$

In this equation, ANISO is the velocity anisotropy value plotted on Figure 4.8d. The anisotropy calculated for the entire logged interval is only 1 to 2 percent. This low value of S-wave anisotropy was unexpected, particularly for the Marcellus Shale, because the Marcellus supposedly has a dense population of

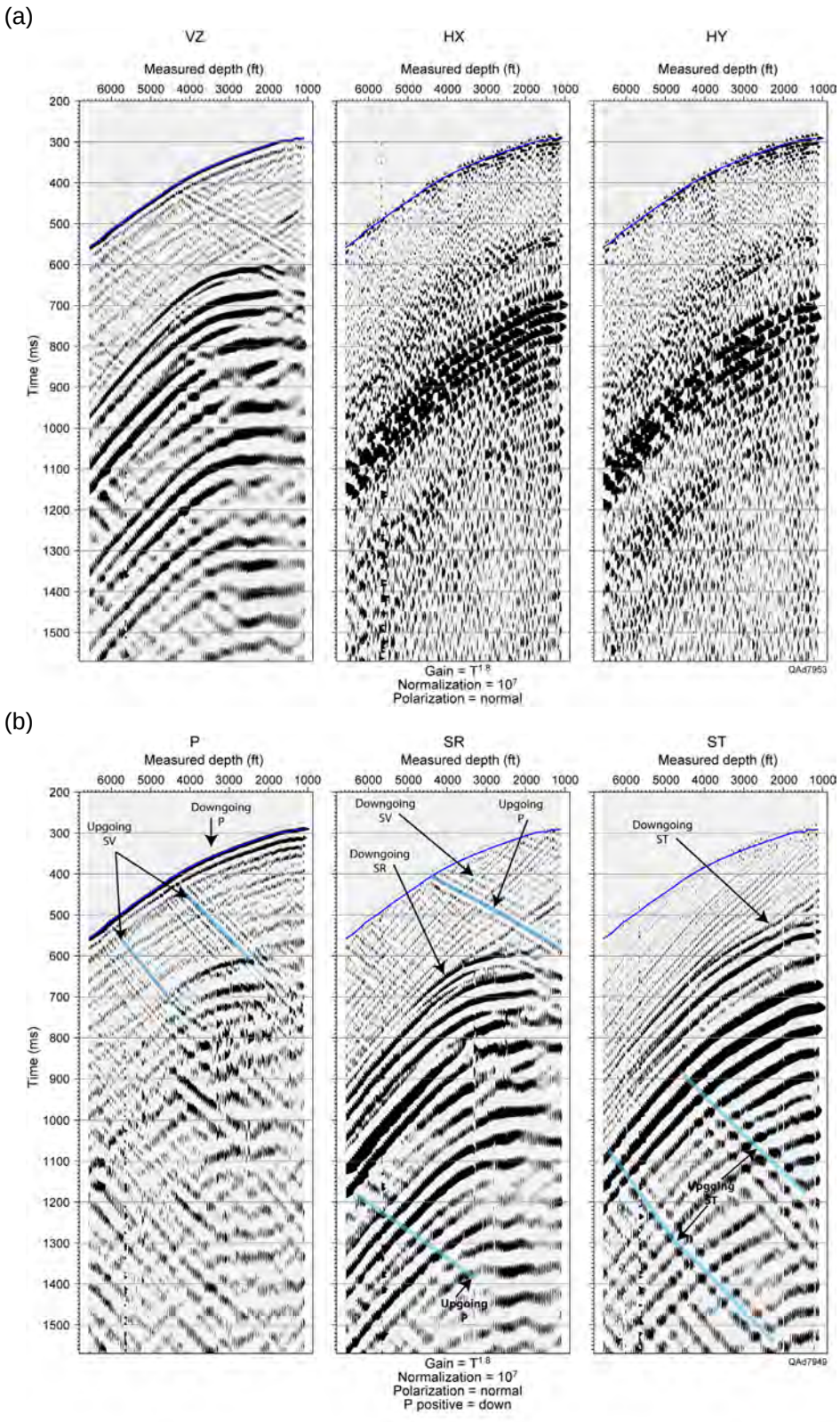

Figure 4.4. VSP data acquired when the source was at the green-flag station southeast of the receiver well. (a) Raw data as recorded. (b) Data after coordinate rotation to P, S-radial (labeled SR or SV), and S-transverse (labeled ST or SH) data space.

3C3D Seismic Data

The survey design that was supposed to be used to acquire 3C3D seismic data across the study site is illustrated on Figure 4.1. As discussed in Chapter 7, the source-receiver geometry shown on this presurvey plot had to be modified as equipment was deployed because surface conditions prevented a significant number of source stations, as well as several receiver stations, from being positioned where this design placed those stations. The final source-receiver arrangement that was deployed is illustrated and discussed in Chapter 7 and will not be repeated here.

The energy source used to generate surface-based P and S data across this 3D survey was an explosive charge of 1 kg (2.2 lb) positioned at a depth of 6 m (20 ft). This is a different source type than the vertical vibrator used to generate VSP data recorded in the calibration well at the center of the 3D image space. Examples of trace gathers created from responses of vertical, radial-horizontal, and transverse-horizontal surface geophones are displayed on Figures 4.5 and 4.6. These data are surface-sensor equivalents of the P, SR (or SV), and ST (or SH) data recorded by the downhole vertical-sensor array exhibited on Figures 4.3 and 4.4. Because the VSP calibration data show robust SR and ST shear modes propagate to deep depths and illuminate geological targets, reflected SR and ST events must be embedded in these surface-based sensor responses even though they are not easily seen in unprocessed data. One of the major challenges of this research was to extract reflected P and S modes embedded in the 3C3D data and to demonstrate the geological value of those modes. The interpreted reflections shown on Figure 4.6 are labeled “Tully” and “Marcellus” with question marks added to emphasize these data are not yet rigorously calibrated to subsurface geology. The intent is only to illustrate that robust S-wave reflections appear on radial-horizontal and transverse-horizontal geophones. Upon examination of several such trace gathers, a general observation that can be made is ***the 3C3D seismic data used in this study have good signal-to-noise properties and provide an excellent opportunity to demonstrate the value of multicomponent seismic data for evaluating Marcellus Shale prospects.***

Other valuable components of the 3C3D seismic database were three processed data volumes—a P-P volume and two P-SV volumes (a fast-S volume and a slow-S volume)—that Geokinetics produced from the 3C3D data and provided for our study. Interpretations of these 3D data volumes are illustrated and discussed in Chapter 9 and will not be presented here. Because the purpose of this chapter is only to describe the research database, it is sufficient to show selected examples of vertical slices through the image volumes to illustrate P and S data quality. Such example profiles are displayed on Figure 4.7a through 4.7 d.

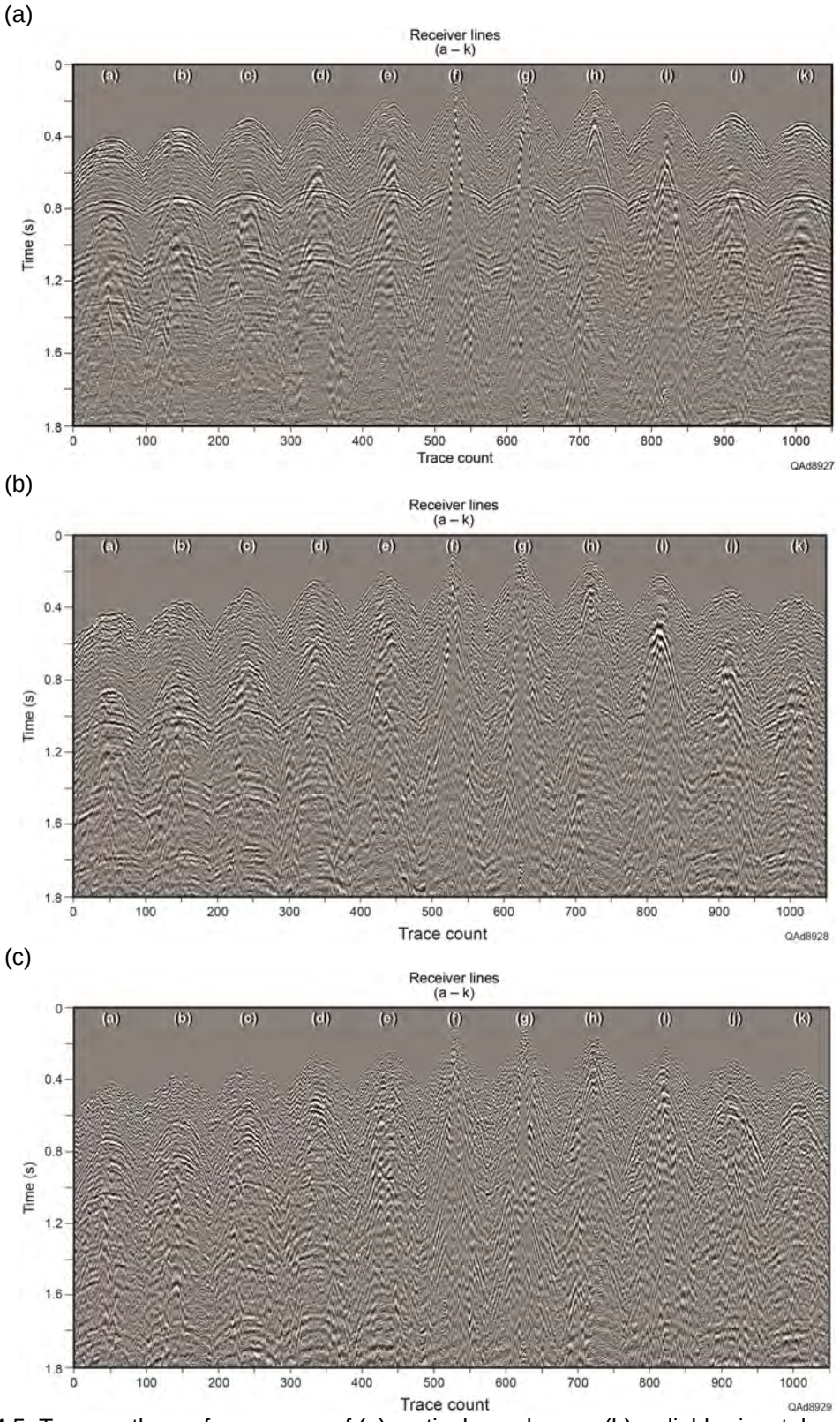

Figure 4.5. Trace gathers of responses of (a) vertical geophones, (b) radial-horizontal geophones, and (c) transverse-horizontal geophones from the 3C3D seismic data used in this investigation.

(a)

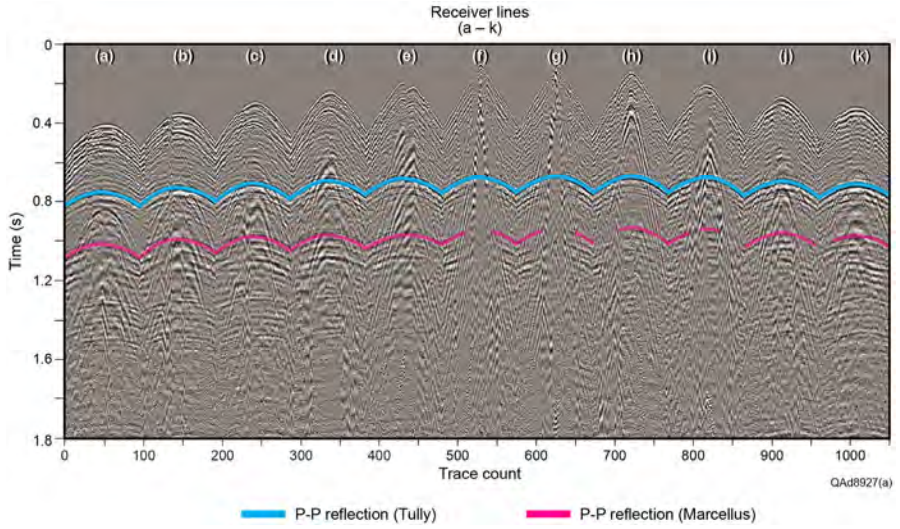

(b)

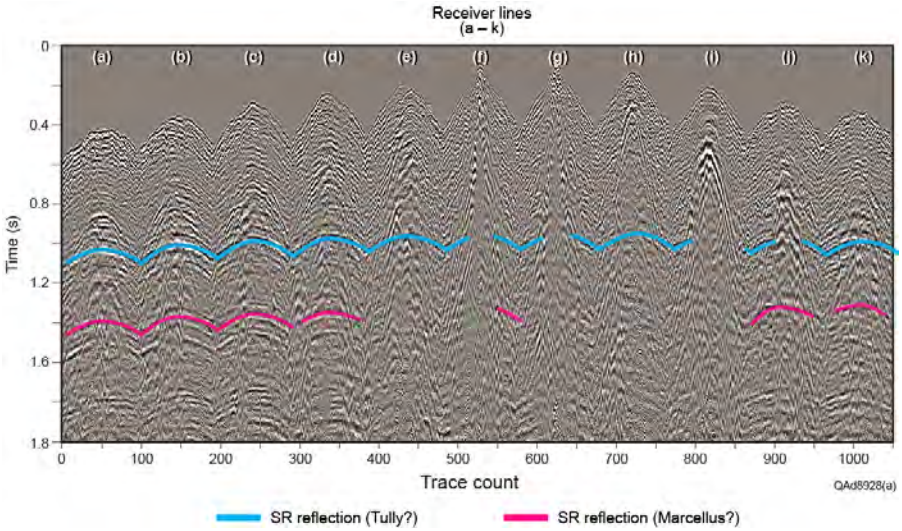

(c)

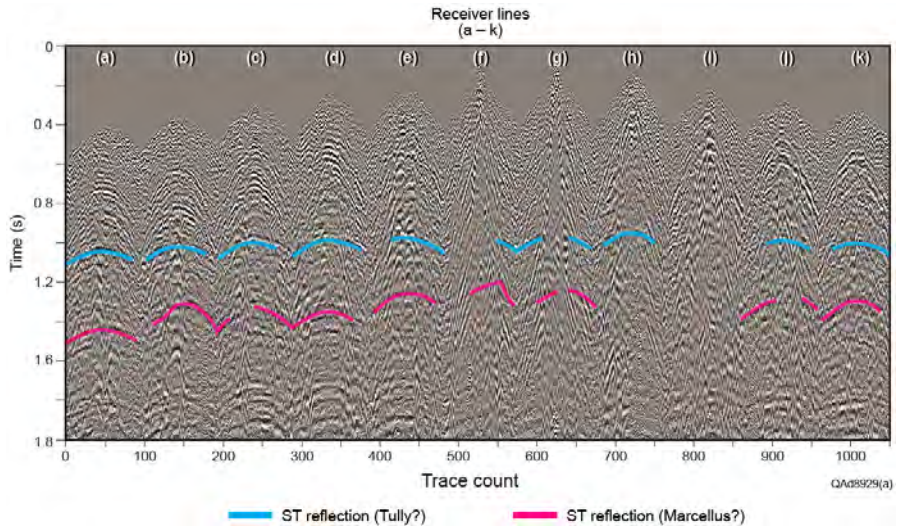

Figure 4.6. Interpreted trace gathers of responses of (a) vertical geophones, (b) radial-horizontal geophones, and (c) transverse-horizontal geophones.

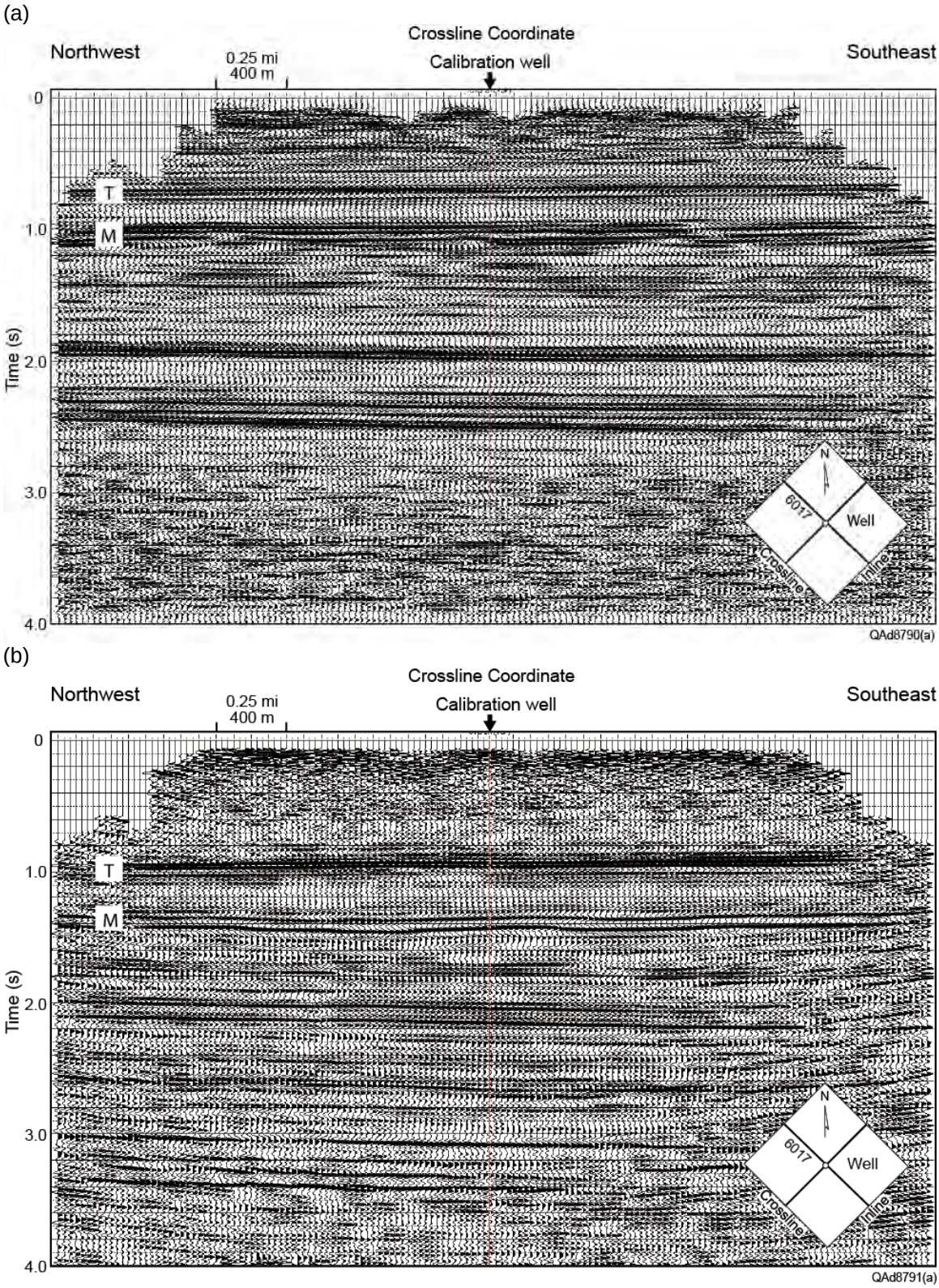

Figure 4.7. Vertical slices through (a) P-P, and (b) P-SV volumes constructed from the 3C3D seismic research data. These northwest-southeast profiles follow inline coordinate 6017 that passes through the central calibration well. T = Tully Limestone. M = Marcellus Shale.

(c)

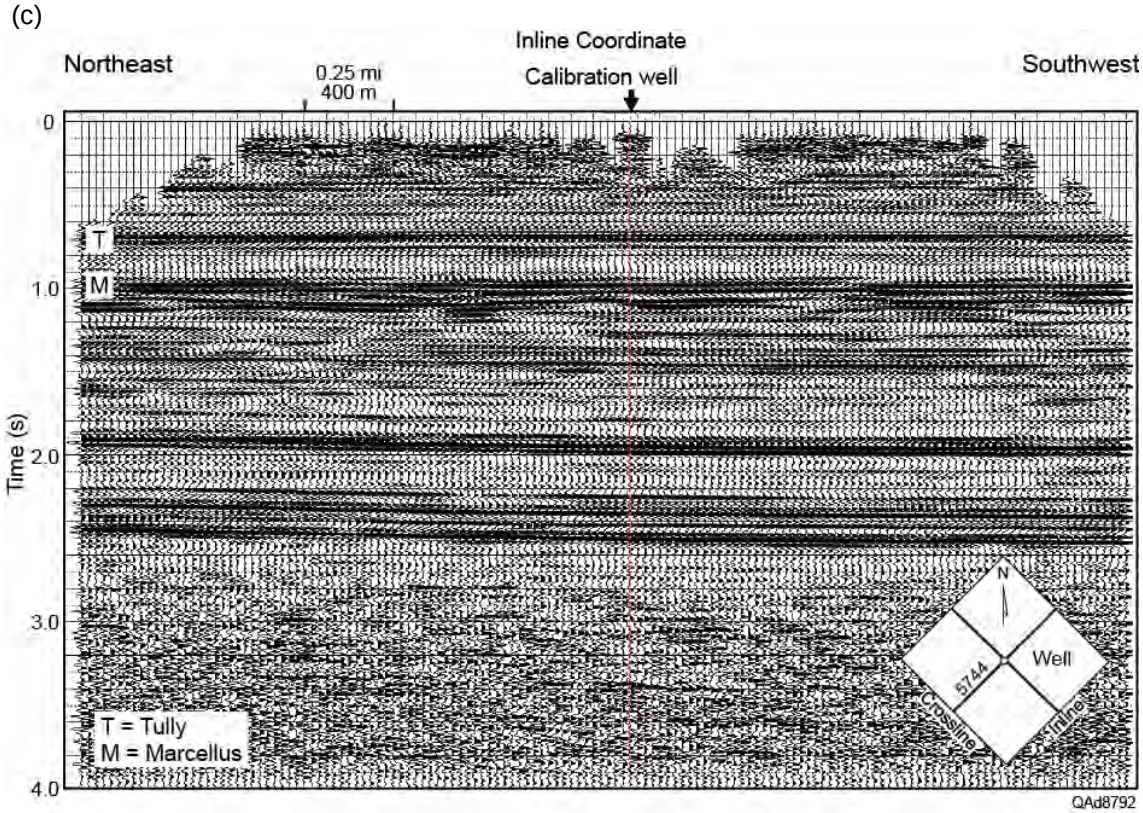

(d)

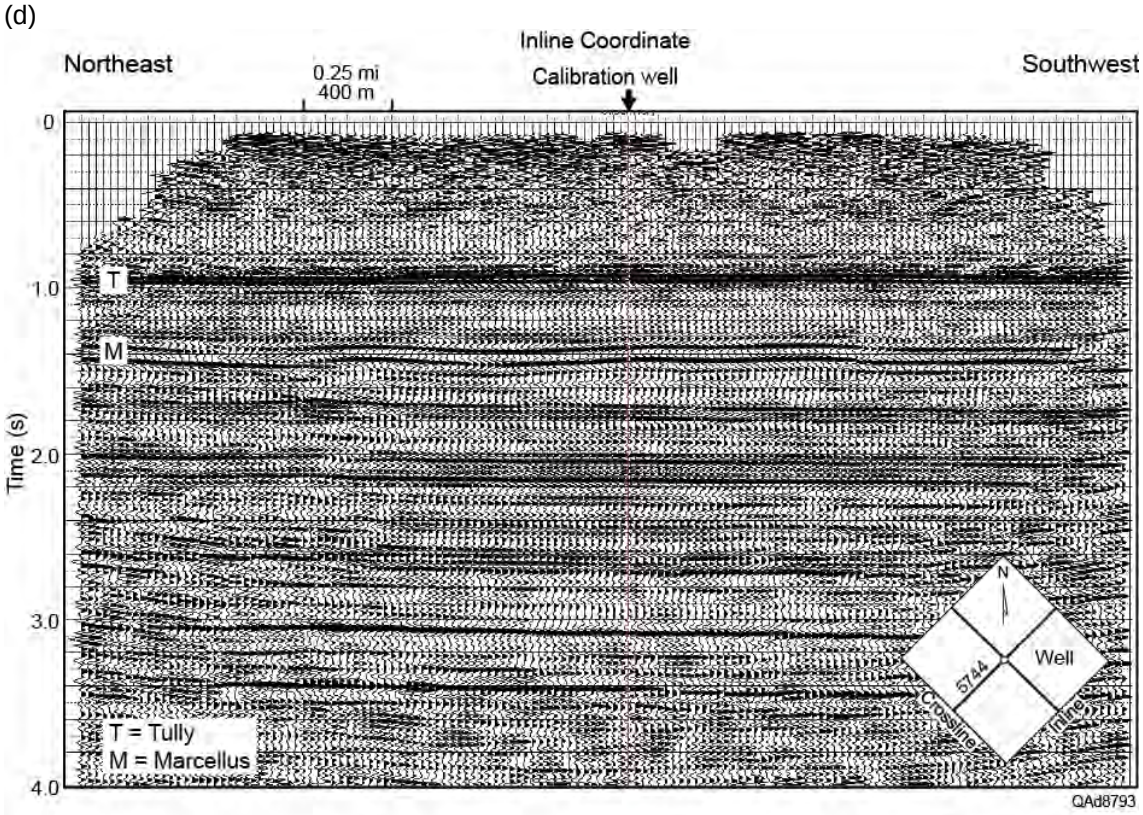

Figure 4.7 continued. (c) Vertical slice through P-P volume and (d) P-SV volume that follows southwest to northeast profile 5744.

orthogonal joints, which were initially assumed would produce significant azimuthal anisotropy. This dipole sonic log thus introduces an interesting and important research problem—the need to do independent measurement, quantification, and modeling of S-wave propagation in orthorhombic media. As a result, a rock physics model was developed for the Marcellus Shale that explains why S-wave anisotropy is low for the type of orthorhombic conditions found within the Marcellus interval. This rock physics model is discussed in Chapter 5.

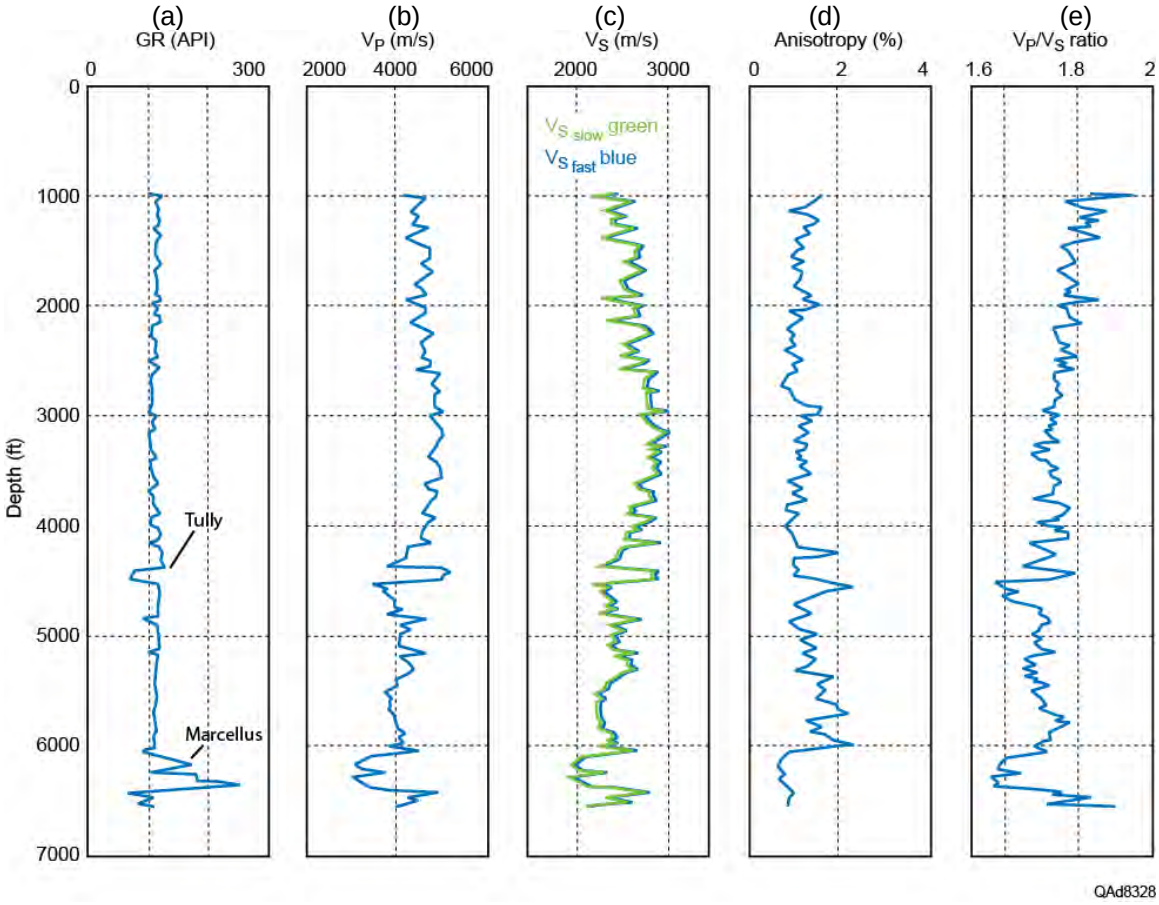

Figure 4.8. (a) Gamma-ray and (b) V_P and (c) V_S velocity logs acquired in the calibration well at the center of the 3D seismic image space. Both fast-S and slow-S velocities are shown on (c) and are used to calculate S-wave anisotropy (d). The V_P/V_S velocity ratio (e) uses the fast-S velocity.

Additional logs acquired in the central-image calibration well are displayed as Figure 4.9. The gamma-ray log is repeated to aid correlation with companion logs on Figure 4.8. The porosity log displayed on Figure 4.9c is particularly important because it indicates the interval below the Tully Limestone (below 4500 ft [1372 m]) has porosities of 15 percent to 18 percent. This porosity range is attractive for water-storage reservoirs.

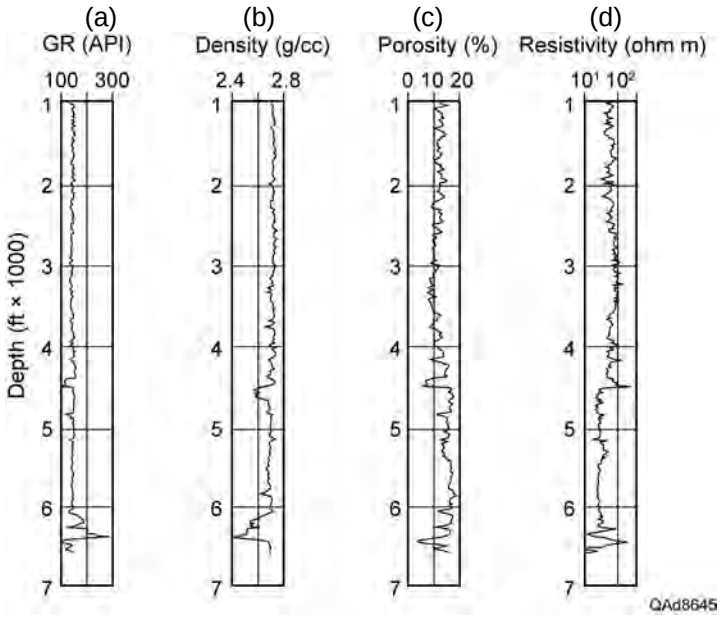

Figure 4.9. Additional logs acquired in the central-image calibration well. (a) Gamma-ray log. (b) Bulk density. (c) Neutron porosity. (d) Deep resistivity.

Commercial and public well log databases were searched to locate additional logs local to our study area. These efforts were moderately successful. Thousands of wells have been drilled and logged in Pennsylvania, but the majority of these wells are not of significant value to this research because they: (1) are shallow and do not reach depths of the Marcellus Shale, Utica Shale, and many water-storage targets, or (2) have minimal logging suites often consisting of only a gamma-ray curve. Wells local to our Bradford County study area where logs were located are indicated on Figure 4.10. Gamma-ray logs along the three labeled profiles, AB, CD, and EF, are displayed in cross-section formats on Figure 4.11.

The logs are helpful in that they show the consistent nature of the Tully Limestone and Marcellus Shale over a wide area. They are not encouraging in the sense that they show no obvious thick, clean-sandstone intervals that could be candidates for water-storage reservoirs. The decreased GR interval labeled “S ?” (for “sandy ?”) on profile AB (Fig.4.11a) is encouraging evidence of possible water-storage reservoir rock, but that trend does not seem to extend to our study area. A message emphasized by these logs is that a principal challenge of our study would be to locate units with sufficient porosity to be considered as water-storage reservoirs. As has been noted, porosities below the Tully Limestone follow a consistent trend of 15 percent to 18 percent (Fig. 4.9) within our 3D seismic image space. These porosities and their associated depths of more than 4500 ft (1372 m) make pre-Tully Middle Devonian units our preferred candidates for water-storage reservoir targets.

A compilation of logged wells integrated into the database and the log suites associated with those wells is provided as Table 4.1.

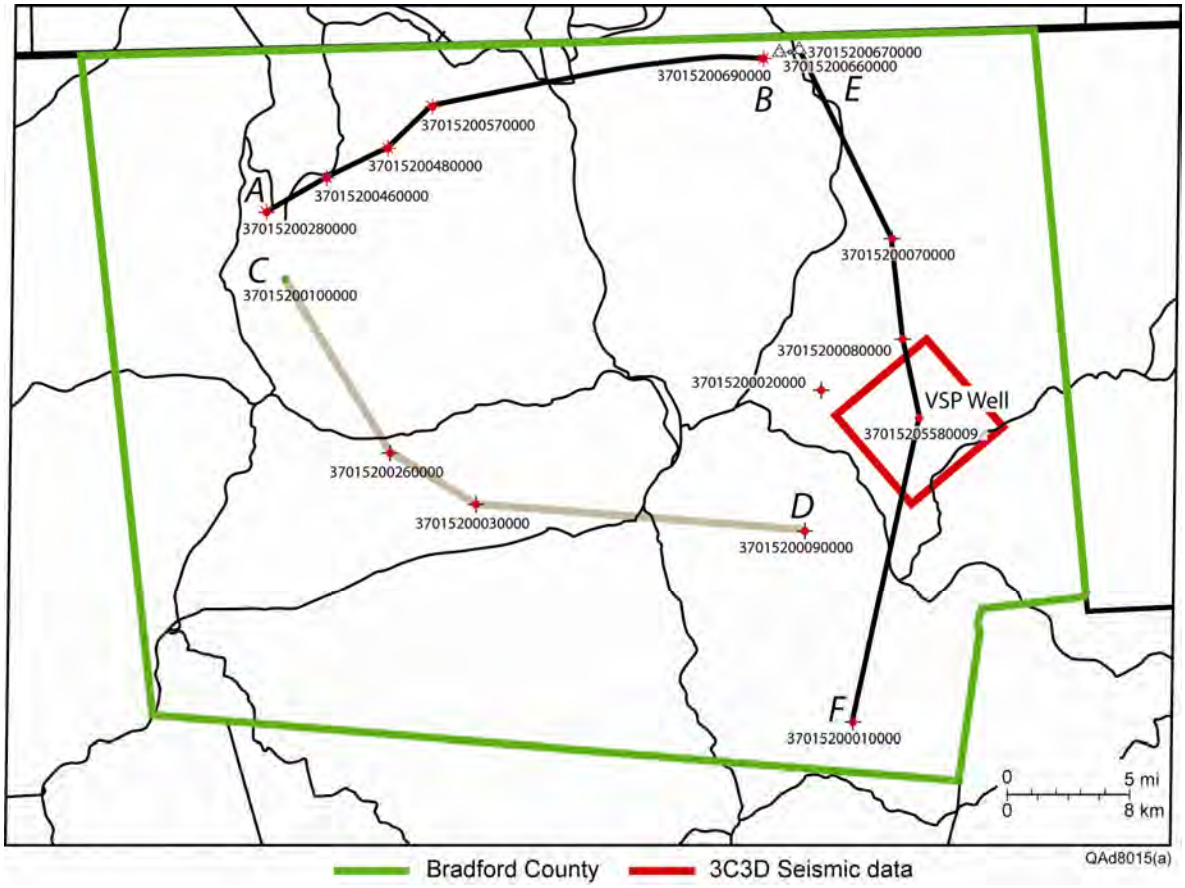

Figure 4.10. Logged wells local to the study site that were integrated into the research database.

(a)

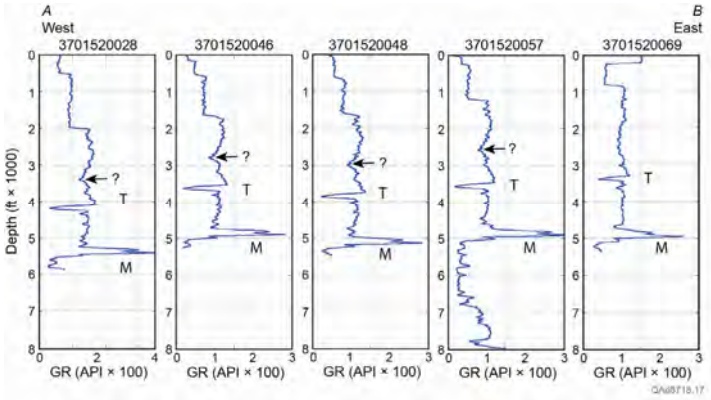

(b)

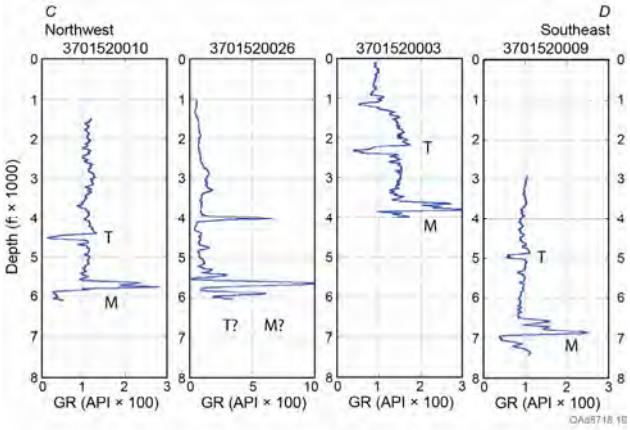

(c)

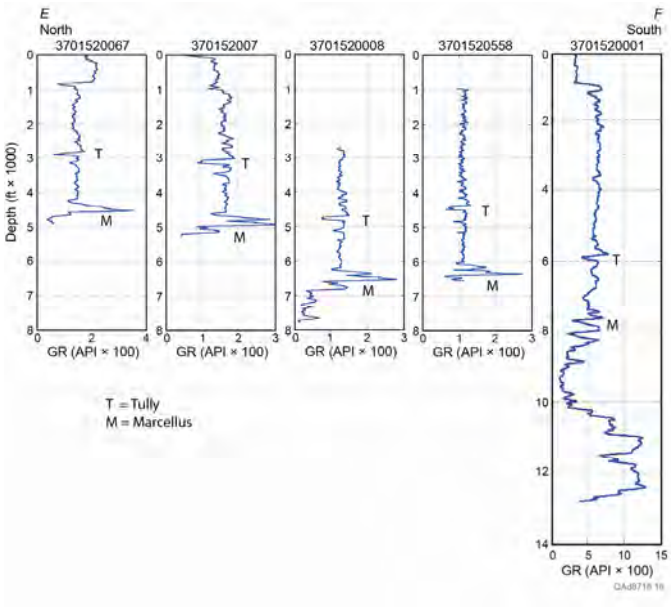

Figure 4.11. Gamma-ray logs along the three profiles labeled on Figure 4.10. (a) Cross section A-B. The label **?** identifies an interval above the Tully that is “possibly sandy.” (b) Cross section C-D. (c) Cross section E-F. **T** = Tully. **M** = Marcellus.

Table 4.1. Well Log Database

Well API	Depth (ft)	Log curves
3701520001	12,852	GR, ILD, rhob
3701520002	6617	GR, ILD, rhob
3701520003	4094	GR, rhob
3701520007	5267	GR, ILD, rhob
3701520008	7846	GR, rhob
3701520009	7505	GR, rhob
3701520010	6123	GR, ILD, ILM, rhob, NPHI
3701520026	6070	GR, LLD, LLS, rhob, cal, DT, NPHI, PEF
3701520028	5922	GR, ILD, ILM, rhob, NPHI, cal, PEF
3701520046	5280	GR, ILD, ILM, rhob, NPHI, cal, PEF
3701520057	5442	GR, rhob, NPHI, cal, PEF, gas temp
3701520066	4935	GR, rhob, RLA5, RLA3, RLA2, NPHI, cal, PEF
3701520067	4812	GR, rhob, RLA5, RLA3, RLA2, NPHI, cal, PEF
3701520069	5387	GR, rhob, RLA5, RLA3, RLA2, NPHI, cal, PEF
3701520070	5034	GR, TT
3701520558	6582	GR, RO90, RO60, RO30, RO20, RO10, RT90, RT60, RT30, RT10, RF90, RF60, RF30, RF20, RF10, rhob, cal, DT, DTFast, DTslow, ANISO, NPHI, PEF

Abbreviations:

ANISO :	Shear-wave anisotropy (%)
cal:	Caliper (inch)
DT:	Compressional transit travel time (microsec/ft)
DTFast:	Fast polarization for the shear transit traveltime (microsec/ft)
DTSlow:	Slow polarization for the shear transit traveltime (microsec/ft)
GR:	GR (API units)
ILD:	Deep induction log (ohm.m)
ILM:	Medium induction log (ohm.m)
NPHI:	Neutron porosity (%)
PEF:	Photoelectric Factor (V/V)
rhob:	Bulk density (gm/cm^3)
RLA5, RLA3, RLA2, RO90, RO60, RO30, RO20, RO10, RT90, RT60, RT30, RT10, RF90, RF60, RF30, RF20, RF10:	Various electrical resistivity measurements with different penetration depths (ohm.m)
TT:	Transit time (microsec)

Conclusions

The database assembled for this study is excellent with respect to the quality of its 3C3D seismic data, which are the primary data needed for this research. The database is also excellent with respect to the calibration VSP data that were acquired at the center of the 3C3D seismic survey. Likewise, well logs acquired in the calibration well at the center of the seismic image space are modern, extensive, and excellent quality. In short, all data acquired within the immediate study area are high-quality and complete in almost every aspect required for our research.

A disappointing aspect of the database is that well logs acquired outside the study area are limited in type, variety, and quality from what is desired for detailed petrophysical analysis. It is difficult to define trends of attractive water-storage reservoirs and to project these trends into the study area using these public logs. Some speculation will be required to identify water-storage targets inside the 3C3D seismic image space, particularly those deeper than the Marcellus Shale because no local log data have been found that span pre-Marcellus geology.

Chapter 5

Rock Physics

Introduction

It is essential to establish rock physics models that relate multicomponent seismic attributes to rock and fluid properties. It is particularly important to develop rock physics principles that establish relationships between azimuth-dependent and angle-dependent reflectivities of P-wave and S-wave modes and rock properties such as fracture orientation, fracture density, matrix porosity, type of pore-filling fluid, mineralogy, effective pressure, and local stress conditions. In this study, rock physics models had to go beyond common assumptions of vertical transverse isotropy (VTI) and horizontal transverse isotropy (HTI) as being appropriate descriptions of seismic propagation media. Although an HTI rock physics assumption allows vertical fractures to be present in a seismic propagation medium, such an Earth model applies to fractures in thick homogeneous media, not to fractures in a thin-layered Earth. A VTI assumption moves away from a thick homogeneous medium and permits thin layering, but a VTI model allows no fractures. To establish proper rock physics principles across our study area, it was necessary to describe P and S wave propagation in orthorhombic media. An orthorhombic medium is more complicated than an HTI or VTI medium in that it describes an Earth system that is both thin layered and also fractured. Targeted strata in Bradford County, Pennsylvania, are orthorhombic in two senses: (1) some intervals, such as the Marcellus Shale, are thin layered and have orthogonal joint systems, and (2) other intervals are thin layered and have only a single set of vertical fractures. Both conditions result in orthorhombic seismic propagation media.

Well Log Data

Well log data acquired in the calibration well at the center of the seismic image space we studied are segregated onto two separate figures so log character can be illustrated in appropriate detail. Gamma-ray, density, porosity, and electrical resistivity data are displayed on Figure 5.1. The gamma-ray log is repeated on Figure 5.2 in combination with P-wave velocity, fast-S and slow-S velocities, S-wave anisotropy for waves traveling at normal incidence, and the $Vp:Vs_{fast}$ velocity ratio. The gamma-ray (GR) curve identifies two key formations: the Tully Limestone with a low GR response, and the Marcellus Shale with a high GR signature. The Marcellus Shale displays the lowest density of all rock units penetrated by the calibration well. The Marcellus also has a higher electrical resistivity than its bounding units because of its high gas content.

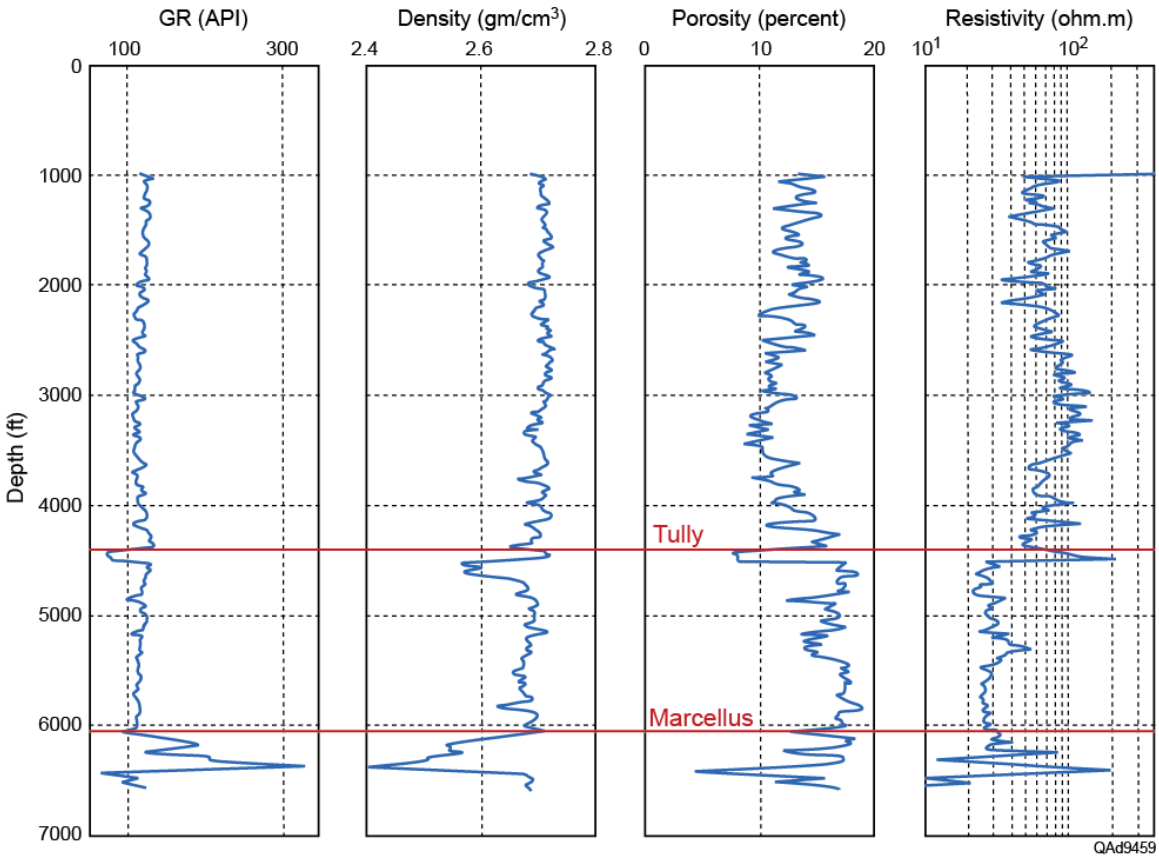

Figure 5.1. Well log data from local calibration well. From left to right are gamma ray (API units), density (gm/cm^3), porosity (percent), and electrical resistivity (ohm.m). The tops of the Tully Limestone and the Marcellus Shale are labeled.

Log measurements that are of most interest are P-wave and S-wave velocities, and the corresponding S-wave anisotropy recorded in the well (Fig. 5.2). These velocity parameters are critical for developing rock-physics fracture models. S-wave anisotropy ANISO computed from cross-dipole sonic log data is defined as:

(5.1) $$ANISO = [(Vs_{fast} - Vs_{slow}) / Vs_{slow}] \times 100.$$

In this formulation, ANISO has units of percent. As shown on Figure 5.2, S-wave anisotropy in the central-image well has low values across the entire logged interval. The smallest S-wave anisotropy occurs in the Marcellus Shale although outcrop information shows the Marcellus to be naturally fractured. The fact that the Marcellus Shale has intense patterns of orthogonal joints and yet has a low S-wave anisotropy led to the development of an important velocity-based rock physics model for the Marcellus Shale in this study.

Our interpretation of the low V_P/V_S velocity ratio across the Marcellus interval is that the Marcellus Shale not only has high gas saturation, but is also

overpressured, and these factors combine to cause a significant reduction in V_P velocity. The overpressure environment within the Marcellus promoted by Engelder (2011) is supported by this low V_P/V_S velocity ratio.

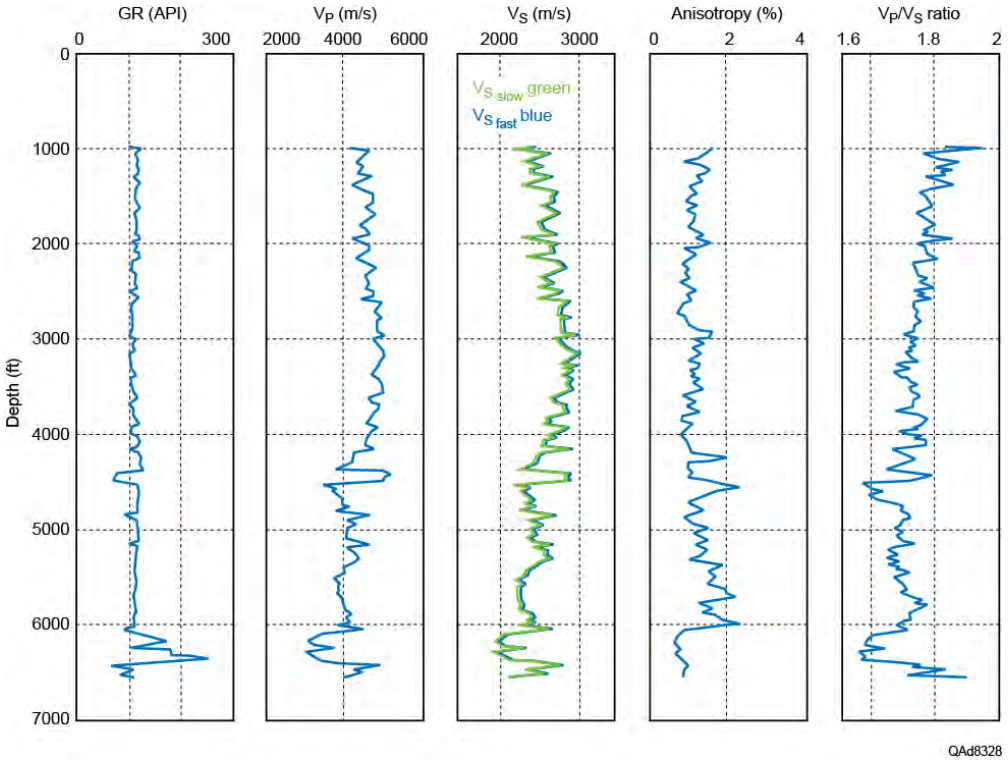

Figure 5.2. Well log data from the calibration well. From left to right: gamma ray (API units), Vp (km/s), Vs_{fast} (blue curve, km/s) and Vs_{slow} (green curve, km/s), S-wave anisotropy (percent), and Vp/Vs_{fast} ratio. There is little difference between Vs_{fast} and Vs_{slow}, and the curves in the third panel plot atop each other.

Porosity of Potential Water-Storage Units

The porosity curve displayed on Figure 5.1 is critical information for selecting geologic units that can serve as potential water-disposal reservoirs for flow-back water recovered in hydrofrac operations. The most attractive porosities occur in the Middle Devonian section between the Tully Limestone and the Marcellus Shale. We thus limited our analysis of possible water-storage reservoirs to the Tully-to-Marcellus stratigraphic interval. A particularly interesting reservoir target was found immediately below the Tully Limestone and is illustrated and discussed in Chapter 9.

Well Log Cross-Plots

Well log data acquired in the central-image well were analyzed to determine rock physics principles for the Marcellus Shale that could assist

interpretation of multicomponent seismic data around this calibration well. P-wave velocity and formation density are cross-plotted on Figure 5.3 with data values color-coded by depth-equivalent gamma-ray measurements. High gamma-ray measurements identify the Marcellus Shale. Even though the Marcellus is the deepest logged formation, it has the lowest P-wave velocities of all the rock units penetrated by the well, in addition to having low bulk density values. This lowered P-wave velocity is assumed to be caused by the combination of high gas saturation and overpressure within the Marcellus

Data from only the Marcellus interval are cross-plotted on Figure 5.4 with the data now color-coded by depth instead of gamma-ray reading. This cross-plot segregates the Marcellus into two units: (1) the Upper Marcellus, with slightly lower P velocities and higher densities, and (2) the Lower Marcellus, which has higher velocities and lower densities. By comparing Figure 5.4 with Figure 5.3, it is obvious the Lower Marcellus exhibits higher gamma-ray values than the Upper Marcellus. These increased gamma-ray values probably indicate the Lower Marcellus has a higher organic-matter content than the Upper Marcellus. As documented on several figures in Chapter 9, the Upper and Lower Marcellus units are separated by the Cherry Valley Limestone.

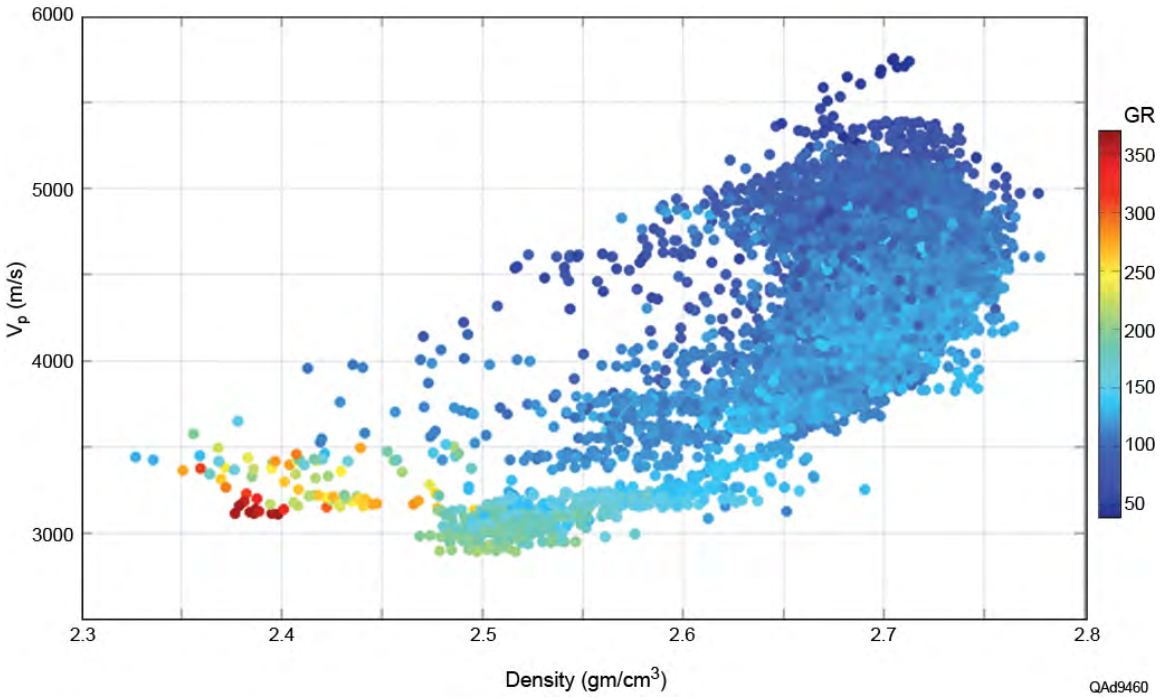

Figure 5.3. P-wave velocity versus bulk density for the entire logged interval, with data points color-coded by gamma-ray value.

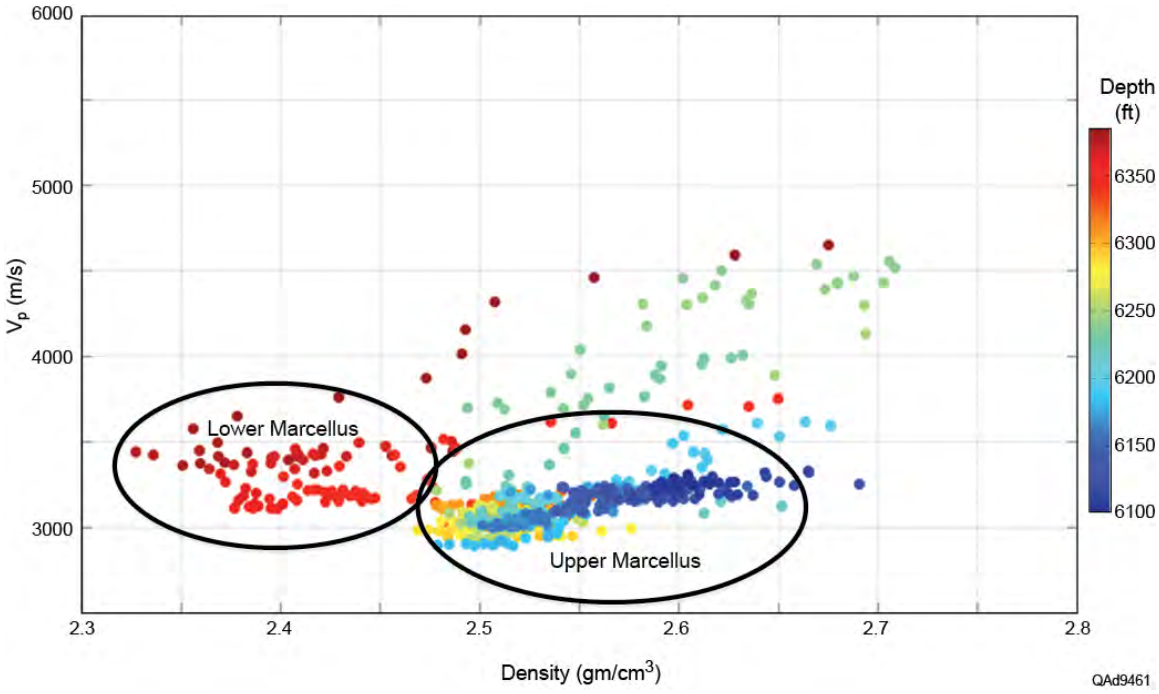

Figure 5.4. P-wave velocity versus bulk density for only the Marcellus interval, with data points color-coded by depth. The Upper Marcellus and Lower Marcellus units are well delineated in this data space.

Formation density across the Marcellus interval is shown as a function of neutron porosity, color-coded by depth, on Figure 5.5. Even though there is significant scatter in this cross-plot, the data cluster into two clouds—one data group representing the Upper Marcellus and another group describing the Lower Marcellus. Although the data show the Upper Marcellus has more porosity than the Lower Marcellus, the Upper Marcellus surprisingly has a higher formation density. This conundrum led to the following analysis of factors that could cause bulk density within the Marcellus interval to increase even though porosity increases.

It is important to understand whether the scatter in the cross-plotted data of Figure 5.5 could be caused by variations in fluids, or in mineralogy, or perhaps by variations in both physical properties. If we assume the Marcellus has a mineral density of 2.75 gm/cm^3 at zero porosity, we can compute a linear trend of density-vs.-porosity for different pore-filling fluids. On Figure 5.6 the red line corresponds to gas filling the porous space, and the blue line corresponds to brine occupying the porous space. The positions of these two lines on the cross-plot show the difference in density between the Upper Marcellus and Lower Marcellus cannot be explained by fluid variability.

Therefore, we investigated the hypothesis that variable mineralogy is the reason why there is higher formation density in the Upper Marcellus even though porosity is higher. Previous studies show that in some locations the Marcellus Shale has disseminated pyrite nodules, with the pyrite volume fraction being as

high as 10-percent. We considered the following mineral assemblage for the Upper Marcellus: 50-percent quartz (grain density = 2.65 gm/cm^3), 40-percent illite (grain density = 3.0 gm/cm^3), and 10-percent pyrite (grain density = 5.0 gm/cm^3). These volume fractions cause the grain density of the Upper Marcellus to be 2.98 gm/cm^3. This adjusted grain density leads to the two linear trends of density-vs.-porosity for the Upper Marcellus shown on Figure 5.7. The red line again corresponds to gas in the porous space, and the blue line corresponds to brine in the porous space.

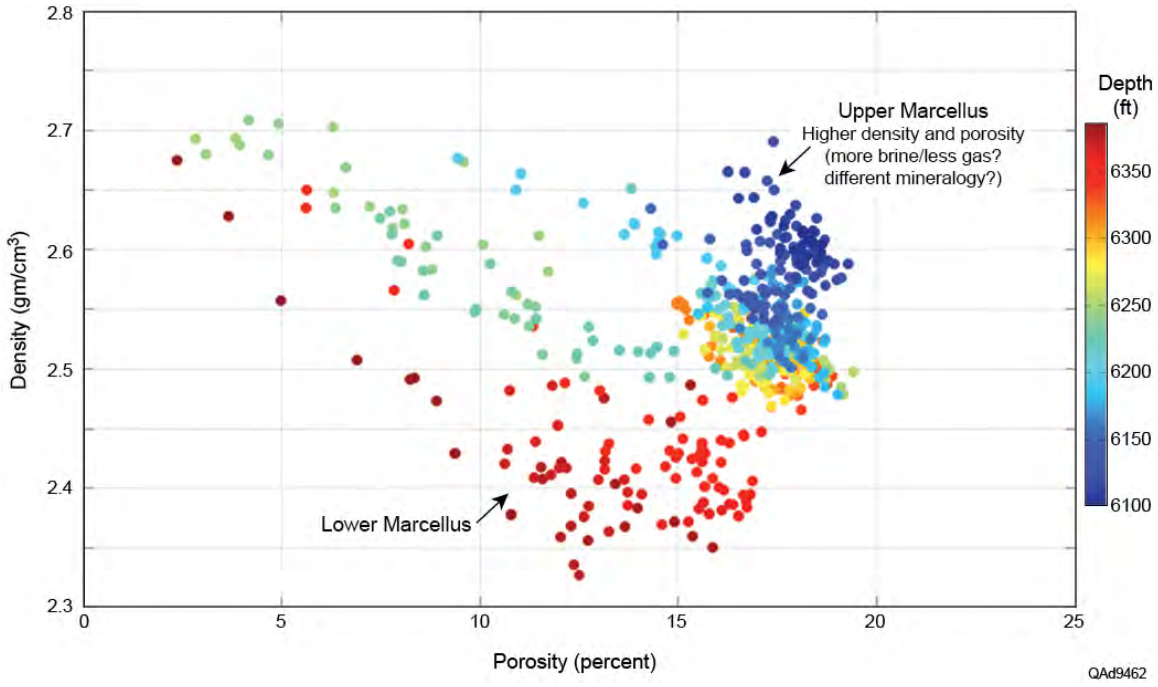

Figure 5.5. Density versus porosity for the Marcellus interval, color-coded by depth. The Upper and Lower Marcellus units segregate into two data clouds in this data space.

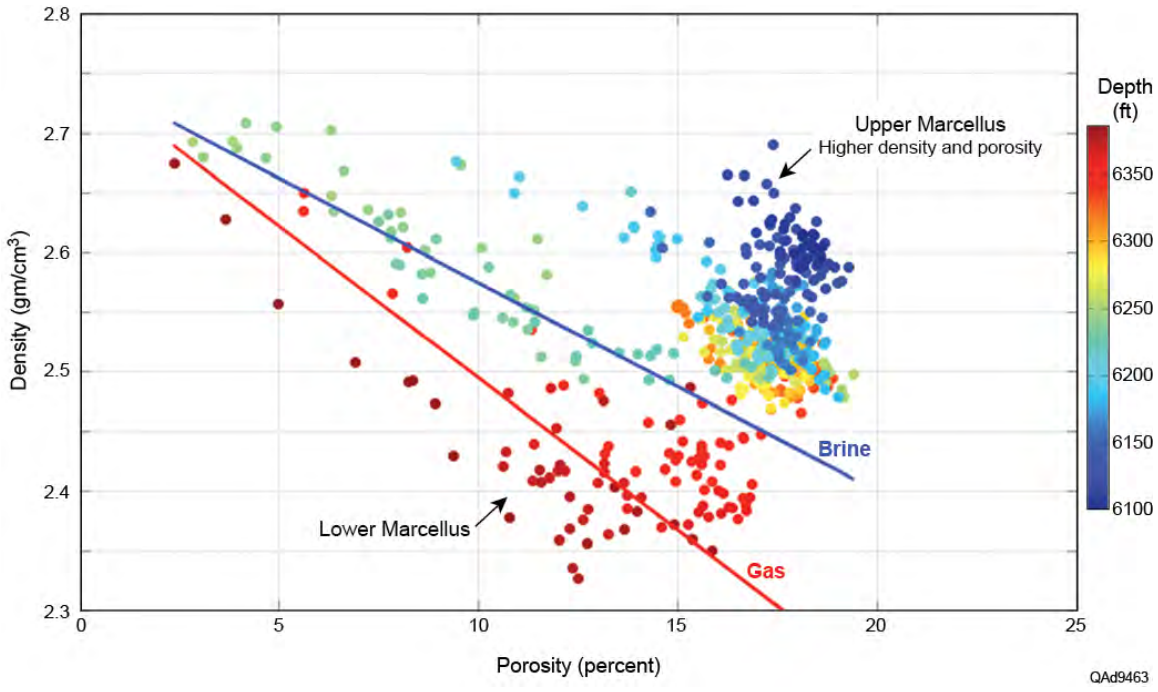

Figure 5.6. Density versus porosity for the Marcellus interval, color-coded by depth. Superimposed are two linear trends for density versus porosity. The blue line represents brine in the pore space, and the red line represents gas-filled pores. Grain density is assumed to be 2.75 gm/cm^3.

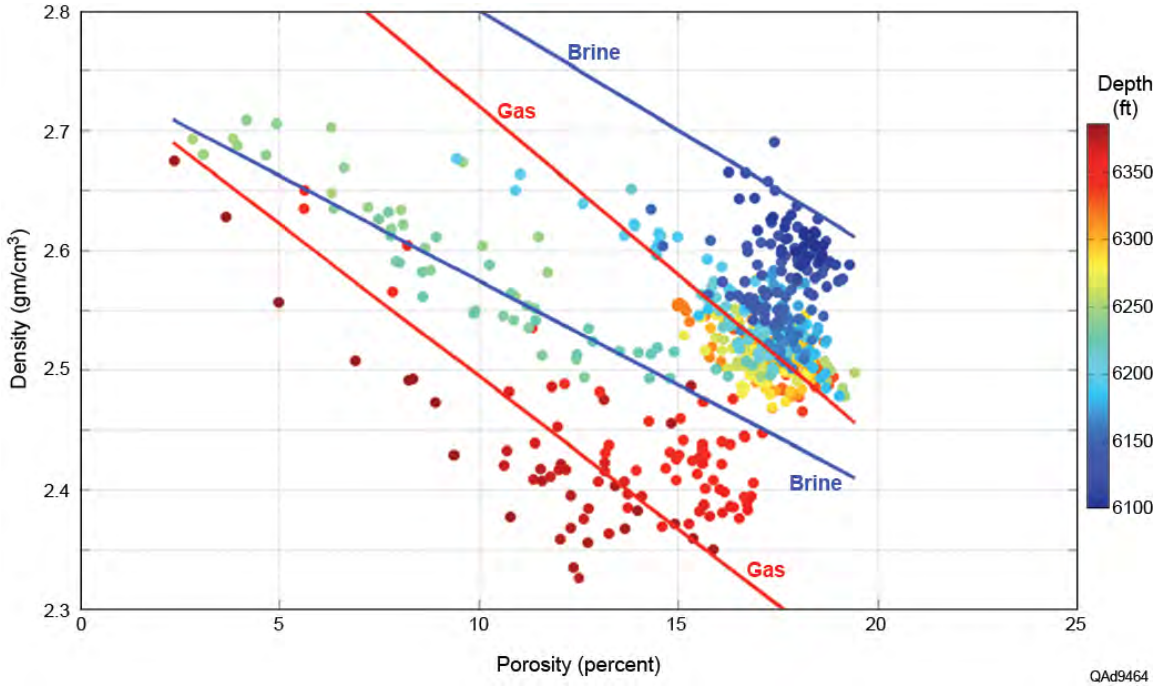

Figure 5.7. Density versus porosity for the Marcellus interval, color-coded by depth. Blue lines represent brine filling the porous space, and red lines assume gas fills the porous space. Grain density is assumed to be 2.75 gm/cm^3 for the Lower Marcellus and 2.98 gm/cm^3 for the Upper Marcellus.

This rock physics model suggests it is primarily a variation in mineralogy that causes different density-porosity relations for the Upper and Lower Marcellus units. Without core information from the central-image well, specific differences in mineralogy cannot be validated for the two Marcellus units. The density-porosity relations for Upper and Lower Marcellus shown on Figure 5.7 can be obtained with other volume fractions and other minerals. For example, a volume fraction of carbonate grains, as well as pyrite, could be assumed to be present in the Upper Marcellus, and a larger percent of organic matter could be assumed in the Lower Marcellus. The possibility of increased organic matter in the Lower Marcellus is supported by the higher gamma-ray response of that unit (Figs. 5.1 and 5.2). For any of these possibilities, the concept of different mineral assemblages forms a plausible scenario that explains data scatter in density-porosity cross-plots across the Marcellus interval.

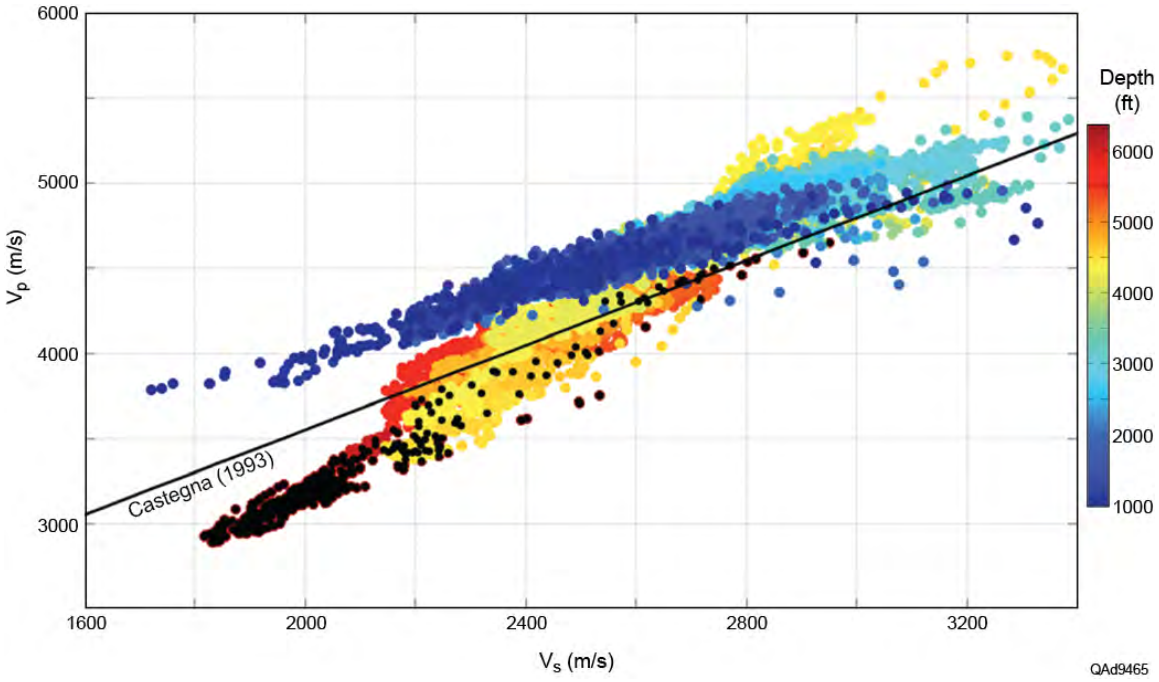

Figure 5.8. P-wave velocity versus fast-S velocity for the entire logged interval, color-coded by depth. Superimposed in black are data from the Marcellus interval. The black line corresponds to the empirical relation for brine shale developed by Castagna (1993).

For seismic interpretation purposes, it is particularly important to understand how log data define variations in P-wave and S-wave velocities between rock units. Figure 5.8 presents a cross-plot of log-based P and S velocities, color-coded by depth, across the entire logged interval. The V_P-to-V_S relation varies with depth, with data shallower than 4000 ft following a different trend than data deeper than 4000 ft. Black data points correspond to the

Marcellus interval. Superimposed on the cross-plot is an empirical relation developed by Castagna (1993) for brine-saturated shales. Because the Marcellus is gas charged, data corresponding to the Marcellus Shale do not fall on this empirical line. P-wave velocities for the Marcellus Shale are lower than values predicted by this empirical trend for brine shales, again an indication of overpressuring within the Marcellus interval.

.

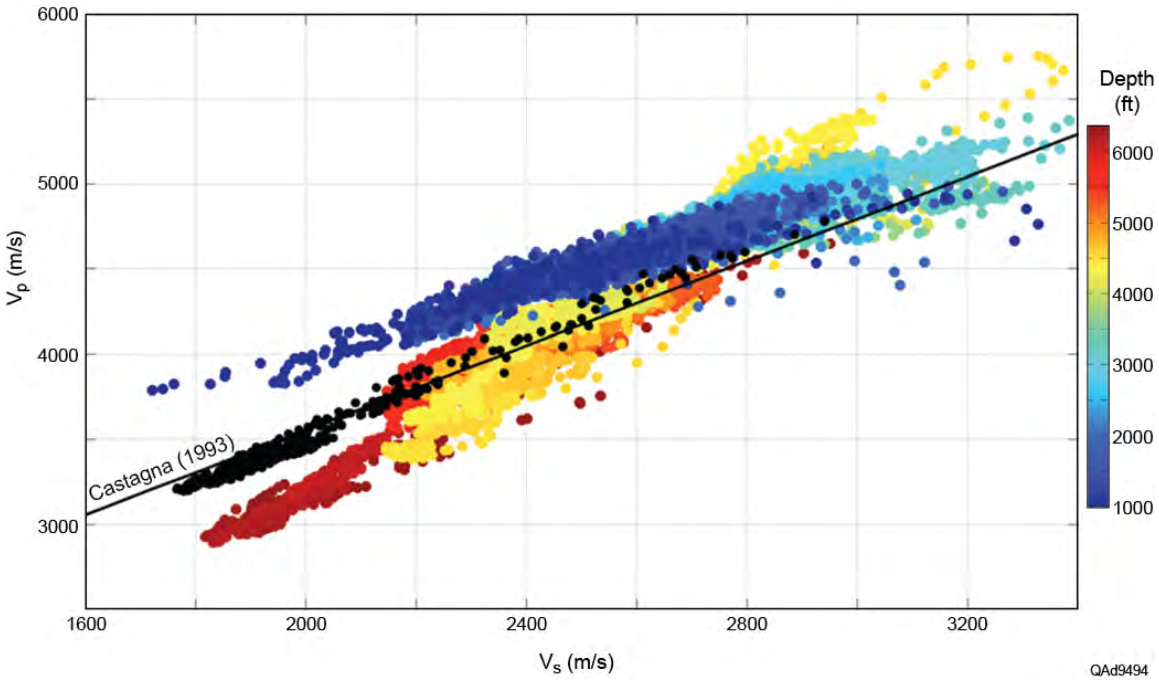

Figure 5.9. P-wave velocity versus S-wave velocity (fast polarization) for the entire logged interval, color-coded by depth. Superimposed in black are theoretical fluid-substitution results using Gassmann's Equation for brine-saturated conditions in the Marcellus interval. The black line corresponds to the empirical relation for brine shale by Castagna (1993). The calculated brine-saturated velocities for the Marcellus Shale fall close to the empirical line for brine shales.

The influence of pore-filling fluid on P-wave velocity can be demonstrated by using a theoretical fluid-substitution theory, such as Gassmann's (1959) Equation, to derive P and S velocities for a brine-saturated Marcellus interval. This calculation shows that when gas is displaced by brine, the data shift to higher P-wave velocities. This effect is demonstrated on Figure 5.9 where theoretical fluid substitutions in the Marcellus Shale are displayed as black data points that position atop Castagna's empirical line for brine shales. This modeling exercise is additional proof that the Marcellus interval is gas charged.

Orthorhombic Media

The simplest form of fractured-rock media can be described in terms of two symmetry planes—an isotropy plane parallel to fractures and a symmetry

plane normal to fractures. Such **horizontal transverse isotropy** (**HTI**) fracture models are appropriate when analyzing elastic wavefields propagating in a thick, non-stratified layer of rock having vertical fractures oriented in a single azimuth. In contrast, if a fracture interval consists of thin, stacked rock layers, then three symmetry planes are embedded in the rock, and the medium becomes **orthorhombic** (Fig. 5.10).

An HTI medium can be described in terms of five stiffness coefficients, but nine stiffness coefficients are required to describe an orthorhombic material. An orthorhombic medium may have one set of aligned fractures as illustrated on Figure 5.10, or two sets of orthogonal fractures. In the latter case, the second set of fractures would be aligned along symmetry plane 1 defined on the figure. If there are two sets of fractures, but the fracture sets are not orthogonal to each other, then the medium is not orthorhombic, but is an even more complicated monoclinic rock.

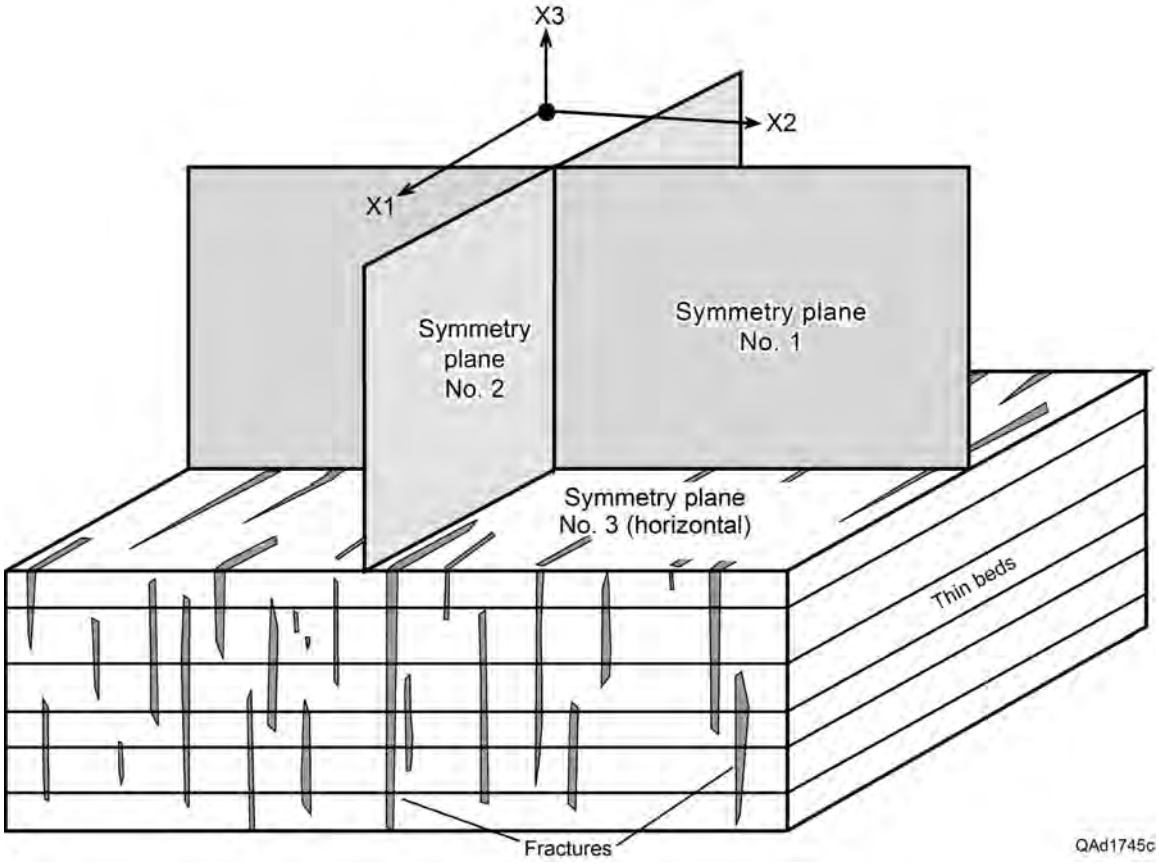

Figure 5.10. An orthorhombic medium has three symmetry planes. The most common forms of orthorhombic rocks are fractured intervals consisting of thin, stacked strata. The fracture system can be one set of fractures aligned with symmetry plane 2 as shown on this illustration, or two sets of orthogonal fractures, with fracture set 2 aligned with symmetry plane 1. When discussing orthogonal joint systems in the Marcellus, J1 joints will be aligned with symmetry plane 1, and J2 joints will be aligned with symmetry plane 2.

An example of an orthorhombic rock is the Marcellus Shale spanning our study site in Bradford County, Pennsylvania. An exposed section of Marcellus Shale is shown as Figure 5.11. The Marcellus has two embedded joint sets, referred to as J1 and J2 that are usually observed to be orthogonal to each other as they are in this exposure. The Marcellus Shale is also stratified in thin layers, completing the requirements for an orthorhombic seismic medium.

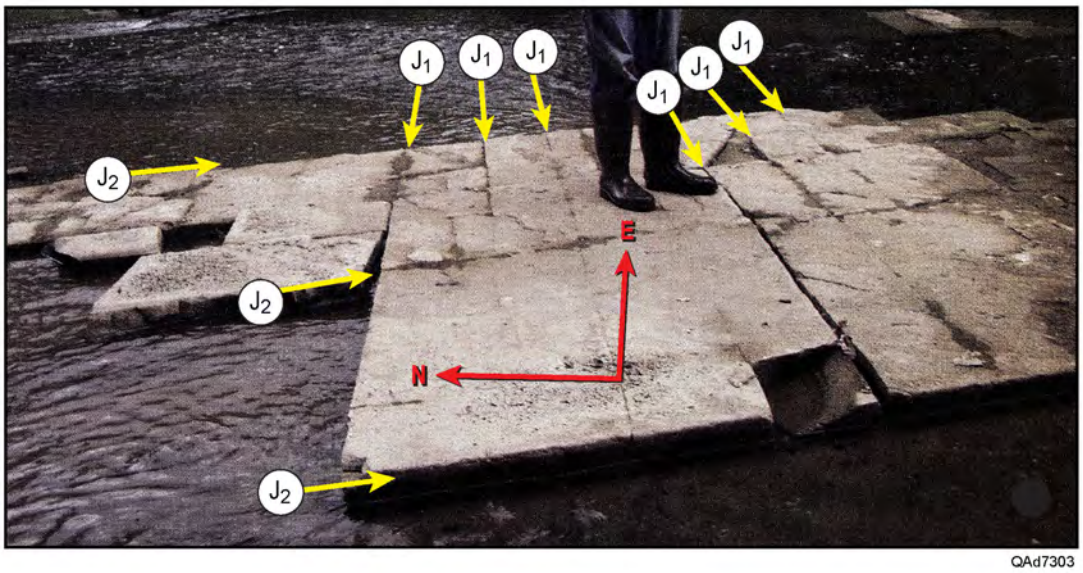

Figure 5.11. Exposure of Marcellus Shale. This unit is stratified into thin layers and has two orthogonal joint sets, J1 and J2, making the Marcellus Shale a classic orthorhombic seismic propagation medium. From Engelder et al. (2009).

Fracture Modeling of Marcellus Shale

Using seismic data to characterize fractures requires that elasticity theories be developed that relate seismic-sensitive properties of rocks to physical parameters of fractures. Fracture attributes of particular interest are fracture density, fracture orientation, and type of fracture-filling fluid. A penny-shaped crack model is one theory that predicts elastic properties of a fractured medium in instances where penny-shaped openings are reasonable approximations of the geometries of cracks distributed within an interval.

Hudson's model (1981, 1990, 1994) is a popular effective-medium theory that assumes a fractured rock can be approximated by an elastic solid with an internal distribution of thin, penny-shaped cracks. Hudson uses **crack density (*e*)** and the **aspect ratio of cracks (*α*)** to describe the structure of fracture

systems. The aspect ratio of a crack is the ratio of the short and long semi-axes of the crack. Crack density, or fracture density, is defined as:

(5.2) $$e = \frac{N}{V} a^3 = \frac{3\phi}{4\pi\alpha},$$

where ***a*** is the crack radius, ***N / V*** is the number of cracks per unit volume, **Φ** is crack-induced porosity, and α is the aspect ratio of the cracks.

The effective elastic-stiffness matrix ***C*** of an elastic medium is:

(5.3) $$C_{ij} = C_{ij}^0 + C_{ij}^1 + C_{ij}^2,$$

where C_{ij}^0 are the components of the isotropic background elastic-stiffness tensor, and C_{ij}^1 *and* C_{ij}^2 are first-order and second-order corrections, respectively, which depend on crack orientation, crack density, aspect ratio, and the bulk and shear moduli of the material filling the cracks. Second-order corrections have the flaw that as crack density increases, a rock does not fall apart. Therefore, we used only first-order corrections in this study, as most researchers do. In this modeling approach, the elastic stiffness of a rock decreases monotonically as crack density increases, until the rock completely loses its strength.

We used Hudson's theory to develop models for diverse crack distributions, with emphasis on models for fractured rocks that have more than one set of fractures. We considered four scenarios. The first three models corresponded to orthorhombic media generated by two sets of vertical joints (J1 and J2) that: (1) were orthogonal to one another, and (2) had different fracture densities (e1 and e2). These models corresponded to fracture conditions observed in outcrops of Marcellus Shale (Fig. 5.11). The fourth model described an HTI media having a single set of vertical joints (J1). The fracture distributions assigned to the joint systems of these models are summarized in Table 5.1

Table 5.1. Fracture densities of Marcellus joint sets.

Joint set	Fracture densities (e_1 and e_2)			
	Model 1	Model 2	Model 3	Model 4
J1	0.04	0.05	0.06	0.07
J2	0.04	0.04	0.03	0.0

Using Hudson's theory we computed an elastic-stiffness matrix describing an orthorhombic medium having two sets of orthogonal, vertical fractures for each of the fracture density pairs listed in Table 5.1. We used averaged well log

velocities and densities across the Marcellus Shale as background properties of the host rock. The aspect ratio of the fractures, α was assumed to be 0.0001 in all calculations. The fluid in the fractures was always represented by gas, with elastic properties of the gas-filled fractured rock determined using Batzle and Wang (1992) empirical relations.

The elastic-stiffness matrix associated with fracture Model 1 (Table 5.1), an equal-fracture-density model, is given in units of GPa as:

$$C1 = \begin{pmatrix} 26.892 & 5.100 & 5.124 & 0 & 0 & 0 \\ 5.100 & 26.892 & 5.124 & 0 & 0 & 0 \\ 5.124 & 5.124 & 27.045 & 0 & 0 & 0 \\ 0 & 0 & 0 & 9.882 & 0 & 0 \\ 0 & 0 & 0 & 0 & 9.882 & 0 \\ 0 & 0 & 0 & 0 & 0 & 8.816 \end{pmatrix}. \tag{5.4}$$

Using this elastic-stiffness matrix, together with the calculation procedures described in Appendix A, we computed Thomsen-type anisotropic parameters and phase velocities in the symmetry planes of the orthorhombic medium. The vertical shear-wave-splitting parameter, $\gamma^{(s)}$, is defined as:

$$\gamma^{(s)} = \frac{C1(4,4) - C1(5,5)}{2C1(5,5)}. \tag{5.5}$$

Index numbers (4,4) and (5,5) in this equation represent coefficient positions in the 6 × 6 elastic-stiffness matrix C1. Inspection of Equation 5.4 shows C1(4,4) = C1(5,5) = 9.882, thus $\gamma^{(s)}$ is zero. Therefore, when the fracture densities of two vertical, orthogonal joint sets J1 and J2 are the same, vertical S-wave anisotropy is zero, meaning there is no S-wave splitting and no fast-S and slow-S modes

If we compute P and S phase velocities in the symmetry-axis planes of the orthorhombic medium as a function of incidence angle, we observe in Figure 5.12 that P-P, P-SV, and SH-SH phase velocities in the [x1 x3] plane (Fig. 5.10) have the same values as their equivalents in the [x2 x3] plane when the fracture densities for the two orthogonal joint sets are equal.

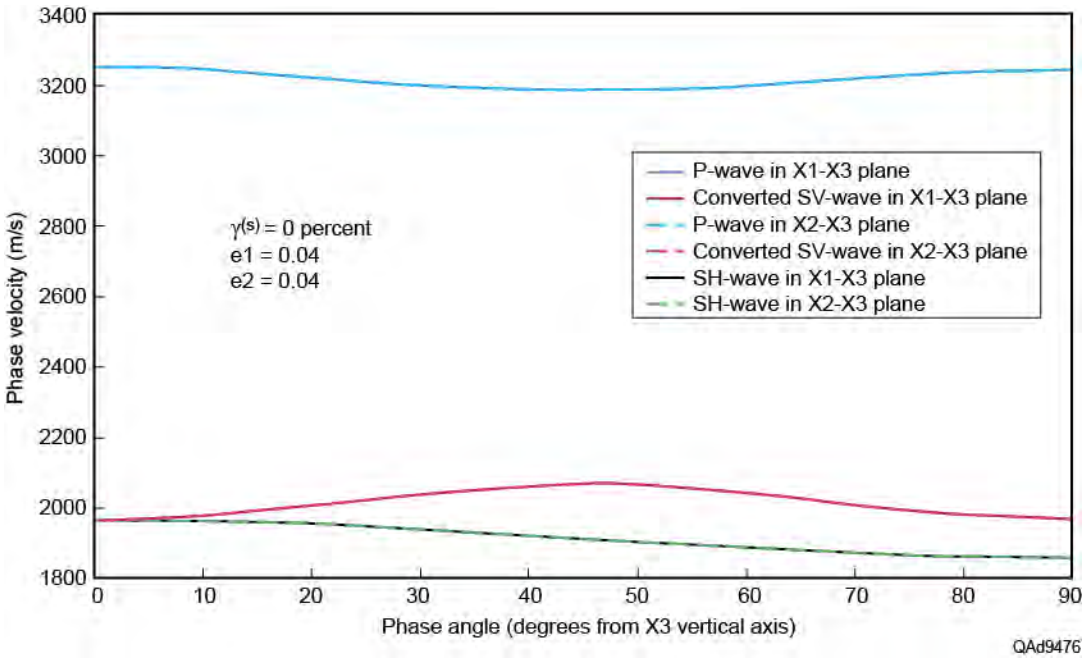

Figure 5.12. Phase velocities, as a function of incident angle, in the two vertical symmetry planes of an orthorhombic medium representing the Marcellus Shale. The calculation assumes two joint sets, J1 and J2, with equal fracture densities, e1=e2=0.04 (Model 1, Table 5.1). The aspect ratio of the fractures is 0.0001, and the fluid inside the fractures is assumed to be gas.

For orthorhombic Model 2 (Table 5.1), where there are small differences in the fracture densities for the two vertical joint sets, Hudson fracture modeling yields the following elastic-stiffness matrix C2 (in units of GPa):

(5.6)
$$C2 = \begin{pmatrix} 26.852 & 5.092 & 5.117 & 0 & 0 & 0 \\ 5.092 & 26.890 & 5.123 & 0 & 0 & 0 \\ 5.117 & 5.123 & 27.044 & 0 & 0 & 0 \\ 0 & 0 & 0 & 9.882 & 0 & 0 \\ 0 & 0 & 0 & 0 & 9.615 & 0 \\ 0 & 0 & 0 & 0 & 0 & 8.549 \end{pmatrix}.$$

In this case, the vertical shear-wave splitting parameter $\gamma^{(s)}$ (Eq. 5.5) is not zero, but has a small value of 0.0139. The result is a trivial S-wave anisotropy of approximately 1.4-percent. The well log data exhibited on Figure 5.2 indicate S-wave anisotropy in the Marcellus Shale is approximately this magnitude (about 1-percent on the log display). Taken at face value, an S-wave anisotropy of this small magnitude implies there are no aligned vertical fractures. However, when this anisotropy result is applied to outcrops of the Marcellus Shale, it indicates

there are two vertical joint systems, orthogonal to each other, that have similar fracture densities.

We also used stochastic simulations in our fracture modeling to account for possible variability in the background rock properties of the Marcellus Shale. We assumed Gaussian distributions for the fracture densities of the two joint sets rather than constraining each joint set to have a constant fracture density throughout the entire Marcellus interval. For Model 2 (Table 5.1), these distribution functions were defined as Gaussian functions having mean values of 0.05 and 0.04, respectively, and small standard deviations of 0.001. Figure 5.13 presents the results of these stochastic simulations on S-wave anisotropy and the actual S-wave anisotropy measured by well log data. The modeled S-wave anisotropy (Fig. 5.13a) has values in the same numerical range as actual well log measurements (Fig. 5.13b), suggesting the two vertical joint sets in the Marcellus interval have similar fracture densities, at least local to the central-image calibration well.

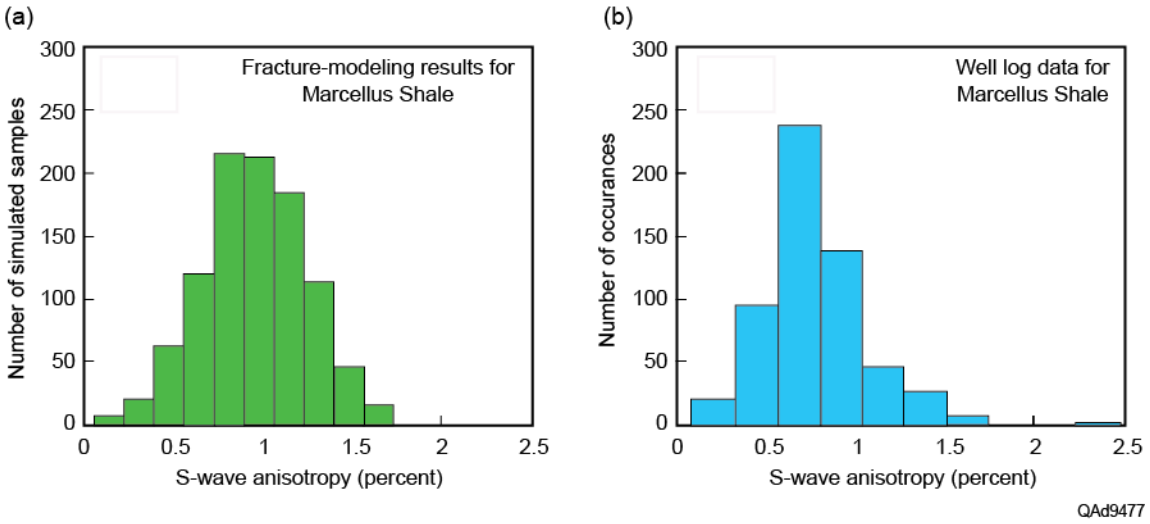

Figure 5.13. Histograms of S-wave anisotropy (in percentages) for (a) stochastic fracture modeling of Marcellus Shale Model 2 (Table 5.1), and (b) well log measurements across the Marcellus Shale. Parameters used in the stochastic simulation are described in the accompanying text.

Figure 5.14 defines phase velocity behavior in the vertical symmetry planes for Model 2 conditions. The symmetry plane nomenclature (x1, x2, x3) used in this analysis is defined on Figure 5.10. In this case, P-P phase velocities are slightly different in the two symmetry planes, in contrast to their behavior in Model 1 which had equal fracture densities (Fig. 5.12). Differences are also observed for P-SV and SH-SH phase velocities in the two symmetry planes when the fracture densities of the two orthogonal joint sets are not equal. Because the difference in fracture densities is small, the corresponding differences in phase velocities in the two vertical symmetry planes are also small.

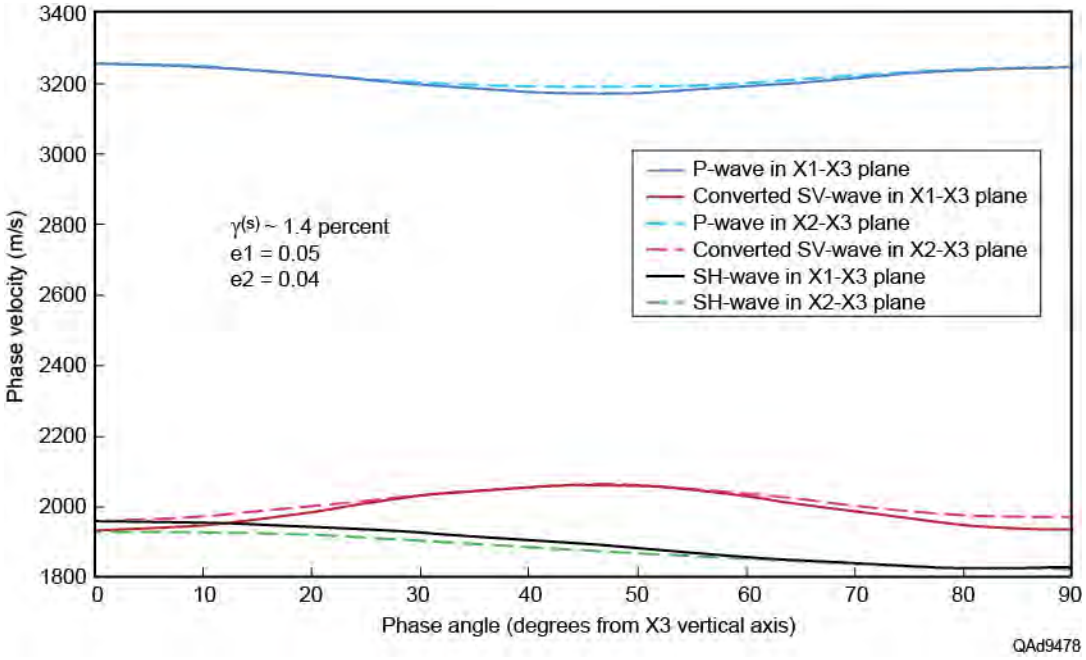

Figure 5.14. Phase velocities, as a function of incidence angle, in the vertical symmetry planes of an orthorhombic medium representing the Marcellus Shale. Joint sets J1 and J2 are assumed to have fracture densities of e1=0.05 and e2=0.04, respectively (Model 2, Table 5.1). The aspect ratio of the fractures is 0.0001, and the fluid inside the fractures is assumed to be gas.

For fracture Model 3 (Table 5.1), with fracture densities e1=0.06 and e2=0.03 for joint sets J1 and J2, respectively, the computed elastic-stiffness matrix in units of GPa is

(5.7)
$$C3 = \begin{pmatrix} 26.814 & 5.092 & 5.110 & 0 & 0 & 0 \\ 5.092 & 26.929 & 5.129 & 0 & 0 & 0 \\ 5.110 & 5.129 & 27.044 & 0 & 0 & 0 \\ 0 & 0 & 0 & 10.149 & 0 & 0 \\ 0 & 0 & 0 & 0 & 9.349 & 0 \\ 0 & 0 & 0 & 0 & 0 & 8.549 \end{pmatrix}.$$

In this case, the vertical shear-wave splitting parameter $\gamma^{(s)}$ (Eq. 5.5) has a value of 0.043 because the difference between crack densities of the two joint systems is larger. The result is a larger S-wave anisotropy slightly larger than 4 percent. Correspondingly, the differences in phase velocities of modes propagating in the two symmetry planes are also larger than what was observed for Models 1 and 2 (Fig. 5.15).

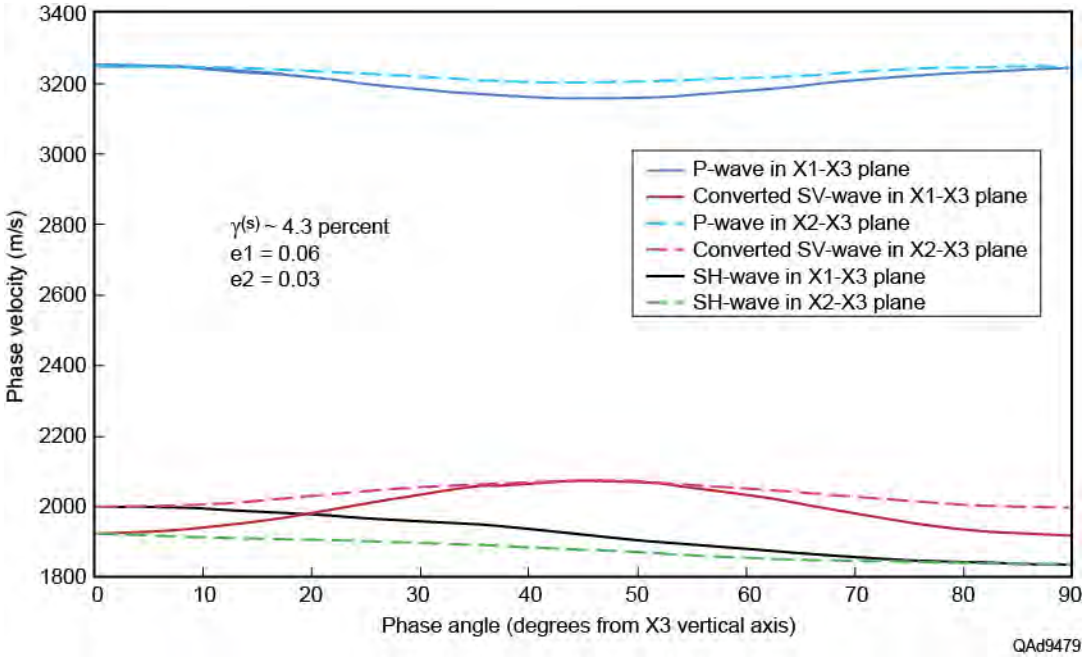

Figure 5.15. Phase velocities, as a function of incidence angle, in the vertical symmetry planes of an orthorhombic medium representing the Marcellus Shale. The two joint sets J1 and J2 have respective fracture densities of e1=0.06 and e2=0.03 (Model 3, Table 5.1). The aspect ratio of the fractures is 0.0001, and the fluid inside the fractures is assumed to be gas.

The fourth model in Table 5.1 assumes a single joint set (J1). This model represents a transversely isotropic medium with a horizontal symmetry axis (an HTI medium). The elastic-stiffness matrix for this medium, computed using Hudson's model, is given by:

(5.8)
$$C4 = \begin{pmatrix} 26.778 & 5.107 & 5.107 & 0 & 0 & 0 \\ 5.107 & 27.047 & 5.150 & 0 & 0 & 0 \\ 5.107 & 5.150 & 27.047 & 0 & 0 & 0 \\ 0 & 0 & 0 & 10.948 & 0 & 0 \\ 0 & 0 & 0 & 0 & 9.082 & 0 \\ 0 & 0 & 0 & 0 & 0 & 9.082 \end{pmatrix}.$$

For this model, there is a larger difference between the C4(4,4) and C4(5,5) matrix terms, and the corresponding S-wave splitting at normal incidence is 0.1027 (Eq. 5.5). For this HTI medium, even though its overall fracture density of 0.07 is smaller than the cumulative fracture density of 0.09 for the two orthorhombic media of Models 2 and 3 (Table 5.1), the S-wave anisotropy is larger than that of either orthorhombic medium. Phase velocity behaviors in the symmetry-axis planes are shown on Figure 5.16.

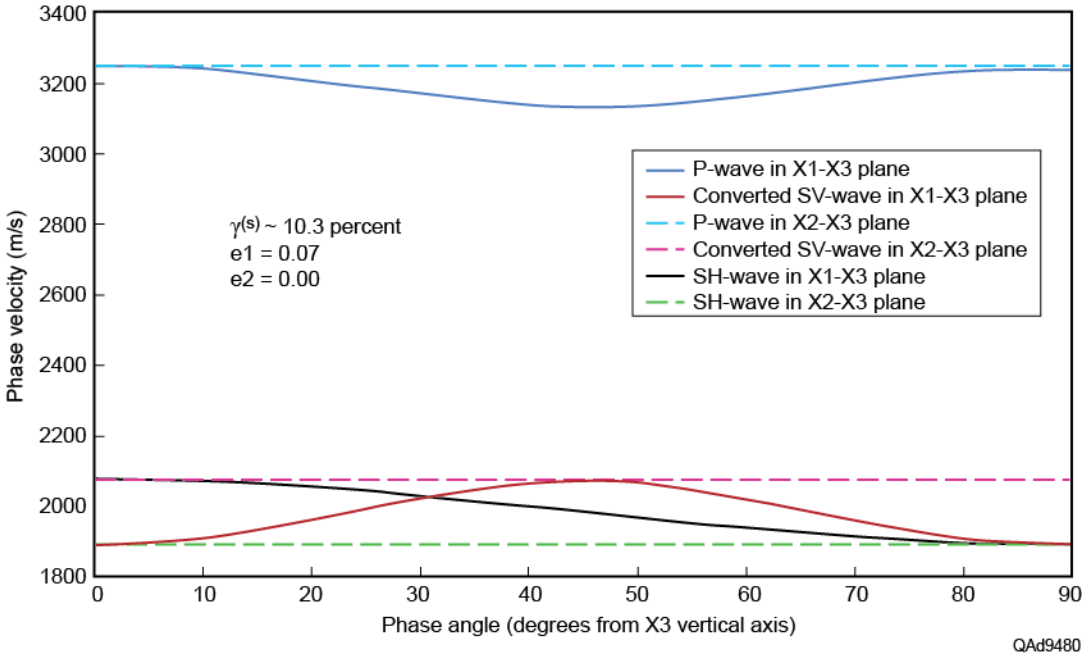

Figure 5.16. Phase velocities, as a function of incidence angle, in the vertical symmetry planes when an HTI medium is assumed for the Marcellus Shale. In this calculation it is assumed the Marcellus has a single joint set J1 with a fracture density of e1=0.07 (Model 4, Table 5.1). The aspect ratio of the fractures is 0.0001, and the fluid inside the fractures is assumed to be gas.

For Model 4, we again used stochastic simulations to account for the variability in background rock properties across the Marcellus interval. Panel (a) of Figure 5.17 presents a histogram of the modeled S-wave anisotropy for this HTI medium. Panel (b) of the same figure repeats the histogram of the modeled S-wave anisotropy for the orthorhombic medium of Model 2 from Figure 5.13a. These side-by-side comparisons show the S-wave anisotropy of the HTI medium with its single joint system J1 is larger than the S-wave anisotropy of the orthorhombic medium with two sets of vertical joints orthogonal to each other. This result is counter intuitive to some interpreters because the overall fracture density of the orthorhombic medium is larger (e1+e2=0.09) than the fracture density of the HTI medium (e1=0.07). This analysis leads to the following important rock-physics principle:

For orthorhombic media having two joint systems orthogonal to one another, S-wave anisotropy is not a good indicator of fracture density, although it is the preferred parameter for indicating fracture density in HTI media having a single set of vertical joints.

As an application of this principle, the low values of S-wave anisotropy observed for the Marcellus interval in the central-image well log data (Fig. 5.2) indicate the Marcellus has two orthogonal joint systems that have similar crack densities.

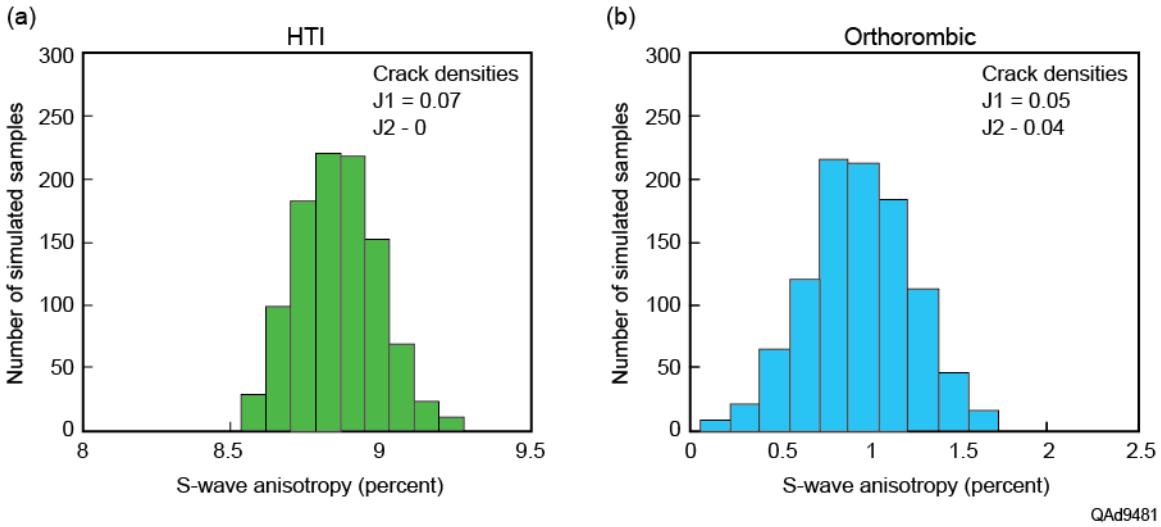

Figure 5.17. Histograms of stochastically modeled S-wave anisotropy for (a) an HTI medium having a single set of vertical joints with a fracture density e1 = 0.07 (Model 4 of Table 5.1), and (b) an orthorhombic medium having two vertical fracture joints orthogonal to each other with fracture densities e1 = 0.05 and e2 = 0.04 (Model 2 of Table 5.1)

.

When there are two sets of vertical joints orthogonal to each other, both slow and fast S-wave polarizations have velocities slower than the V_S velocity of the unfractured background rocks, because both polarizations directions are orthogonal to fracture systems. Therefore, to characterize fractures in such media we need to look for decreases in shear velocity within a targeted fracture interval and compare these decreases with the shear velocity of the unfractured rock. For optimal calibration, these comparisons need to be made in the laboratory or from log measurements acquired in intervals with and without fractures.

Because S-wave velocity decreases when S modes propagate in orthogonal joint sets, the V_P/V_S ratio increases in an orthorhombic medium. Therefore, seismic-derived V_P/V_S ratios may be good indicators of fracture density variations across a fractured orthorhombic target such as the Marcellus Shale

There are properties other than fractures, such as lithology variations and fluid changes, that could increase the V_P/V_S ratio within the Marcellus. For example, Figure 5.18 shows cross-plots of S-wave velocity and V_P/V_S ratio for three situations: (1) the in-situ Marcellus log data, (2) fracture modeling results for Model 2 (Table 5.1), and (3) a theoretical brine-saturated Marcellus Shale. These data show that an increase in V_P/V_S ratio can be caused by either the

presence of fractures or by brine replacing gas. In these two scenarios, the increase in V_P/V_S ratio is the result of decreasing S-wave velocity when fractures are present, and due to increasing P-wave velocity when brine replaces gas. The latter effect occurs because the bulk modulus of brine is larger than the bulk modulus of gas.

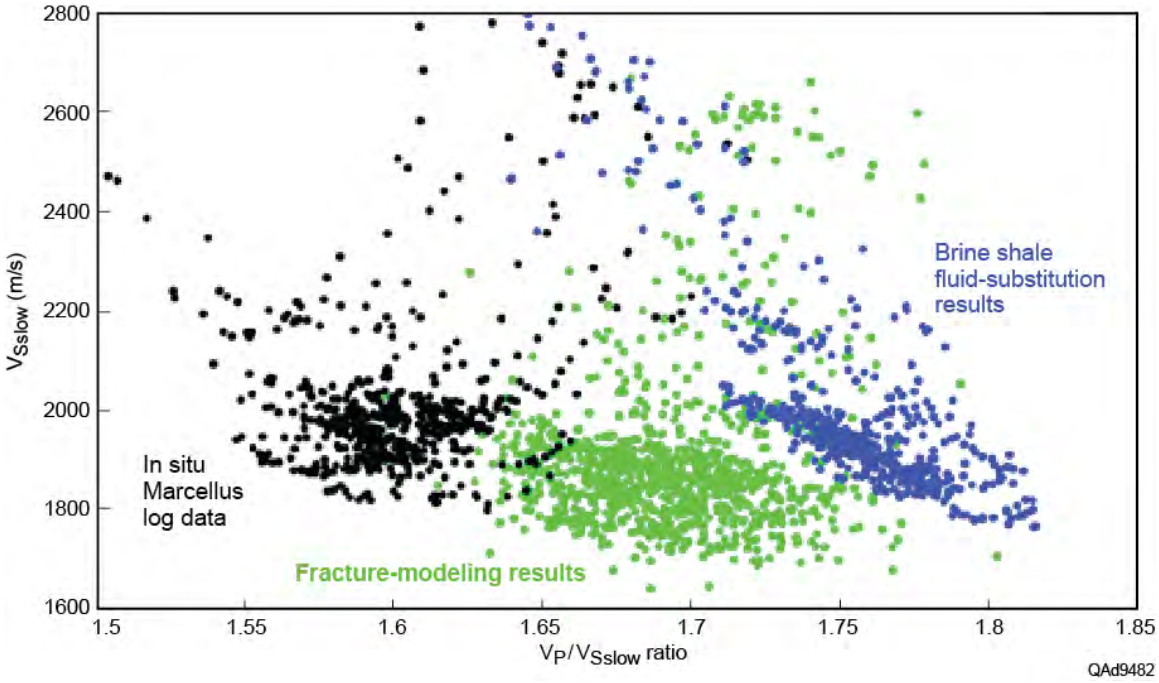

Figure 5.18. Slow S-wave velocity versus V_P/V_{slow} ratio for actual Marcellus well log data (black dots), fracture modeling results (green dots), and fluid substitution results that create a brine-saturated Marcellus (blue dots).

This rock-physics modeling shows that for orthorhombic media, classical S-wave anisotropy is not the attribute to use to estimate fracture density because large degrees of fracturing do not cause large differences in fast-S and slow-S velocities when a medium has two sets of vertical joints orthogonal to each another. However, fracture density of orthogonal joint sets does lower S-wave velocity relative to the S velocity of the unfractured background rocks. Also, by using both P and S velocities, it should be possible to differentiate between fracture effects and fluid effects on V_P/V_S ratios.

P and S Amplitude Variations with Incidence Angle and Azimuth

Some rock and fluid properties can be inferred from seismic data by the way these properties affect P and S reflection amplitudes as wave modes arrive at targeted interfaces at different incident angles and azimuth approach directions. We modeled how P and S amplitudes varied as functions of incidence angle and azimuth at the top of Marcellus Shale for three wave modes: P-P, P-SV_1, and P-SV_2. The acronym **AVAZ** will be used to indicate “amplitude versus

angle and azimuth." In this modeling, we considered fracture properties within the Marcellus could be approximated by the four model conditions listed in Table 5.1. For the rock layer above the Marcellus, we used average properties for V_P, V_S, and density observed in well log data. To calculate P-P reflection modes, we used equations developed by Vavricuk and Psencik (1998). To model the reflectivity behavior of converted P-SV_1 and P-SV_2 waves, we used equations developed by Jilek (2002).

Modeling results of P-P reflectivity for the four fracture scenarios described in Table 5.1 are presented as Figures 5.19 through 5.22. Modeling results for P-SV_1 reflectivity are illustrated on Figures 5.23 through 5.26, and P-SV_2 results are displayed as Figures 5.27 through 5.30. In all of these figures, the left panel shows reflectivity behavior as a function of incidence angle and azimuth. In this display format, incidence angle increases from 0 at the center of the circle to 45 degrees at the circumference along any chosen radius, and azimuth varies from 0 to 360 degrees around the circle. An azimuth of 0-degrees is oriented along the x1 axis (orthogonal to the J1 fracture system). The right-side panel in each figure shows the reflection behavior at incidence angles of 20 and 45 degrees as a function of azimuth, which allows azimuth effects on reflectivity to be more easily compared at small and large incidence angles.

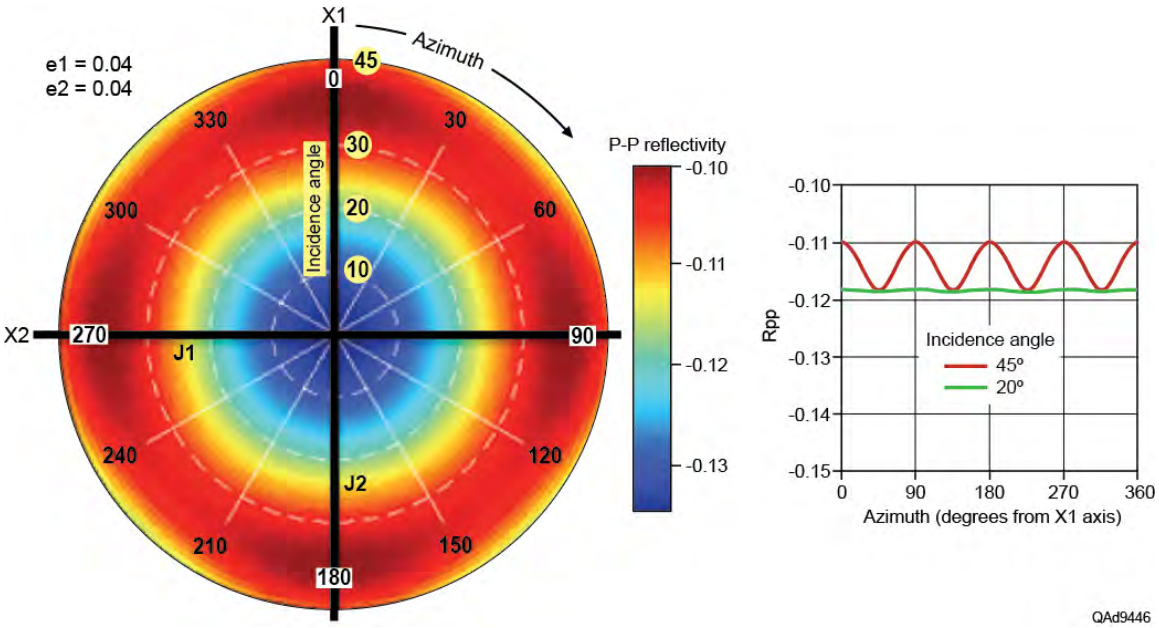

Figure 5.19. Modeling results for P-P reflectivity from the top of the Marcellus Shale when fracture conditions within the Marcellus are described by Model 1 of Table 5.1 (fracture density of J1 and J2 joint sets = 0.04). J1 joints align with the X2 axis; J2 joints align with the X1 axis. Left: P-P reflectivity as a function of incidence angle and azimuth. Right: P-P reflectivity as a function of azimuth for incidence angles of 20 and 45 degrees.

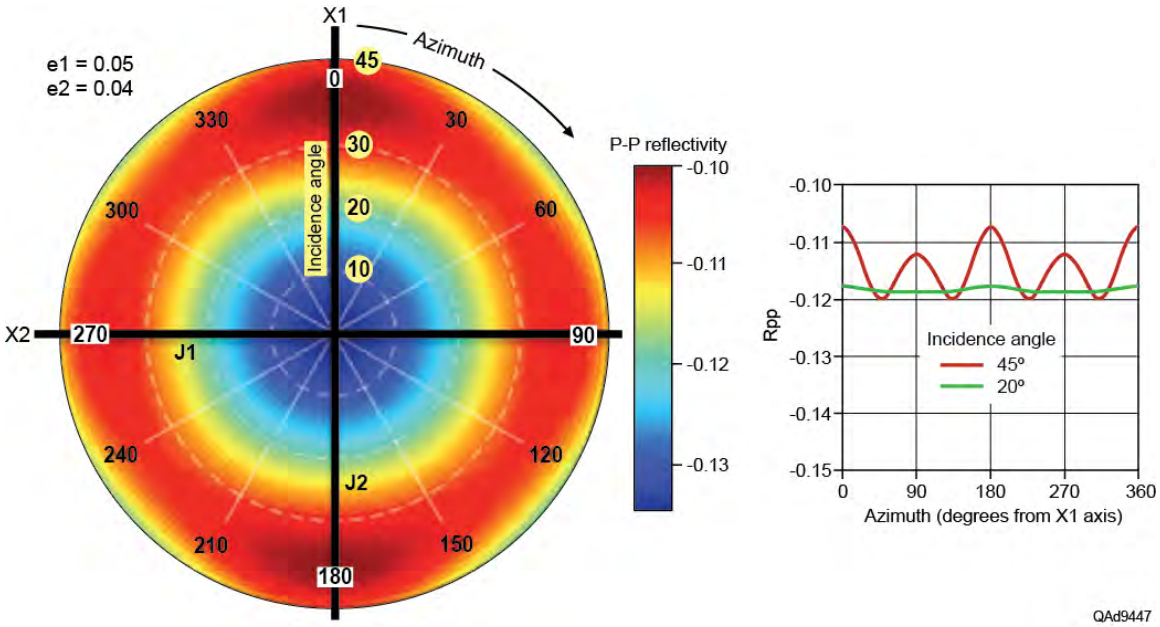

Figure 5.20. Modeling results for P-P reflectivity from the top of the Marcellus Shale when fracture conditions within the Marcellus are described by Model 2 of Table 5.1 (fracture density of J1 and J2 joint sets = 0.05 and 0.04). J1 joints align with the X2 axis; J2 joints align with the X1 axis. Left: P-P reflectivity as a function of incidence angle and azimuth. Right: P-P reflectivity as a function of azimuth for incidence angles of 20 and 45 degrees.

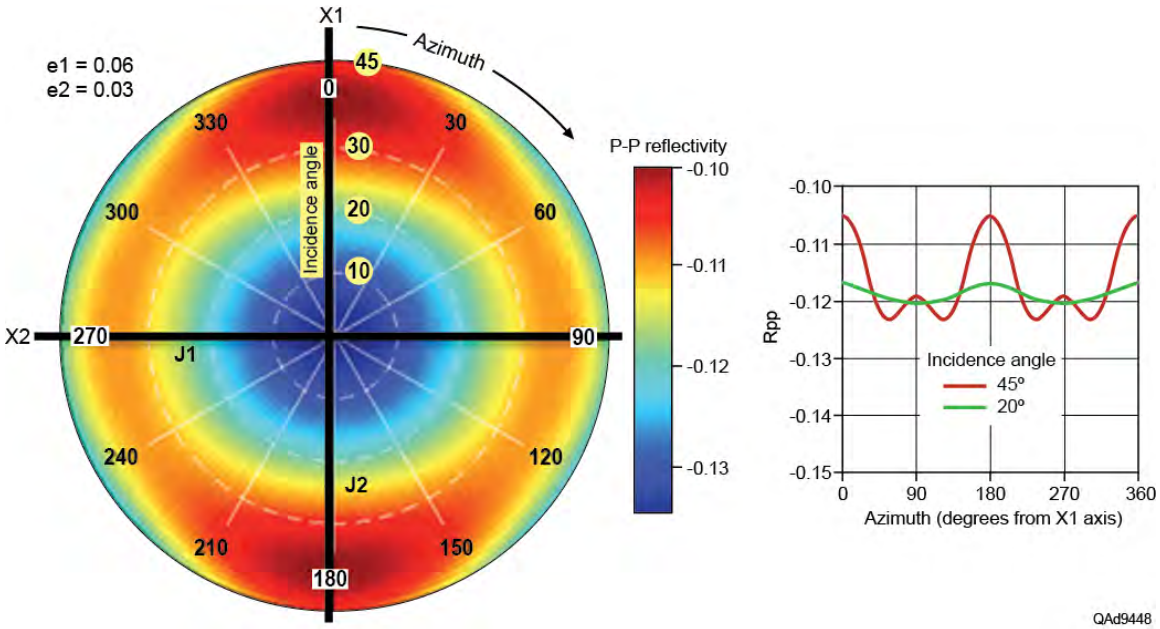

Figure 5.21. Modeling results for P-P reflectivity from the top of the Marcellus Shale when fracture conditions within the Marcellus are described by Model 3 of Table 5.1 (fracture density of J1 and J2 joint sets = 0.06 and 0.03). J1 joints align with the X2 axis; J2 joints align with the X1 axis. Left: P-P reflectivity as a function of incidence angle and azimuth. Right: P-P reflectivity as a function of azimuth for incidence angles of 20 and 45 degrees.

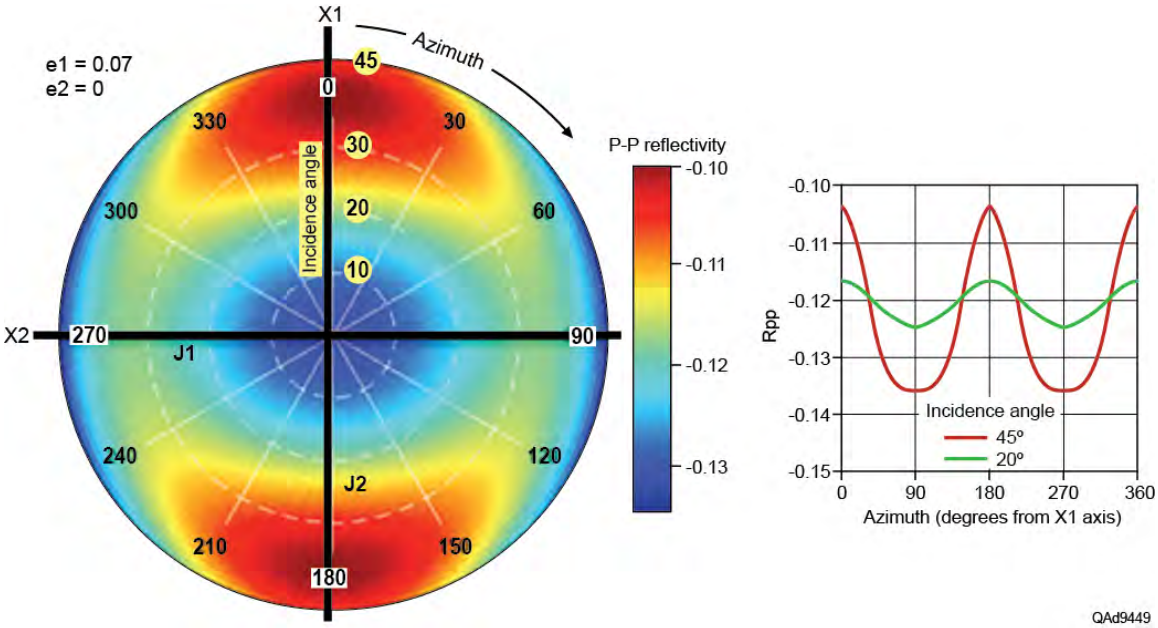

Figure 5.22. Modeling results for P-P reflectivity from the top of the Marcellus Shale when fracture conditions within the Marcellus are described by Model 4 of Table 5.1 (fracture density of J1 and J2 joint sets = 0.07 and 0.0). J1 joints align with the X2 axis; J2 joints align with the X1 axis. Left: P-P reflectivity as a function of incidence angle and azimuth. Right: P-P reflectivity as a function of azimuth for incidence angles of 20 and 45 degrees.

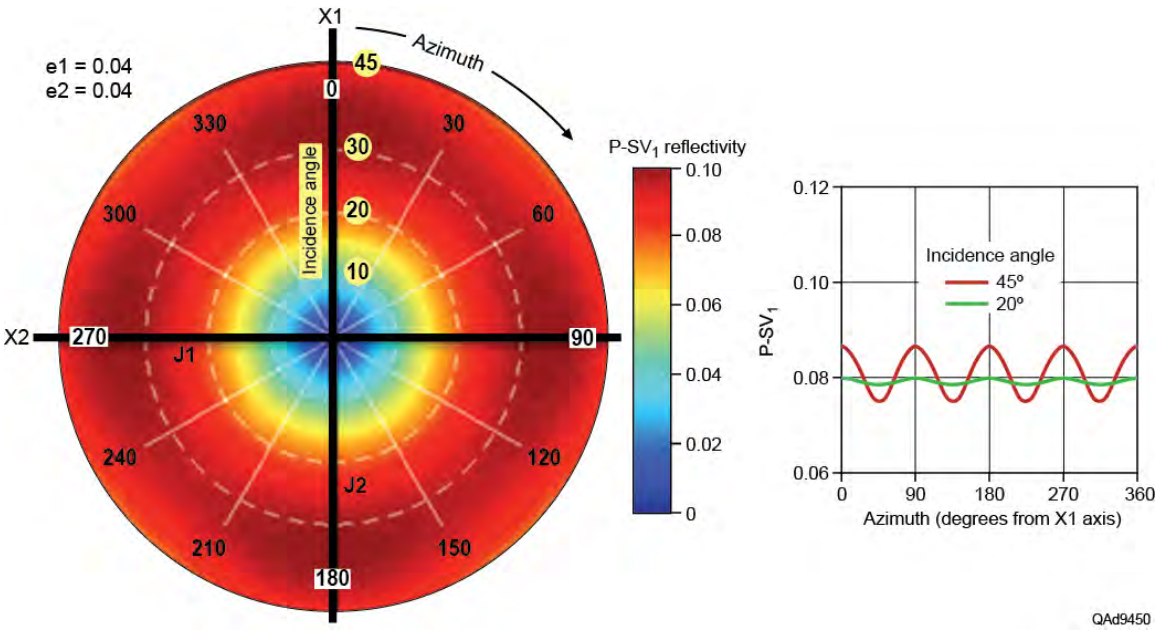

Figure 5.23. Modeling results for P-SV_1 reflectivity from the top of the Marcellus Shale when fracture conditions within the Marcellus are described by Model 1 of Table 5.1 (fracture density of J1 and J2 joint sets = 0.04). J1 joints align with the X2 axis; J2 joints align with the X1 axis. Left: P-SV_1 reflectivity as a function of incidence angle and azimuth. Right: Azimuth behavior of P-SV_1 reflectivity at incidence angles of 20 and 45 degrees.

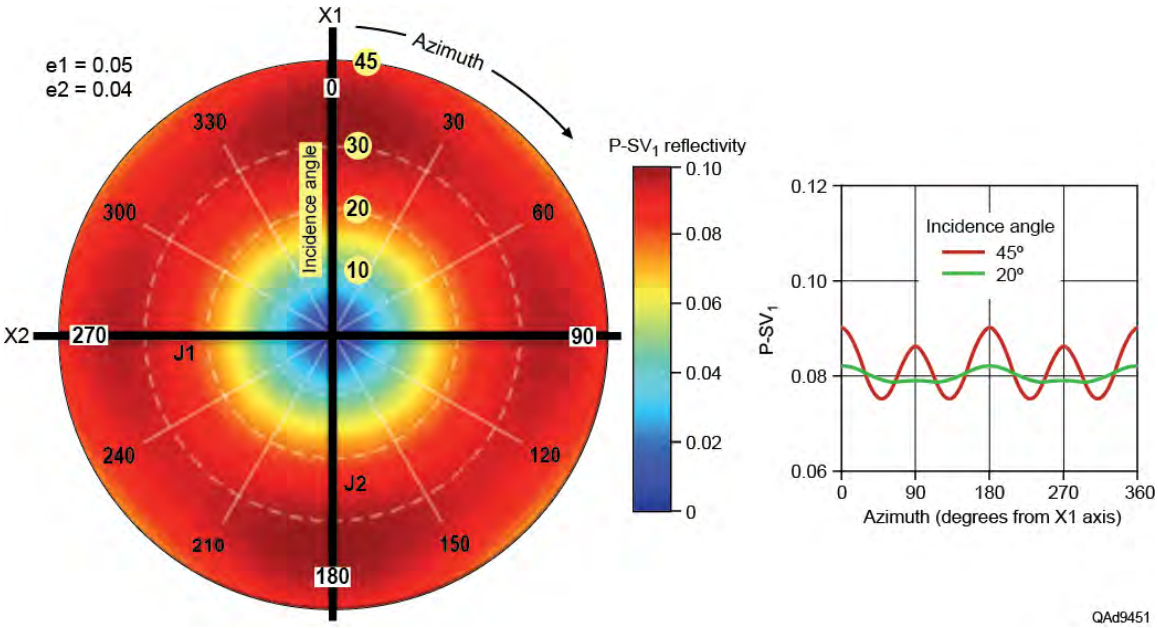

Figure 5.24. Modeling results for P-SV_1 reflectivity from the top of the Marcellus Shale when fracture conditions within the Marcellus are described by Model 2 of Table 5.1 (fracture density of J1 and J2 joint sets = 0.05 and 0.04). J1 joints align with the X2 axis; J2 joints align with the X1 axis. Left: P-SV_1 reflectivity as a function of incidence angle and azimuth. Right: Azimuth behavior of P-SV_1 reflectivity at incidence angles of 20 and 45 degrees.

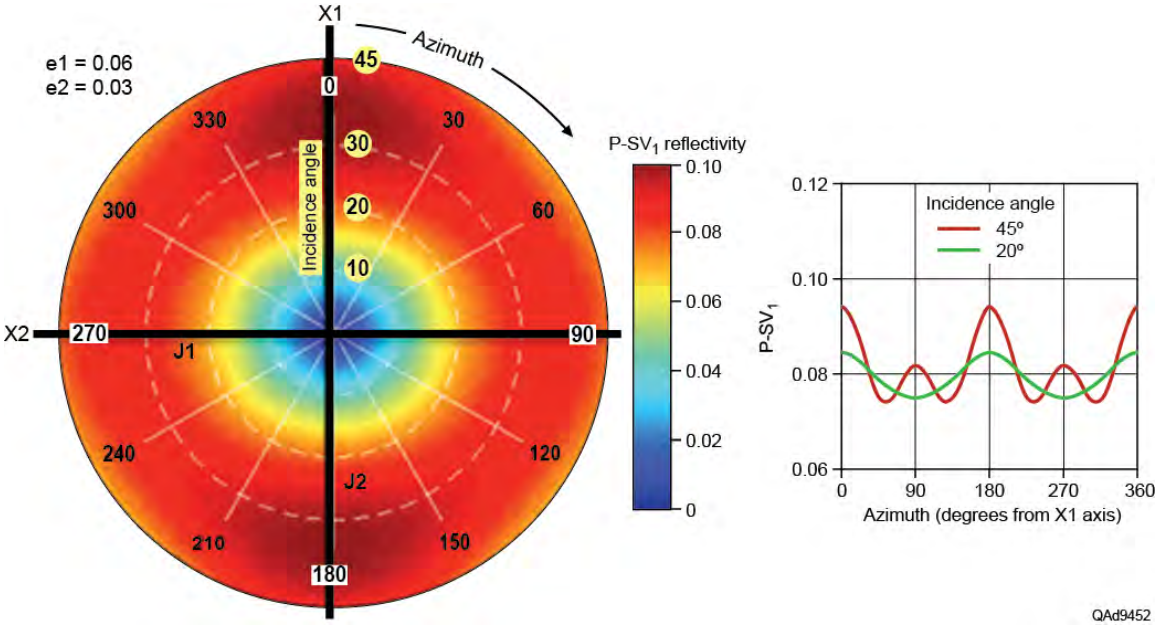

Figure 5.25. Modeling results for P-SV_1 reflectivity from the top of the Marcellus Shale when fracture conditions within the Marcellus are described by Model 3 of Table 5.1 (fracture density of J1 and J2 joint sets = 0.06 and 0.03). J1 joints align with the X2 axis; J2 joints align with the X1 axis. Left: P-SV_1 reflectivity as a function of incidence angle and azimuth. Right: Azimuth behavior of P-SV_1 reflectivity at incidence angles of 20 and 45 degrees.

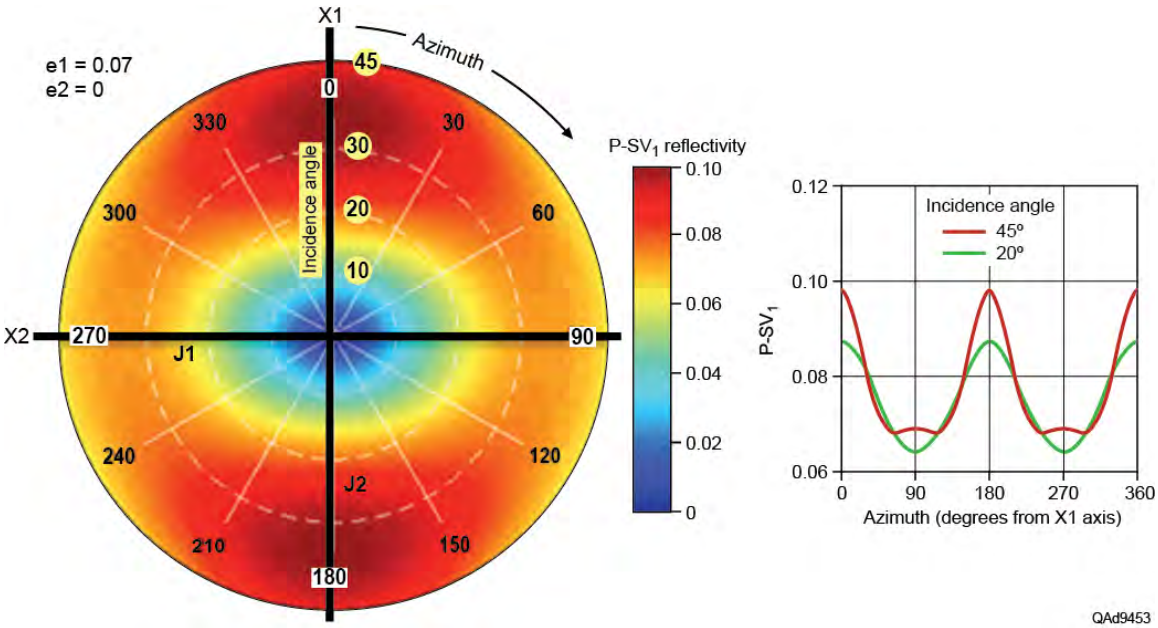

Figure 5.26. Modeling results for P-SV_1 reflectivity from the top of the Marcellus Shale when fracture conditions within the Marcellus are described by Model 4 of Table 5.1 (fracture density of J1 and J2 joint sets = 0.07 and 0.0). J1 joints align with the X2 axis; J2 joints align with the X1 axis. Left: P-SV_1 reflectivity as a function of incidence angle and azimuth. Right: Azimuth behavior of P-SV_1 reflectivity at incidence angles of 20 and 45 degrees.

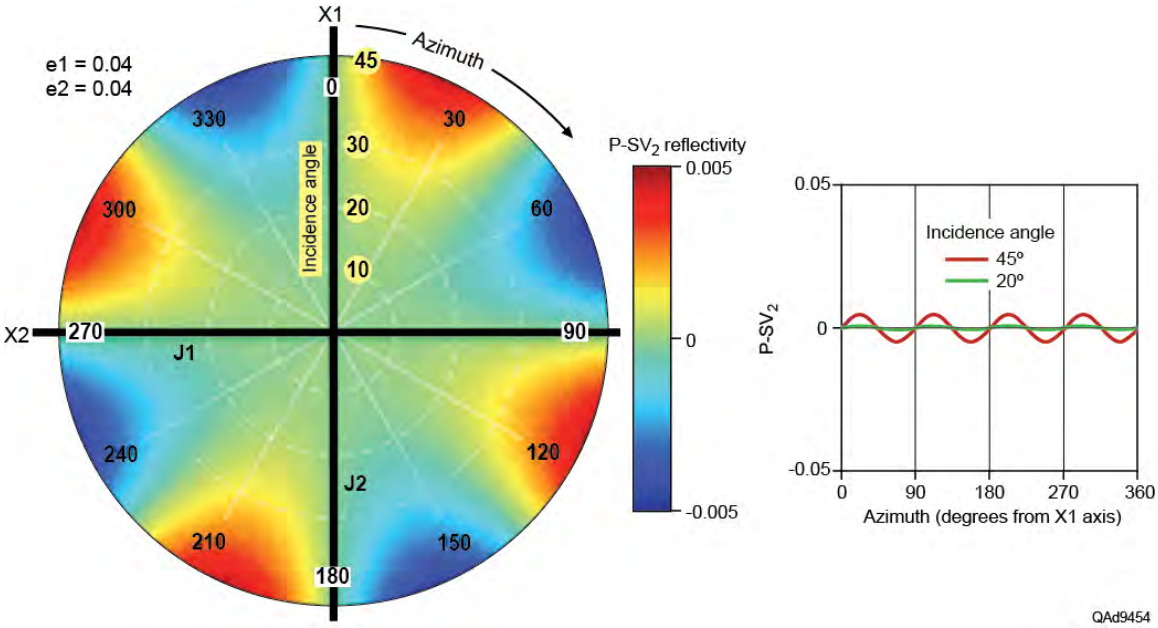

Figure 5.27. Modeling results for P-SV_2 reflectivity from the top of the Marcellus Shale when fracture conditions within the Marcellus are described by Model 1 of Table 5.1 (fracture density of J1 and J2 joint sets = 0.04). J1 joints align with the X2 axis; J2 joints align with the X1 axis. Left: P-SV_2 reflectivity as a function of incidence angle and azimuth. Right: Azimuth behavior of P-SV_2 reflectivity at incidence angles of 20 and 45 degrees.

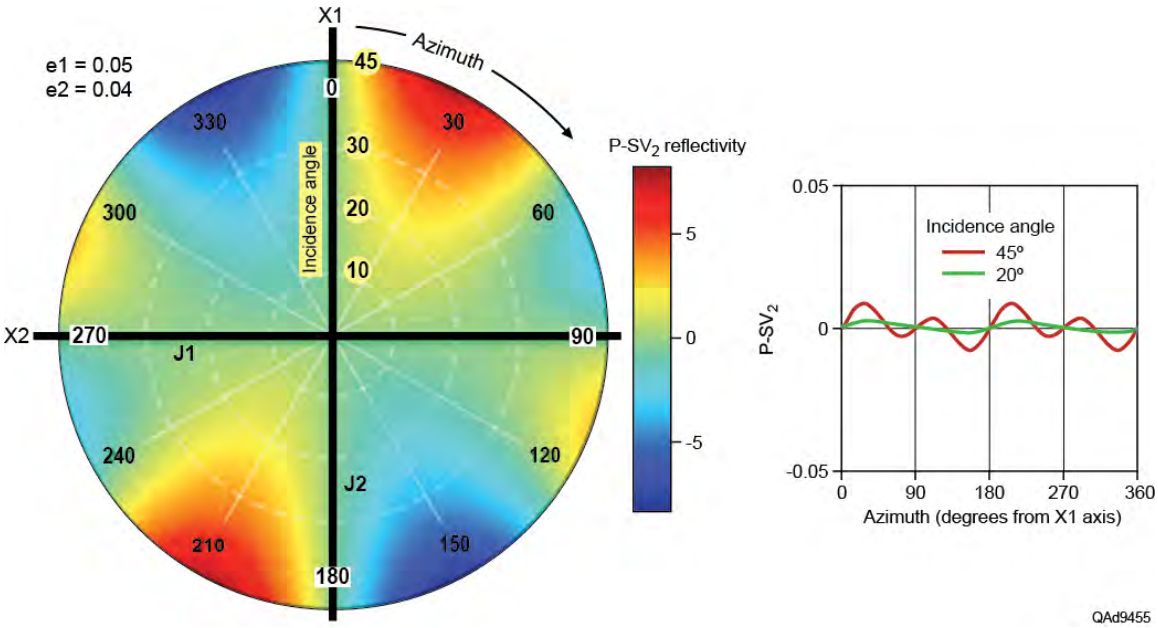

Figure 5.28. Modeling results for P-SV_2 reflectivity from the top of the Marcellus Shale when fracture conditions within the Marcellus are described by Model 2 of Table 5.1 (fracture density of J1 and J2 joint sets = 0.05 and 0.04). J1 joints align with the X2 axis; J2 joints align with the X1 axis. Left: P-SV_2 reflectivity as a function of incidence angle and azimuth. Right: Azimuth behavior of P-SV_2 reflectivity at incidence angles of 20 and 45 degrees.

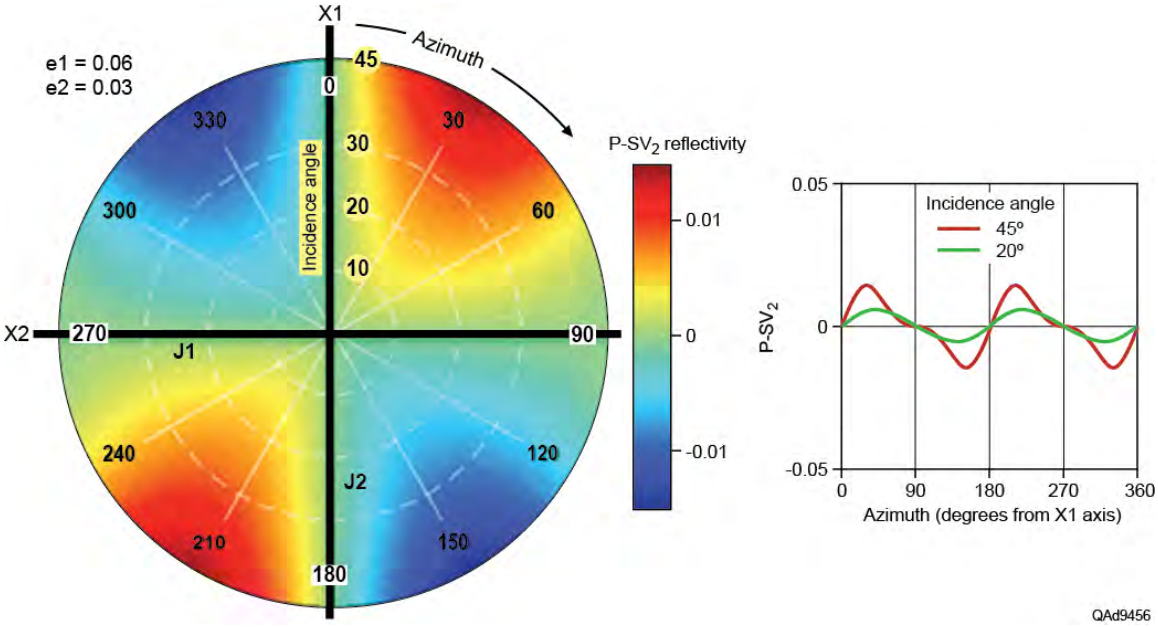

Figure 5.29. Modeling results for P-SV_2 reflectivity from the top of the Marcellus Shale when fracture conditions within the Marcellus are described by Model 3 of Table 5.1 (fracture density of J1 and J2 joint sets = 0.06 and 0.03). J1 joints align with the X2 axis; J2 joints align with the X1 axis. Left: P-SV_2 reflectivity as a function of incidence angle and azimuth. Right: Azimuth behavior of P-SV_2 reflectivity at incidence angles of 20 and 45 degrees.

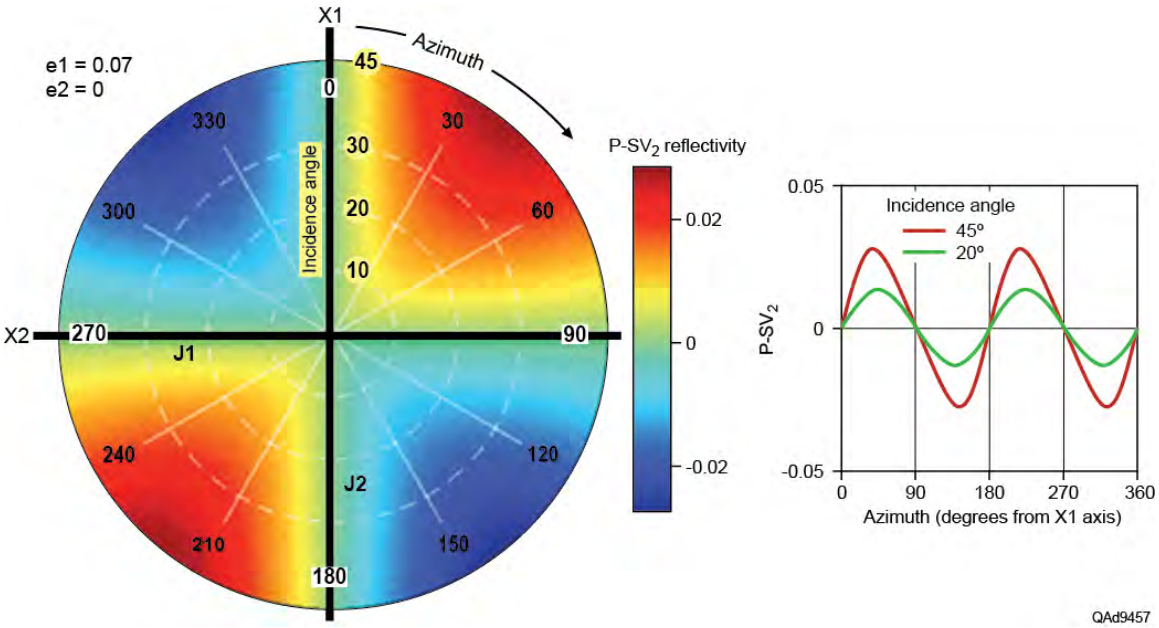

Figure 5.30. Modeling results for P-SV_2 reflectivity from the top of the Marcellus Shale when fracture conditions within the Marcellus are described by Model 4 of Table 5.1 (fracture density of J1 and J2 joint sets = 0.07 and 0.0). J1 joints align with the X2 axis; J2 joints align with the X1 axis. Left: P-SV_1 reflectivity as a function of incidence angle and azimuth. Right: Azimuth behavior of P-SV_1 reflectivity at incidence angles of 20 and 45 degrees.

All of the reflection modes show larger azimuthal variations at larger incidence angles. For Model 1 conditions, the amplitude of the azimuthal variation is the same in the two symmetry axes planes for each mode (azimuths 0 and 90 degrees on Figures. 5.19, 5.23, and 5.27). This result was predicted by the equivalent phase velocities that were calculated when P and S modes propagate in these two symmetry planes (Figs. 5.12). However, the amount of reflectivity variation with azimuth, even at far offsets, is small for all reflection modes. Therefore, measurable AVAZ effects will be difficult to observe in real seismic data when analyzing P and S reflection events from an interval, such as the Marcellus, where there are two sets of orthogonal fractures with similar fracture densities.

P-SV_2 reflectivity offers a small ray of hope for estimating some joint-set properties because that reflected mode undergoes a change in polarity at every 45-degree azimuth increment around the azimuth compass when orthogonal joints have equal (or almost equal) fracture densities (Models 1 and 2; Figures 5.27 and 5.28. In each symmetry plane ([x1 x3] and [x2 x3]), there is no converted P-SV_2 mode, and the amplitude of the reflected P-SV_2 mode is zero (azimuths of 0 and 90 degrees on Figures 5.27 through 5.30). Usually, these reflection characteristics are welcome news because polarity reversals and zero crossings are among the easiest seismic attributes to detect and recognize. However, the problem with the P-SV_2 mode is that it has weak amplitudes when there are orthogonal joints, with reflectivities not reaching even 1-percent except

at high incidence angles (Figs. 5.27 to 5.29). When seismic data have only a small amount of noise, it will be difficult, perhaps impossible, to recognize when A reflection signal of such small amplitude undergoes a polarity reversal or has true zero reflectivity.

For Models 2 and 3, where the J1 joint set has a larger fracture density than the J2 joint set, all reflection modes have asymmetric azimuth responses. For the P-P mode, negative, greater-magnitude reflections occur along the x2 axis (Figs. 5.20 and 5.21), which is parallel to the J1 fracture system. For the P-SV_1 mode, positive, greater-magnitude reflections occur along the x1 axis (Figs. 5.24 and 5.25), which is parallel to the J2 fracture set. As the difference between fracture densities of the two fracture sets increases, the azimuthal variation of P-P and P-SV_1 mode reflectivities become more asymmetric. For these same J1 and J2 densities (Models 2 and 3), a reflection asymmetry appears for the P-SV_2 mode, with its reflection amplitude being zero in the symmetry axes planes and changing polarity every 45 or 90 degrees around the azimuth compass (Figs. 5.28 and 5.29).

For Model 4 where there is a single set of joints, the amplitude variation with azimuth is the largest for all reflection modes. For this HTI symmetry (a single set of aligned fractures), AVAZ can be used for fracture characterization just as it has been in many other fracture studies. However, within our study area, the Marcellus Shale has orthogonal joints, not a single set of fractures, and an HTI interpretation approach cannot be implemented. This orthogonal joint set fracture condition appears to be appropriate for the Marcellus Shale across most of the Appalachian Basin.

Conclusions

On the basis of the modeling results presented in this chapter, we conclude it will be challenging to identify seismic attributes that will characterize an orthorhombic medium with two embedded orthogonal joint systems, as long as those joint sets have similar fracture densities. The presence of orthogonal joint systems can be overlooked in seismic data because there are such small variations in P and S reflection amplitudes with azimuth, even at large incidence angles. Seismic data can be effective for characterizing an orthorhombic medium such as the Marcellus Shale when seismic data quality is excellent and there are large differences between the fracture densities of the two embedded joint sets. In such conditions, it should be possible to identify the presence of the higher-density joint system. The companion lower fracture-density joint system may also be identified at large incidence angles with appropriate-quality seismic data.

In contrast to an orthorhombic medium with two orthogonal joint sets, AVAZ analysis techniques can be used to characterize an HTI medium with a

single set of vertical joints, even with marginal-quality seismic data. For such a medium, AVAZ procedures applied to P-SV_1 and P-SV_2 modes can usually identify the presence, orientation, and relative degree of fracturing.

As a result of our rock physics modeling, we departed from the classic approach of utilizing azimuth-dependent P-SV_1 and P-SV_2 reflectivity and velocity behaviors to define fracture attributes, and implemented new procedures for characterizing joint systems embedded in the Marcellus Shale. To estimate fracture densities of orthogonal joints, we created maps showing spatial variations in S-wave interval velocity across the Marcellus Shale. Fracture density of Marcellus joint sets increases when this S-wave interval velocity decreases, and the fracture density decreases when the S-wave interval velocity increases. The Marcellus S-wave interval velocity map developed in this study and our joint-density interpretation of the map are exhibited and discussed in Chapter 9.

A second seismic interpretation technique that estimates trends of increased joint fracturing is also described in Chapter 9. In this approach, we create P-P and P-SV_1 maps that define the structural curvature of the Upper and Lower Marcellus units. Because fracture density should increase as structural curvature increases, identifying maximum-curvature trends on these maps is a seismic proxy for defining trends of maximum fracture density.

Regarding interpretation of possible water-storage reservoirs, log data showed rocks between the Tully Limestone and the Marcellus Shale have the highest porosities of the entire section drilled by the central-image calibration well, with porosities being in the range of15-percent to 18-percent. This magnitude of pore volume is sufficient for these Tully-to-Marcellus units to be the focus of our efforts to demonstrate the advantages of evaluating reservoir targets with multicomponent seismic data rather than with single-component P-wave seismic data.

Chapter 6

Seismic Sources, Sensors, and Recording Systems and Their Effects on P and S Wave Modes

Introduction

To fulfill the first three secondary objectives listed on Figure 1.1 of Chapter 1, a field-test program was done to: (1) quantify the relative strengths of compressional (P) wave and shear (S) wave modes produced by a variety of vertical-force seismic sources, (2) compare the relative merits of cable-based and cable-free data recording systems, and (3) document and compare the quality of 3C data acquired with moving-coil geophones and MEMS solid state accelerometers. These equipment tests were done at the Devine Test Site owned by The University of Texas at Austin. Vertical-force sources deployed for the tests were: 1-kg (2.2 lb) packages of explosive positioned at a depth of 6 m (20 ft), a 27,273-kg (60,000-lb) vertical vibrator, and a vertical impact accelerated-weight source that delivered 30,202 joules (22,276 ft-lb) of energy to the Earth. Horizontal-force sources used in the tests were this accelerated-weight source impacting at various non-vertical incident angles and a Mertz Model 18 horizontal vibrator operating with a drive force of 24,000 lbs (10,900 kg). Data were acquired with three recording systems—a Sercel 428 cable-based system, Sercel's EUnite cable-free boxes, and Sigma cable-free boxes provided by Seismic Source of Ponca City, Oklahoma, and iSeis of Denver, Colorado.

Field Test Procedure

The University's seismic test site is called the Devine Test Site because of its proximity to the community of Devine, Texas, shown on the map displayed as Figure 6.1a. An aerial photo of the test site property is included as Figure 6.1b. The most valuable assets on the property are the three equipment tests wells drilled and cased to depths of 3000 ft (914 m). The locations of these wells are indicated by the solid circles labeled 4, 2, 9 on Figure 6.1b.

The stratigraphy penetrated by the test wells is labeled on the well log curves displayed as Figure 6.2. These logs were recorded in well 4 and define compressional velocity V_P, shear velocity V_S, and gamma-ray readings across the rock units that form the first 3000 ft (914 m) of the seismic propagation medium beneath the property. These log measurements start immediately below the base of surface casing, which is at a depth of 532 ft (162 m) in well 4 where these logs were recorded.

(a)

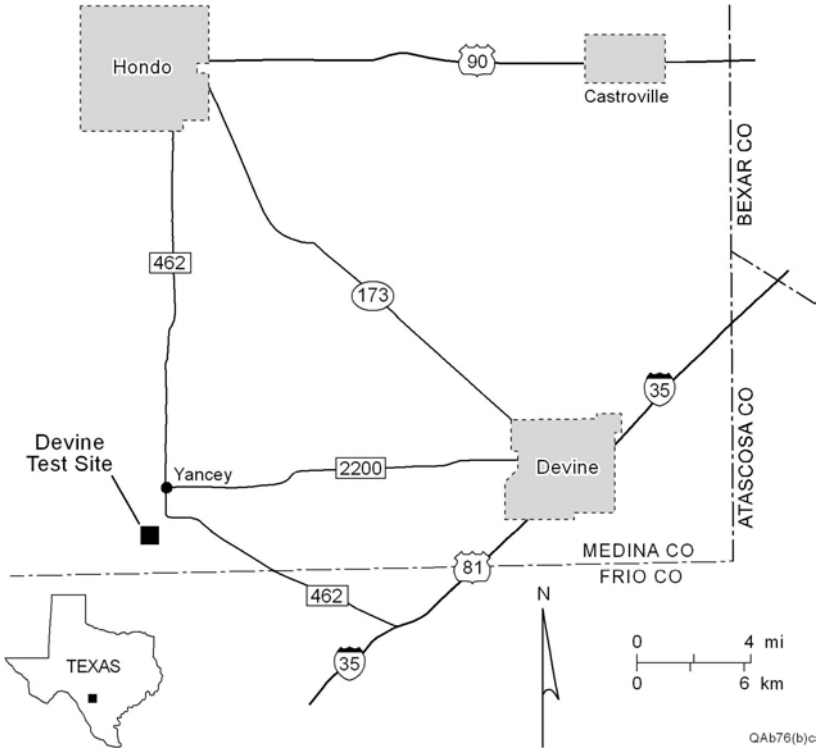

(b)

Figure 6.1. (a) Location of the Devine Test Site in Medina County, Texas. The city of San Antonio is approximately 50 km east of the town of Hondo shown on this map. (b) Aerial photo of the Devine Test Site. Test wells 4, 2, and 9 were constructed for the purpose of deploying downhole instrumentation, particularly seismic sources and receivers and well logging tools. All wells are 3000 ft (914 m) deep. The site spans 100 acres.

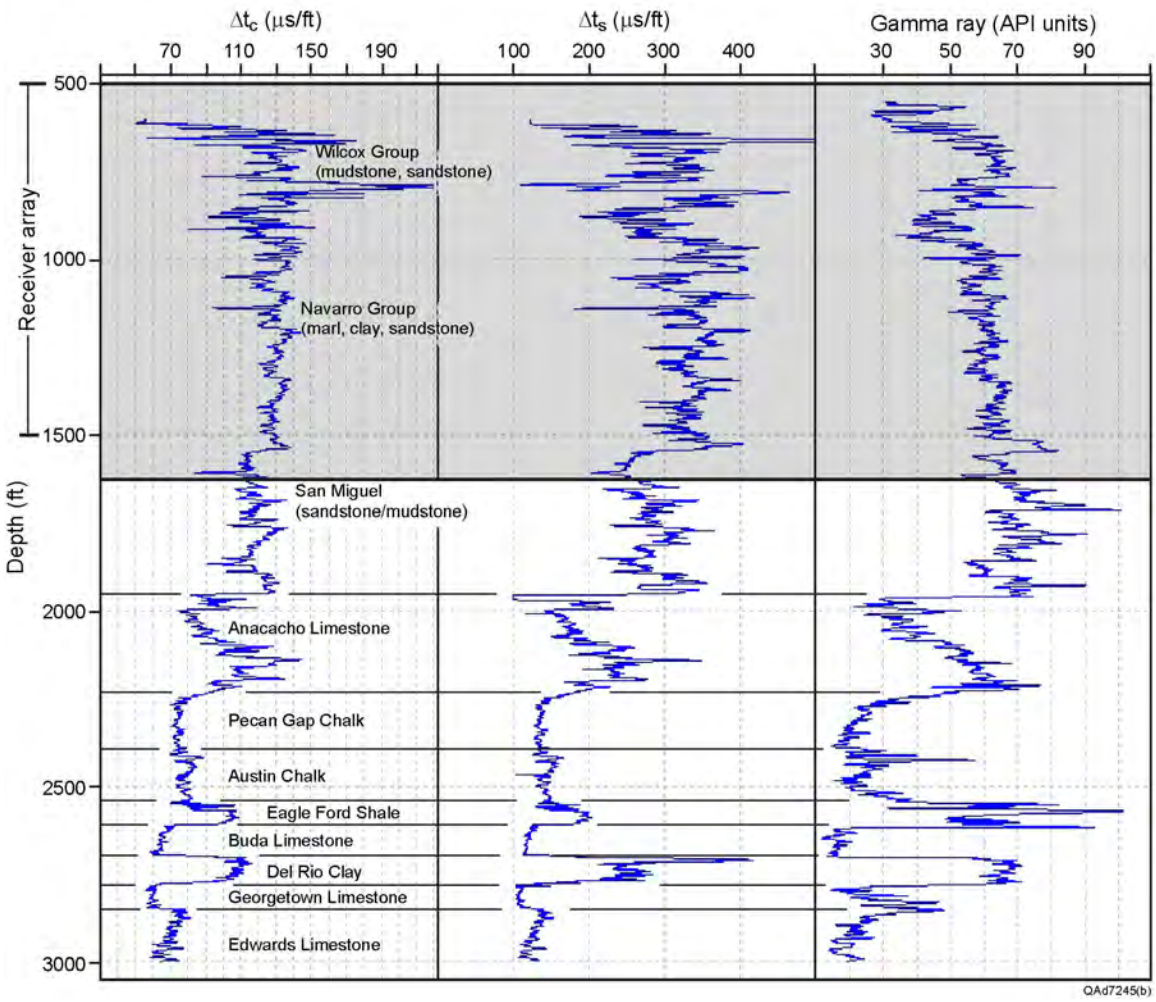

Figure 6.2. V_P and V_S velocity logs and gamma-ray log acquired in well 4 on the Devine Test Site. The shaded interval defines the depth range over which downhole geophones were deployed for source tests in this study.

Source-Receiver Test Geometry

The source-receiver geometry utilized for these tests combined the concepts of horizontal wave testing (involving only a horizontal receiver array) and vertical wave testing (involving only a vertical receiver array) as described by Hardage (2009, 2010).

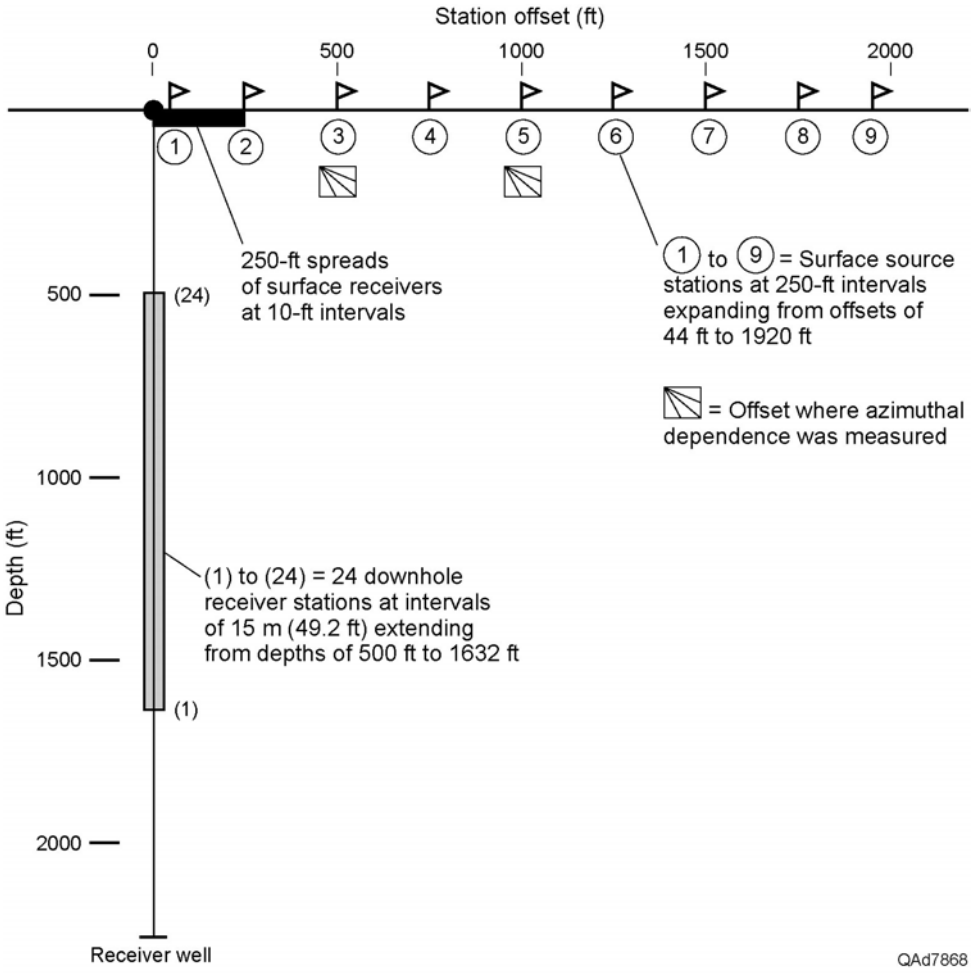

Figure 6.3. Source-receiver geometry used to compare relative merits of multicomponent seismic sources, sensors, and recording systems. A 24-station vertical array of 3C geophones spaced at intervals of 15 m (49.2 ft) spanned the depth interval from 500 to 1632 ft (152 to 497 m) in well 4. Several 25-station horizontal arrays of 3C sensors spaced 10 ft (3 m) apart spanned the offset range 0 to 250 ft (0 to 76 m) immediately next to well 4. Source stations were offset from the well at intervals of 250 ft (76 m), the linear dimension of the horizontal surface-receiver arrays.

Well 4 (Fig. 6.1b) was chosen for the location of the vertical receiver array. A 24-station MaxiWave receiver system provided by Mitcham Industries was deployed in this well, with receiver stations spanning a depth interval extending from 500 to 1632 ft (152 to 497 m). The velocity layering local to this vertical sensor array is defined by the log character inside the shaded interval shown on Figure 6.2. Several parallel arrays of 2D horizontal sensors extended eastward 250 ft (76 m) from well 4, and a series of nine inline source stations continued eastward a distance of 1920 ft (585 m), as illustrated on Figure 6.3. Within each 250-ft (76 m) horizontal-receiver array (the heavy black line between source stations 1 and 2 on Figure 6.3), a single 3C sensor was buried at inline intervals of 10 ft (3 m) so that the top of each sensor case was flush with the ground surface. The X,Y,Z sensor elements at each 3C sensor station were recorded as individual data channels.

Photographs of the surface equipment deployed for the tests are shown on Figure 6.4. Along each horizontal receiver array, the first sensor station was 10 ft (3 m) from well 4 and sensor station 25 ended at source station 2, offset 250 ft (76 m) from the receiver well (Fig. 6.3). As shown by the labeling on the photographs, the instrumentation deployed along these parallel arrays consisted of:

1. 25 stations of 3C geophones recorded by Sigma cable-free boxes provided by Seismic Source and i-Seis.

2. 25 stations of DSU3 MEMS sensors recorded by a Sercel 428 cable-based system.

3. 25 stations of 3C geophones recorded by Sercel's EUnite cable-free boxes.

4. 25 stations of 3C geophones recorded by a Sercel 428 cable-based system.

5. 5 stations at which OyoGeospace deployed high-sensitivity geophones and special packaging of 3C geophones with all sensors recorded by OyoGeospace GSR cable-free boxes.

The 3C geophones utilized in surface spreads 1, 3, and 4 of this list were Oyo Geospace Model 20DX (10-Hz resonance) geophones.

(a)

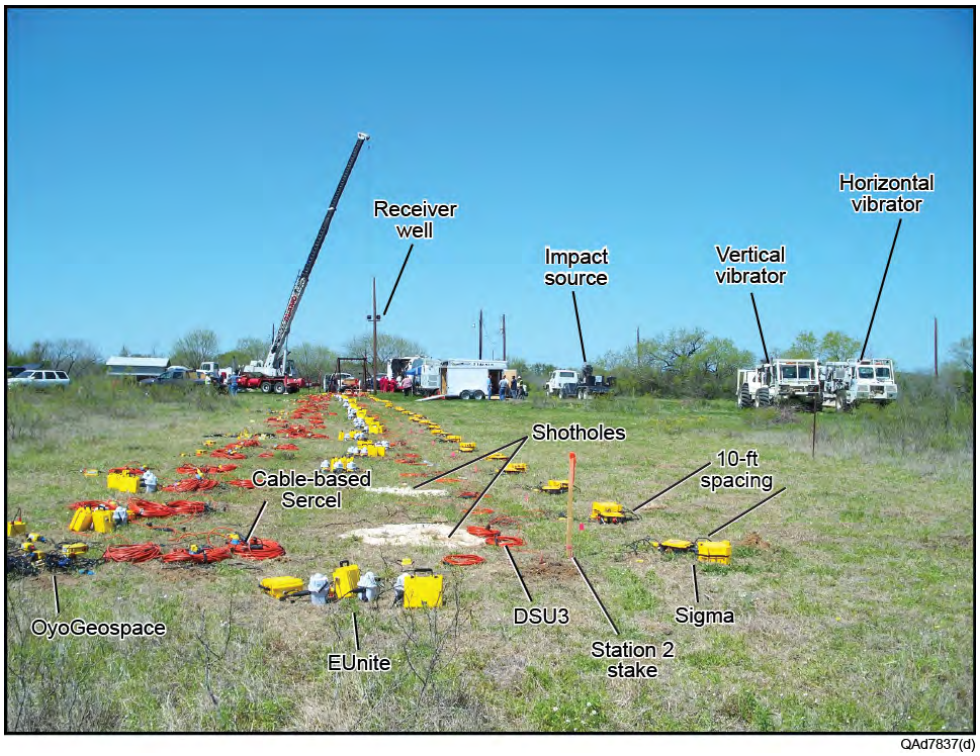

(b)

Figure 6.4. (a) View of the receiver well from a position near source station 2 on the source-station profile. This view shows parallel, 25-station arrays of horizontal-wave-test instrumentation deployed over the offset range 0 to 250 ft (0 to 76 m) and some of the source and data-acquisition technologies assembled for the test. (b) View from the receiver well looking down the source-station profile.

Vertical Aperture of Test Geometry

An important requirement of the test was to record downgoing P and S modes over a wide aperture of vertical takeoff angles from surface source stations. This requirement allowed the maximum amount of energy contained in each wave mode propagating away from source stations to be captured for analysis. The shallowest takeoff angle involved data generated at source station 9 (offset 1920 ft [585 m]) and recorded at downhole receiver station 24 (depth of 500 ft [152 m]). The steepest takeoff angle involves source station 2 (offset 250 ft [76 m]) and downhole receiver station 1 (depth of 1632 ft [497 m]). A first-order approximation of the aperture range created by the source-receiver geometry can be done by assuming straight raypaths from source to downhole receiver, which yields the result shown on Figure 6.5.

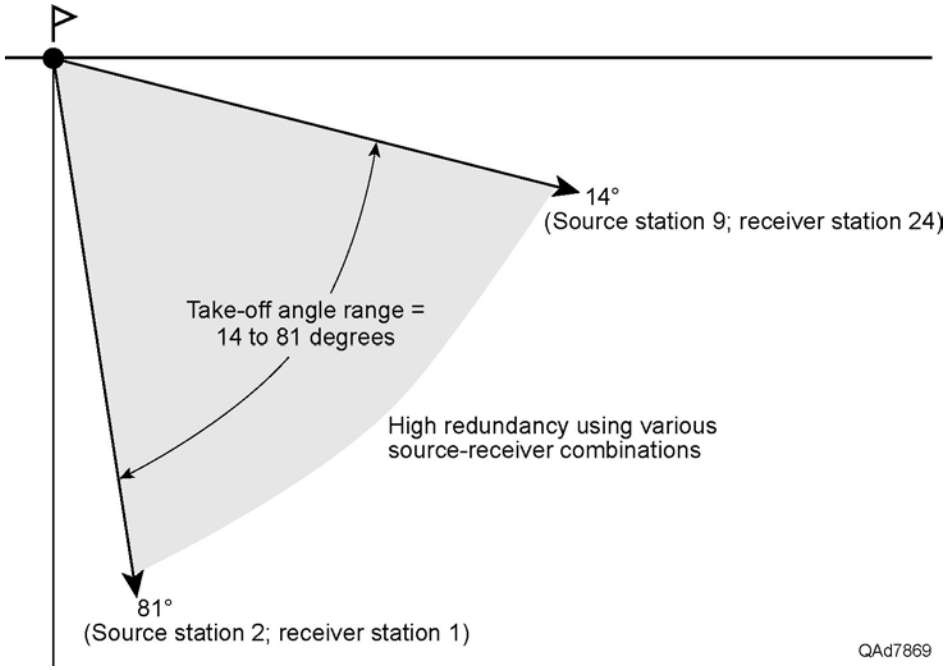

Figure 6.5. Takeoff angle aperture when straight raypaths are assumed between surface sources and downhole receivers.

Wave Components Embedded in Test Data

Three independent, vector-based, seismic wave modes propagate in a simple homogeneous Earth**:** a compressional mode, **P**, and two shear modes, **SV** and **SH** (Fig. 6.6). These are the wave modes the seismic industry creates when wavefields produced by three orthogonal source-displacement vectors are recorded with three orthogonal vector sensors. These are the wave modes that were evaluated in the wavefields generated by the seismic sources evaluated at the Devine Test Site.

Each mode of an elastic wavefield travels through the Earth at a different velocity, and each mode distorts the Earth in a different direction as it propagates. In a homogeneous medium, the orientations of the P, SV, and SH displacement vectors relative to the propagation direction of each mode are defined on Figure 6.6. The propagation velocities of SH and SV shear modes differ by only a few percent, but both shear velocities ($\mathbf{V_S}$) are significantly less than P-wave velocity ($\mathbf{V_P}$). The velocity ratio V_P/V_S can vary by an order of magnitude in Earth media, from a value of 50 or more in deep-water, unconsolidated, near-seafloor sediment to a value of approximately 1.5 in a few dense, well-consolidated rocks.

A convenient way to distinguish between SH and SV shear modes in a homogeneous medium is to imagine a vertical plane passing through a source station and a receiver station. SV vector displacement occurs in this vertical plane; SH vector displacement is normal to the plane (Fig. 6.7). This vertical plane passing through the coordinates of a source station, a receiver station, and a reflection point produced by that source-receiver pair is called a **sagittal plane**.

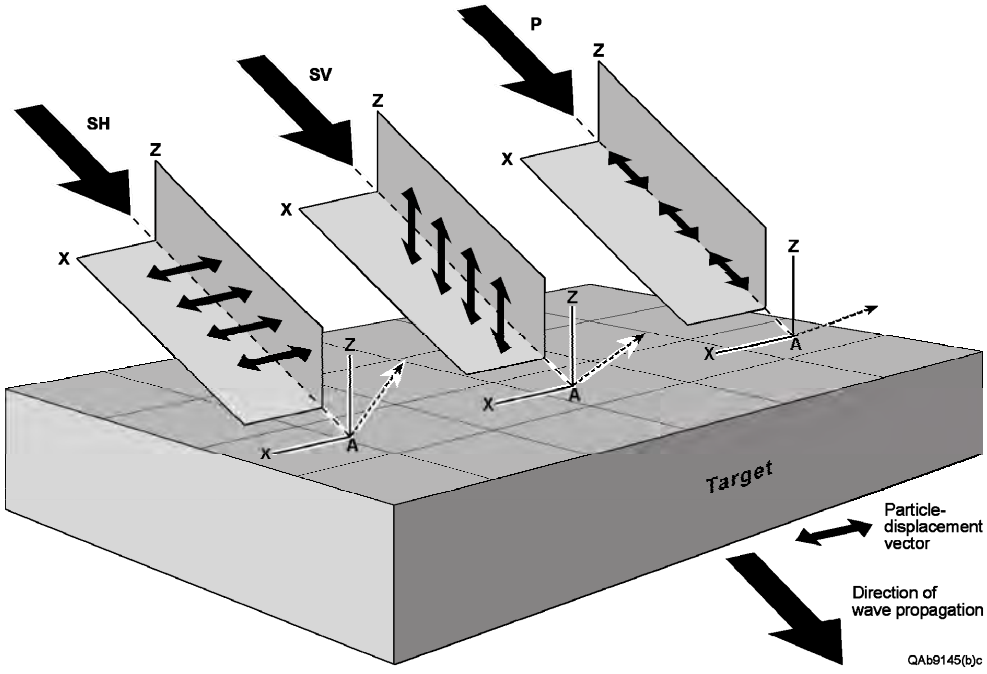

Figure 6.6. A full-elastic, multicomponent seismic wavefield propagating in a homogeneous Earth consists of a compressional mode P and two shear modes, SV and SH. A key distinction among these wave modes is that each mode distorts the Earth in a different direction along its propagation path. The direction in which each mode displaces the Earth is indicated by double-headed arrows.

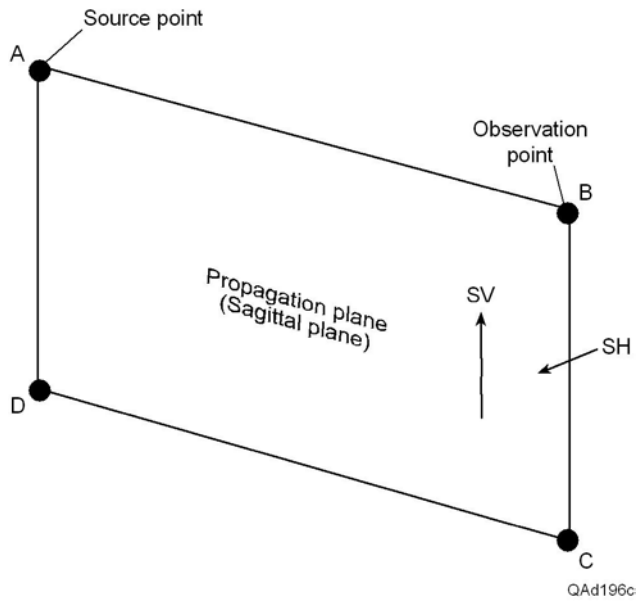

Figure 6.7. Distinction between SH and SV shear wave displacements in a homogeneous medium. SV displacement occurs in the vertical plane that passes through a source station and an observation point. SH displacement is normal to this plane.

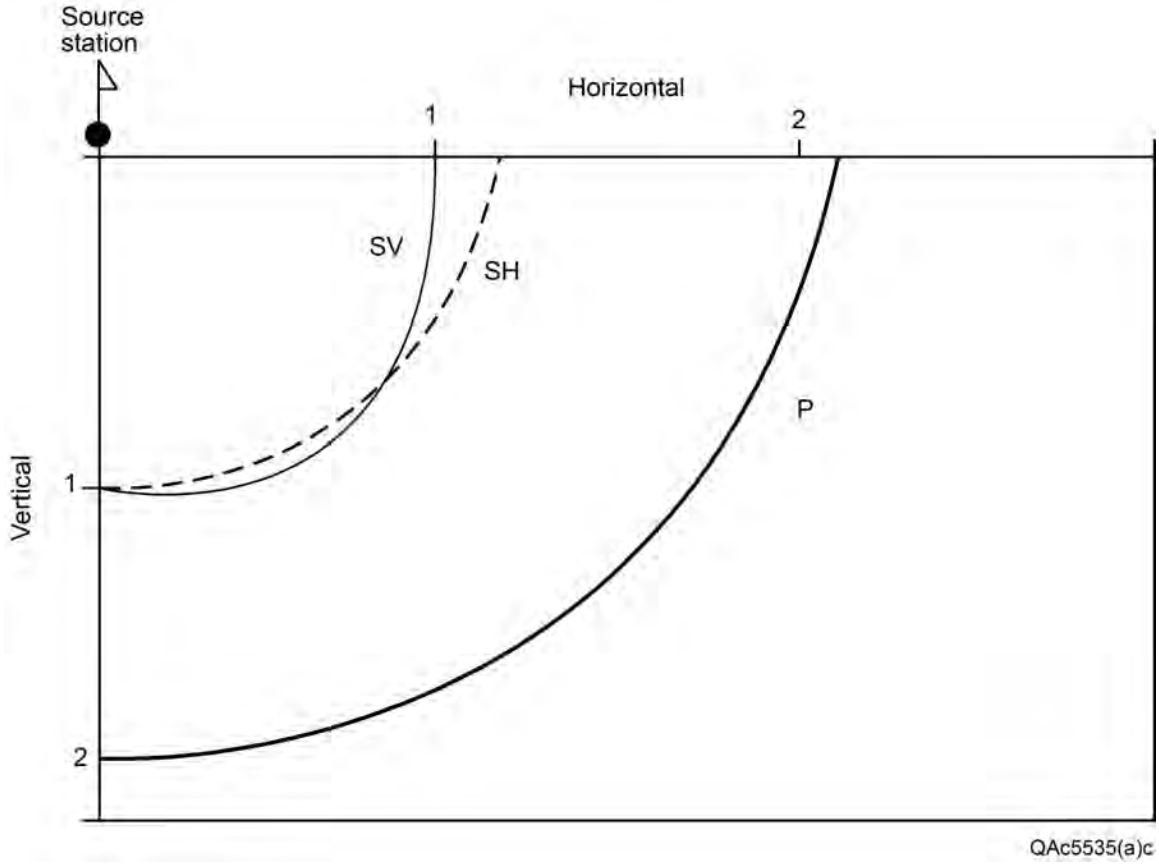

Figure 6.8. Comparison of SH, SV, and P velocity behavior for elastic wave propagation in horizontally layered [vertical transverse isotropic (VTI)] media. From Levin (1979, 1980).

Because SV and SH modes cause orthogonal displacements with these orientations, some geophysicists prefer to use the terms **radial-S** (**SR**) and **transverse-S** (**ST**) when describing S-wave propagation in layered media and to restrict the terms SV and SH to S-wave propagation in homogeneous media, or to S-wave modes that propagate only in symmetry-axis planes. Both styles of nomenclature are used in this study.

Levin (1979, 1980) expanded the physics of S-modes from a homogeneous Earth to a layered Earth and found SH and SV modes propagating through a layered medium exhibit velocity behaviors like those displayed on Figure 6.8. An important point to note is that at all take-off angles from the source station, except for true vertical and for the one angle that points to the subsurface coordinate where the SH and SV wavefronts intersect, SV and SH modes propagate with different velocities, with the SH mode having a significantly faster velocity at shallow take-off angles from a source station. This wave physics will be important when examining seismic test data shown later.

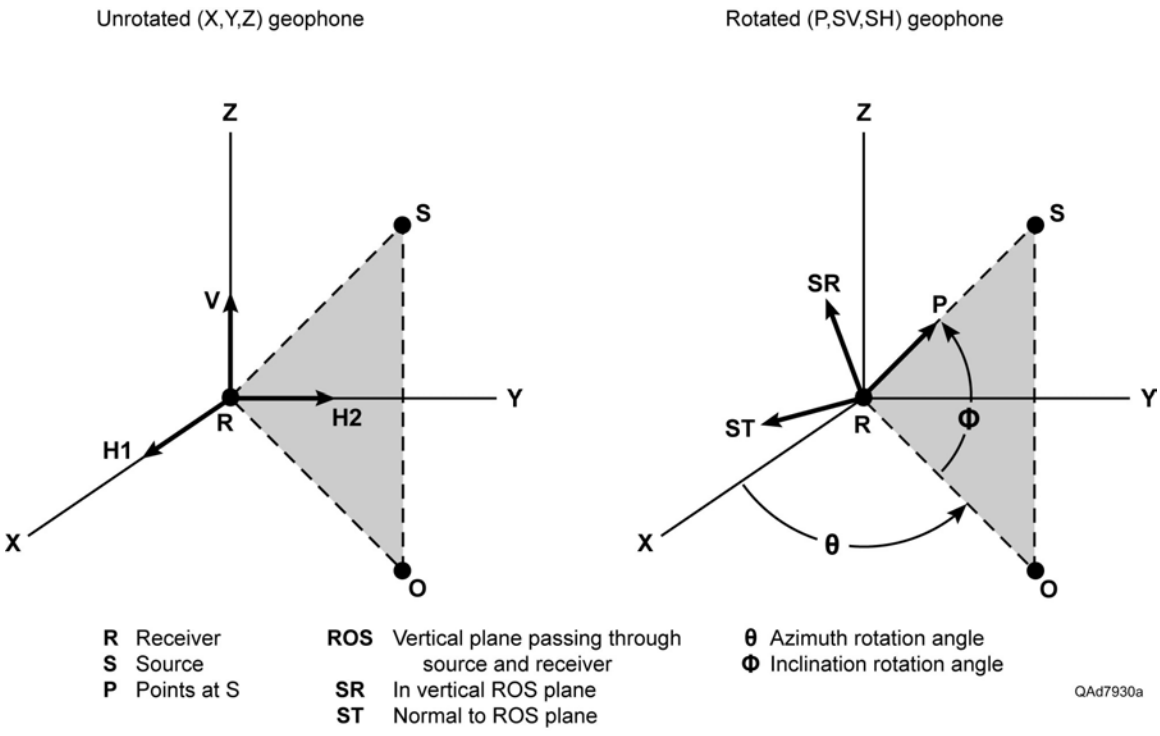

Figure 6.9. Reorientation of X, Y, Z receivers to P, SR, and ST receivers.

Transforming VSP Test Data to Wave-Mode Data

In a vertical receiver well, azimuth orientations of X,Y horizontal geophones differ at each downhole station because sensor packages are deployed on twisted-wire cable that rotates as it spools off a cable reel. As a result, sensors rotate by different amounts when they reach different deployment depths. Phase shifts and amplitude variations introduced into horizontal-sensor data by station-to-station variations in receiver orientation do not allow individual events or distinct wave modes to be recognized, particularly S-wave events that dominate horizontal-sensor response. Receivers must be mathematically oriented to consistent azimuths and to proper inclinations to define downgoing and upgoing P and S modes.

Transformations of borehole receivers from in situ X, Y, Z orientations to a data space where receivers are oriented to emphasize P, radial-shear (SR), and transverse-shear (ST) events have been practiced in VSP technology for several decades. A graphical description of the transformation of receivers from X, Y, Z data space to P, SR, ST data space is shown on Figure 6.9. Azimuth rotation angle θ and inclination angle Φ have to be calculated at each receiver station so that P-wave displacement vectors are aligned along raypath RS, SV displacement vectors are confined to vertical plane ROS, and SH displacement vectors are orthogonal to plane ROS.

Vertical Array Measurements of Wave-Mode Amplitudes and Frequencies Produced by Test Sources

Examples of this receiver orientation procedure applied to vertical-impact, shot-hole explosive, and vertical-vibrator sources positioned at selected source stations are illustrated on Figures 6.10, 6.11, and 6.12. The data windows used to determine geophone azimuth θ and inclination angle Φ (Fig. 6.9) to apply at each receiver station spanned 40 ms immediately following the onset of the interpreted P-wave direct arrival (top row of Figures 6.10, 6.11, 6.12).

Because each of the three seismic sources (explosive, vertical vibrator, vertical impact) generated a different amount of seismic energy, a different plot gain was used to display data produced by each source. However, a constant plot gain is used within individual figures (Figs. 6.10, 6.11, 6.12) so that P, SR, and ST wave mode amplitudes produced by each specific source can be compared visually to judge their relative energy levels. Such comparisons confirm S modes radiating away from a vertical-force source often have amplitudes greater than their companion P mode (for example, Figs 6.10 and 6.11). Because data-display gains differ for each source, P and S amplitudes produced by one source should not be visually compared with P and S amplitudes produced by other sources.

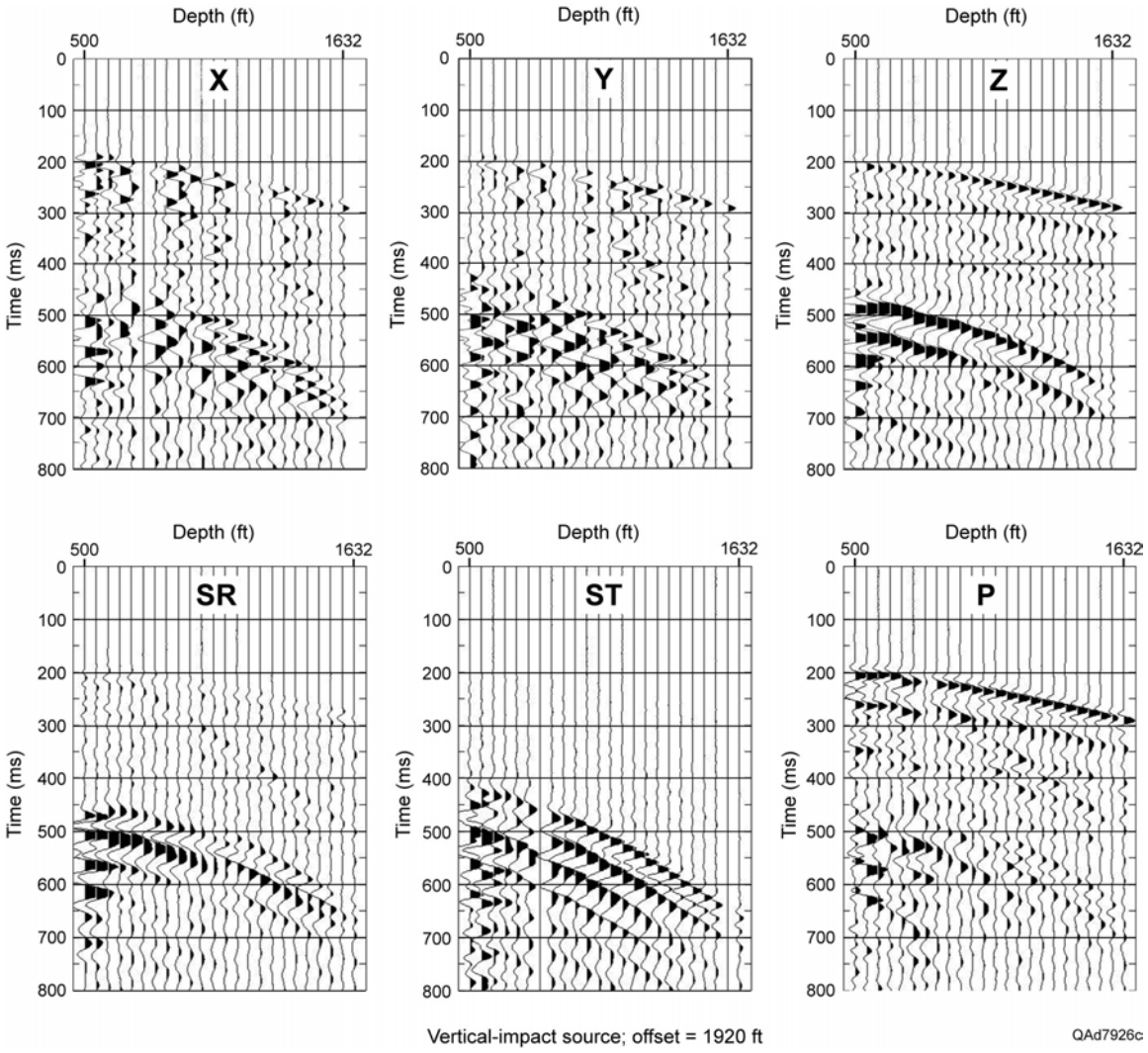

Figure 6.10. (a) Example of X, Y, Z data acquired with the test-site vertical sensor array when a vertical-impact source was positioned at source station 9, offset 1920 ft (585 m) from the array. (b) Data rotated to P, SR, and ST data space. All data panels are shown with a constant display gain.

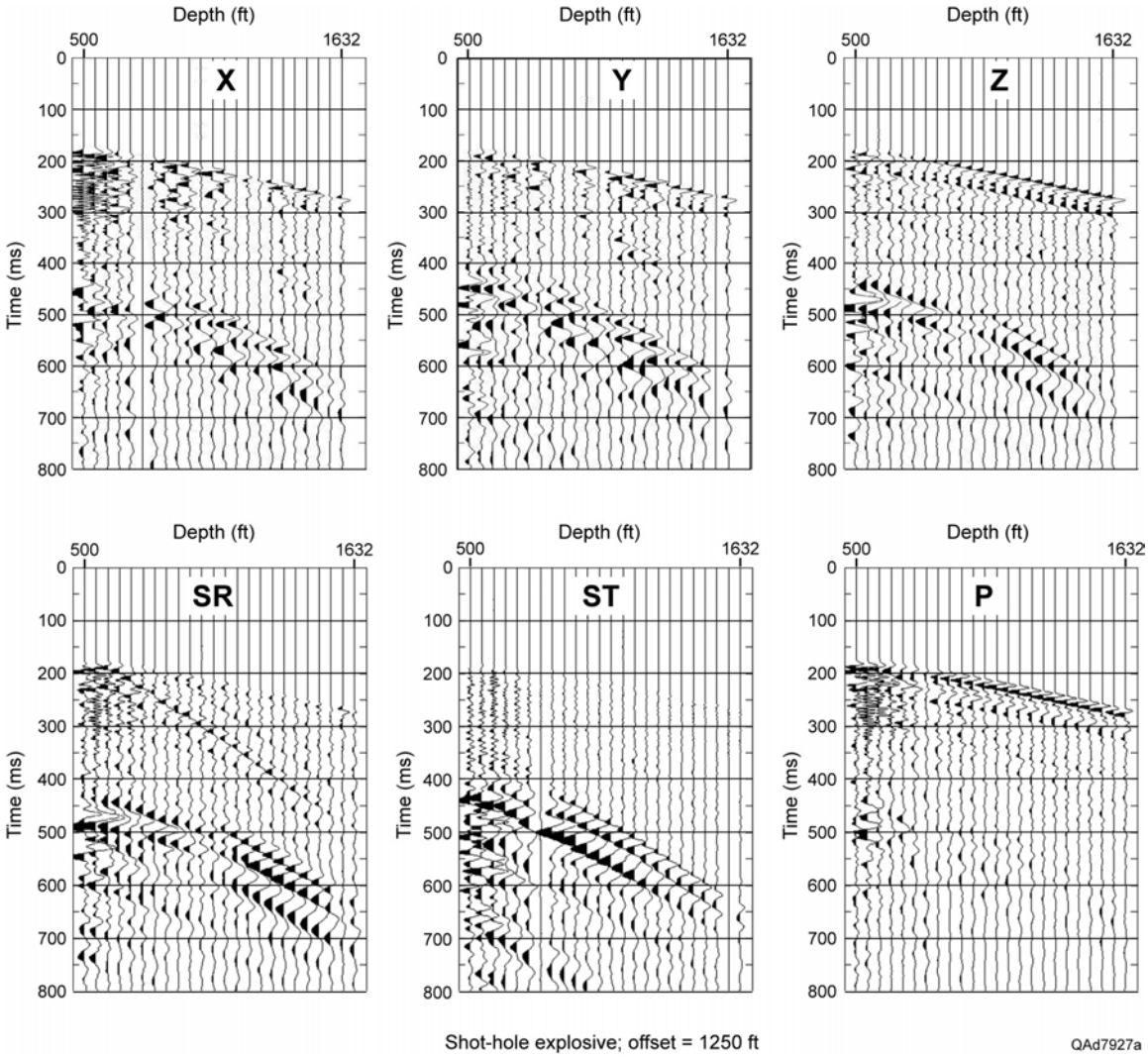

Figure 6.11. (a) Example of X, Y, Z data acquired with the test-site vertical sensor array when a shot-hole explosive source was positioned at source station 5, offset 1250 ft (381 m) from the array. (b) Data rotated to P, SR, and ST data space. All data panels are shown with a constant display gain.

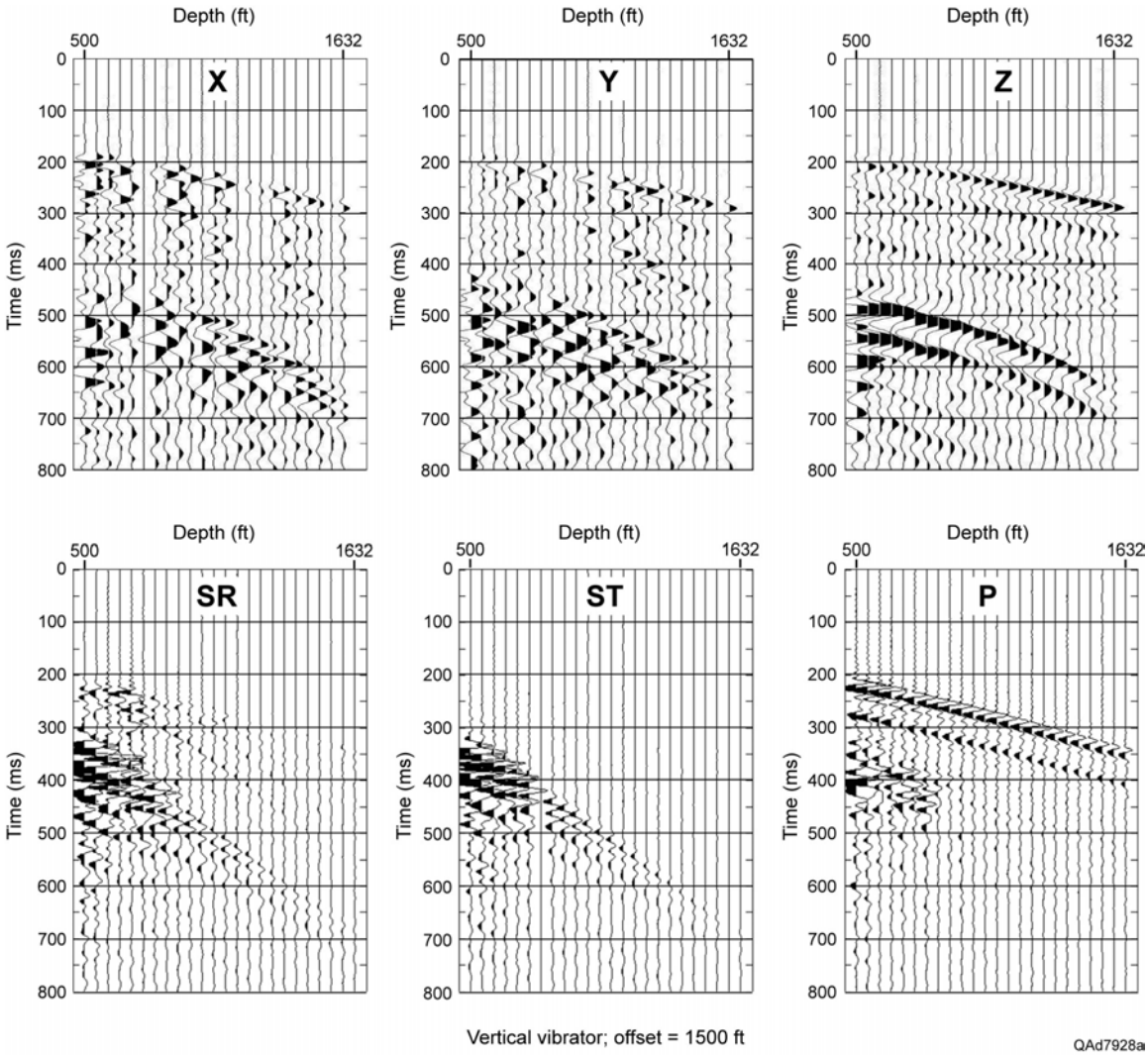

Figure 6.12. (a) Example of X, Y, Z data acquired with the test-site vertical sensor array when a vertical-vibrator source was positioned at source station 6, offset 1500 ft (457 m) from the array. (b) Data rotated to P, SR, and ST data space. All data panels are shown with a constant display gain.

Only data rotated to coordinate axes that isolate downgoing P, SR, and ST modes (the bottom rows of Figures 6.10, 6.11, and 6.12) were analyzed for energy content. Examination of these rotated data shows it is reasonably simple to define narrow windows that span the downgoing first arrivals of P, SR, and ST modes. After defining first-arrival times at each receiver station for each wave mode produced by each source, wavelet amplitudes were analyzed in 40-ms windows starting at the interpreted first-break times of each arriving mode. Wavelets inside these data windows represent the downgoing illumination wavelets for each wave mode. Curves of root-mean-square (rms) wavelet amplitudes calculated in these first-arrival windows for data generated at various source stations are exhibited on Figures 6.13 through 6.15.

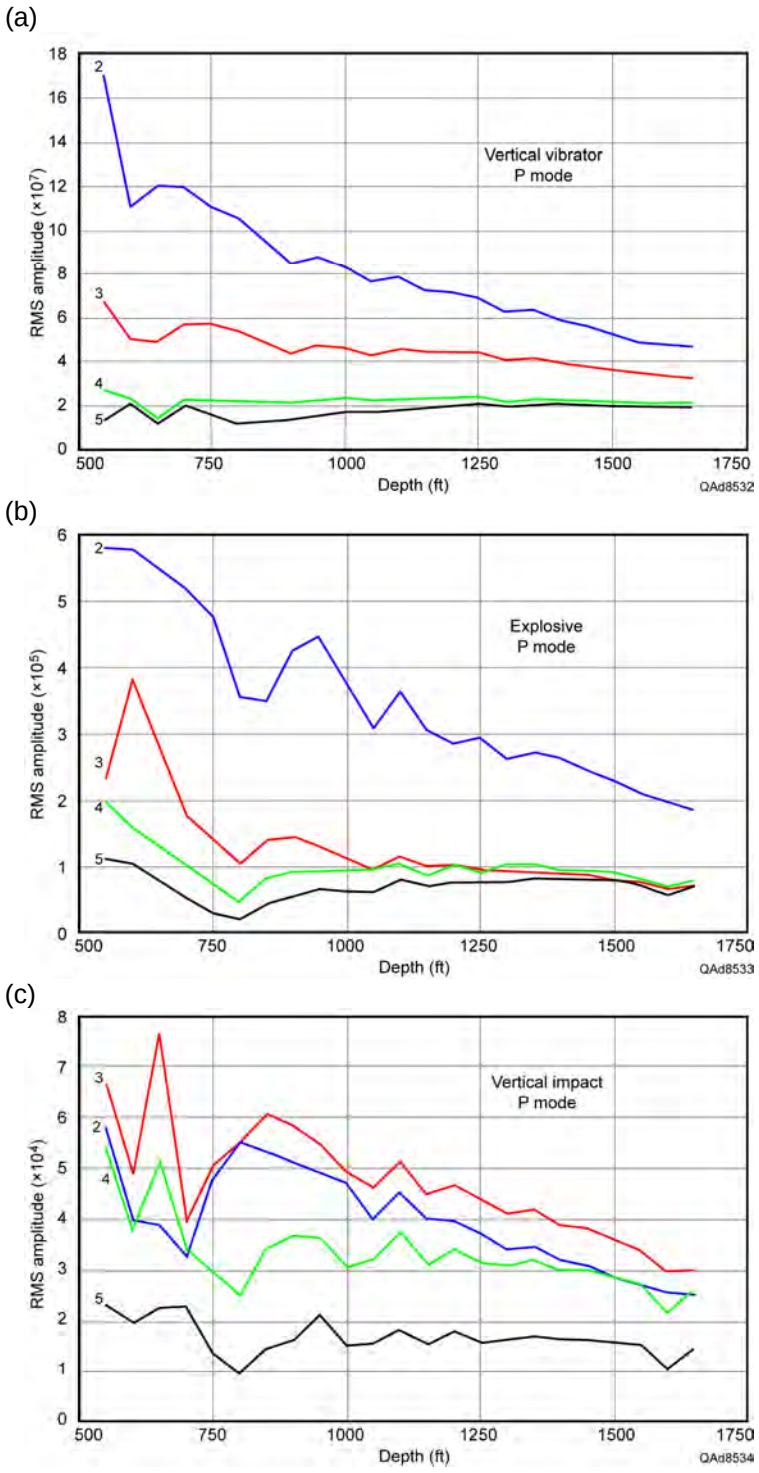

Figure 6.13. Root-mean-square (rms) amplitudes of downgoing P modes measured across the downhole vertical sensor array when sources are positioned at offset stations 2 through 5 (Fig. 6.3). Source station locations are indicated by the numbers on the curves. (a) Source is 60,000-lb (27,733-kg) vertical vibrator. (b) Source is 1 kg charge at depth of 6 m. (c) Source is an accelerated-weight impact delivering 22,276 ft-lb (30,202 joules) to the Earth.

(a)

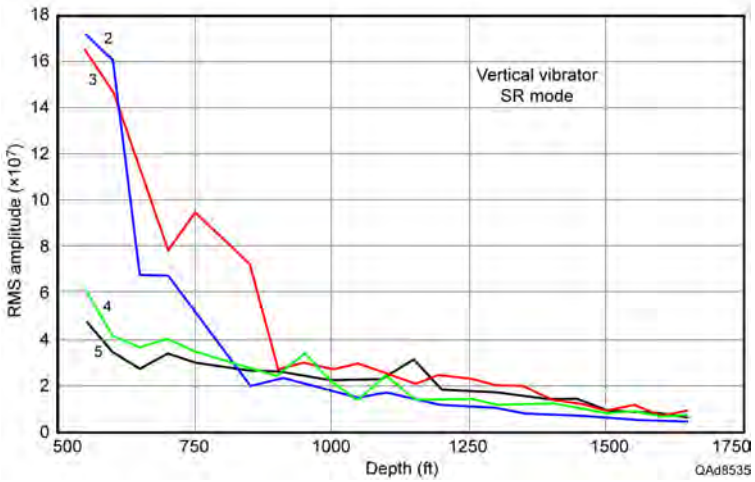

(b)

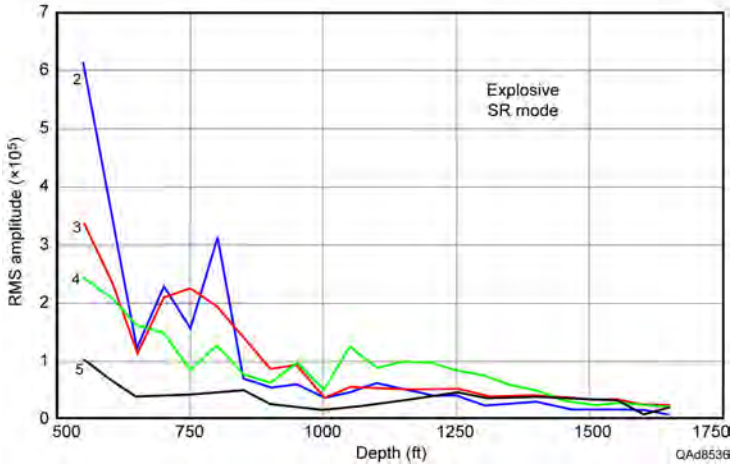

(c)

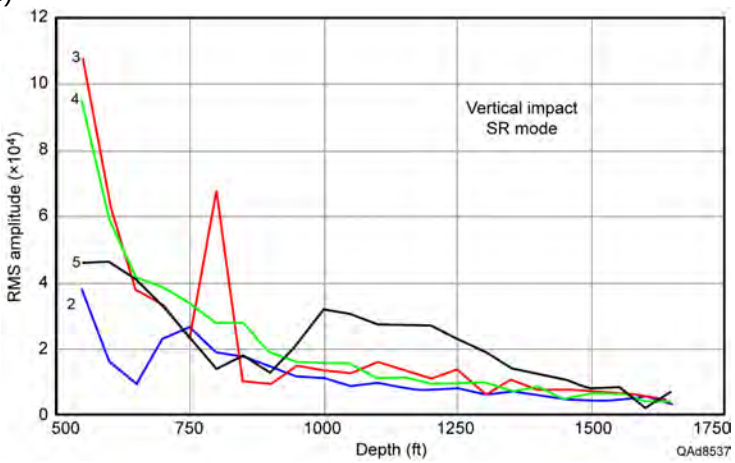

Figure 6.14. Root-mean-square (rms) amplitudes of downgoing SR modes measured across the downhole vertical sensor array when sources are positioned at offset stations 2 through 5 (Fig. 6.3). Source station positions are indicated by the numbers on the curves. (a) Source is 60,000-lb (27,733-kg) vertical vibrator. (b) Source is 1 kg charge at depth of 6 m. (c) Source is an accelerated-weight impact delivering 22,276 ft-lb (30,202 joules) to the Earth.

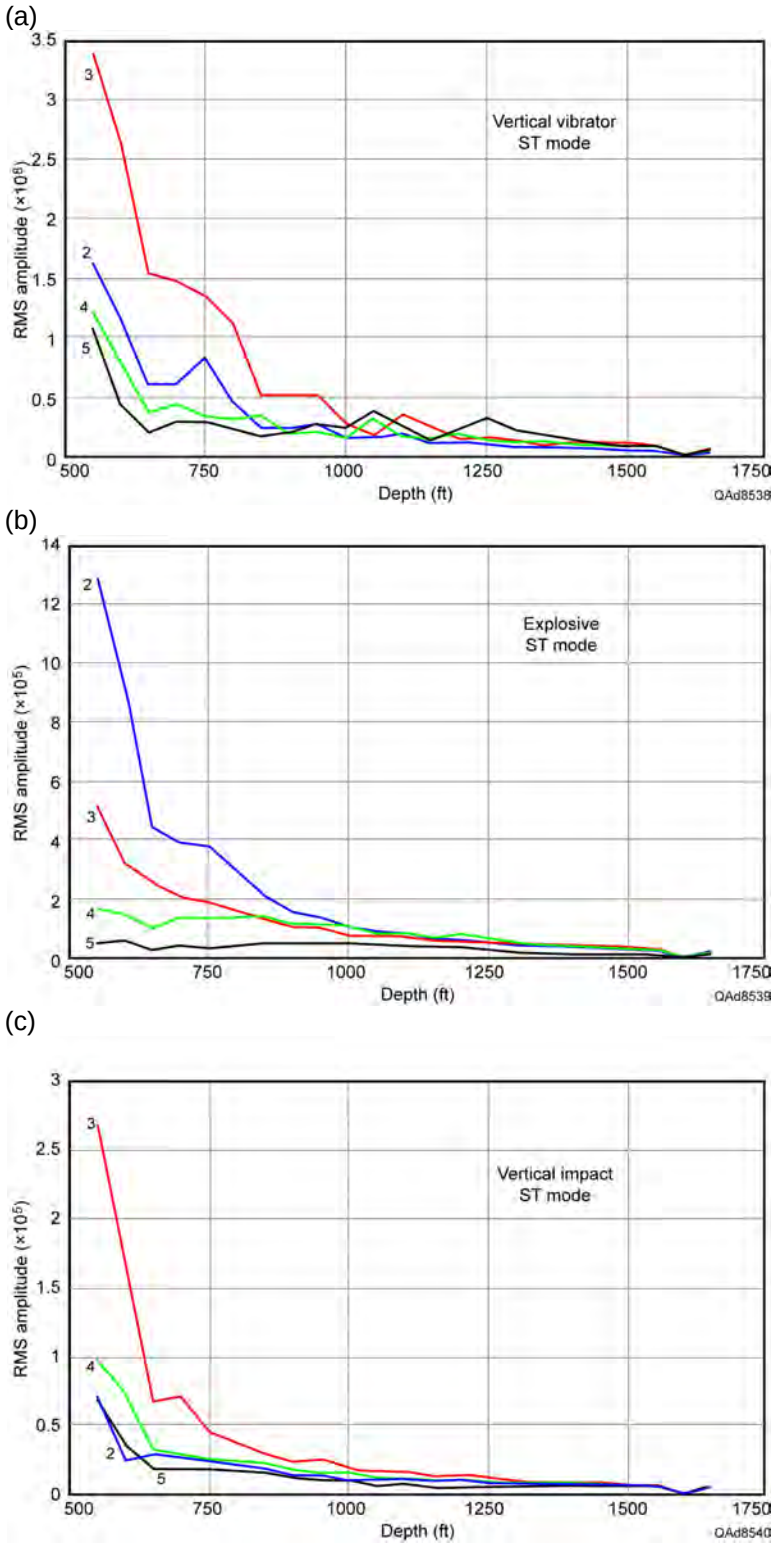

Figure 6.15. Root-mean-square (rms) amplitudes of downgoing ST modes measured across the downhole vertical sensor array when sources are positioned at offset stations 2 through 5 (Fig. 6.3). Source station positions are indicated by the number on the curves. (a) Source is 60,000-lb (27,733-kg) vertical vibrator. (b) Source is 1 kg charge at depth of 6 m. (c) Source is an accelerated-weight impact delivering 22,276 ft-lb (30,202 joules) to the Earth.

Important energy-related characteristics of the sources that were tested which should be kept in mind as data on Figures 6.10 through 6.15 are examined include the following specifications:

- Vertical vibrator: I/O AHV IV PLS 362 with a hold-down weight of 60,000 lb (27,733 kg). Linear 8-seconds sweep from 8 to 96 Hz.

- Explosive: One kilogram (2.2 lb) placed at a depth of 6 m (20 ft).

- Vertical impact: 33,000-lb vehicle with 1000-psi nitrogen-spring weight-acceleration system that delivers impact energy of 22,276 ft-lb (30,202 joules).

.

Figure 6.16. VSX^{TM} accelerated-weight impact source provided by Vecta Technology and United Services Alliance. This source can deliver a vertical impact to the Earth, or an inclined force vector can be applied in any azimuth direction and at any incident angle between 0 and 45 degrees without moving the vehicle. Vehicle weight is 33,000 lb. Its compressed-nitrogen spring system delivers 22,276 ft-lb (30,202 joules) of energy to the Earth.

The vertical vibrator used in the test is shown in both photos of Figure 6.4. The accelerated-weight impact source from United Service Alliance, which is powered by a compressed-nitrogen spring, is shown as Figure 6.16. These photos, together with the source characteristics just listed, imply the vertical vibrator is quite powerful and should put more energy into the ground than does either the explosive shot or the vertical-impact source. Test data exhibited as Figures 6.13 through 6.15 confirm this expected energy advantage of the vibrator, with the amplitudes of vibrator-produced wave modes being approximately 1000 times larger than the amplitudes of corresponding modes produced by the weight-impact source and approximately 100 times stronger than amplitudes of modes produced by a 1-kg explosive detonated at a depth of 6 m.

Frequency attributes of the wave modes produced by the sources are illustrated as Figures 6.17 through 6.19. These analyses show the narrow data windows spanning the downgoing illumination wavelets where frequency spectra were calculated. These data windows differ slightly from those used to measure the wavelet amplitude curves exhibited as Figures 6.13 through 6.15. The data within each shaded analysis window are almost pure wave-mode signal and have a minimal amount of non-mode noise. For this reason, each frequency spectrum is assumed to be a reasonable indication of the signal-frequency content in each downgoing illumination wavelet. Amplitudes that are more than 20 dB below the peak of an amplitude spectrum are assumed to be too small to make significant contributions to images and are ignored. The position of the -20 dB cutoff line that indicates frequency bandwidth is labeled on each spectrum. The effective signal-frequency content of each wave mode is defined as the frequency spectrum extending above each 20 dB cutoff line. Defining effective signal frequency with a 20 dB cutoff is only an approximation, because this assumption results in some signal energy extending beyond the limits of the 8 to 96 Hz sweep of the vertical vibrator (Fig. 6.17).

Frequency and amplitude-strength characteristics of wave modes measured by the downhole vertical-receiver array are summarized on Table 6.1. On this table, the amplitude measures displayed on Figures 6.13 to 6.15 are listed as “order of magnitude” quantities rather than as specific numerical values. In contrast to the amplitude information that was analyzed at four source stations (stations 2, 3, 4, 5) on Figures 6.13 to 6.15, the frequency characteristics summarized on Table 6.1 relate to data generated only at source station 3. Key principles defined by these tabulated amplitude and frequency characteristics are:

1. The ST (transverse S) mode is the most energetic mode produced by each source, with ST amplitudes often tending to be almost 10 times larger than P and SR amplitudes (Table 6.1).

2. Explosive-source wave modes have amplitudes approximately 100 times smaller than the amplitudes of vertical-vibrator wave modes (Table. 6.1).

3. Vertical-impact wave modes have amplitudes approximately 1,000 times smaller than the amplitudes of vertical-vibrator wave modes (Table 6.1).

4. All three vertical-force sources (vibrator, explosive, impact) produce robust P and S wave modes, and each source would be effective for many P and S imaging objectives.

5. For the vertical vibrator, the signal frequencies of SR and ST wave modes are essentially the same as the signal frequencies of the P mode. The frequency bandwidths of all vibrator wave modes are constrained by the 8–96 Hz sweep used to generate the data (Fig. 6.17).

6. For the explosive source, the signal frequency bandwidth of the P mode (approximately 5 to 200 Hz) is approximately twice the signal bandwidths of the SR and ST shear modes (Fig. 6.18). However, the 5 to 80 Hz (approximate) bandwidths of the SR and ST signal frequencies exceed the bandwidths of S modes that experience shows can be produced with horizontal vibrators, which tend to be about 4 to 50 Hz (or less).

7. The vertical-impact source (Fig. 6.19) produces a P mode that has a bandwidth (5 to 130 Hz) that is approximately twice that of the bandwidths of the SR mode (5 to 60 Hz) and the ST mode (5 to 70 Hz). However, P-mode frequencies greater than 50 Hz are significantly weaker in amplitude than frequency components less than 50 Hz (Fig. 6.19), causing all three modes (P, SR, ST) generated by the impact source to have approximately the same “effective” bandwidth. The ST shear mode has much of its energy concentrated in the frequency range between 30 and 50 Hz, which interestingly causes the amplitude of that mode to be 4 dB to 6 dB greater than the amplitudes of the P and SR modes.

Table 6.1. Amplitude and frequency attributes of wave modes measured by downhole sensors.

Source	P mode		SR mode		ST mode	
	Amplitude	Freq (Hz)	Amplitude	Freq (Hz)	Amplitude	Freq (Hz)
Vertical vibrator	10^7	8–96	10^7	8–96	10^8	8–96
Explosive	10^5	5–200	10^5	5–80	10^5	5–80
Vertical impact	10^4	5–130	10^4	5–60	10^5	5–70

Amplitude properties taken from Figures 13 - 15 for source stations 2, 3, 4, and 5.
Frequency properties taken from Figures 17 – 19 for source station 3 only.

(a)

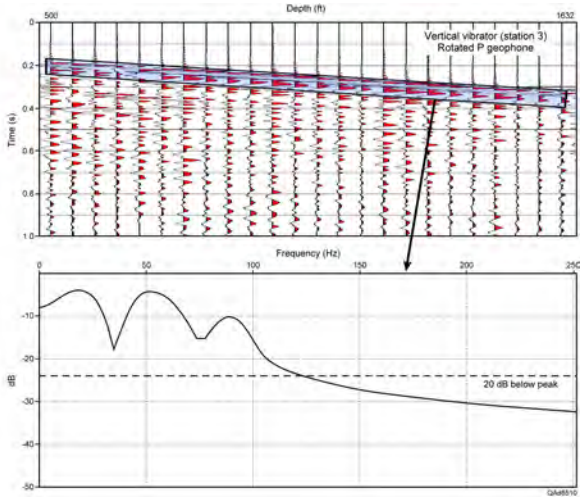

(b)

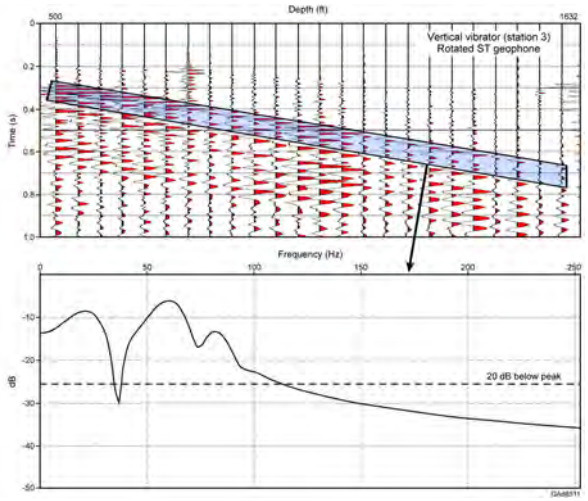

(c)

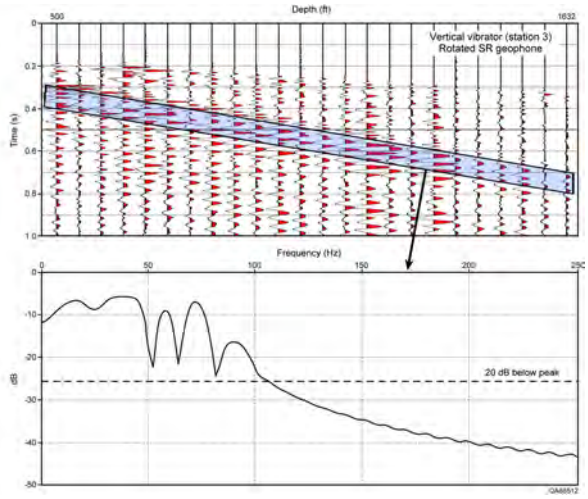

Figure 6.17. Frequency analysis of elastic wave modes produced by the 60,000-lb (27,733-kg) vertical vibrator at source station 3 and recorded by the downhole vertical array. (a) P mode. (b) ST mode. (c) SR mode. Amplitudes of the frequency spectra indicate relative strengths of the wave modes propagating away from the source station.

(a)

(b)

(c)

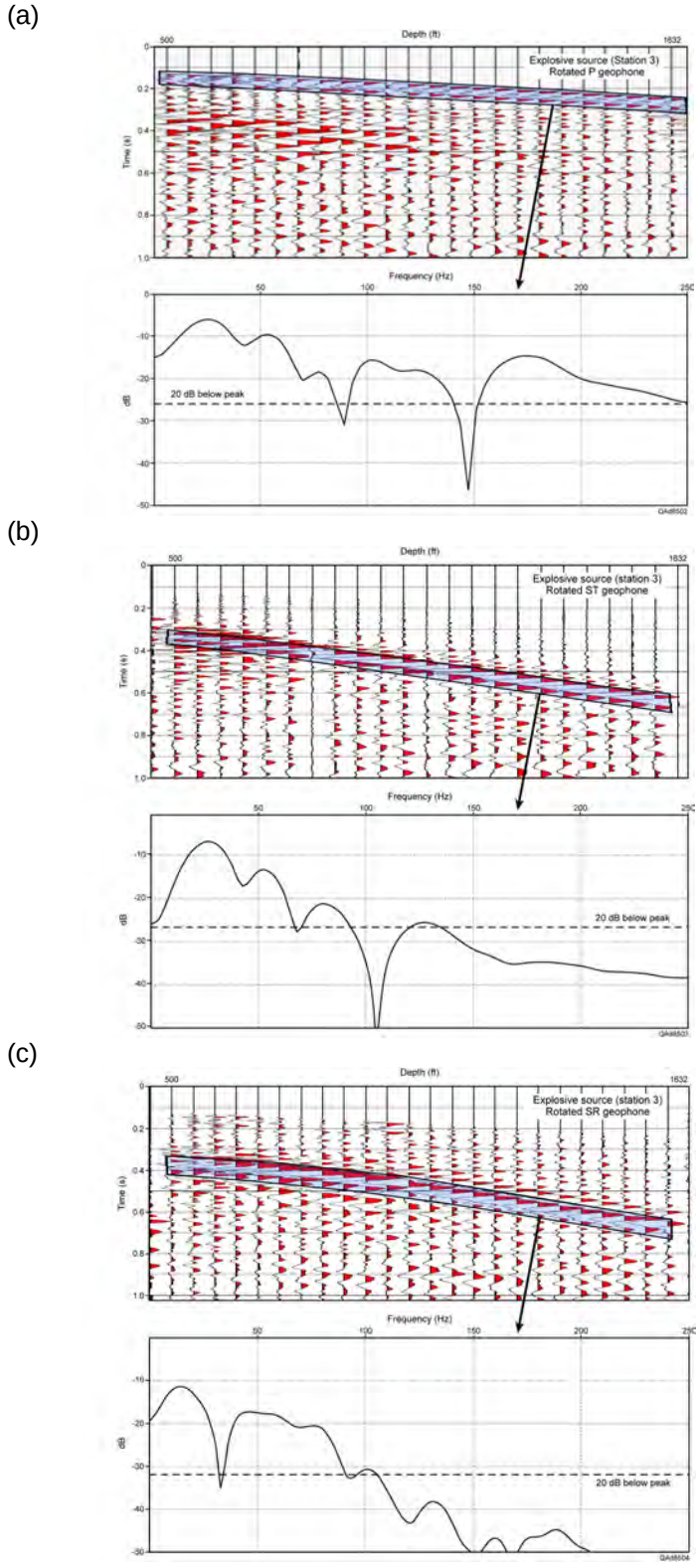

Figure 6.18. Frequency analysis of elastic wave modes produced by a 1-kg explosive shot at a depth of 6 m at source station 3 and recorded by the downhole vertical array. (a) P mode. (b) ST mode. (c) SR mode. Amplitudes of the frequency spectra indicate relative strengths of the wave modes propagating away from the source station.

(a)

(b)

(c)

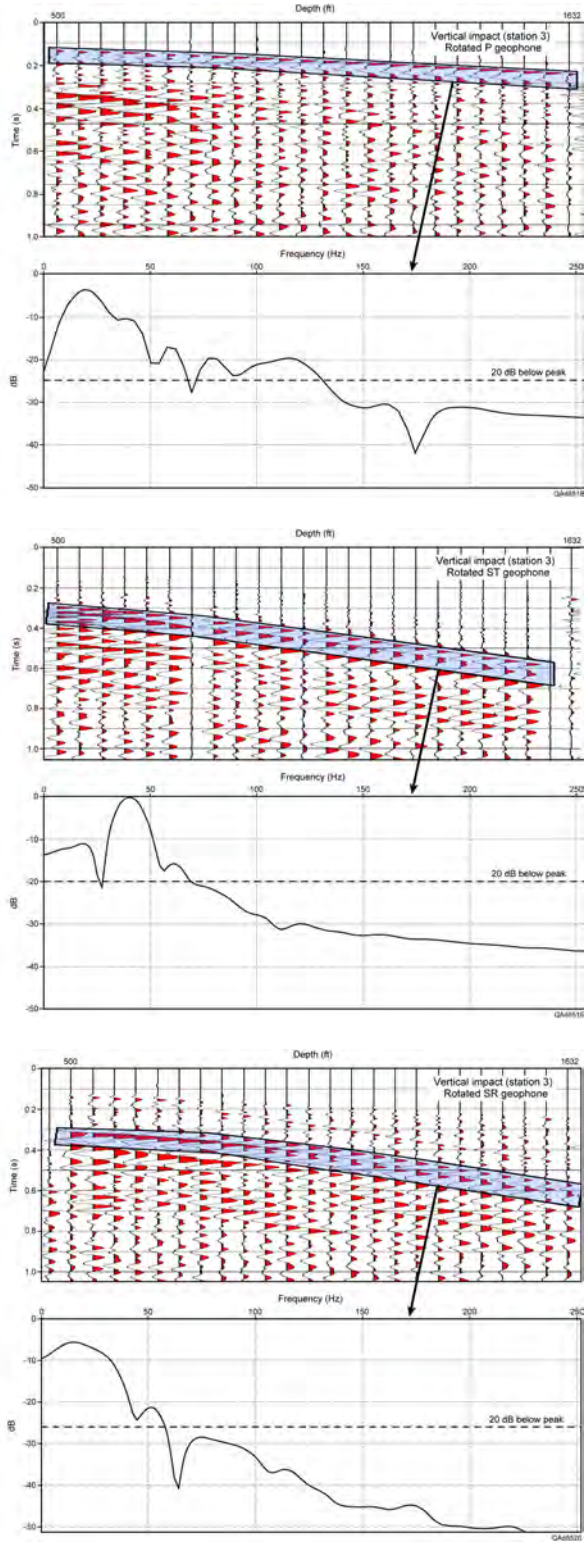

Figure 6.19. Frequency analysis of elastic wave modes produced by a vertical-impact source delivering 22,276 ft-lb (30,202 joules) of energy at source station 3 and recorded by the downhole vertical array. (a) P mode. (b) ST mode. (c) SR mode. Amplitudes of the frequency spectra indicate relative strengths of the wave modes propagating away from the source station.

Surface Array Measurements of Wave-Mode Amplitudes and Frequencies Produced by Test Sources

Offset distances of source stations from receiver Well 4 are defined on Table 6.2. Except for the first (No. 1) and last (No. 9) stations in this list, sources were offset at uniform distance increments of 250 ft (76.2 m) from the vertical receiver array in Well 4. These source-station intervals are the same distance as the dimension of the 25-station horizontal arrays of surface receivers. A graphical illustration of this tabulated source and receiver geometry is illustrated on Figure 6.3.

Table 6.2. Source station offsets.

Source station	Offset (ft)	Offset (m)
1	44	13.4
2	250	76.2
3	500	152.4
4	750	228.6
5	1000	304.8
6	1250	381.0
7	1500	457.2
8	1750	533.4
9	1920	585.2

QAd8474

With this source geometry, data acquired by orthogonal X,Y,Z sensors deployed across the 25-station surface receiver array can be represented as 192-trace, single-fold field records having trace spacings of 10 ft (3 m) and extending 1920 ft (585.2 m) from the vertical receiver array. Examples of field records produced when the vertical impact source was positioned at source stations 2 through 9 are displayed on Figure 6.20a. For each sensor profile, static shifts occur in 25-trace blocks along the source line because no P or S source-station static corrections have been applied to the individual common-source gathers. The convex-shape of P-wave refraction arrivals within each 25-trace common-source segment is caused by intra-array P-wave receiver statics across the 250-ft (76.2 m) interval spanned by the surface receiver spread.

These same data are displayed as Figure 6.20b with P-wave static adjustments applied to each trace of the 192-trace record. P-wave refractions, and by inference P-wave reflections, none of which are obvious in the data displays, are now reasonably phase aligned. However, discontinuities in S-wave refractions still exist between adjacent source gathers because S source statics differ from P source statics. Likewise, within each common-source gather, S-wave refractions have nonlinear moveouts because intra-array S-wave statics across the 250-ft (76.2 m) distance spanned by the surface receivers differ from P-wave statics. Additional static corrections are required to create optimal alignment of S events.

(a)

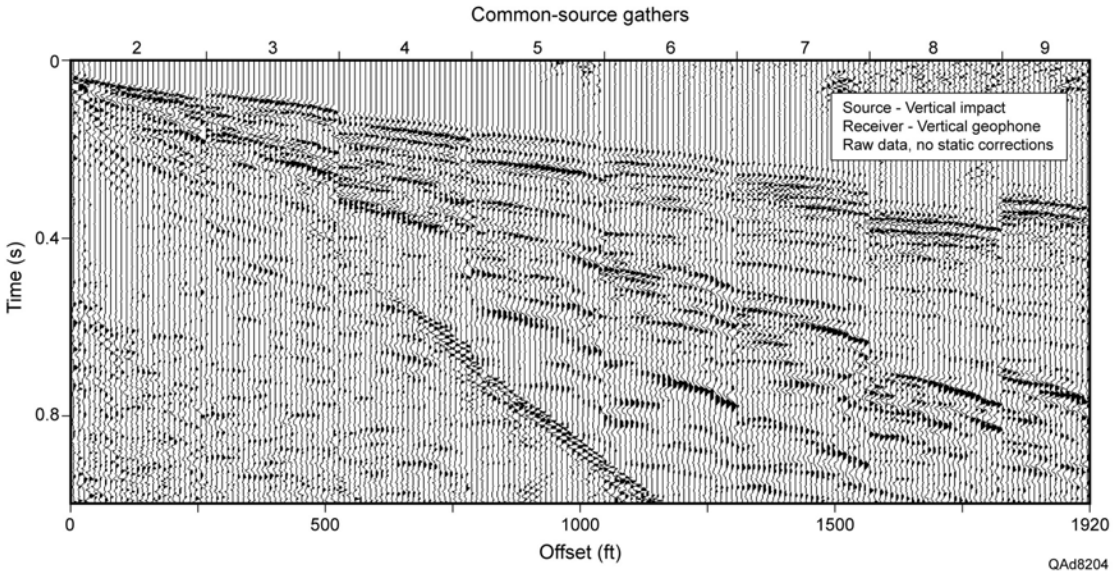

(b)

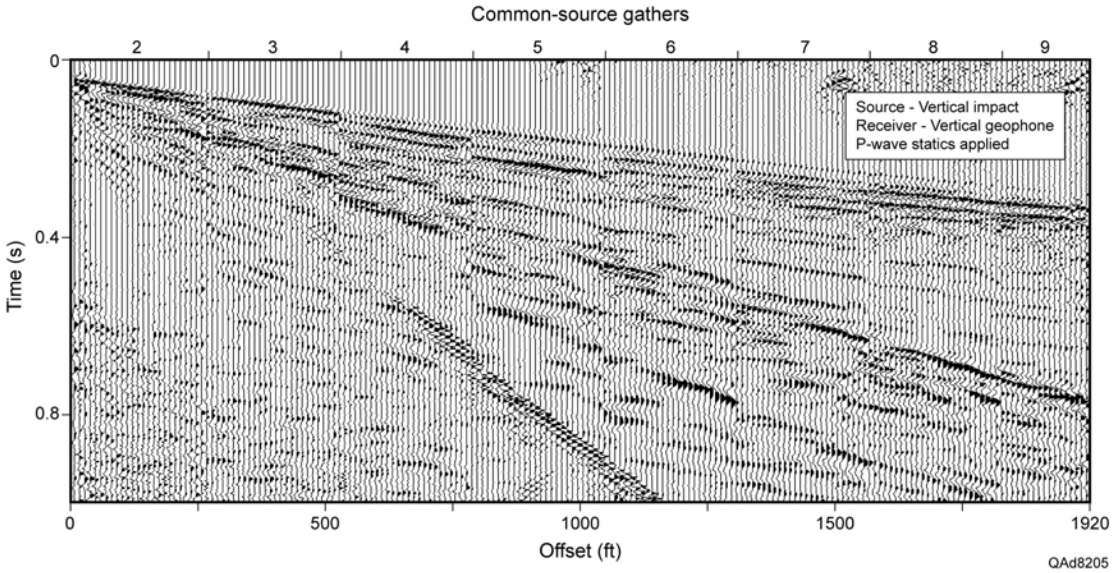

Figure 6.20. (a) Data generated by a vertical weight-impact source positioned at source stations 2 through 9 and recorded by surface vertical geophones. Discontinuities between each 25-trace group of source-station gathers are caused by source-station statics and variations in time-zero for this impact source. (b) Same data with adjustments made to align the earliest P-wave refraction arrivals.

Test data acquired with surface-based 3C geophones and Sigma cable-free boxes are analyzed in this section to compare the energy content and frequency bandwidth of P and S modes produced by each of the three tested vertical-force source types. The data windows illustrated on Figures 6.17 through 6.19 consist of downgoing target-illuminating P and S wavelets that are

essentially pure signal and have minimal noise contamination. In contrast, the data on Figures 6.21 through 6.29 were acquired by a surface-positioned horizontal sensor array and contain not only P and S reflections and refractions, but also intrabed multiples and horizontally traveling surface-wave noise. The signal-to-noise ratio of downgoing target-illumination wavelets acquired by downhole vertical receiver arrays (Figs. 6.17 to 6.19) is high; whereas, the signal-to-noise ratio of reflection data acquired with surface-based horizontal receiver arrays (Figs. 6.21 to 6.29) is much lower.

Because the surface-array data are only 1-fold and the short length of the profile does not allow significant reflection curvature to be recognized, it is difficult to identify reflection signal in the data shown on Figures 6.21 through 6.29 by visual inspection. For this reason, a simple analysis procedure is used in which amplitude strengths and frequency bandwidths are calculated for refracted P, S, and surface waves that sweep across the horizontal receiver array. Reflection signal analyses of these surface-recorded data will be shown and discussed in a following section of this chapter.

Analyses of vertical-vibrator data are shown as Figures 6.21 to 6.23; explosive source data are analyzed on Figures 6.24 to 6.26; and vertical-impact source results are presented as Figures 6.27 to 6.29. For each source, separate analyses are done for vertical geophones, inline-horizontal (radial) geophones, and crossline-horizontal (transverse) geophones. For each geophone orientation, wave-mode velocity and frequency characteristics are calculated in data windows constrained to span only interpreted P, S, or surface-wave modes.

Velocity and frequency behavior are displayed as frequency-wavenumber (FK) spectra. On these FK plots, the vertical axis defines how energy embedded in a wave mode is distributed as a function of frequency. The horizontal axis spans a positive half-plane of wavenumber space (K) and a negative half-space. The negative-K half-space defines events that propagate left-to-right from zero offset to an offset of 1920 ft. This left-to-right direction is the propagation direction for all wave modes that are analyzed. The positive half-plane defines events that propagate right-to-left, from an offset of 1920 ft back to zero offset. In this display format, no events propagate right-to-left, so no energy appears in positive wavenumber half-space in any figure. The slope of energy distribution on these FK plots defines the propagation velocity of a wave mode, with steeper slopes implying higher wave-mode propagation velocities.

Data acquired with vertical and radial-horizontal geophones have three embedded wave modes: a P-wave mode (labeled **P**), A radial shear mode (labeled **SR**), and a surface Rayleigh wave (labeled **R**). Data acquired with transverse-horizontal geophones have only two wave modes: a transverse shear mode (labeled **ST**) and a surface Love wave (labeled **L**). No effective P-wave energy appears on transverse horizontal geophones.

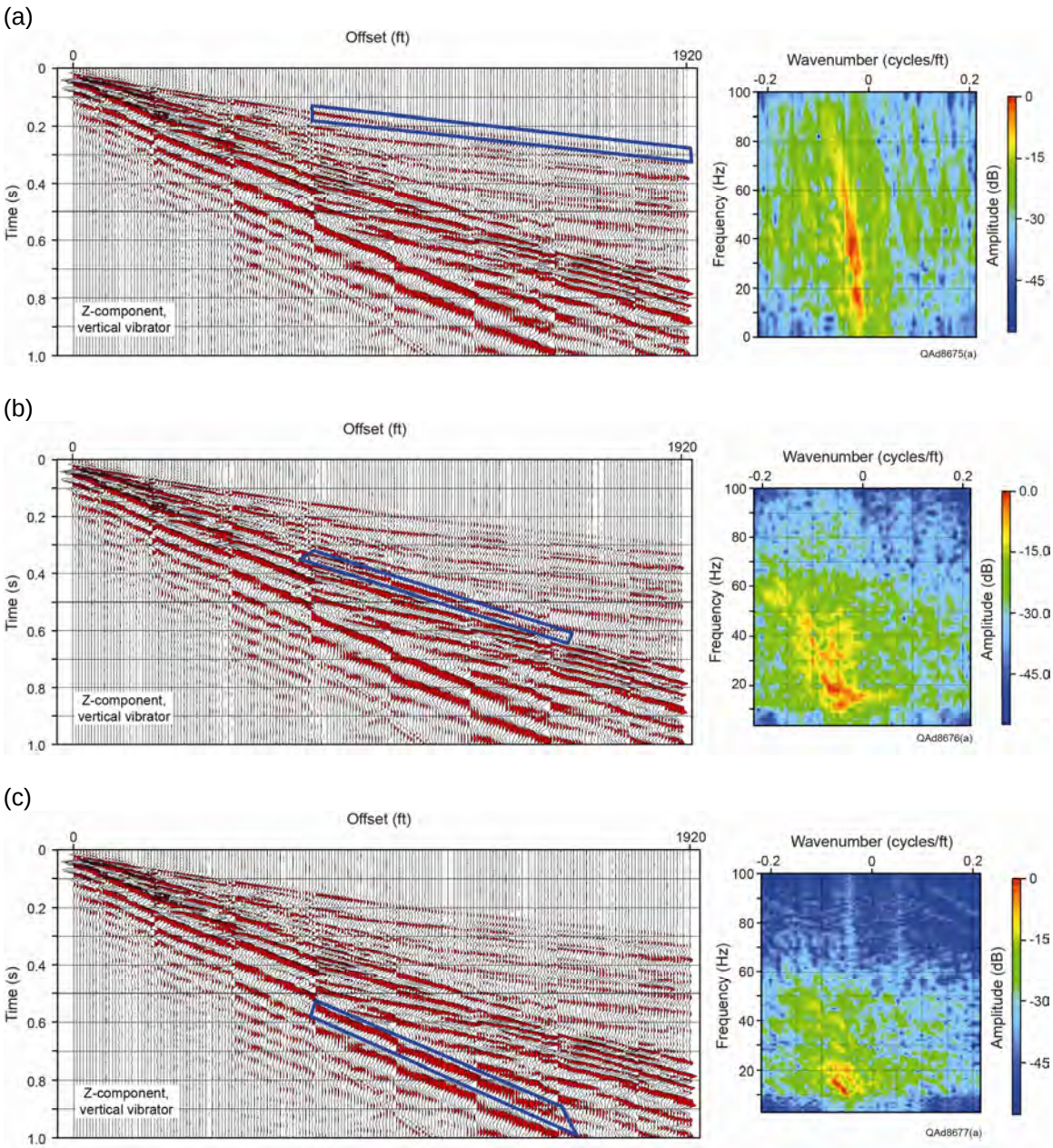

Figure 6.21. Analysis of refracted P, S, and Rayleigh wave modes produced by a vertical-vibrator source and recorded by vertical geophones deployed as a surface-based horizontal array. (a) Compressional mode, P. (b) Radial shear mode, SR. (c) Rayleigh wave mode, R. Data recorded by Sigma cable-free boxes.

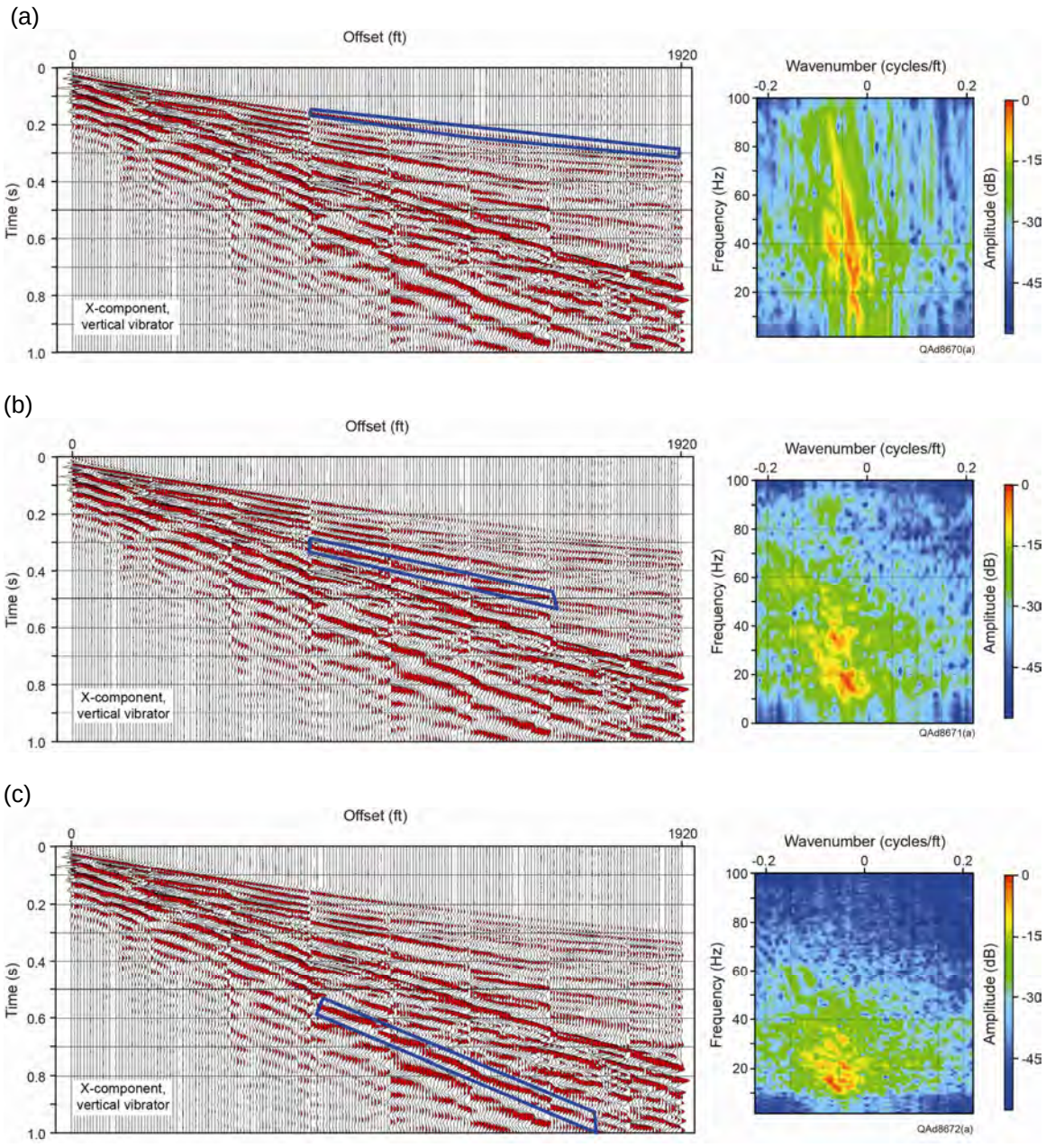

Figure 6.22. Analysis of refracted P, S, and Rayleigh wave modes produced by a vertical-vibrator source and recorded by inline-horizontal (radial) geophones deployed as a surface-based horizontal array. (a) Compressional mode, P. (b) Radial shear mode, SR. (c) Rayleigh wave mode, R. Data acquired by Sigma cable-free boxes.

(a)

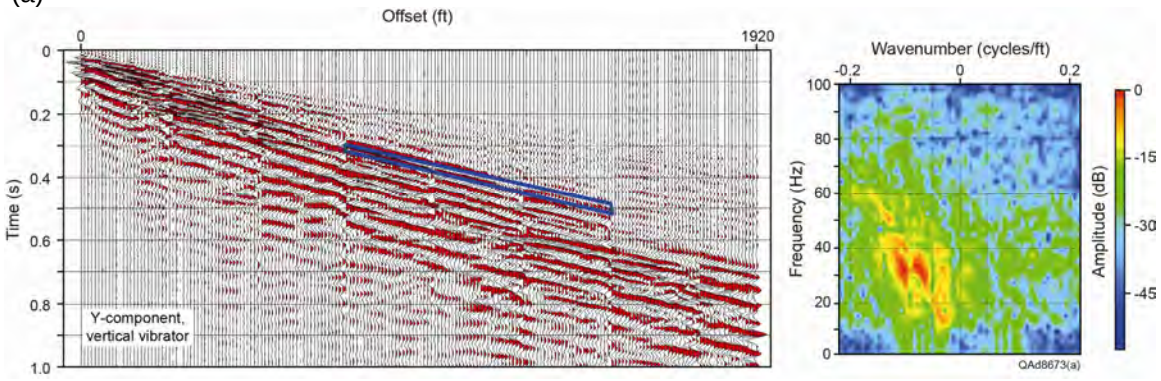

(b)

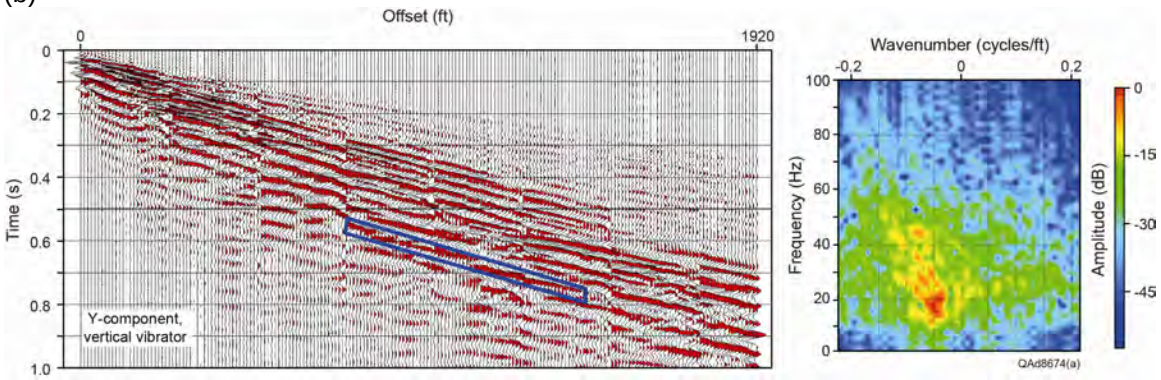

Figure 6.23. Analysis of refracted S and Love wave modes produced by a vertical-vibrator source and recorded by crossline-horizontal (transverse) geophones deployed as a surface-based horizontal array. (a) Transverse shear mode, ST. (b) Love wave mode, L. No P mode is recorded by transverse horizontal geophones. Data recorded by Sigma cable-free boxes.

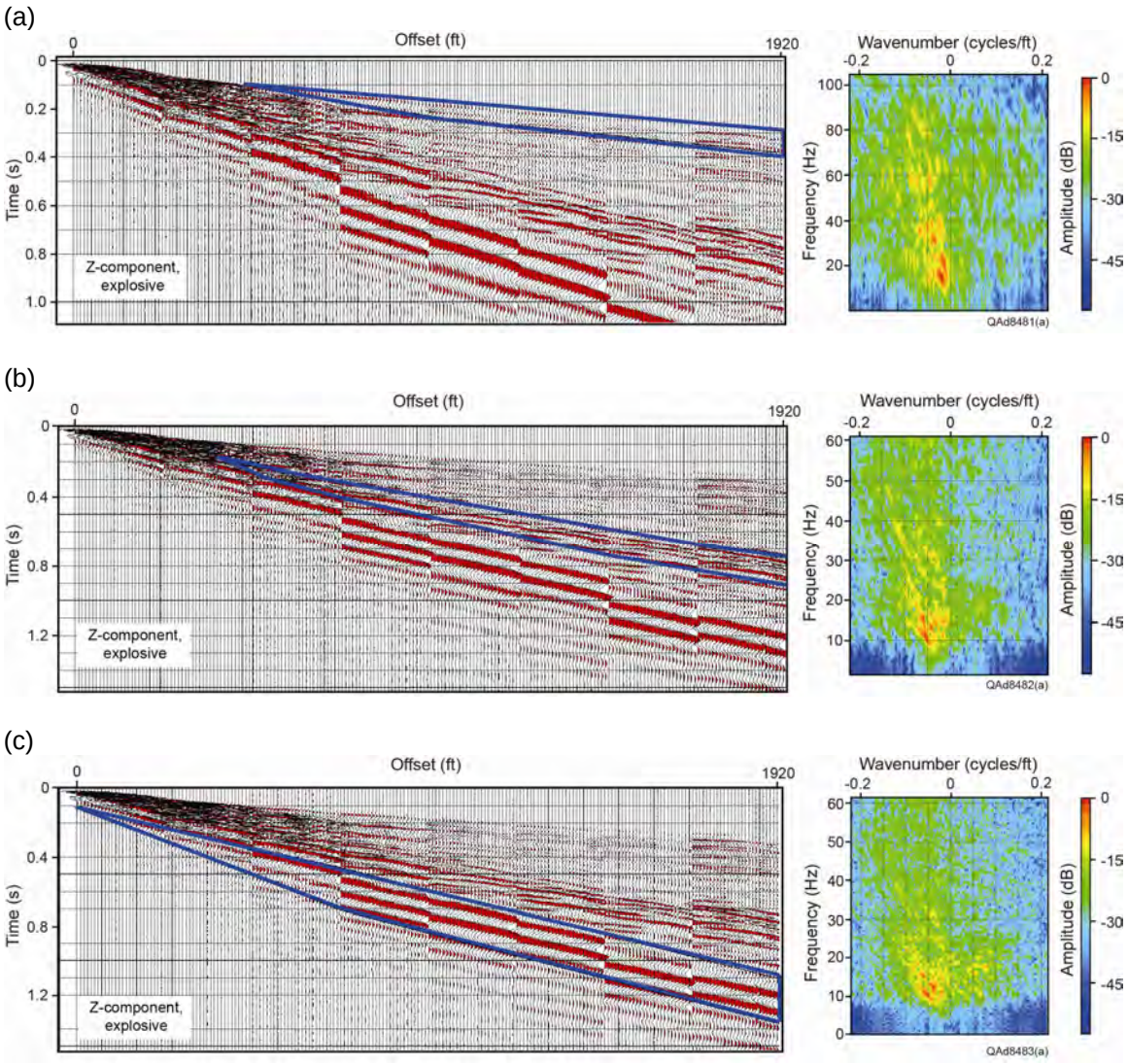

Figure 6.24. Analysis of refracted P, S, and Rayleigh wave modes produced by an explosive source and recorded by vertical geophones deployed as a surface-based horizontal array. (a) Compressional mode, P. (b) Radial shear mode, SR. (c) Rayleigh wave mode, R. Data recorded by Sigma cable-free boxes.

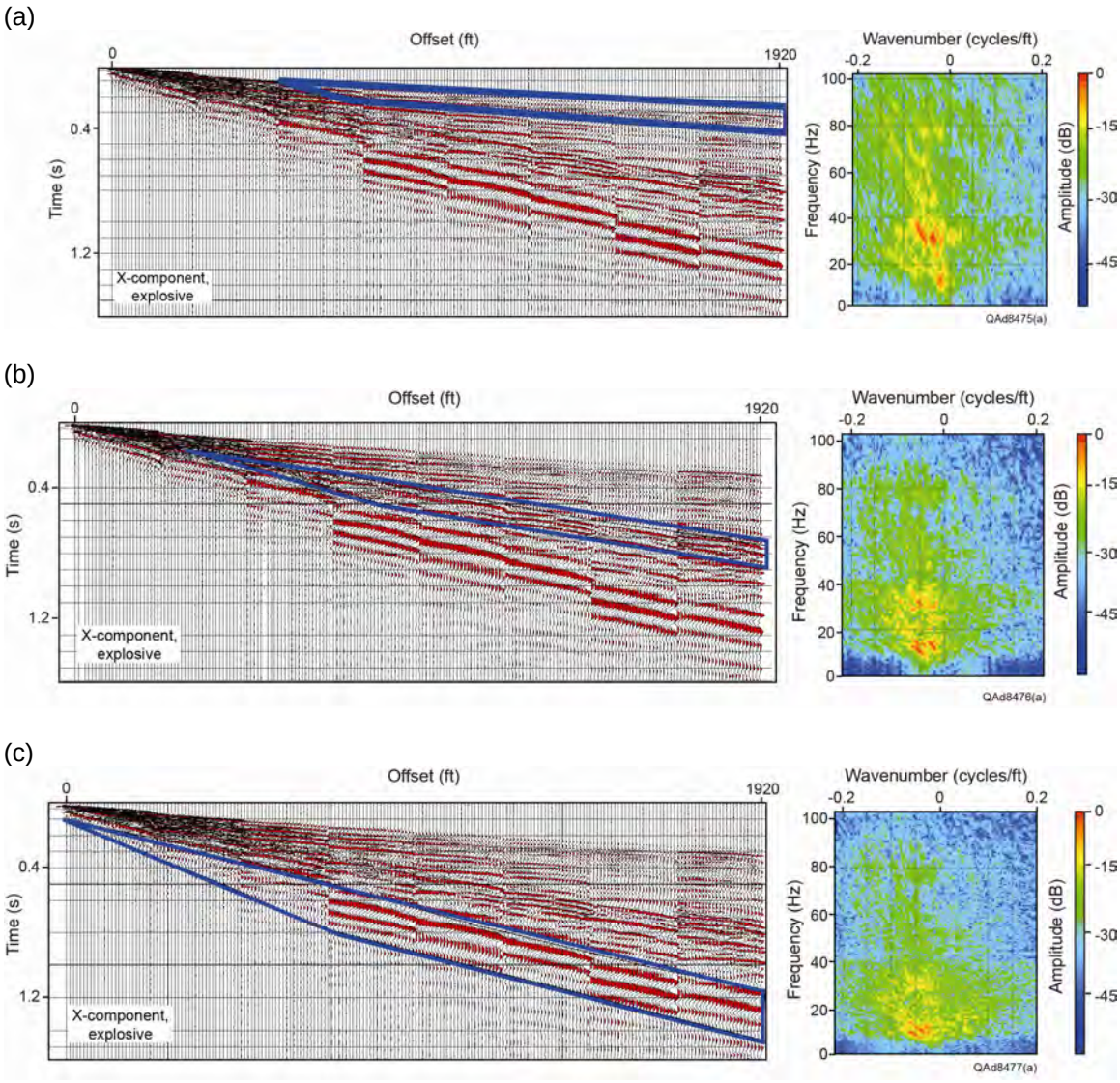

Figure 6.25. Analysis of refracted P, S, and Rayleigh wave modes produced by an explosive source and recorded by inline-horizontal (radial) geophones deployed as a surface-based horizontal array. (a) Compressional mode, P. (b) Radial shear mode, SR. (c) Rayleigh wave mode, R. Data recorded by Sigma cable-free boxes.

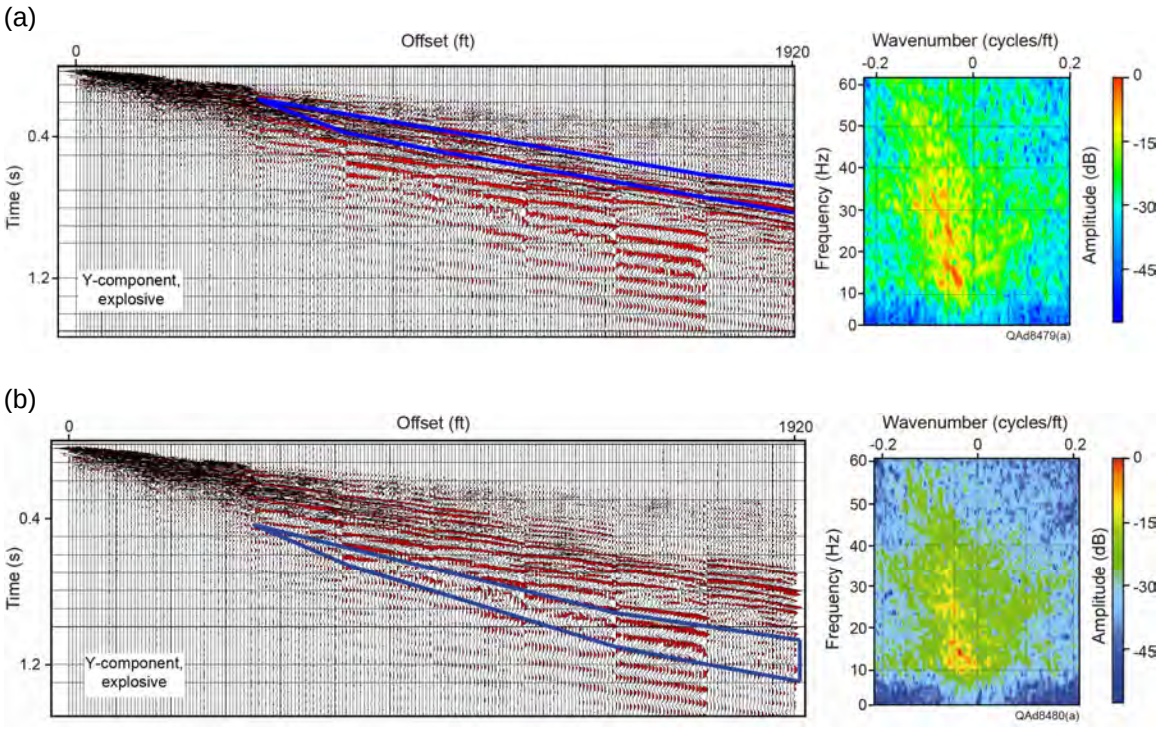

Figure 6.26. Analysis of refracted S and Love wave modes produced by an explosive source and recorded by crossline-horizontal (transverse) geophones deployed as a surface-based horizontal array. (a) Transverse shear mode, ST. (b) Love wave mode, L. No P mode is recorded by transverse horizontal geophones. Data recorded by Sigma cable-free boxes.

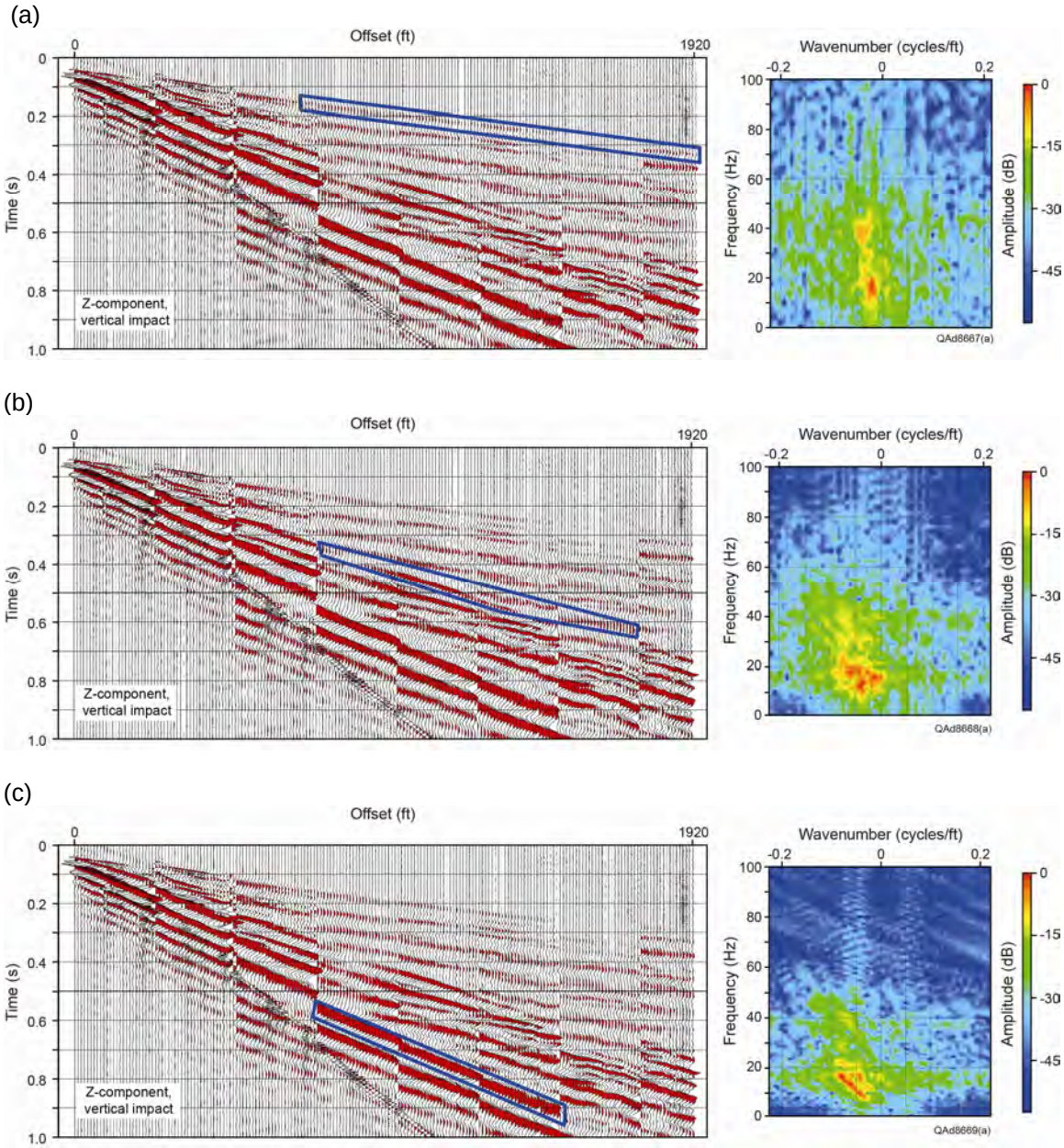

Figure 6.27. Analysis of refracted P, S, and Rayleigh wave modes produced by a vertical-impact source and recorded by vertical geophones deployed as a surface-based horizontal array. (a) Compressional mode, P. (b) Radial shear mode, SR. (c) Rayleigh wave mode, R. Data recorded by Sigma cable-free boxes.

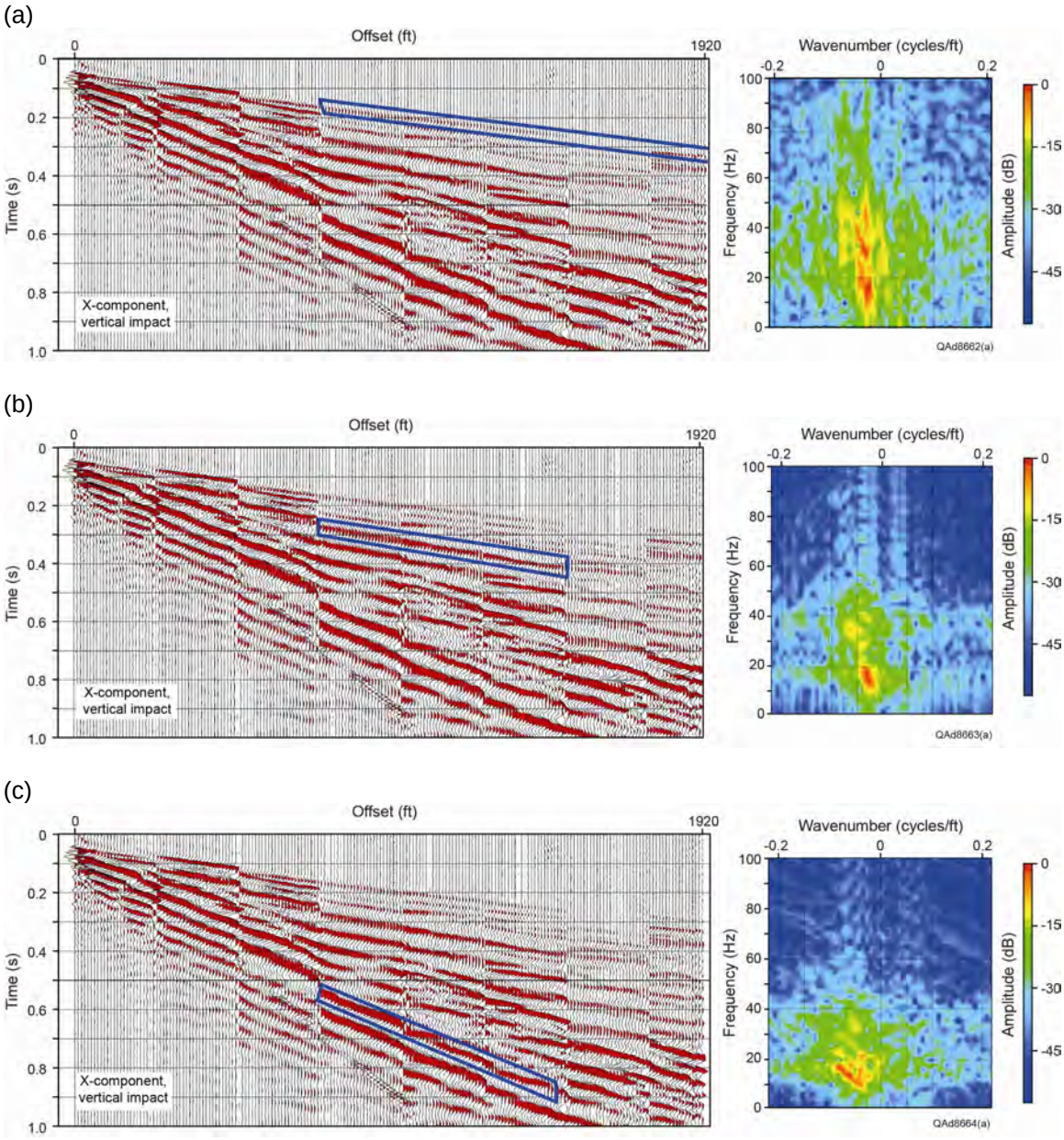

Figure 6.28. Analysis of refracted P, S, and Rayleigh wave modes produced by vertical-impact source and recorded by inline-horizontal (radial) geophones deployed as a surface-based horizontal array. (a) Compressional mode, P. (b) Radial shear mode, SR. (c) Rayleigh wave mode, R. Data recorded by Sigma cable-free boxes.

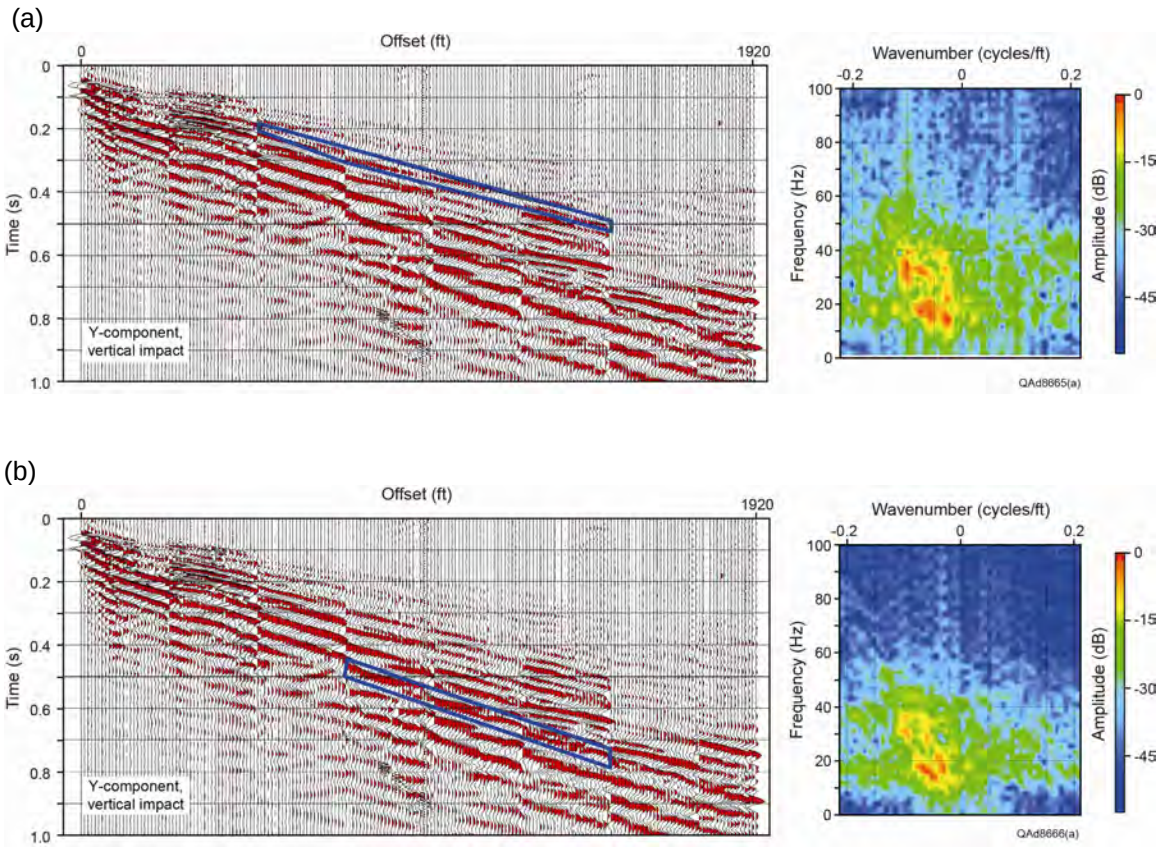

Figure 6.29. Analysis of refracted S and Love wave modes produced by vertical-impact source and recorded by crossline-horizontal (transverse) geophones deployed as a surface-based horizontal array. (a) Transverse shear mode, ST. (b) Love wave mode, L. No P mode is recorded by transverse horizontal geophones. Data recorded by Sigma cable-free boxes.

Source-specific amplitude and frequency characteristics of P, S, and surface-wave modes (either Rayleigh waves or Love waves) that can be inferred from these horizontal-array data are summarized below:

1. By visual inspection of the wiggle-trace data, refracted waves segregate into rather obvious P, S, and surface-wave modes for each source, allowing mode-specific data analysis windows to be positioned on the data.

2. FK spectra calculated for P, S, and surface-wave data windows vary from source to source.

3. Surface-wave modes are lower frequency than P and S modes for all sources, both by visual inspection of wiggle-trace data and by comparison of calculated FK spectra.

4. Examination of FK spectra shows P-mode spectra calculated for vertical geophones and inline-horizontal geophones are approximately equivalent for vertical vibrator and explosive sources (Figs. 6.21 and 6.24). P-mode spectra produced by the vertical impact source span a frequency band approximately 70-percent (one-third less) than that of the vertical vibrator and explosive sources, with diminished energy content occurring at the higher-frequency end of the impact-source spectra (Fig. 6.27).

5. FK spectra calculated from horizontal-transverse geophone data (Figs. 6.23a, 6.26a, 6.29a) show ST-mode spectra are roughly equivalent for the vertical vibrator and explosive sources. ST spectra for the vertical impact source span a frequency band slightly less than that of the vertical vibrator and explosive sources.

When horizontal vibrators are used to generate S-wave data, S-wave modes have frequencies that usually extend to only 50 Hz. This upper-frequency constraint is caused by mechanical limitations of horizontal vibrators. Although a horizontal vibrator can sweep to frequencies higher than 50 Hz, numerous mechanical problems develop if a large number of high-frequency sweeps are done. For this reason, S-wave data generated by horizontal vibrators typically have frequency spectra that span 4 to 48 Hz or 5 to 50 Hz so that S-wave data can be acquired at a large number of source stations with minimal down time for vibrator repair. In contrast to the S-wave frequency limitation imposed by traditional S-wave sources, an important research finding provided by these test data is that S modes produced by vertical-force sources have frequency spectra that exhibit appreciable energy for frequencies higher than 50 Hz. Examples of broadband S-wave data produced by vertical vibrator and explosive sources are displayed as Figures 6.21b, 6.22b, 6.23a, and 6.26a. S-mode spectra calculated for the impact source (Figs. 6.27 through 6.29) span a frequency bandwidth equivalent to that usually generated by horizontal vibrators.

Each of the vertical-force sources (vertical vibrator, shot-hole explosive, vertical impact) creates good-quality elastic wavefields. Specifically, each source produces more S-wave energy than P-wave energy, and although energy output varies from source to source, the ratio of S-wave energy to P-wave energy is approximately the same for each source. Some sources can image deeper geology simply because they are more energetic. For example, the 60,000-lb vertical vibrator used in these tests produced wave-modes having amplitudes approximately 1000 times greater than wave-mode amplitudes produced by the impact source and approximately 100 times greater than wave-mode amplitudes created by the explosive source. As a result, this particular vertical vibrator should image deeper geology than what can be imaged with the vertical-impact source or the shot-hole explosive source. However, any of the three vertical-force sources can provide P and S images extending to depths of principal targets across most oil and gas prospects. Our test data do not cause us to conclude that one type of vertical-force source should be used to the exclusion of other

vertical-force sources. Source selection will be dictated by factors such as surface conditions across a prospect, source availability, source cost, and target depth.

Comparisons of Geophones and Accelerometers as 3C Sensors

One objective of the equipment tests done at the Devine Test Site was to compare P and S wave modes acquired with 3C accelerometers and 3C geophones to determine if one type of sensor provided more attractive multicomponent data than the other. Several factors were considered when analyzing these sensor data, with key requirements being:

1. Geophones and accelerometers had to be planted in the same sediment,

2. All sensors had to be coupled to the Earth in the same manner,

3. All sensor outputs had to be recorded by the same recording system, and

4. Geophones and accelerometers had to record data generated by the same seismic source.

These four data constraints were addressed by: (Requirement 1) placing geophone stations and accelerometer stations side-by-side within 1 meter of each other (Fig. 6.4); (Requirement 2) taking care to bury all sensors flush with the ground surface and tamping soil around each sensor with the same consistency; (Requirement 3) recording geophone and accelerometer data with the same data-acquisition system—a cable-based Sercel 428, and (Requirement 4) recording data generated by only an explosive source.

As a result of these field test procedures, it is reasonably correct to assume that differences in P and S wave modes observed in data outputs from test-site geophone arrays and accelerometer arrays should be caused by the type of sensor that recorded the seismic wavefields rather than by other factors.

(a)

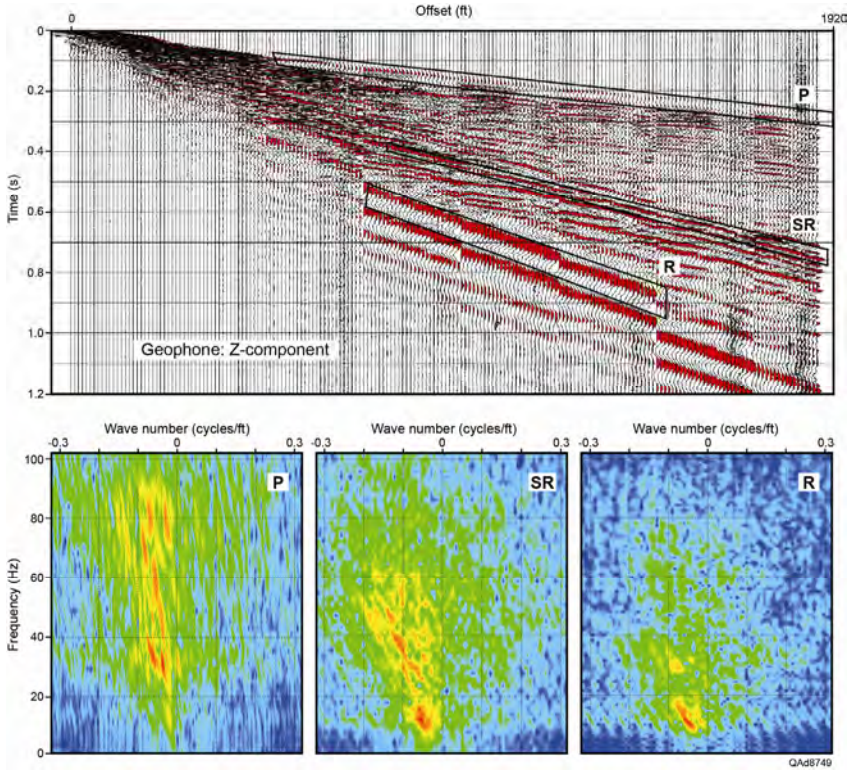

(b)

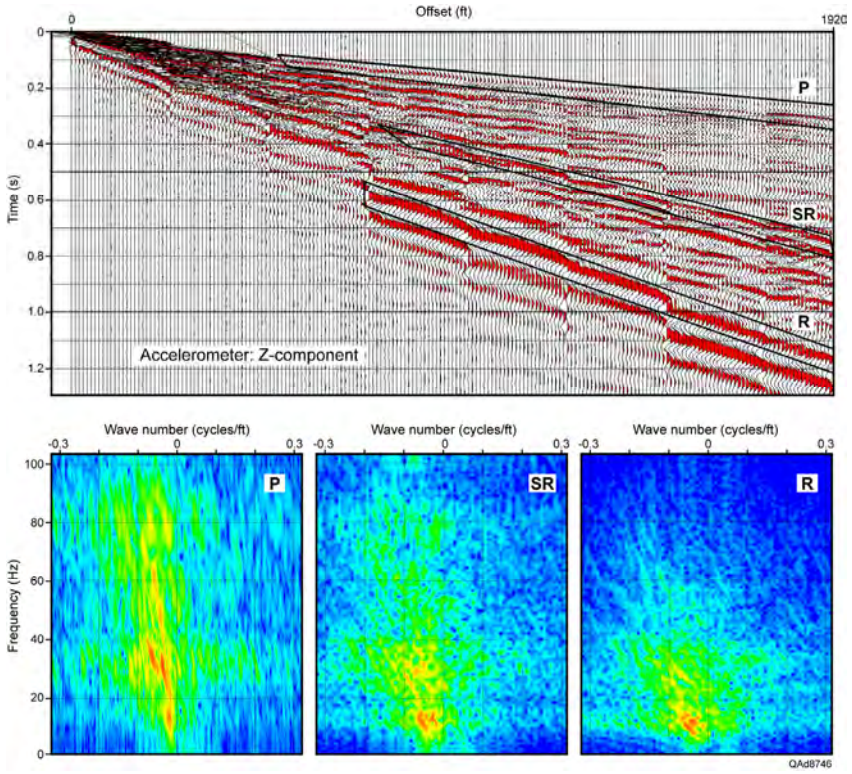

Figure 6.30.Comparison of seismic sensor data. (a) Response of vertical component of 3C geophones. (b) Response of vertical component of 3C accelerometers. P = P-wave mode. SR = radial shear mode. R = Rayleigh surface wave.

(a)

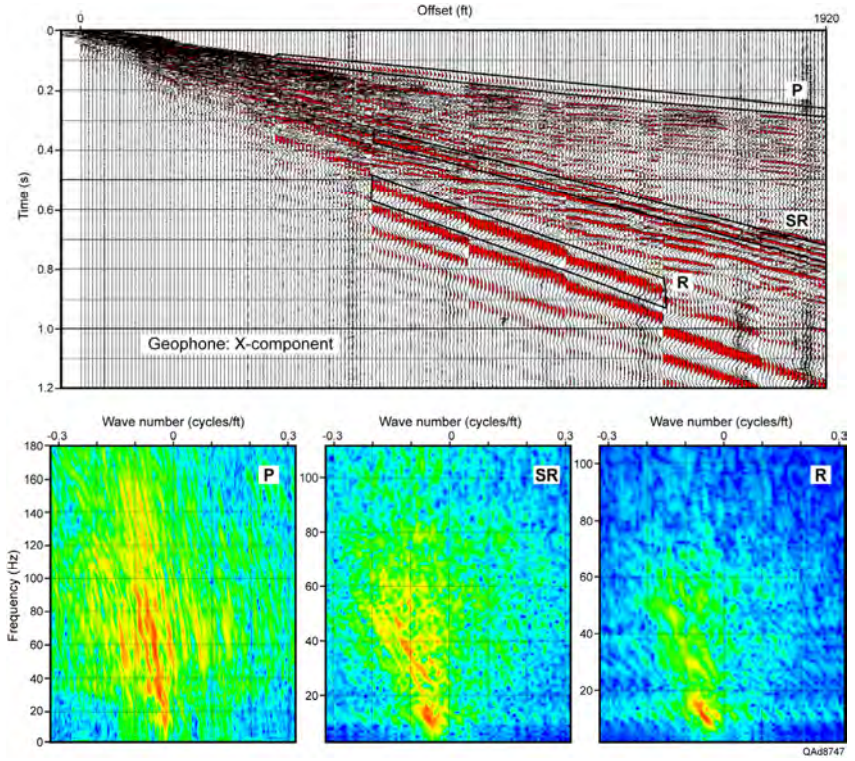

(b)

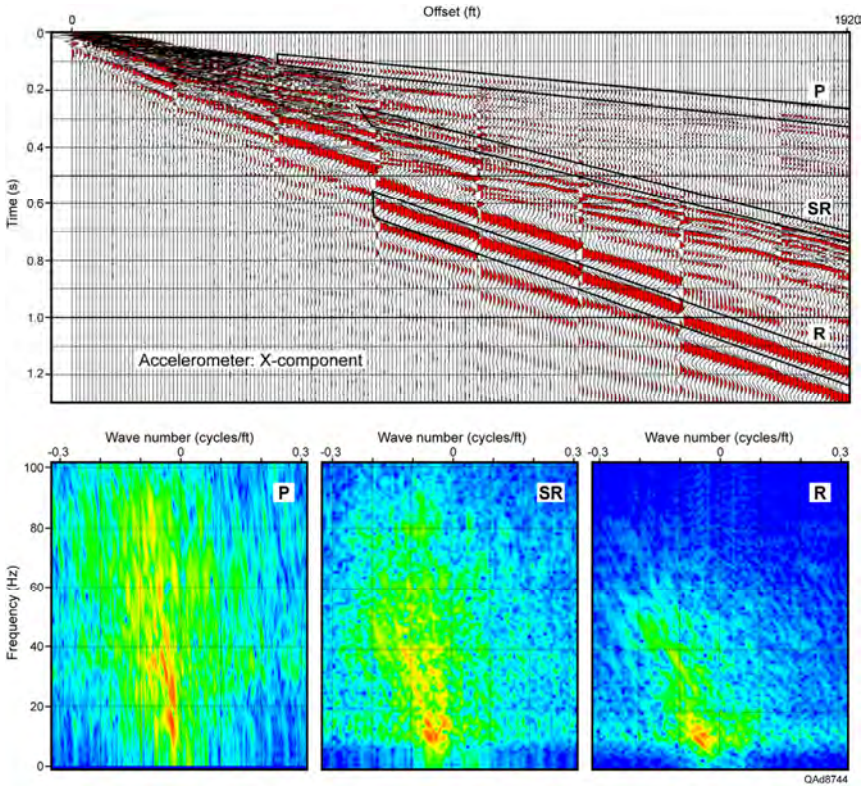

Figure 6.31.Comparison of seismic sensor data. (a) Response of horizontal-radial component of 3C geophones. (b) Response of horizontal-radial component of 3C accelerometers. P = P-wave mode. SR = radial shear mode. R = Rayleigh surface wave.

(a)

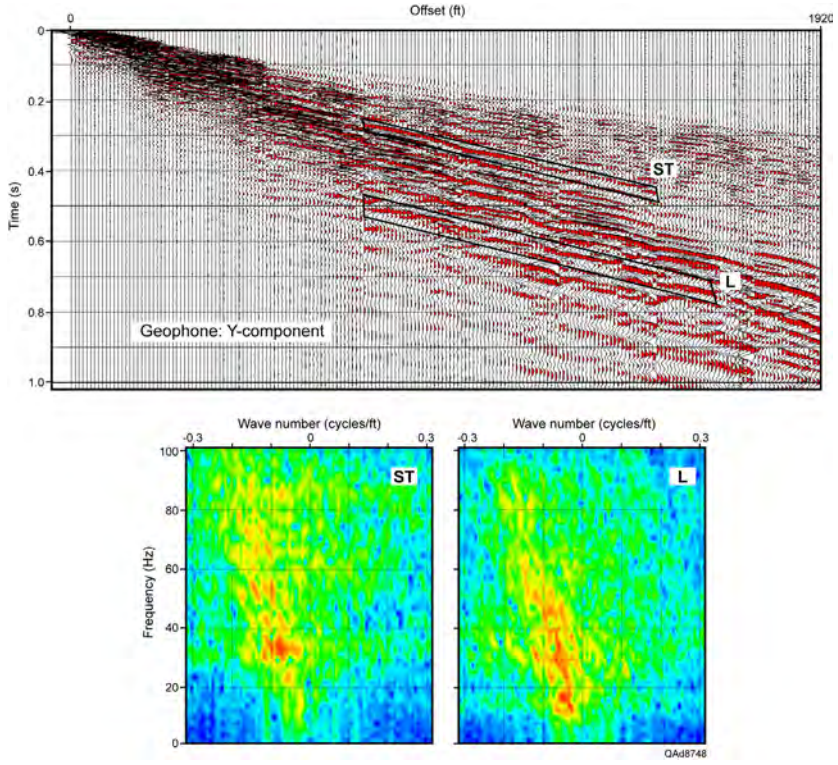

(b)

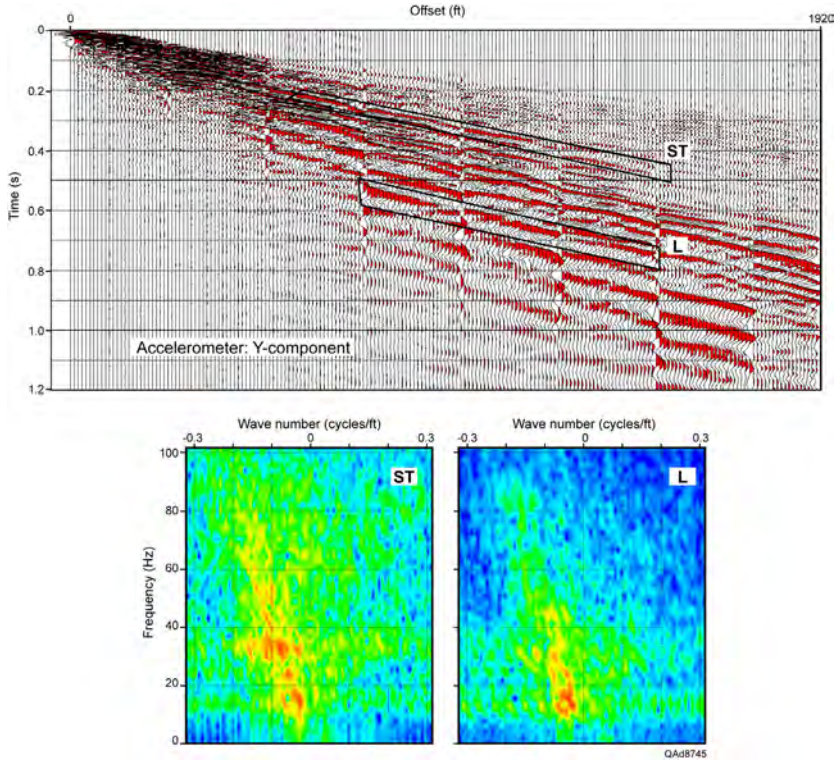

Figure 6.32.Comparison of seismic sensor data. (a) Response of horizontal-transverse component of 3C geophones. (b) Response of horizontal-transverse component of 3C accelerometers. ST = transverse shear mode. L = Love wave.

Test data acquired by 3C geophones and 3C accelerometers are compared on Figures 6.30 through 6.32. The geophones deployed for the test were Oyo Geospace Model 20DX types (10-Hz resonance suspension spring). The accelerometers were Sercel DSU3 MEMS solid-state sensors. The energy source that generated the sensor test data was a 1 kg (2.2 lb) explosive charge detonated at a depth of 6 m (20 ft).

Visual inspection of the wiggle-trace test data displayed on Figures 6.30 through 6.32 implies accelerometers record slightly more robust low-frequency components than do geophones. This distinction in sensor frequency response is verified by most (not all) of the FK spectra that accompany the wiggle-trace plots. In any multicomponent seismic application where it is essential to emphasize low frequencies, serious consideration should be given to using accelerometers rather than geophones for data acquisition.

A unique attribute of MEMS solid-state accelerometers is that they function as gravity meters when they are not reacting to Earth vibrations. The benefit of this gravity meter behavior is that a 3C accelerometer can identify which of its three sensors is in a vertical orientation. As a result, any of the three orthogonal accelerometers in a 3C accelerometer package can be the vertical sensor. An advantage of this sensor physics is that in situations where ground conditions make it difficult to plant a MEMS sensor package in its normal vertical orientation, the sensor package can be laid on its side, covered with a small sandbag or mound of dirt, and still record high-quality data. In our field tests, this property of MEMS sensors was utilized at two receiver stations located 20 and 30 ft (6 and 9 m) from the receiver well. At these locations, a thick layer of coarse gravel prohibited deploying a DSU3 sensor package in its normal vertical orientation. The DSU3 package was laid on its side at these two stations and covered with dirt-filled bags to make a reasonable sensor-to-Earth coupling. The internal electronics of the MEMS data-acquisition system switched the definitions of vertical, radial horizontal, and transverse horizontal to the appropriate accelerometers. The data acquired at these two receiver stations look identical to data acquired at all other receiver stations and cannot be identified when inspecting the wiggle-trace data on Figures 6.30 to 6.32. Thus there is considerable appeal to using MEMS 3C accelerometers to acquire multicomponent seismic data across areas where it is difficult to plant geophones in a vertical orientation, for example across prospects covered with hard rock outcrops.

In most seismic data-acquisition projects, vertical orientation of 3C geophones is not a serious handicap. Also for most studies, it is not necessary that amplitudes of low-frequency components (less than 10 Hz) be greater than the amplitudes provided by 3C geophones. In such conditions, there is no significant difference between multicomponent data acquired with 3C geophones and data acquired with 3C accelerometers.

An important principle of S-wave physics demonstrated on Figures 6.30 to 6.32 has nothing to do with the type of sensor that recorded the data. This principle

is that FK spectra show the frequency bandwidth of an ST shear mode is significantly broader than the frequency bandwidth of an SR shear mode. Examples of this frequency difference are shown by comparing ST spectra on Figure 6.32, where high-energy frequency components extend from 10 to 100 Hz, with SR spectra on Figures 6.30 and 6.31, where high-energy frequency components extend from 10 Hz to only 40, 60, or 80 Hz, depending which sensor data are considered (vertical sensor data or horizontal-radial sensor data).

Comparisons of Cable-Based and Cable-Free 3C Data

The third objective of the equipment test program was to compare P and S wave modes acquired with cable-based and cable-free data acquisition systems to determine if equivalent data are acquired with each recording system. Constraints placed on data subjected to this analysis were:

1. Identical sensors (3C Oyo Geospace Model 20DX geophones [10-Hz resonance suspension spring]) generated the data inputs to the two recording systems, and

2. Sensor arrays recorded by each system were planted side-by-side in equivalent sediment and with equivalent sensor-to-earth coupling (Fig. 6.4).

3. The geophone responses that were input to each recording system were produced by the same source (a shot-hole explosive).

The cable-based recording system was a Sercel 428. Two cable-free systems were utilized: EUnite boxes provided by Sercel and Sigma boxes provided by Seismic Source and iSeis.

As a result of the three field test procedures listed above, any differences in P and S wave modes observed in the test data should be caused by the type of data-acquisition system that recorded the wave modes rather than by differences in sensor type, sensor coupling, source wavefields, or other factors.

Test data acquired by these three data-acquisition systems are compared on Figures 6.33 through 6.35. In these displays, data are segregated according to geophone orientation. Vertical geophone responses are shown in Figure 6.33, horizontal-radial geophone responses are displayed on Figure 6.34, and horizontal-transverse geophone responses are on Figure 6.35. As was the case for seismic sensor comparison (Figs. 6.30 to 6.32), the energy source that generated the data was 1 kg (2.2 lb) of explosive detonated at a depth of 6 m (20 ft).

Comparing FK spectra on each figure leads to the conclusion that data acquired with the 428 cable-based system have wider frequency spectra than data acquired with either cable-free system. This difference is particularly obvious for P-wave spectra where 428-system frequencies extend above 100 Hz (Fig. 6.34 in

(a)

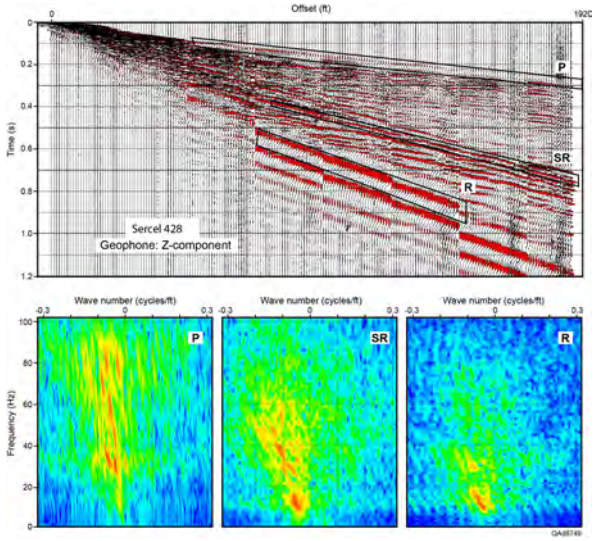

(b)

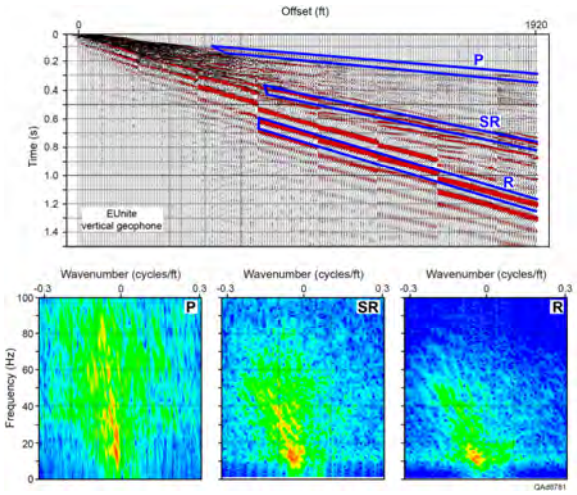

(c)

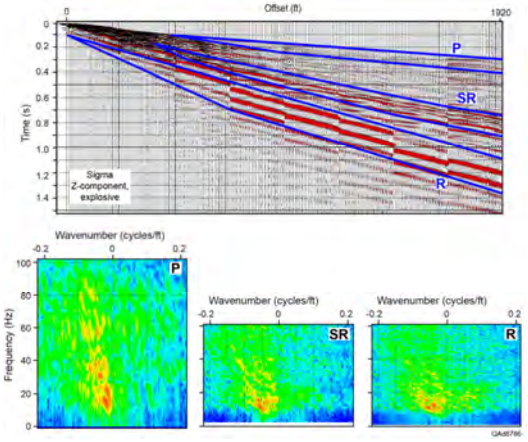

Figure 6.33. Comparison of vertical-geophone data acquired with a cable-based recording system and cable-free recording systems. (a) Vertical component data acquired with cable-based Sercel 428. (b) Vertical component data acquired with cable-free EUnite system. (c) Vertical component data acquired with cable-free Sigma system. P = P-wave mode. SR = radial shear mode. R = Rayleigh surface wave.

(a)

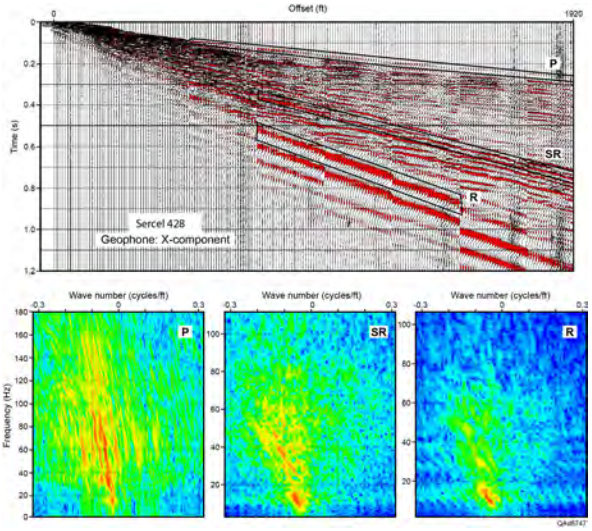

(b)

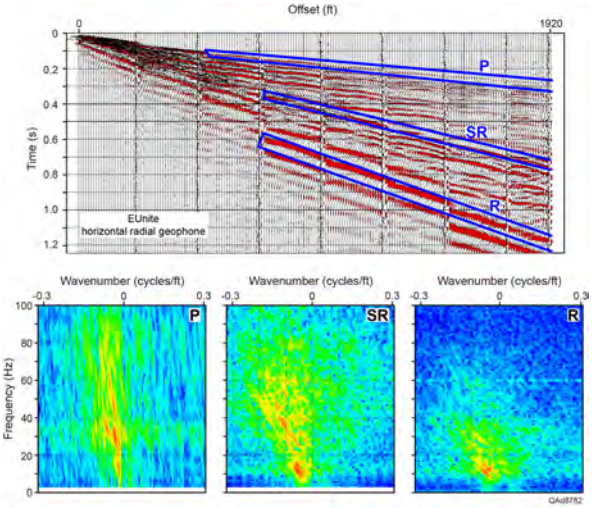

(c)

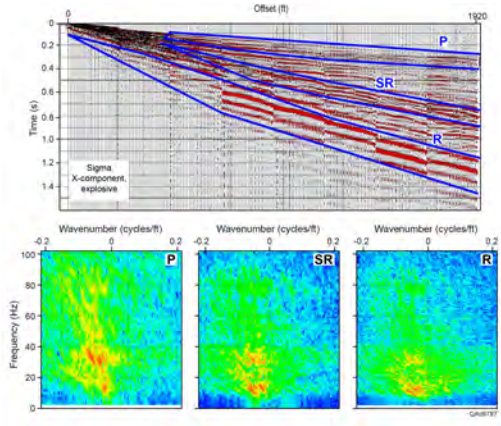

Figure 6.34. Comparison of horizontal-radial-geophone data acquired with a cable-based recording system and cable-free recording systems. (a) Horizontal-radial component data acquired with cable-based Sercel 428. (b) Horizontal-radial component data acquired with cable-free EUnite system. (c) Horizontal-radial component data acquired with cable-free Sigma system. P = P-wave mode. SR = radial shear mode. R = Rayleigh surface wave.

(a)

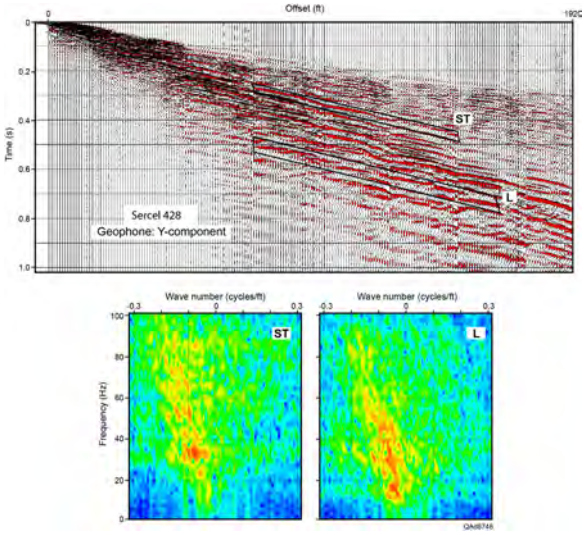

(b)

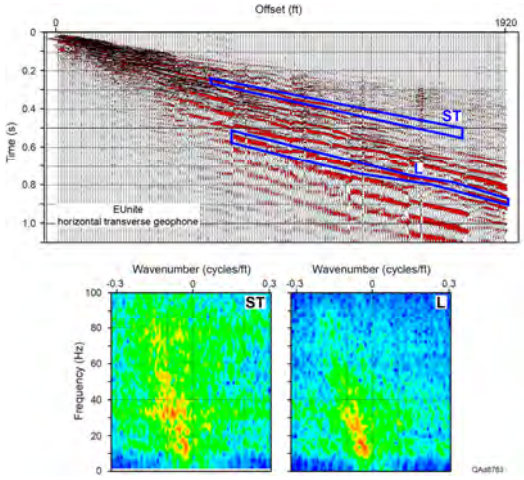

(c)

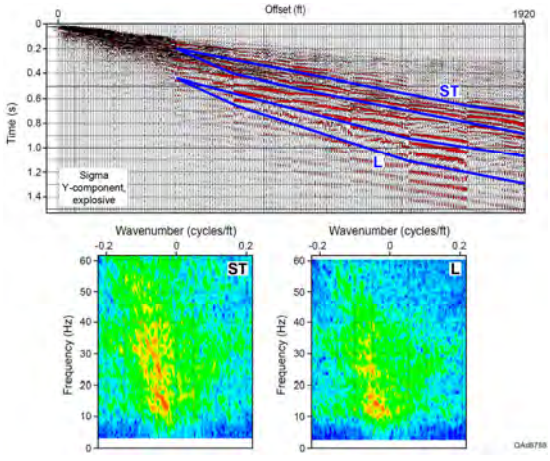

Figure 6.35. Comparison of horizontal-transverse-geophone data acquired with a cable-based recording system and cable-free recording systems. (a) Horizontal-transverse component data acquired with cable-based Sercel 428. (b) Horizontal-transverse component data acquired with cable-free EUnite system. (c) Horizontal-transverse component data acquired with cable-free Sigma system. ST = transverse shear mode. L = Love surface wave.

particular), but Sigma-system and EUnite-system frequencies extend to only 100 Hz (or less). Extensions of energy to higher-frequency components also occur for SR and ST shear modes acquired with the cable-based system.

Extracting P and S Reflections from Surface-Array Data

Downgoing P and S wave modes can be observed in displays of unprocessed vertical-force-source data acquired with downhole vertical-receiver array (Figs. 6.10 through 6.12). However, P and S reflection events are not obvious in displays of unprocessed data acquired with horizontal receiver arrays (Figs. 6.21 through 6.35). It is problematic that reflections can be identified in the 1-fold source gathers displayed in these latter figures. To search for reflections, surface-array data were processed using a patented hyperbolic Radon transform algorithm available from RARE Technology (Wood, 2004a, 2004b). This algorithm is particularly effective at finding weak signal embedded in relatively high noise.

Examples of surface-array data after application of hyperbolic Radon filtering are displayed as Figures 6.36 through 6.38. The velocity range over which the algorithm searched when filtering the data to extract P-wave signal was 6,000 to 18,000 ft/s (1828 to 5486 m/s). The algorithm was constrained to a velocity range of 2,000 ft/s to 6,000 ft/s (610 to 1828 m/s) when searching for S-wave signal.

Inspection of Figures 6.36 to 6.38 shows P and S reflection events were recorded on vertical component, horizontal-radial component, and horizontal-transverse component sensors for all three types of vertical-force sources – vertical vibrator, vertical impact, and shot-hole explosive. This result demonstrates two important concepts:

1. RARE's hyperbolic Radon transform is a powerful velocity filter for extracting reflection signal from noisy seismic data, and

2. P, SR, and ST wave modes exist in surface-recorded data produced by vertical-force sources just as they do in downhole sensor data.

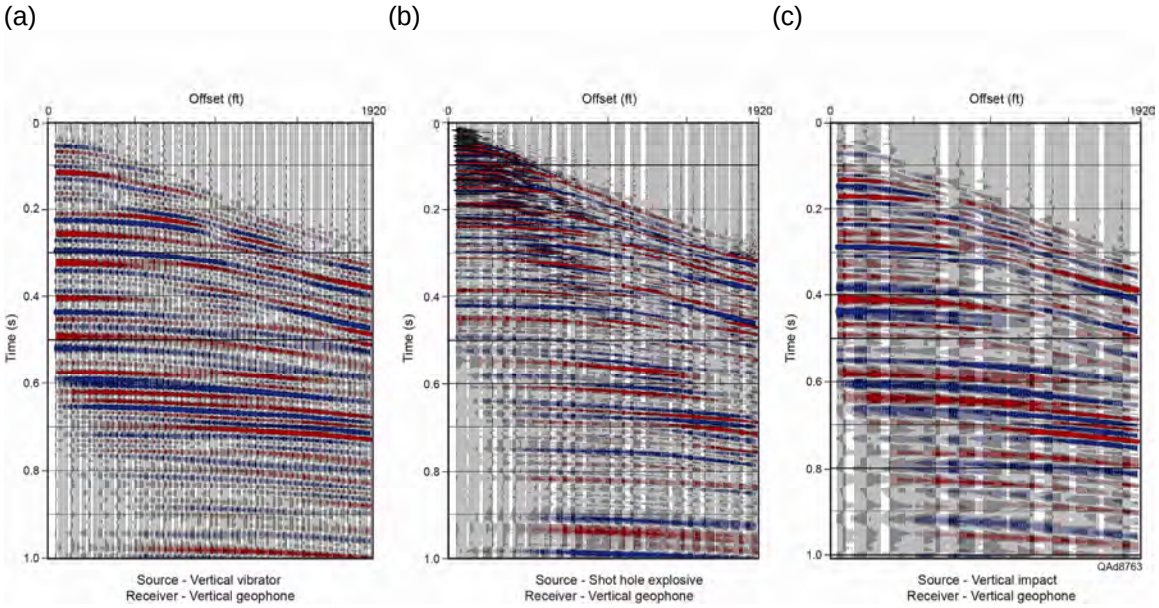

Figure 6.36. P-wave reflections and intra-bed multiples extracted from vertical-geophone response for (a) vertical vibrator, (b) shot-hole explosive, and (c) vertical impact.

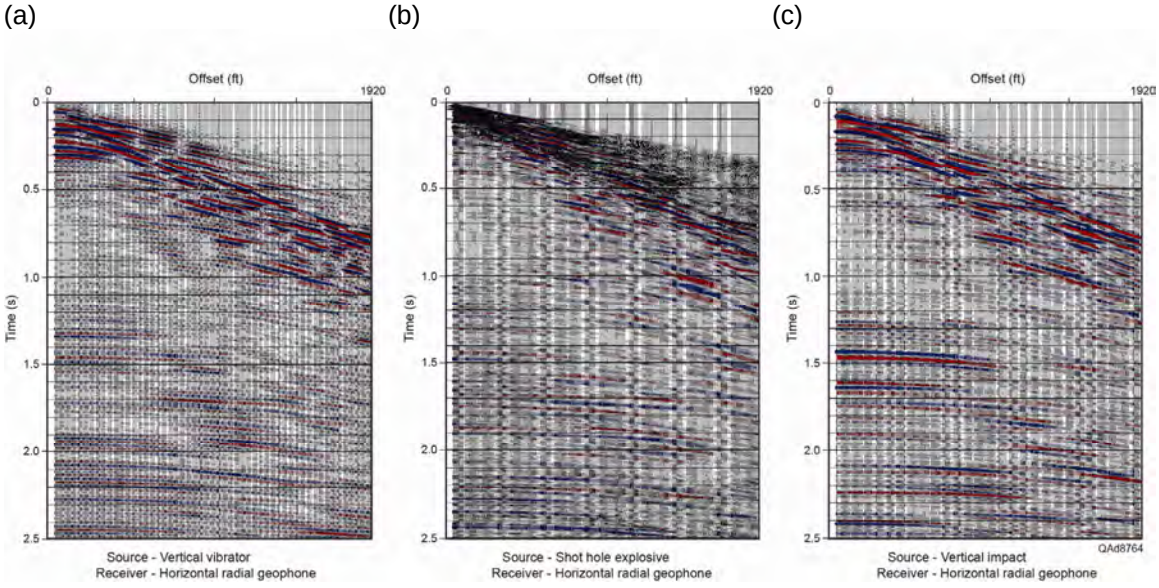

Figure 6.37. SR-wave reflections and intra-bed multiples extracted from horizontal-radial-geophone response for (a) vertical vibrator, (b) shot-hole explosive, and (c) vertical impact.

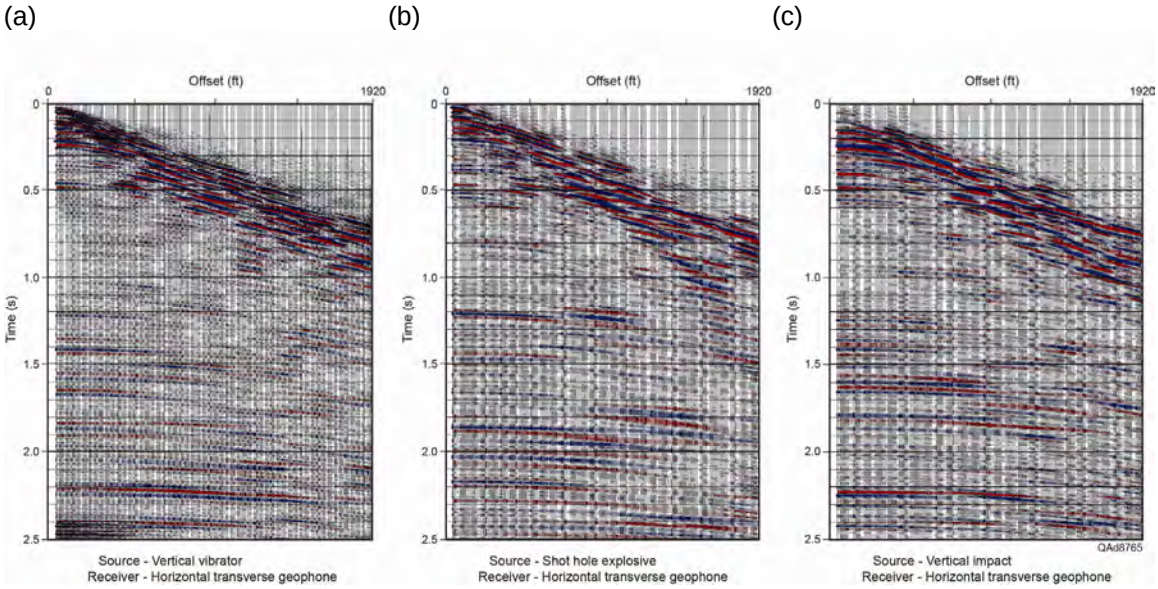

Figure 6.38. ST-wave reflections and intra-bed multiples extracted from horizontal-transverse-geophone response for (a) vertical vibrator, (b) shot-hole explosive, and (c) vertical impact.

Conclusions

The equipment test program implemented at the Devine Test Site focused on three objectives:

1. Record and analyze P and S modes produced by vertical-force, horizontal-force, and inclined-force seismic sources,

2. Compare data acquired by geophones and accelerometers, and

3. Determine whether seismic data acquired with a cable-based recording system are equivalent to data acquired with cable-free data-acquisition systems.

Source comparisons

Vertical-force sources can be classified into three generic types: vertical vibrators, shot-hole explosives, or vertical impacts. A representative source from each of these three general source classes was deployed for the test program conducted at the Devine Test Site. The fundamental physics documented by these tests was ***all vertical-force sources produce full elastic wavefields having robust compressional (P), radial shear (SR), and transverse shear (ST) modes***. One conclusion reached in this study is that these full-elastic wavefields are created directly at the point where each source applies its vertical

force vector to the Earth. This observation should be a fundamental hypothesis in multicomponent seismic projects.

Wave modes propagating away from each source station are best seen if they are captured by a vertical array of downhole receivers. Vertical-array data define the properties of downgoing wave modes that illuminate subsurface targets, thus analyzing vertical-array data is the preferred way to evaluate seismic source performance. Analysis of vertical-array data acquired at the Devine Test Site shows all three tested sources (vertical vibrator, shot-hole explosive, and vertical impact) are effective for multicomponent seismic data acquisition. Encouraging aspects of these data are that each source generates radial (SR) and transverse (ST) shear modes in addition to the expected P mode, and that the energy content of these S modes equals or exceeds the energy content of the P mode.

Although vertical-array data show high-quality P and S modes propagate into the subsurface, it is important to analyze horizontal-array data acquired by surface-based sensors to evaluate the amount of surface-wave noise produced by each source and the P and S reflection-signal quality associated with each source. Horizontal-array data acquired during the test program show that P, SR, and ST modes exist in surface-sensor data and, even though some sources are more energetic than others, the relative ratios of the amounts of P, S, and surface-wave mode energy embedded in surface-recorded data do not greatly differ from source to source.

A continuing topic of research will be to compare SR and ST shear modes produced with a vertical-force source with SV and SH modes produced by horizontal-force sources to determine similarities and differences between S-wave modes produced by these two fundamentally different seismic sources. For example the ST mode observed in vertical-force test data may not be a true SH mode but a split shear mode created when an SV shear mode, known to be produced by a vertical-force source, propagates in an azimuthally anisotropic near-surface layer local to a source station.

Sensor comparisons

Only minor differences were found when comparing multicomponent seismic data acquired with 3C geophones against data acquired with 3C accelerometers. One difference was that the energy content of frequency components less than 8 Hz was higher for accelerometer data than for geophone data, which may be important in some studies. A second difference between geophones and accelerometers is that where ground conditions do not allow a 3C sensor package to be planted in a normal vertical orientation, a 3C accelerometer package can be placed horizontally on the Earth surface and still acquire good quality data if adequate weight is placed atop the package to ensure good sensor-to-Earth coupling. In contrast, 3C geophones cannot be

deployed in this manner. This ability to deploy a 3C sensor in a vertical orientation, or on the ground surface in a horizontal orientation, allows 3C data to be acquired across hard ground surfaces where it is difficult to embed vertical 3C sensors so they have good sensor-to-Earth coupling.

In the majority of seismic data-acquisition programs, there is no particular advantage to which type of sensor—3C geophone or 3C accelerometer—is used to acquire multicomponent seismic data.

Recording system comparisons

We were surprised to see P and S wave modes acquired with a cable-based data-acquisition system had broader frequency spectra than data acquired with cable-free systems. The increase in higher-frequency content is significant, being of the order of 20-percent or more, depending on which wave mode is considered. These test results warrant more study. More comparisons of data acquired with cable-based systems and with cable-free systems will be done in future projects.

Chapter 7

Multicomponent Seismic Data Acquisition

Introduction

Multicomponent seismic data were the essential part of the research database needed for this study. Numerous attributes of seismic data, and particularly attributes of multicomponent seismic data, are affected by the source-receiver geometry that is deployed across a survey area and the field procedures that are used to acquire the data. Specifically, an acquisition geometry should create adequate stacking folds not only for common-midpoint (CMP) P-P and S-S data but also for common-conversion point (CCP) P-SV and SV-P data. In addition, a seismic data-acquisition geometry must create a full range of source-to-receiver offsets and azimuths for all P and S wave modes. Full-offset and full-azimuth data are particularly important if fracture intervals are to be detected and quantified, or if stress fields and geomechanical rock properties are to be analyzed.

This chapter describes how the 3D P and S seismic data used in this study were acquired and illustrates stacking-fold magnitudes, offset distributions, azimuth dependence, and other multicomponent seismic data properties that influence rock and fluid information extracted from P and S wave modes.

Survey Design

The 3D multicomponent seismic survey that was to be implemented in this research was intended to be an orthogonal brick pattern in which 13 receiver lines spaced 880 ft (268 m) apart were deployed northwest-to-southeast to form a 2 mi × 2 mi (3.2 km × 3.2 km) square of 3C geophone stations, with 97 receiver stations spaced at intervals of 110 ft (33.5 m) along each receiver line. The total number of planned receiver stations was 1261. This receiver grid was to be positioned in the center of a 5 mi × 5 mi (8 km × 8 km) square array of source stations arranged in a southwest-to-northeast brick pattern in which 41 source lines were spaced 660 ft (201 m) apart. Each source line consisted of a sequence of four source stations spaced at intervals of 220 ft (67 m) with a gap of 880 ft (268 m) between successive 4-station groups. This source-station pattern created 60 source stations per line, with a total of 2460 source points across the survey area. Each source involved a 1-kg (2.2 lbs) explosive positioned at a depth of 6 m (20 ft). This presurvey design geometry is illustrated on Figure 7.1a.

Presurvey geometry can rarely be implemented in practice because numerous constraints exist that prohibit source and receiver stations being positioned at regularly spaced intervals. Among these constraints are pipelines,

(a)

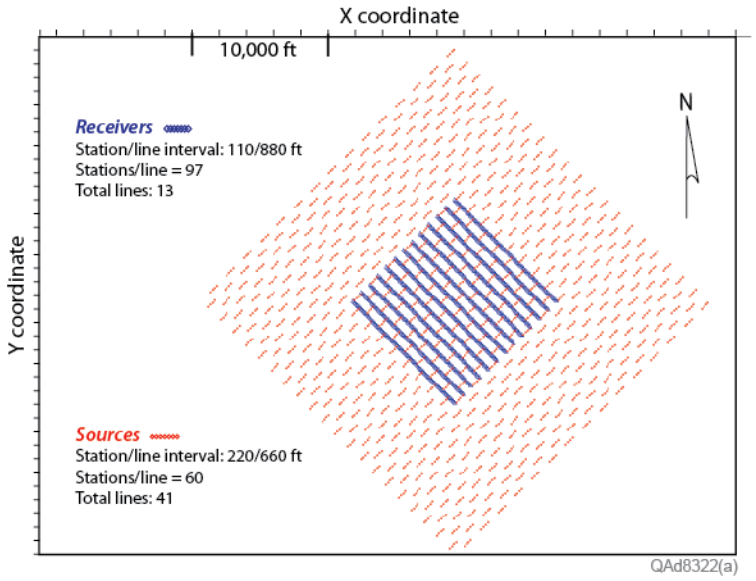

(b)

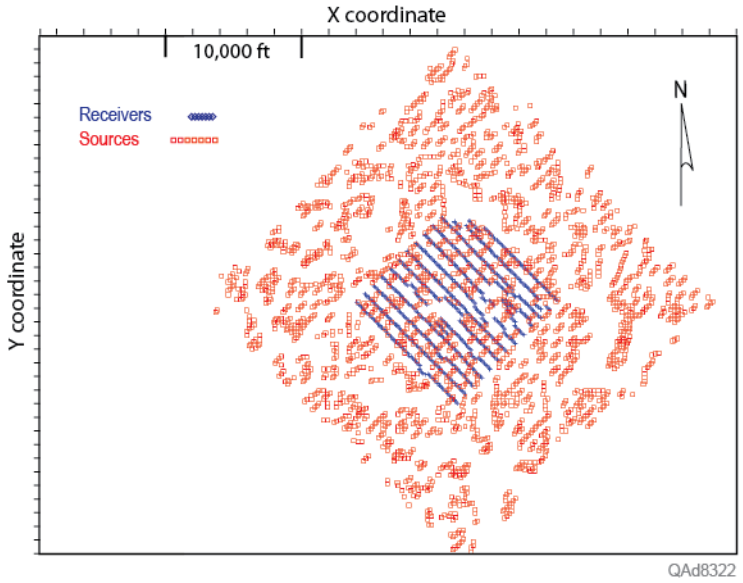

Figure 7.1. (a) Presurvey design that was intended to be used to acquire the 3C3D seismic data for this study. The objective was to deploy source and receiver stations as a uniform, regular geometry in which there were consistent distances and azimuths between source-receiver lines and stations. Source and receiver line spacings and station spacings are labeled on the plot. (b) Postsurvey geometry that was actually implemented. Source station positions were not at regular intervals. Although receiver stations were positioned with some degree of regularity, distances and azimuths between source-receiver station pairs were irregular and random.

electrical power lines, water wells, roads, buildings, agricultural crops, streams, marshes, dense forests, impassable topography, and an endless list of similar barriers. Topography, streams, and timber were principal barriers across our study site. As a result of surface constraints, the actual source and receiver station geometry that was implemented (Fig. 7.1b) differed from the presurvey design. The number of actual source stations was 2350, not the planned number of 2460. The number of receiver stations that were deployed was 1225, not the planned number of 1261.

Two adjectives are used by geophysicists to describe the basic properties of the presurvey and postsurvey source-receiver geometries illustrated on Figure 7.1. Because of the consistent distances and azimuths between source/receiver lines and stations, the presurvey geometry (Fig. 7.1a) is called a **regular geometry**. The postsurvey geometry (Fig. 7.1b) is referred to as a **random geometry**. There are advantages to introducing a modest amount of randomness into the positioning of source and receiver stations in a 3D seismic data-acquisition grid (Alkan, 2007; Alkan and Hardage, 2007). The amount of randomness exhibited by the actual source-receiver geometry used to acquire our multicomponent seismic research data created several attractive data properties, as will be shown.

Fold Attributes

Stacking fold is usually the first attribute of a 3D data-acquisition design that geophysicists examine to decide if the design is appropriate for imaging specific geologic targets. If adequate fold is not created by the source-receiver geometry utilized in the design, the quality of seismic images will not be adequate for many geologic applications. The magnitude of stacking fold that should be created across a particular prospect area is often not an easy decision to make. Proper stacking fold varies from prospect to prospect depending on the depth of the principal target that needs to be imaged, the strength of the energy source that is used, and the nature of the signal-to-noise ratio exhibited by propagating wave modes.

Two types of stacking fold were considered in this study: (1) common-midpoint (CMP) fold, and (2) common-conversion point (CCP) fold. CMP fold affects images made from wave modes that have the same propagation velocity on their downgoing and upgoing travel paths. CMP modes utilized in this study were P-P (pure compressional) data and S-S (pure shear) data. In contrast to CMP fold, CCP fold affects images made from wave modes that have a different propagation velocity on their downgoing travel path than they do on their upgoing travel path. CCP wave modes considered in the survey design analysis in this report involve P-SV data (downgoing P and upgoing converted-SV) and SV-P data (downgoing SV and upgoing converted-P).

CMP stacking folds are considered first. CMP folds created by the proposed regular-station geometry when offsets are restricted to 5,000 ft

(1,524 m), 10,000 ft (3,048 m), 15,000 ft (4,572 m), and 26,000 ft (7,925 m) are shown in Figure 7.2. CMP folds created by the implemented random-station geometry for these same offset conditions are presented as Figure 7.3. Folds associated with these four offset ranges are important because they represent CMP stacking folds expected for target depths of 2,500 ft (762 m), 5,000 ft (1,524 m), 7,500 ft (2,286 m), and 13,000 ft (3,962 m), respectively, based on the principle that a target at depth H is appropriately imaged using source-receiver

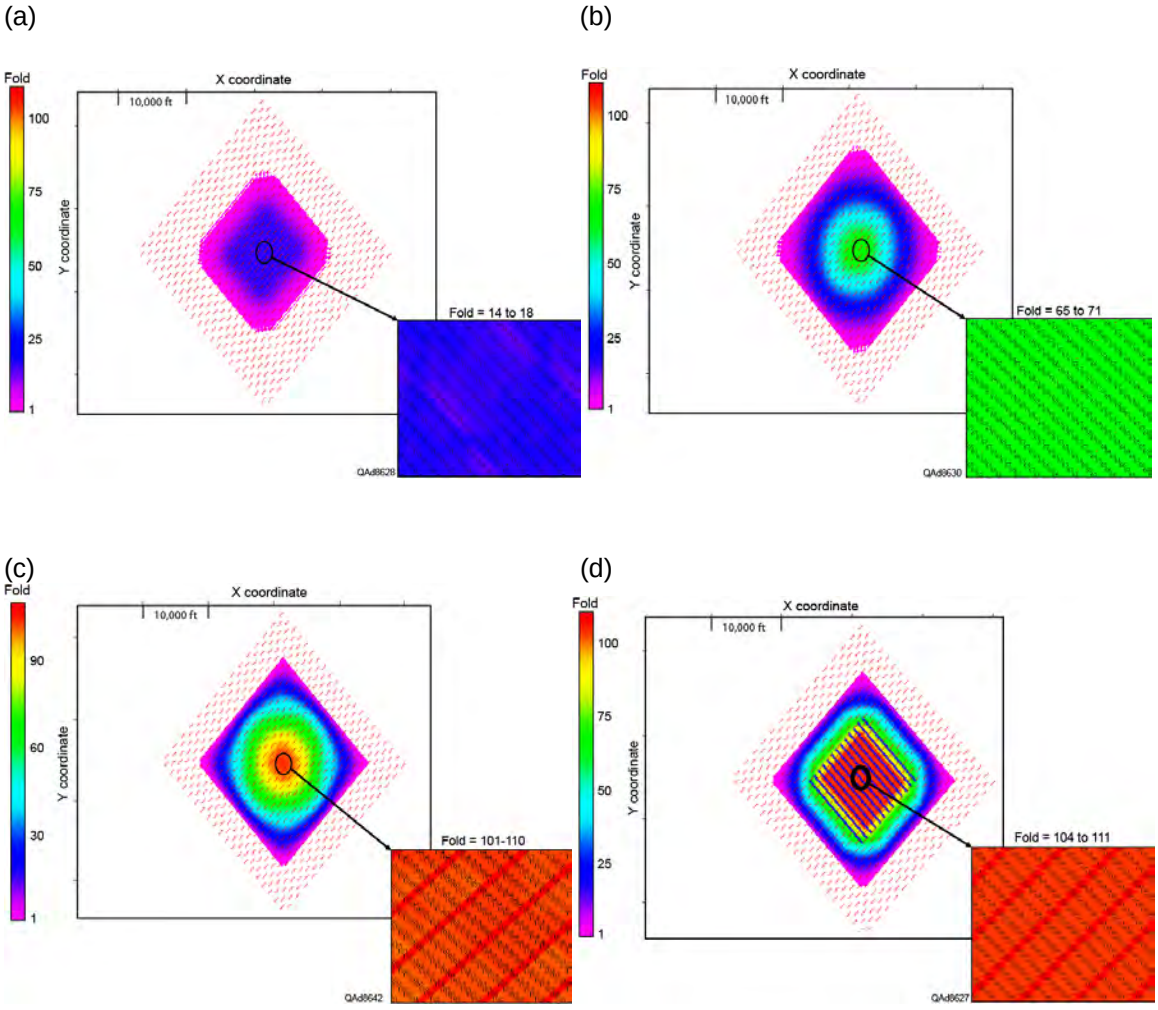

Figure 7.2. Stacking fold for P-P and S-S CMP modes that would have occurred if the presurvey source-receiver geometry could have been implemented. (a) CMP fold when source-to-receiver offsets do not exceed 5,000 ft (1,524 m). (b) CMP fold when source-to-receiver offsets do not exceed 10,000 ft (3,048 m). (c) CMP fold when source-to-receiver offsets do not exceed 15,000 ft (4,572 m). (d) CMP fold when all source-to-receiver offsets are used, an offset range extending to 26,000 ft (7,925 m).

offsets that range from 0 to 2H. Targets of interest in this study (Marcellus Shale, Utica Shale, and numerous porous sandstones and carbonates that could be water-storage reservoirs) are positioned over a depth range of 3,000 to 13,000 ft (914 to 3,962 m). Seismic basement is thought to be approximately 13,000 ft (3,960 m) deep across our study area.

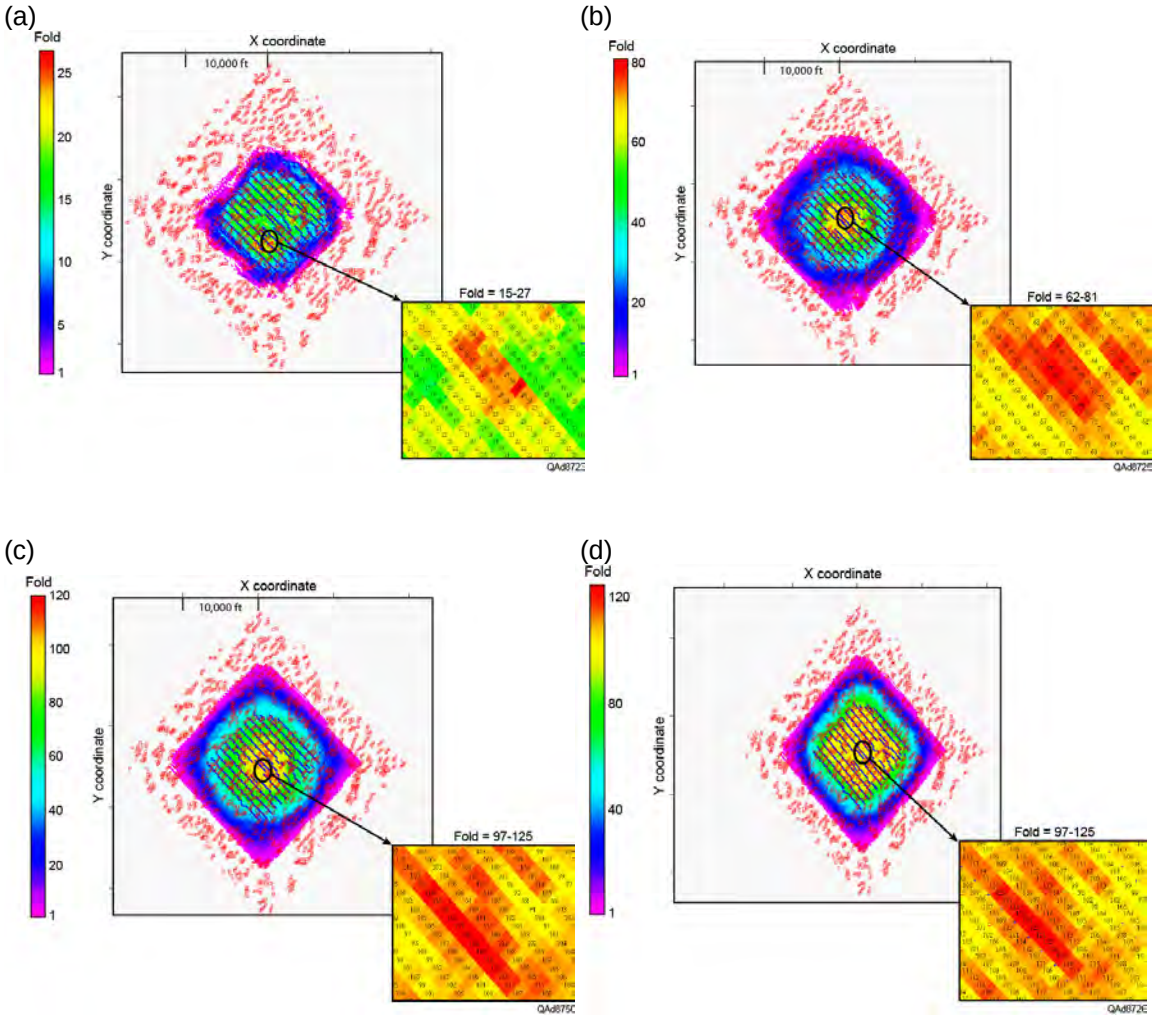

Figure 7.3. Stacking fold for P-P and S-S CMP modes when the actual postsurvey source-receiver geometry was implemented. (a) CMP fold when source-to-receiver offsets do not exceed 5,000 ft (1,524 m). (b) CMP fold when source-to-receiver offsets do not exceed 10,000 ft (3,048 m). (c) CMP fold when source-to-receiver offsets do not exceed 15,000 ft (4,572 m). (d) CMP fold when all source-to-receiver offsets are used, an offset range extending to 26,000 ft (7,925 m).

CCP stacking folds created by the two survey designs are presented as Figures 7.4 (regular geometry) and Figure 7.5 (random geometry). These displays are fold maps for the P-SV converted shear mode that is commonly utilized when 3C3D data are acquired. CCP fold patterns are controlled by the

V_P/V_S velocity ratio of the propagation medium, and fold maps change when the magnitude of a V_P/V_S ratio varies by only small amounts of ±0.1 or ±0.2. Examination of dipole sonic log data acquired in the calibration well at the center of the seismic image space (Figs. 4.1 and 4.7) suggested a V_P/V_S value of 1.6 to 1.7 should be appropriate for much of the stratigraphic depth of interest. A velocity ratio of 1.6 was used for the CCP fold calculations shown on Figures 7.4 and 7.5.

Because a single value of V_P/V_S is used for the entire propagation paths that downgoing and upgoing modes traverse in these CCP fold calculations, the fold patterns and magnitudes shown on the maps are those associated with **asymptotic bins**, which are deep bins in CCP image space (Hardage et al., 2011). Even though the fold calculations do not apply to shallow targets, they are still valuable for selecting a data-acquisition geometry that produces appropriate CCP stacking fold at critical target depths. During data processing, data-dependent V_P/V_S velocity ratios that vary as a function of image time (vertically) and X-Y image coordinates (laterally) are calculated at several locations across seismic image space. These spatially and dynamically varying V_P/V_S functions allow accurate stacking of CCP data to be done throughout the entirety of 3D image space. As a result, the asymptotic-bin approximation used in survey design is abandoned when CCP data are converted to images, and true CCP binning is used to create P-SV images. In summary, asymptotic-bin fold calculations are useful for evaluating a data-acquisition design but have little value in seismic data processing or interpretation.

Part of our research focus was to illustrate that an additional CCP mode—the SV-P mode—can be used for shale-gas exploitation. To date, SV-P data have not been utilized by geophysicists. This mode is the inverse of the popular P-SV mode presented on Figures 7.4 and 7.5. A P-SV mode involves a downgoing P mode and an upgoing SV mode. In contrast, an SV-P mode involves a downgoing SV mode and an upgoing P mode. SV-P fold maps produced by the two data-acquisition geometries are displayed on Figure 7.6 (regular geometry) and Figure 7.7 (random geometry). As was the case for P-SV fold calculations, a V_P/V_S velocity ratio of 1.6 is assumed for the entire thickness of the propagation medium, and the SV-P stacking fold conditions shown on the figures are those associated with asymptotic bins.

Several seismic imaging principles are revealed when comparing stacking-fold maps shown on Figures 7.2 through 7.7.

1. CCP fold is more erratic than CMP fold. Some of the oscillating behavior of CCP fold is caused by forcing the fold to be asymptotic-bin fold and by not using optimal values of V_P/V_S for calculating CCP coordinates. However, even if spatially varying and time varying V_P/V_S ratios were used, CCP fold would still not be expected to be as smooth and uniform as CMP fold across seismic image space.

2. For the data-acquisition geometry used to acquire these 3C3D data, where the source-station area is larger than the receiver-station area, SV-P data produce images that span a larger portion of XY coordinate space than do P-SV data. If source stations and receiver stations were exchanged, the opposite would be true, and P-SV data would span a larger area than SV-P data.

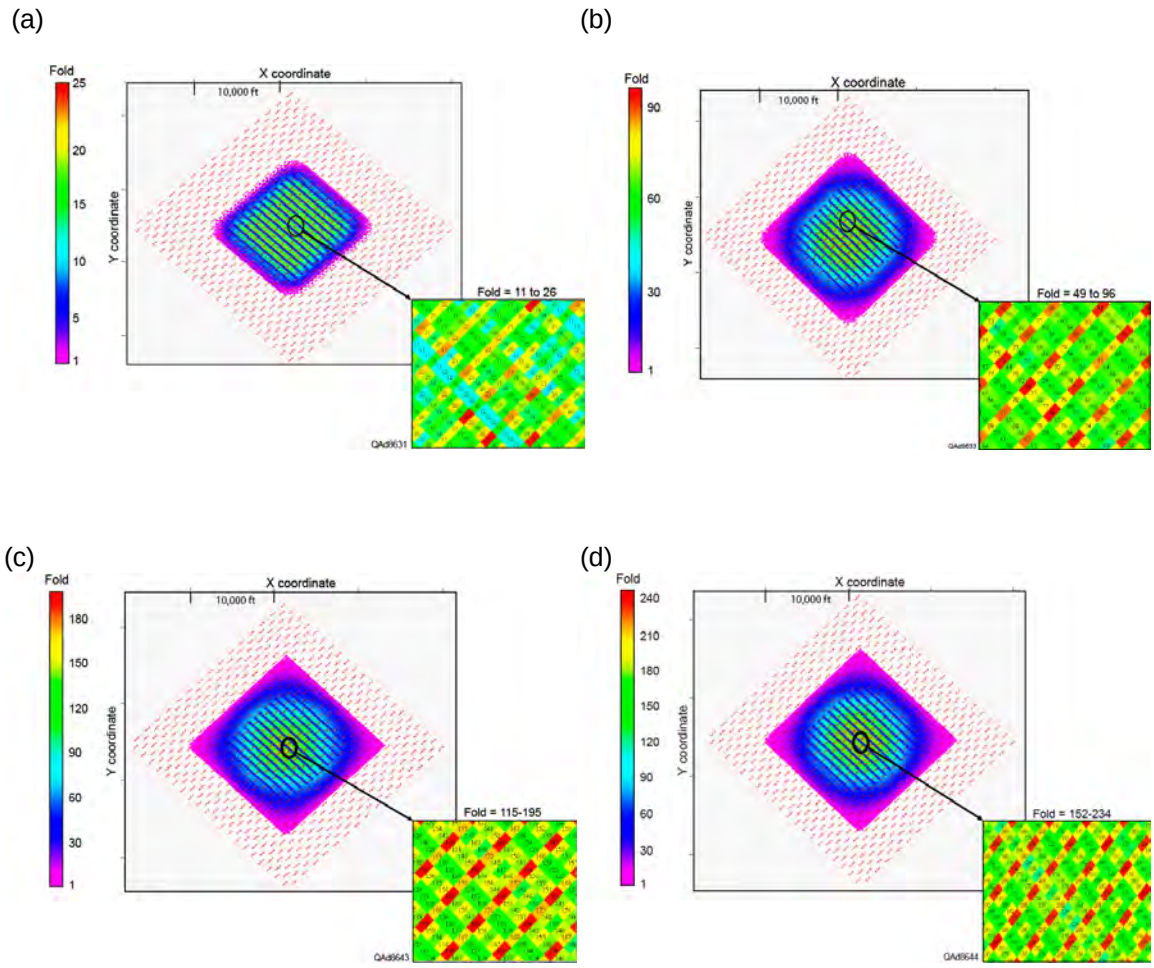

Figure 7.4. Stacking fold for CCP P-SV modes that would have occurred if the presurvey source-receiver geometry could have been implemented. (a) CCP fold when source-to-receiver offsets do not exceed 5,000 ft (1,524 m). (b) CCP fold when source-to-receiver offsets do not exceed 10,000 ft (3,048 m). (c) CCP fold when source-to-receiver offsets do not exceed 15,000 ft (4,572 m). (d) CCP fold when source-to-receiver offsets are extended to 26,000 ft (7925 m). The stacking bin properties shown are those associated with asymptotic bins.

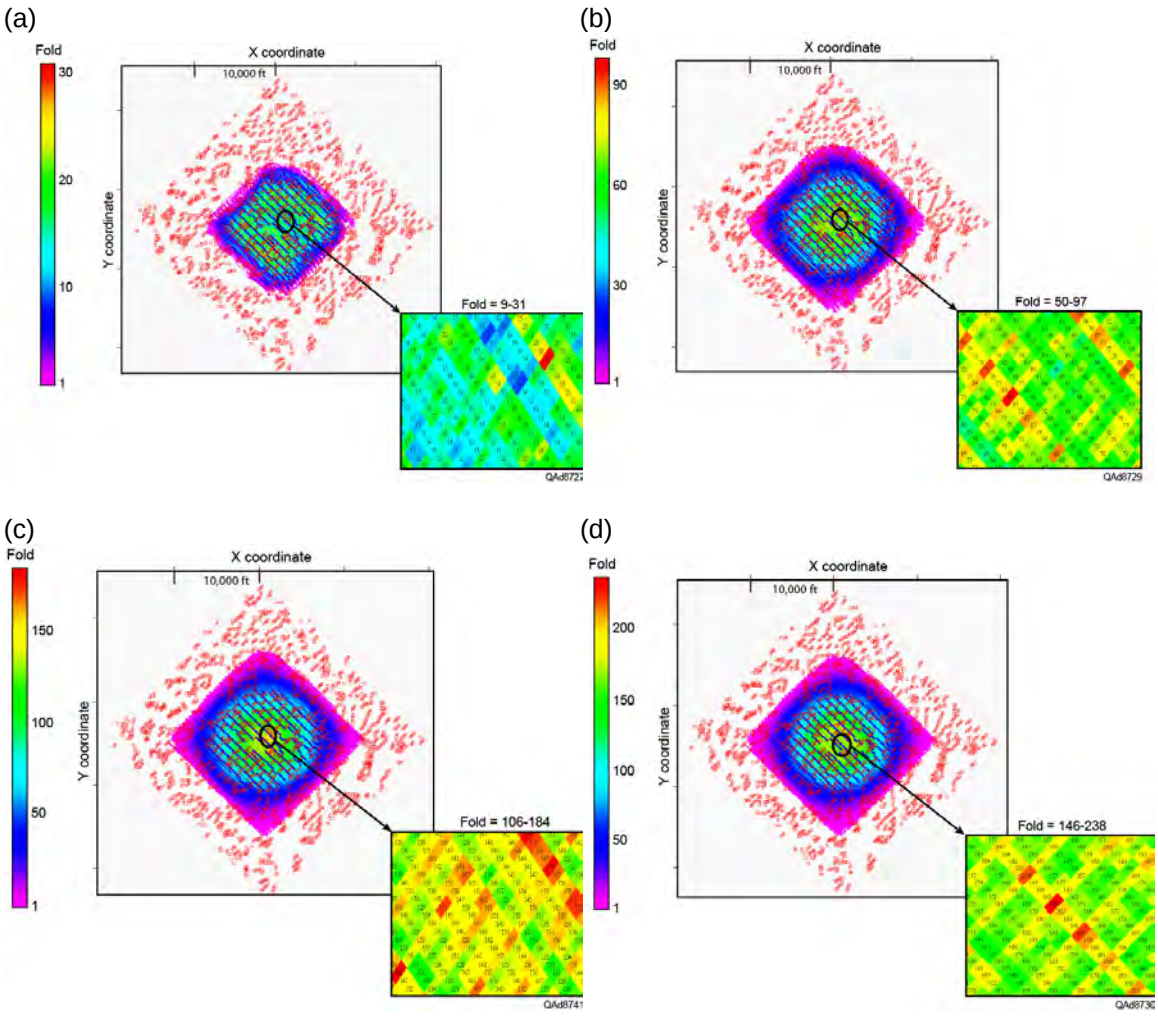

Figure 7.5. Stacking fold for CCP P-SV modes when the actual postsurvey source-receiver geometry was implemented. (a) CCP fold when source-to-receiver offsets do not exceed 5,000 ft (1,524 m). (b) CCP fold when source-to-receiver offsets do not exceed 10,000 ft (3,048 m). (c) CCP fold when source-to-receiver offsets do not exceed 15,000 ft (4,572 m). (d) CCP fold when source-to-receiver offsets are extended to 26,000 ft (7,925 m). The stacking bin properties shown are those associated with asymptotic bins.

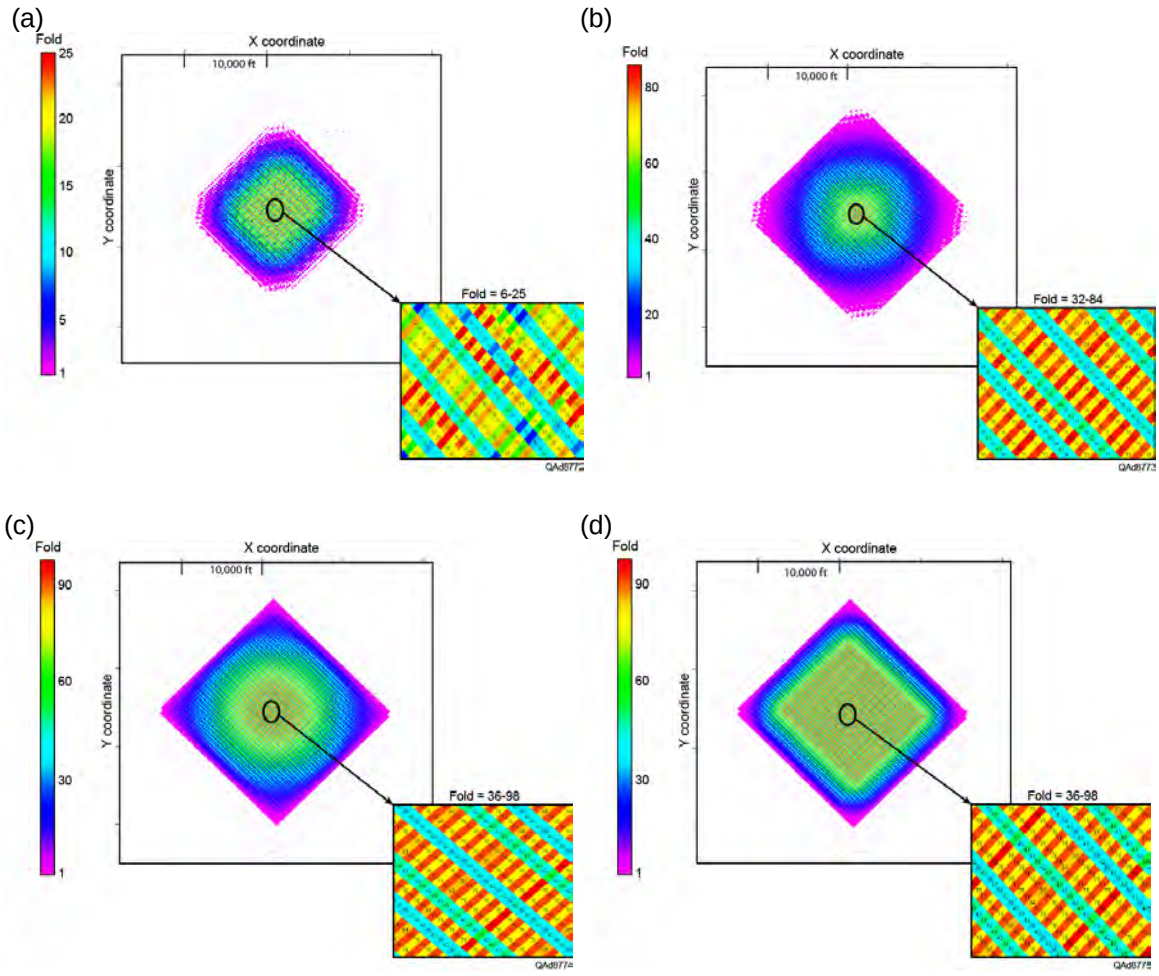

Figure 7.6. Stacking fold for CCP SV-P modes that would have occurred if the presurvey source-receiver geometry could have been implemented. (a) CCP fold when source-to-receiver offsets do not exceed 5,000 ft (1,524 m). (b) CCP fold when source-to-receiver offsets do not exceed 10,000 ft (3,048 m). (c) CCP fold when source-to-receiver offsets do not exceed 15,000 ft (4,572 m). (d) CCP fold when source-to-receiver offsets are extended to 26,000 ft (7,925 m). The stacking bin properties shown are those associated with asymptotic bins.

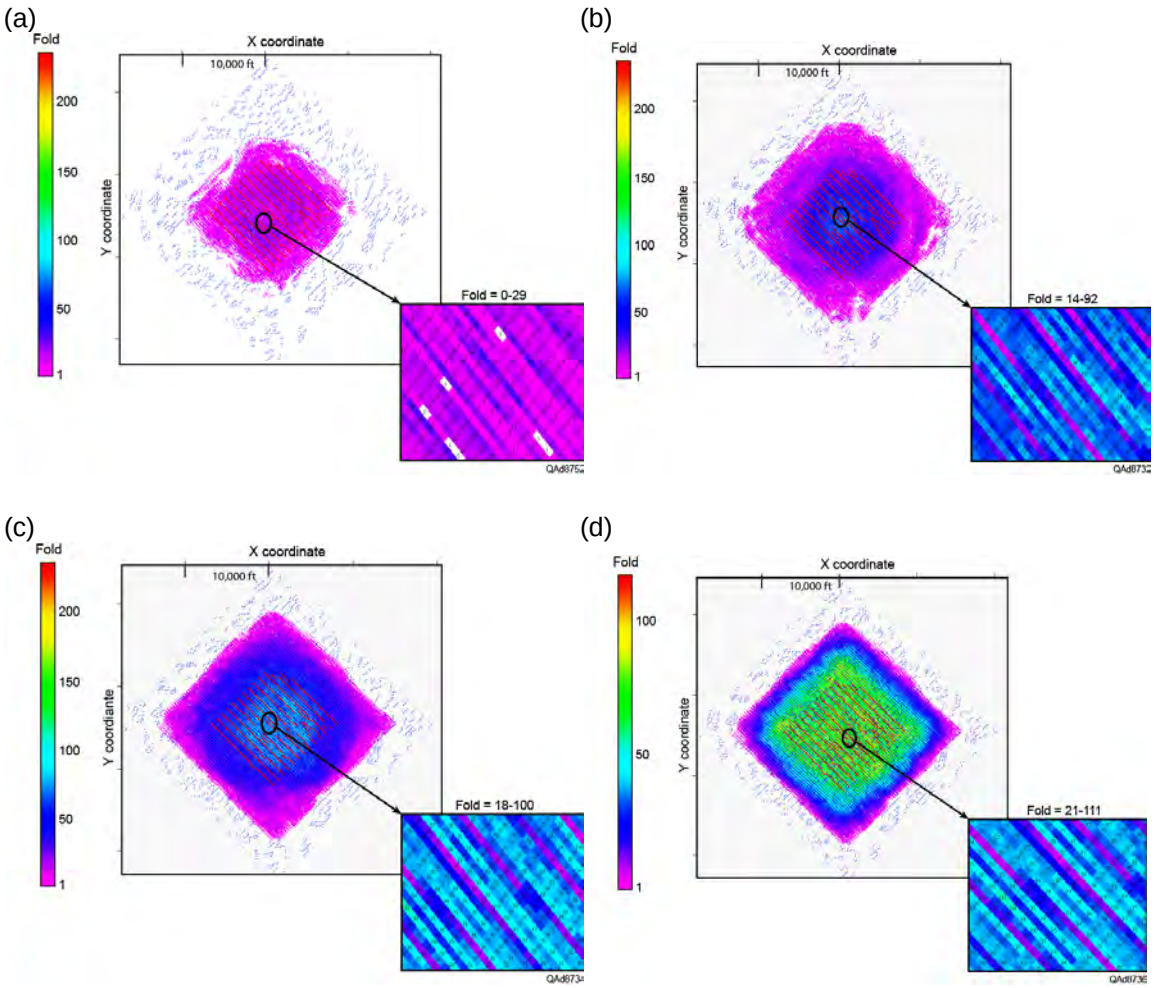

Figure 7.7. Stacking fold for CCP SV-P modes when the actual postsurvey source-receiver geometry was implemented. (a) CCP fold when source-to-receiver offsets do not exceed 5,000 ft (1,524 m). (b) CCP fold when source-to-receiver offsets do not exceed 10,000 ft (3,048 m). (c) CCP fold when source-to-receiver offsets do not exceed 15,000 ft (4,572 m). (d) CCP fold when source-to-receiver offsets are extended to 26,000 ft (7,925 m). The stacking bin properties shown are those associated with asymptotic bins.

Offset Attributes

Each data trace recorded during a 3D seismic survey involves a propagation path from a particular source station to a specific receiver station. The horizontal, straight-line distance between the source-receiver pair that generates a seismic data trace is referred to as source-receiver **offset**. To create the maximum amount of rock and fluid information in seismic data, it is important to construct trace gathers in every azimuth direction that have offsets that vary from near-zero to a value that equals or exceeds twice the depth of the deepest target that needs to be imaged. Such full-offset trace gathers allow wave mode reflectivities to be evaluated at targeted interfaces for wide ranges of incident

angles and permit wave-mode images to be made using traces having narrow incident-angle ranges to better emphasize selected rock/fluid conditions. The benefits are improved estimations of porosity, pore fluid type, mineral percentages, fracture properties, and other rock/fluid properties that affect angle-dependent wave mode reflectivity.

Optimal 3D seismic survey designs create smooth, continuous distributions of offsets in trace gathers created at critical image coordinates across seismic image space. In suboptimal surveys, trace gathers summed at image points have erratic offset distributions where there are large trace populations in a few narrow offset ranges and other offset ranges where there are no data traces. To show the influence of 3D survey design on source-receiver offsets, the offset distributions associated with the presurvey, regular-geometry design that was intended to be deployed across our study area is compared on Figure 7.8 with the offsets created by the postsurvey random geometry that was actually implemented.

Because of the compressed horizontal scale used in these plots, the line segments connecting adjacent data points are essentially vertical. Thus the vertical extent of each plot at each offset coordinate indicates how the number of data traces varies as offset distance increases from 0 to 26,000 ft (7,925 m). If plotted data have a large vertical dimension, the number of traces available for analysis and imaging behaves in an erratic manner between adjacent offset bins, with a small number of traces occurring at one offset increment and a large number of traces occurring in the adjacent offset increment. The result is a tall, quasi-vertical line connecting two different trace populations, a small population and a large population, in the plot scale used for Figure 7.8.

In contrast, if data span a small vertical plot dimension, there is a reasonably smooth distribution of data traces across source-receiver offset space, with small variations in trace populations in adjacent offset increments. Comparison of the data plotted on Figure 7.8 shows trace populations exhibit more erratic behavior when source and receiver stations have consistent, regular spacings (presurvey design) than they do when they are positioned so there is randomness in the distances and azimuths between station pairs (postsurvey design). This conclusion has been documented by Alkan (2007) and Alkan and Hardage (2007).

Note also that no data point of the offset distribution for the postsurvey random-station geometry drops to zero, which means data traces exist for every offset value. In contrast, many data points drop to zero, or near to zero, for the presurvey regular-geometry design, showing that no data traces are available for analysis for numerous offset values. A conclusion made from these plots is that randomness in station positions across a 3D seismic data-acquisition area is desirable and beneficial from the viewpoint of creating a smoother and more continuous distribution of source-to-receiver offset distances.

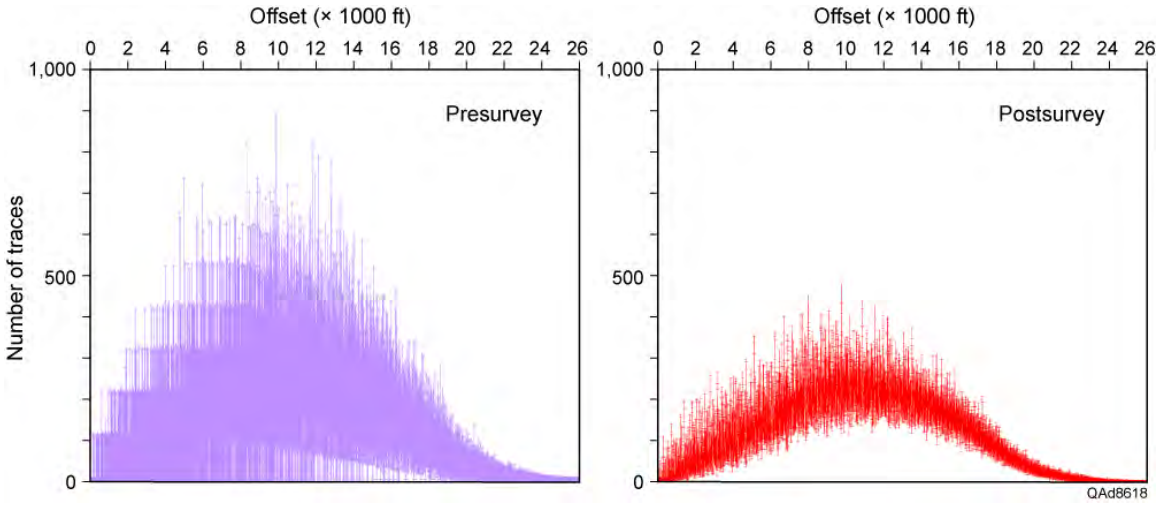

Figure 7.8. Distribution of source-receiver offsets for the presurvey, regular-geometry design (left) that was planned for deployment, and for the postsurvey, random-station geometry that was actually implemented (right).

Azimuth Attributes

Numerous seismic properties exhibit azimuth-dependent behavior. Of foremost importance is the possibility that seismic propagation velocities of P and S modes vary with azimuth. It is therefore important that a 3D seismic data-acquisition geometry be implemented that allows azimuth-dependent analysis of prestack seismic velocities and reflectivities to be done for all wave modes.

Azimuth relationships between all source-receiver pairs embedded in the two survey design options are compared on Figure 7.9. Both designs show essentially the same azimuth dependency for data traces recorded by the two source-receiver geometries. The curves on the figure are separated from each other vertically because the number of traces involved in the random-geometry data acquisition is less than the number of traces involved in the regular-geometry design. Examination of the source-receiver geometries displayed on Figure 7.1 verifies fewer source and receiver stations were used to record the data than were considered in the regular-geometry design. Thus fewer source-receiver pairs were available to generate independent data traces in the actual postsurvey random-geometry deployment.

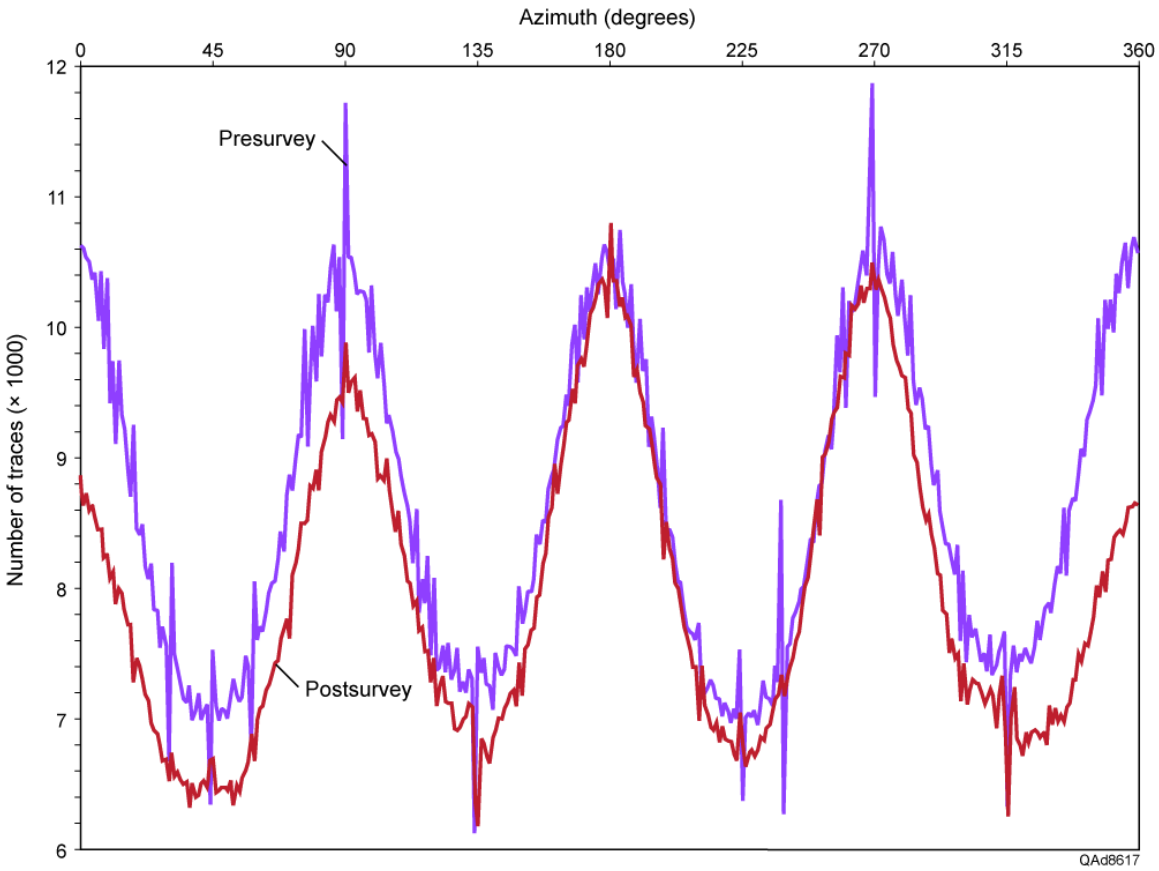

Figure 7.9. Relationship between number of data traces and the source-to-receiver azimuths that raypaths traveled to generate the traces. The random-geometry (postsurvey) curve (red curve) is lower magnitude because fewer source and receiver stations were used than were intended in the original regular-geometry (presurvey) design (blue curve).

Offset-Azimuth Maps

An informative way to display offset and azimuth properties related to seismic survey designs is a map format that shows offset behavior in all azimuth directions. Offset-azimuth attribute maps developed in this study are presented as Figure 7.10. These maps show how trace populations are distributed as a function of offset for narrow 10-degree azimuth corridors. Offsets are longer in north-south and east-west directions than in other azimuths because those directions are the diagonals of the square source-receiver grids (Fig. 7.1). Although the regular-geometry offset distribution shown on Figure 7.8 implies there are offsets that have zero trace populations, the distance and azimuth scales used on Figure 7.10 do not show these small areas of zero-trace occurrence. Every fifth circle is emphasized on the maps, and every tenth circle is labeled to allow quick recognition of offset distance in any azimuth direction. All distance labels have units of 1000-ft, thus “15” is equivalent to 15,000 ft.

An encouraging message provided by the map describing the offset-azimuth properties of the actual recorded data (Fig. 7.10b) is that there are full offset distributions in all azimuth directions. Thus the 3C3D data should be appropriate for prestack azimuth analysis of trace gathers to determine azimuth-dependent velocities and the existence of fast/slow S-wave modes.

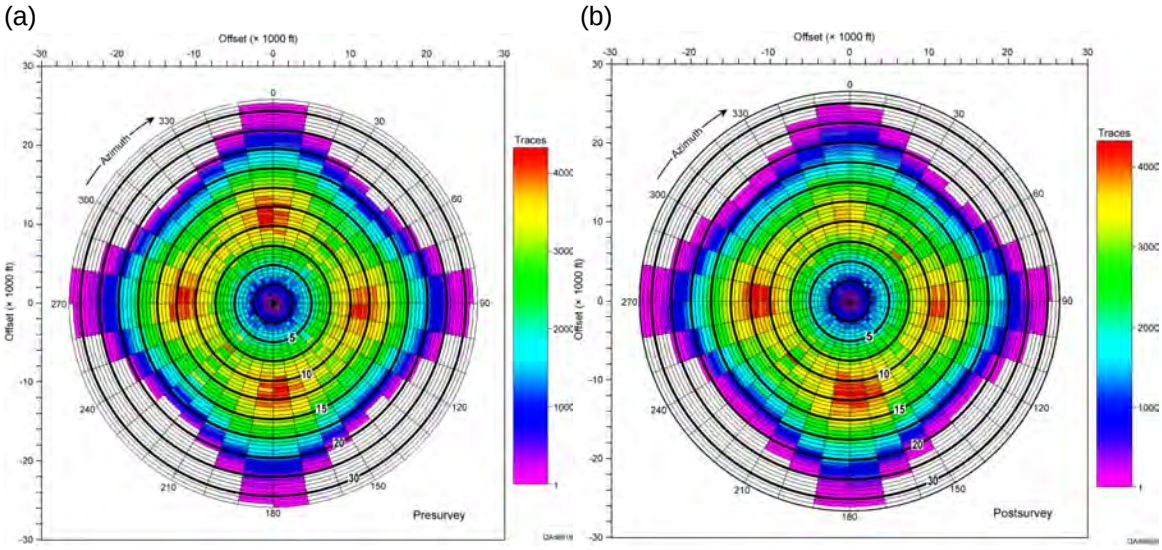

Figure 7.10. Maps of offset and azimuth attributes for (a) the intended regular-station geometry, and (b) the implemented random-station geometry. The numbered circles indicate offset distance in units of 1000-ft. Azimuth effects are shown in 10-degree corridors.

Conclusions

The uniform line spacing and uniform station spacing that was intended to be used to acquire 3C3D seismic data in Bradford County could not be implemented. Instead, surface constraints (rough topography, buildings, water wells, electrical lines, roads, agricultural activity, etc.) forced source stations to be positioned in a random pattern across the seismic grid. Several receiver stations also had to be positioned at irregular intervals. The end result was a postsurvey source-receiver geometry that differed significantly from the intended presurvey geometry. This outcome is typical of most land seismic surveys. Actual postsurvey distributions of sources and receivers are almost always different from what is assumed for station distributions when planning a 3D survey.

The randomness that local field conditions forced on the Bradford County seismic program had a positive influence on data quality, not a negative effect. A reasonable amount of randomness in positioning source and receiver stations in a 3D seismic program has minimal impact on stacking fold and results in smoother distributions of source-receiver offsets and azimuths. These smoother

offset/azimuth distributions tend to allow offset-dependent and azimuth-dependent seismic attributes to be more reliably extracted from P and S data, which is an important benefit for estimating rock and fluid properties with seismic data.

The seismic data-acquisition geometry used to acquire the Bradford County 3C3D data had an appropriate amount of randomness. As a result, the P and S modes embedded in the data are well suited for the research objectives of this study.

A unique objective of this study was to consider the SV-P converted mode, which seismic data processors have not attempted to do to date. Based on the numerical analysis presented in this chapter, fold maps calculated for the SV-P converted mode are more erratic than fold maps for the conventional P-SV converted mode. This erratic fold is a factor that requires careful attention during data processing if viable SV-P data are to be produced.

Chapter 8

Multicomponent Seismic Data Processing

Introduction

Many seismic data processors think the term “seismic image” should be used to describe only data that have been migrated. In this discussion, we will be more flexible in our terminology and use the word “image” to describe stacked, but unmigrated, data as well as migrated data. Stacked data are an image; the data are simply a distorted and inaccurate image until they are migrated.

Two different concepts have to be implemented to create stacked, unmigrated images of multicomponent seismic data. One concept is based on common-midpoint (CMP) imaging concepts. The second concept is based on common-conversion-point (CCP) imaging principles. CMP imaging applies when the propagation velocity of an upgoing wavefield reflecting from a geologic target is the same as the propagation velocity of the downgoing wavefield that illuminated the target. CMP data processing has been used for decades to image geology with single-component P-wave seismic data. CMP data-processing procedures can also be used to create SH-SH and SV-SV shear wave images when SH and SV shear modes are produced directly at a source station.

CCP data-processing procedures are used when the propagation velocity of an upgoing reflected wavefield differs from the propagation velocity of the downgoing wavefield that produced the reflected wavefield. The most common use of CCP data processing is to create converted-SV (or P-SV) images, a procedure which involves a downgoing P-wave mode and an upgoing SV mode. In this study, traditional CCP data processing was used to produce P-SV images. In theory, an altered form of CCP imaging can be used to create a converted-P (or SV-P) image when an SV mode is produced directly at a source station. SV-P data involve a downgoing SV illumination wavefield and an upgoing P reflected wavefield. In practice, no one has generated a SV-P image, or at least no such image has been shared with the geophysical community.

Seismic data can be migrated before or after stacking the data. Post-stack migration is more common than prestack migration because post-stack migration is a lower-cost procedure. However, prestack migration is more accurate than post-stack migration unless inaccurate or insufficient velocities are used by the migration algorithm.

Prestack migration can be done as either a time-based procedure or as a depth-based procedure. The cost of time-based prestack migration is becoming

more common as seismic data-processing groups expand computational capabilities. Depth-based migration is relatively expensive because it requires many hours for machine time to perform the calculations, and the procedure may have to be done several times to create an appropriate layered-Earth model with appropriate layer velocities. The multicomponent seismic data from Bradford County, Pennsylvania, used in this study were prestack time migrated.

Coordinate Data Spaces

Several different coordinate systems are used when processing multicomponent seismic data. Three coordinate systems that are utilized are shown on Figure 8.1. The map view on this figure shows a seismic source station and a receiver station positioned on the Earth's surface above a fracture system. When acquiring 3D multicomponent seismic data, a common practice is to deploy source lines orthogonal to receiver lines. An orthogonal source-line and receiver-line geometry was used to acquire the 3C3D seismic data used in this study, as discussed in Chapter 7.

In geophysical terminology, the direction in which receiver lines are deployed is called **inline**. The direction orthogonal to inline (usually the source line direction) is called **crossline**. The inline/crossline directions used on Figure 8.1 are indicated by axes with subscripts **i** (for inline) and **x** (for crossline). Together, these two axes—inline and crossline—define a seismic data-acquisition coordinate system. Axes and terminology other than orthogonal inline and crossline directions can be used to describe seismic data-acquisition geometry. For simplicity, inline and crossline terminology will be used to identify data-acquisition space in this discussion.

During seismic data processing, data are usually transformed to a second coordinate system referred to as **radial/transverse** data space. For the source-receiver pair drawn on Figure 8.1, this coordinate transformation is achieved by mathematically rotating inline and crossline axes by angle β so one axis is in the vertical plane passing through the source and receiver stations. The coordinate axis rotated into this vertical plane is the radial axis for this particular source-receiver pair. The axis normal to this vertical plane is the transverse axis for the same source-receiver pair. Angle β differs for each source-receiver pair and is calculated from GPS coordinates defining locations of source and receiver stations across a survey area. On Figure 8.1, radial and transverse axes are identified by axes labeled with subscripts **r** (for radial) and **t** (for transverse). Together, these two axes—radial and transverse—define a seismic data-processing coordinate system.

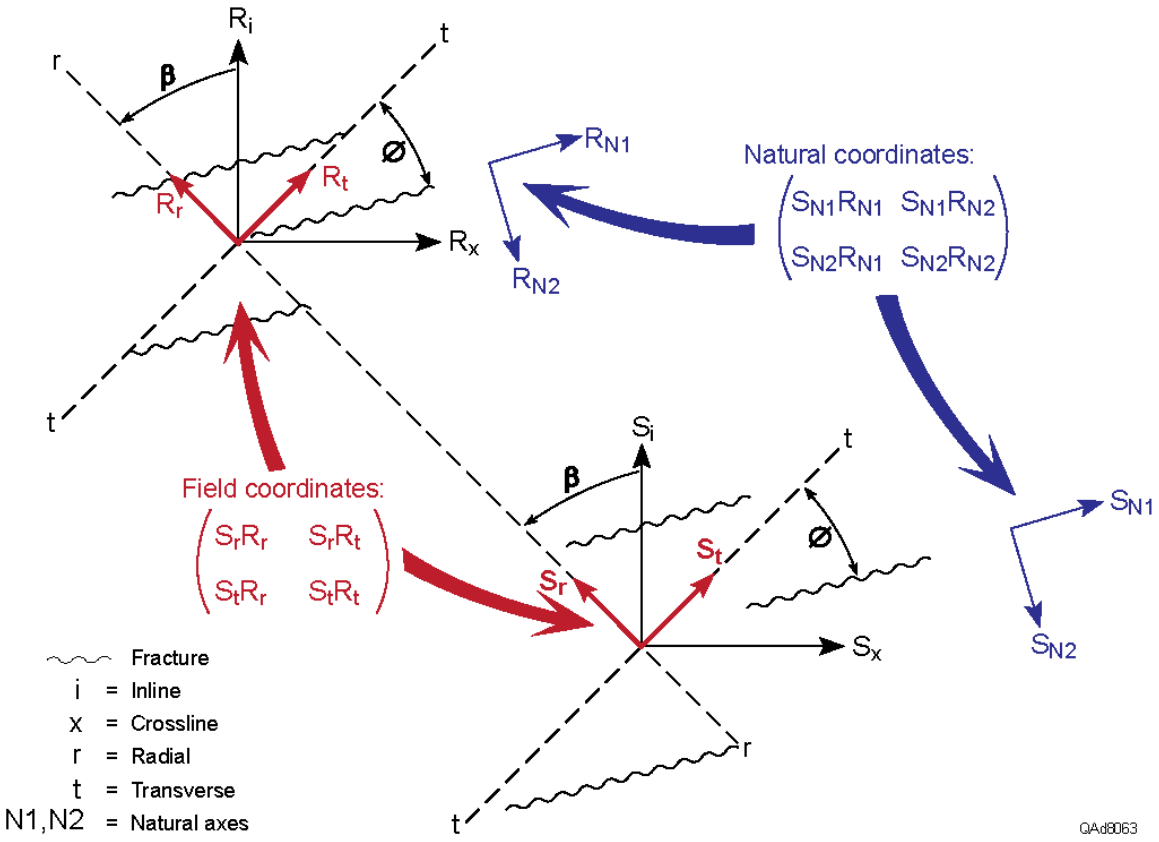

Figure 8.1. Vectors and quantities labeled **R** relate to a receiver station. Vectors and quantities labeled **S** relate to a source station. This map view illustrates three coordinate systems encountered when using multicomponent seismic technology to analyze fracture systems. The first coordinate system is an **inline** and **crossline** geometry used to deploy sources and receivers for data acquisition (subscripts **i** and **x**). The second coordinate system is a **radial-transverse** system created when processing data (subscripts **r** and **t**). The third coordinate system is the **natural coordinate** system that needs to be determined to interpret fracture properties (subscripts **N1** and **N2**).

The third coordinate system will be called **natural coordinates** in this report. Natural coordinates align with principal anisotropy axes of the Earth. For this reason, the axes are referred to as **principal axes** in some technical papers. For the fracture system depicted on Figure 8.1, the principal anisotropy within the Earth is a system of aligned fractures. The challenge of utilizing multicomponent data in fracture analysis is to rotate radial and transverse data-processing axes to natural coordinate axes. On Figure 8.1, natural coordinate axes and natural coordinate data terms are identified by subscripts **N1** and **N2**. Together, these two axes—natural coordinate axis N1 and natural coordinate axis N2—define a seismic data-interpretation coordinate system. The prestack converted-SV shot gathers that Geokinetics provided our research team were data that had been

rotated to natural coordinate data space appropriate for our study area in Bradford County, Pennsylvania.

Techniques used to determine the azimuths of natural coordinate axes depend on whether the azimuth of maximum horizontal stress σ_1 within the seismic propagation medium is known. There are several procedures by which the azimuth of maximum horizontal stress can be determined. For example, when wells are drilled in areas of horizontal stress, a cross-section through a well bore shows the hole is elliptical, not circular. The azimuths of the short axes of these elliptical cross-sections of stressed wells define the azimuth of σ_1. As a second procedure, when wells are hydrofractured, the direction in which the largest population of induced fractures is oriented is the direction of σ_1. A third procedure is to determine the azimuths of dilational fractures in borehole image logs. An interpretation of fracture distributions from a Marcellus borehole image log acquired inside the image space of the 3C3D seismic data used in this study is included in Chapter 9 to show one interpretation of σ_1 azimuth.

When the azimuth of σ_1 is known by one of these methods, or by an alternate technique, or simply by guessing, one natural coordinate axis is defined to have the same azimuth as σ_1, and the azimuth of the second natural coordinate axis is defined to be perpendicular to σ_1. Based on σ_1 azimuths known from Marcellus Shale drilling, the converted-SV shot gathers that Geokinetics provided our research team were rotated to natural coordinate axes determined to be approximately east-west and approximately north-south local to our study site in Bradford County, Pennsylvania. At the location of our study site, natural coordinate axis N1 (the polarization direction of the fast-S mode), as determined from an analysis of the horizontal-radial and horizontal-transverse geophone data, was oriented 80 degrees clockwise from North. Natural coordinate axis N2 (the polarization direction of the slow-S mode), as indicated by the seismic data, was oriented 170 degrees clockwise from North, perpendicular to the N1 axis. These natural-coordinate axis azimuths agree reasonably well with the log-based σ_1 azimuth information displayed in Chapter 9.

When the azimuth of σ_1 is not known, a popular procedure that allows natural coordinates axis azimuths to be determined is the Alford rotation procedure. Although Alford rotation was not used in this study, the technique is explained in the following section to make a complete documentation of natural coordinate analysis procedures.

Alford Rotation

The Alford rotation procedure for estimating the orientations of natural coordinate axes was described publically as an oral presentation at the 56th Annual Meeting of the Society of Exploration Geophysicists (SEG). The Expanded Abstract of that SEG presentation (Alford, 1986) is one of the more

widely cited references in geophysical literature. A detailed explanation of the logic and physics embedded in the coordinate transformation procedure was later published as U.S. Patent 4,817,061 (Alford et al., 1989).

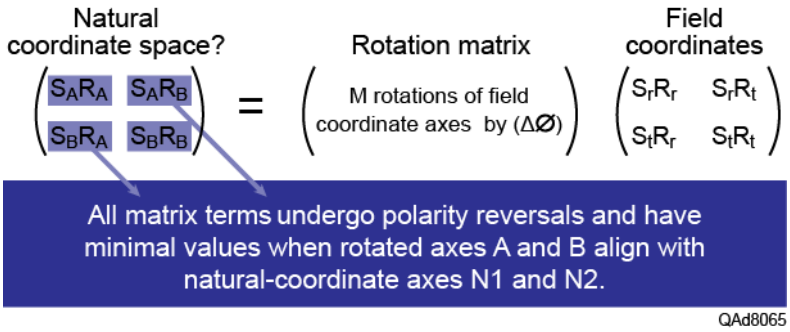

Figure 8.2. The Alford rotation procedure used to define natural coordinate data space. **S** is a source displacement vector; **R** is a receiver orientation vector. Subscripts **r** and **t** define radial/transverse coordinate space (or data-processing data space). Subscripts **A** and **B** define axes rotated from radial and transverse axes by azimuths that successively increase by small increments of Δθ. When this coordinate rotation aligns axes **A** and **B** with natural coordinate axes **N1** and **N2**, the terms in the left-hand-side matrix undergo polarity reversals and tend to assume minimal values. At this same azimuth, each diagonal term represents data propagating in one of the two natural coordinate directions.

Once a fracture target is illuminated with orthogonal S-wave displacement vectors, Alford rotation techniques can be used to estimate natural coordinate axes oriented parallel and orthogonal to fracture trends. The mathematics of Alford rotation is illustrated on Figures 8.2 and 8.3. The right-hand-side matrix of the equation displayed on these figures defines data components created by orthogonal S-wave source displacements and recorded by orthogonal S-wave sensors. Radial and transverse data (subscripts **r** and **t**) are used on Figures 8.2 and 8.3, but the calculation procedure can utilize inline and crossline data, or data defined by any orthogonal field-coordinate axes. The fundamental requirement for applying Alford rotation is that a fracture system be illuminated with orthogonal S-wave vectors and the Earth response be recorded with orthogonal S-wave sensor elements.

The target-illuminating data (right-hand-side matrix) are repeatedly transformed to a new coordinate system (left-hand-side matrix), in which axes are rotated in small azimuth increments of Δθ. This calculation is typically done over an azimuth range of 180° (or 360°) at increments of 1, 5, or 10° of azimuth, depending on the preferences of a data processor. For each new choice of azimuth, the left-hand-side matrix defines the azimuth orientation of a “possible” natural coordinate system having one axis parallel to a fracture trend and one axis orthogonal to that trend. If Δθ = 1°, these 180 (or 360) possible choices for the orientation of a natural coordinate system are analyzed to determine which azimuth value caused the terms of the left-hand-side matrix to undergo polarity

reversals. The rotation angle at which terms exhibit a phase reversal defines the azimuth of a natural coordinate axis. Often terms will also exhibit minima values in addition to phase reversals when a data-space rotation sweeps past a natural-coordinate axis azimuth.

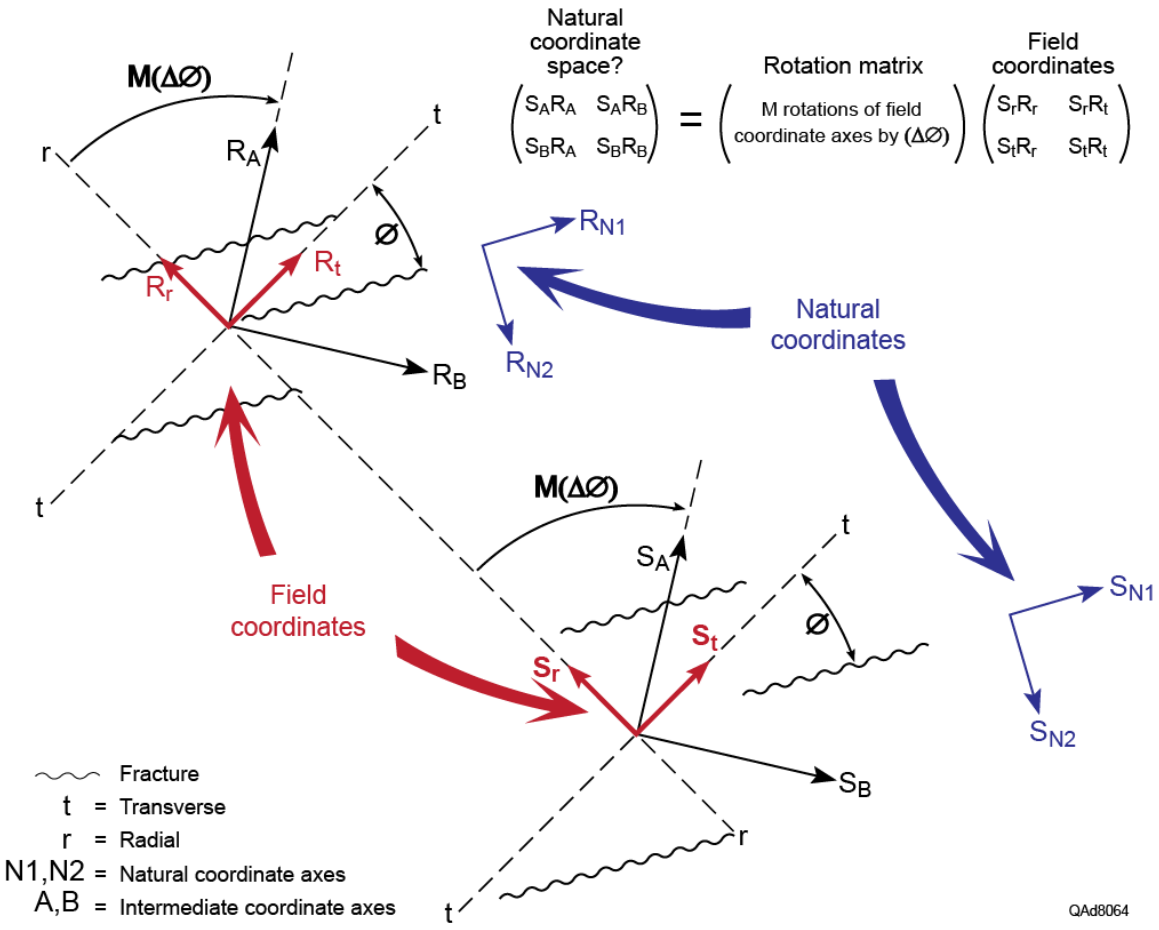

Figure 8.3. Graphical description of the Alford rotation procedure described on Figure 8.2. Axes with subscripts **A** and **B** have been rotated from radial/transverse axes by **M** increments of **Δθ**. At each new rotated coordinate position, the left-hand-side matrix is calculated and saved. When this calculation is done over an appropriate azimuth range, typically 180° (or 360°), these matrices are examined to find which azimuth rotation caused the terms of the matrix to undergo polarity reversals. When that polarity reversal occurs, axes **A** and **B** should be aligned with natural coordinate axes **N1** and **N2**, and matrix terms $\mathbf{S_AR_A}$ and $\mathbf{S_BR_B}$ define data propagating in the two natural coordinate axis directions. Quantities using label **R** are associated with a receiver station, and quantities labeled **S** are associated with a source station.

Some data processors prefer to produce Alford rotation results for a full 360° rotation rather than a half-circle rotation of 180° so that they see a second confirmation of the azimuths at which off-diagonal terms exhibit phase reversals. Either rotation angle range (360° or 180°) is sufficient, depending on a data processor's preference.

Imaging Strategies

The concept of **common-midpoint** imaging was developed in the 1950's to produce P-P stacked images of the Earth's subsurface. In a flat-layered Earth, when the velocity of the downgoing wavefield that illuminates a geologic target is the same as the velocity of the upgoing reflected wavefield from that target, as it is for P-P data, the reflection point (image point) is half way between the source and the receiver. Hence the terms "common midpoint" or "**CMP**" are used to describe this imaging concept.

When seismic images are made using a downgoing illuminating wavefield that has a velocity that differs from the velocity of the upgoing reflected wavefield, a different concept called **common-conversion-point** imaging is used to construct stacked images of geologic targets. The abbreviation "**CCP**" is used to indicate this seismic imaging strategy. CCP imaging techniques are required to construct stacked images from SV-P data because the downgoing SV mode has a velocity that differs from the velocity of the upgoing P mode.

CMP and CCP imaging raypaths are illustrated on Figure 8.4. In this example, P-P imaging (a CMP type of imaging) is compared with one type of CCP imaging – an image that involves the SV-P mode. Segments of downgoing and upgoing raypaths are labeled either P or SV to indicate the specific wave mode that travels along each segment of each raypath. Circled arrows on each raypath segment identify the direction in which the wave mode acting on that raypath segment displaces the Earth. The data polarities indicated by these particle displacement vectors agree with the polarity conventions defined by Aki and Richards (1980). The upgoing events that arrive at a receiver station are P-wave events for both P-P and SV-P modes.

The imaging principles of P-SV and SV-P modes illustrated on Figure 8.5 emphasize an SV-P mode images geology closer to a source station than to a receiver station. In contrast, a P-SV mode images geology closer to a receiver station than to a source station. For our Bradford County study area, receivers occupied an area smaller than did source stations (Fig. 7.1b). Although no SV-P data were extracted from the Bradford County 3C3D data by Geokinetics and Geopursuit, if such data had been processed, the image space covered by P-SV data (Fig.7.5) would have been smaller than the image space covered by SV-P data (Fig.7.7), as demonstrated on Figures 7.5 and 7.7 of Chapter 7.

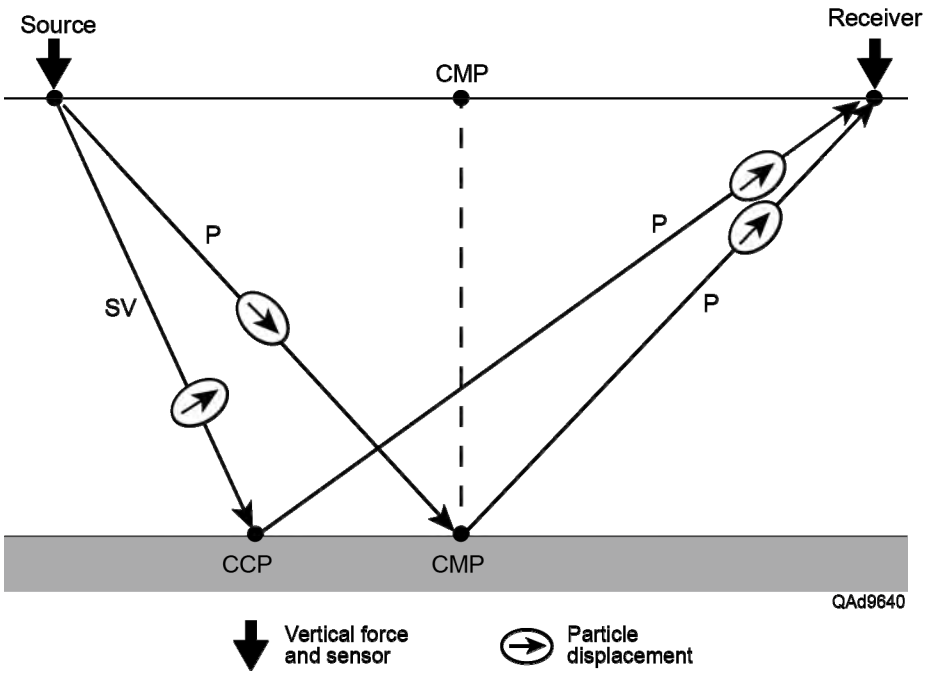

Figure 8.4. Comparison of P-P and SV-P imaging of subsurface geology. Point CMP is the common midpoint (image point) for P-P data for this source-receiver pair. Point CCP is the common-conversion point (image point) for SV-P data.

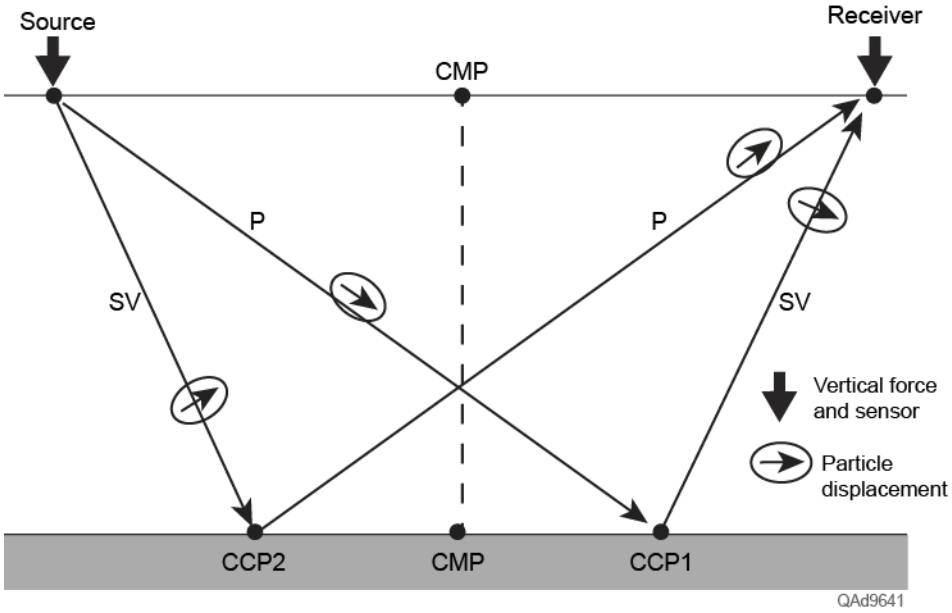

Figure 8.5. Comparison of P-SV and SV-P raypaths. The image points for these converted modes are common-conversion points CCP1 and CCP2. An image point for a P-SV mode (CCP1) is closer to the receiver station than to the source station. The image point for an SV-P mode (CCP2) is closer to the source station than to the receiver station.

Velocity Analysis

Velocity analysis is a crucial data-processing step when constructing seismic images. When CMP data are processed, it is not necessary to be concerned about which offset domain (positive or negative) data reside in when performing velocity analyses. If the velocities of downgoing and upgoing wave modes are the same (CMP data processing), the same velocity behavior occurs in both offset directions. However, when converted modes are involved, it is essential to do two velocity analyses—one analysis for positive-offset data and a second analysis for negative-offset data.

The reason for this dual-domain velocity analysis is illustrated on Figure 8.6 which shows two distinct rock facies between two surface-based source and receiver stations. Laterally varying rock conditions such as shown on this diagram are common across many depositional basins. In this diagram, SV-P data generated at Source A and recorded at Receiver A are labeled SV_A for the downgoing SV mode and P_A for the upgoing P mode. The offset direction from Source A to Receiver A is arbitrarily defined as **positive offset**. When the positions of source and receiver are exchanged, creating Source B and Receiver B, the offset direction reverses and is defined as **negative offset**. The raypath for negative-offset SV-P data is labeled SV_B for the downgoing SV mode and P_B for the upgoing P mode. The polarities shown for the downgoing SV particle-displacement vector conform to the polarity convention established by Aki and Richards (1980).

For purposes of illustration, assume the P and S velocities in Facies A are significantly different from the P and S velocities in Facies B. The travel time required for a positive-offset SV-P event to travel raypath SV_A-P_A is not the same as the traveltime for a negative-offset SV-P event to travel raypath SV_B-P_B. This difference in travel time occurs because the SV_A mode is totally in Facies A, but the SV_B mode is almost entirely in Facies B, Likewise, all of mode P_B is in Facies A, but mode P_A has significant travel paths inside both Facies A and Facies B. Because travel times differ in positive-offset and negative-offset directions, one velocity analysis has to be done on positive-offset data, and a separate velocity analysis has to be done for negative-offset data. This same requirement of dual-domain velocity analyses is known by people who process P-SV data, so the concept should not be considered as being novel to processing SV-P modes.

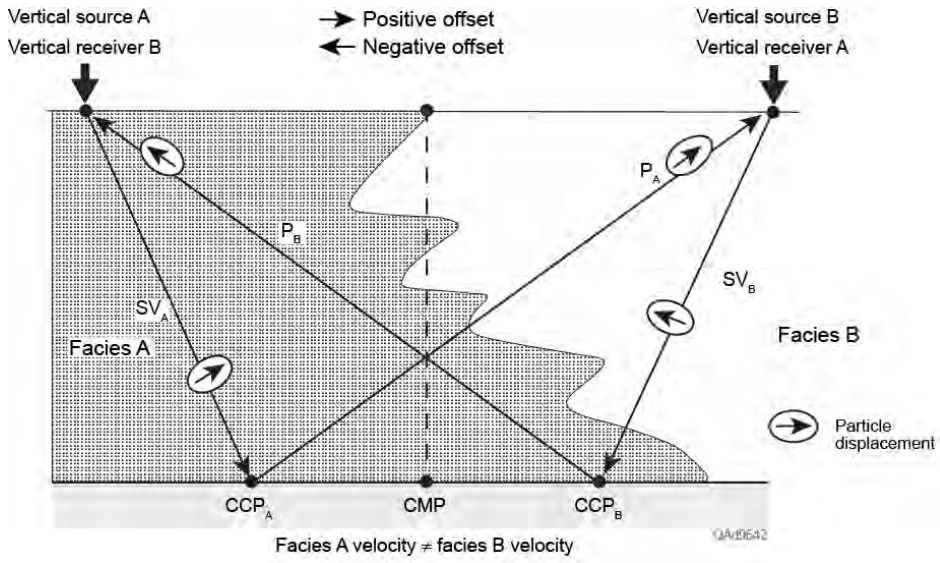

Figure 8.6. Positive-offset and negative-offset domains for SV-P data. V_P and V_S velocities in Facies A are different than they are in Facies B. Straight raypaths are drawn for simplicity.

Constructing Converted-Mode Images

Converted-mode imaging can be done in two ways: (1) by CCP binning and stacking of P-SV and SV-P reflections, followed by post-stack migration of the stacked data, or (2) by implementing prestack migration of SV-P and P-SV reflections. Method 2 (prestack migration) is the more rigorous approach, but method 1 (CCP binning/stacking and post-stack migration) is the more common strategy because of its lower cost. To perform CCP binning and migration of converted-mode data, it is important to note CCP coordinates of SV-P image points are mirror images of CCP image points associated with P-SV data, as illustrated on Figure 8.7.

Because positive-offset and negative-offset converted-mode data have different velocity behaviors, two separate CCP binning/stacking steps need to be done to create a converted-mode stacked image. In Step 1, positive-offset data are binned and stacked into an image using velocities determined from positive-offset data, and in Step 2, negative-offset data are binned and stacked into a second image using velocities determined from negative-offset data. The final image is the sum of these two opposing-offset images. This same dual-image strategy is implemented when binning and stacking P-SV data. All three stacked images should be migrated and used in geological applications. As documented by Hardage et al. (2011) relative to P-SV imaging, some geologic features are sometimes better seen in one of these three images than in its two companion images. Thus all three stacked and migrated images are used in geological interpretations.

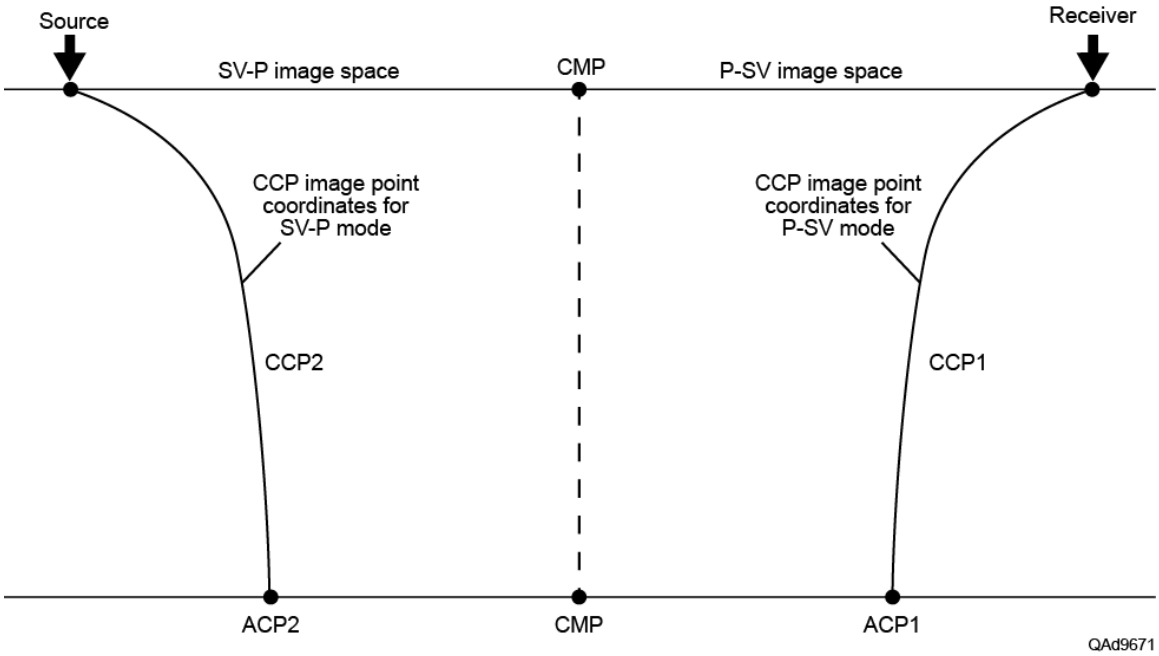

Figure 8.7. SV-P and P-SV CCP imaging principles. Curve CCP1 shows the trend of common-conversion points for P-SV data. Curve CCP2 shows the trend of common-conversion points for SV-P data. ACP1 and ACP2 are asymptotic conversion points for trends CCP1 and CCP2, respectively. CCP1 and CCP2 are mirror images of each other relative to the common midpoint CMP for this source-receiver pair.

Imaging Option 1 - CCP Binning, Stacking, and Post-Stack Migration

Regarding commercial seismic data-processing software that can be purchased or leased by the geophysical community, none of these software packages calculates true CCP image points. Instead, leased software calculates converted-mode image coordinates called **asymptotic conversion points**, which are abbreviated as **ACP.** An ACP is an image coordinate where the trend of correct CCP image points for a specific source-receiver pair becomes quasi-vertical (Fig. 8.7). Deep geology is correctly imaged using P-SV data binned by ACP principles, and would also be correctly imaged by SV-P data binned using ACP concepts that are adjusted for SV-P data. However, shallow geology is not correctly imaged for either P-SV data or SV-P data when ACP binning methods are used. Only true CCP binning produces correct stacked images of both shallow and deep geology for converted modes appropriate for post-stack migration. On Figure 8.7, the asymptotic conversion point for the P-SV mode is labeled ACP1, and the asymptotic conversion point for the SV-P mode is labeled ACP2. Neither image point is correct except where their associated CCP binning profile is quasi-vertical (i.e., for deep targets). As emphasized above, these two image points are mirror images of each other relative to the common midpoint (point CMP on Figure 8.7) for any source-receiver pair involved in a seismic survey.

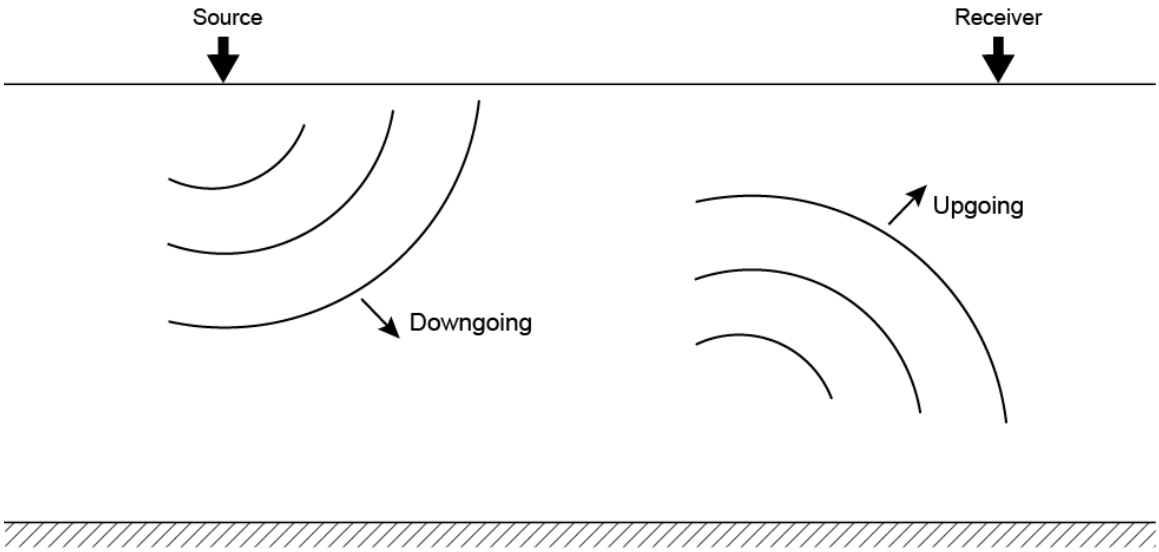

Option	Velocity of D	Velocity of U	Seismic image
1	V_P	V_P	P-P
2(1)	V_P	V_{SV}	P-SV
3	V_{SV}	V_P	SV-P
4(1)	V_{SV}	V_{SV}	SV-SV
5(2)	V_{SH}	V_{SH}	SH-SH

QAd9672

(1) Requires a high-velocity surface if vertical single-component geophones are used; otherwise requires 3C geophones.

(2) Always requires 3C geophones.

Figure 8.8. Simple illustration of prestack migration. A time-space distribution of velocities for a specific seismic mode is defined so that a specific downgoing wavefield (D) can be propagated through this Earth velocity model from every source station to illuminate targets. A second time-space distribution of velocities for a second specific seismic mode is then imposed to propagate that specific reflected upgoing wavefield (U) to every receiver station.

Imaging Option 2—Prestack Migration

Prestack migration can be done so as to create either a time-based seismic image or a depth-based seismic image. For convenience of discussion, this material will be limited to a brief description of prestack time migration of seismic data. Referring to Figure 8.8, prestack migration is done by numerically propagating a specific seismic wavefield downward from each source station to illuminate geologic targets, and then numerically propagating a specific seismic wavefield upward from reflecting interfaces to each receiver station.

The specific wavefields used in prestack migration are created by applying velocity filters so that reflection events having only a specific velocity behavior remain after velocity filtering. The specific velocity behaviors of interest are those associated with the following seismic modes: P-P, P-SV, SH-SH, SV-SV, and SV-P. The result is an image of geologic interfaces seen by each specific seismic mode. For simplicity, only one source station and only one receiver station are shown on Figure 8.8. The table on Figure 8.8 considers all possible wave modes produced by P and S sources and receivers. For an Earth with isotropic velocity layers, there are five possible combinations of downgoing (D) and upgoing (U) modes. These possibilities are labeled Option 1 through Option 5 in the figure table.

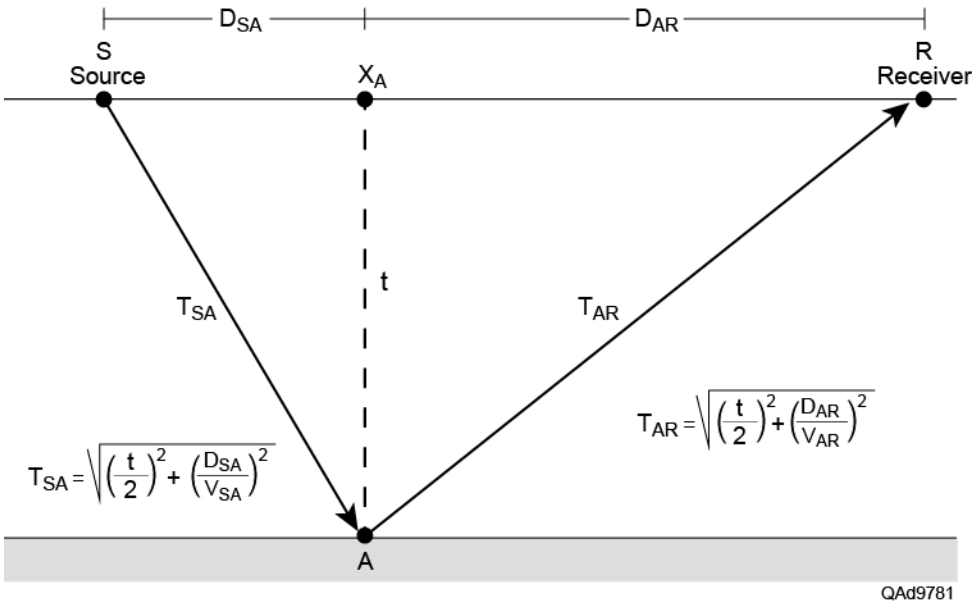

A = Image point
t = Image-trace time coordinate
X_A = Image trace coordinate
D_{SA} = Horizontal distance from S to A
D_{AR} = Horizontal distance from A to R
T_{SA} = One-way time from S to A
T_{AR} = One-way time from A to R
V_{SA} = RMS velocity for downgoing mode at (X_A, t)
V_{AR} = RMS velocity for upgoing mode at (X_A, t)
$T = T_{SA} + T_{AR}$ = Time coordinate of data sample placed at image coordinates (X_A, t)

Figure 8.9. The principles of prestack time migration. Every data point of every trace of every shot record is positioned in migrated image space using a double square-root calculation.

The raypath diagram drawn on Figure 8.9 shows how one data point from a single trace of a shot record is positioned in seismic image space. In this example, a migrated data trace is being created at image coordinate X_A, and the migration procedure has progressed downward to time coordinate t. In data-acquisition space, the space-time coordinates of the data point being migrated are R and T, respectively (see calculation step 1 on Figure 8.10). One square-root equation calculates downgoing travel time T_{SA}. A second square-root equation calculates upgoing travel time T_{AR}. These travel time calculations are functions of known coordinates D_{SA} and D_{AR} and require knowledge of the RMS velocities of the downgoing and upgoing wave modes that travel along the downgoing and upgoing raypaths. These RMS interval velocities are determined in a separate velocity analysis and preserved in a file that defines RMS velocity at all space-time coordinates of migrated image space. Because of the two square-root calculations required to position a data point in seismic image space, prestack time migration algorithms are referred to as **double square-root equations** in geophysical literature.

In prestack time migration, raypaths are assumed to be straight, whereas in prestack depth migration, raypaths refract and bend when they exit from one velocity layer and enter another layer. Inaccuracies involved in positioning a migrated image point that result because of this straight-raypath assumption are partially corrected by using accurate, detailed, time-varying, and space-varying interval velocities in the square-root calculations.

The data flow diagram on Figure 8.10 simplifies prestack time migration to a 5-step procedure. In step 1, a single trace generated by a source at coordinate S and recorded by a receiver at coordinate R is selected for migration. In step 2, a migrated data trace is being constructed at coordinate X_A between source coordinate S and receiver coordinate R. In step 3, the values of the RMS velocities of the downgoing and upgoing wave modes at space-time image coordinates (X_A, t) are read from velocity files. In step 4, the double square-root calculation is done to determine the time coordinate T of the data point from field trace R that needs to be positioned at image coordinates (X_A, t). In step 5, the data point at coordinates (R, T) in data-acquisition space is moved to coordinates (X_A, t) in migrated image space. Because this double square-root calculation has to be done for every data point of every trace of every shot record, the calculations are computer intensive and require several hours of clock time on multi-node computer clusters.

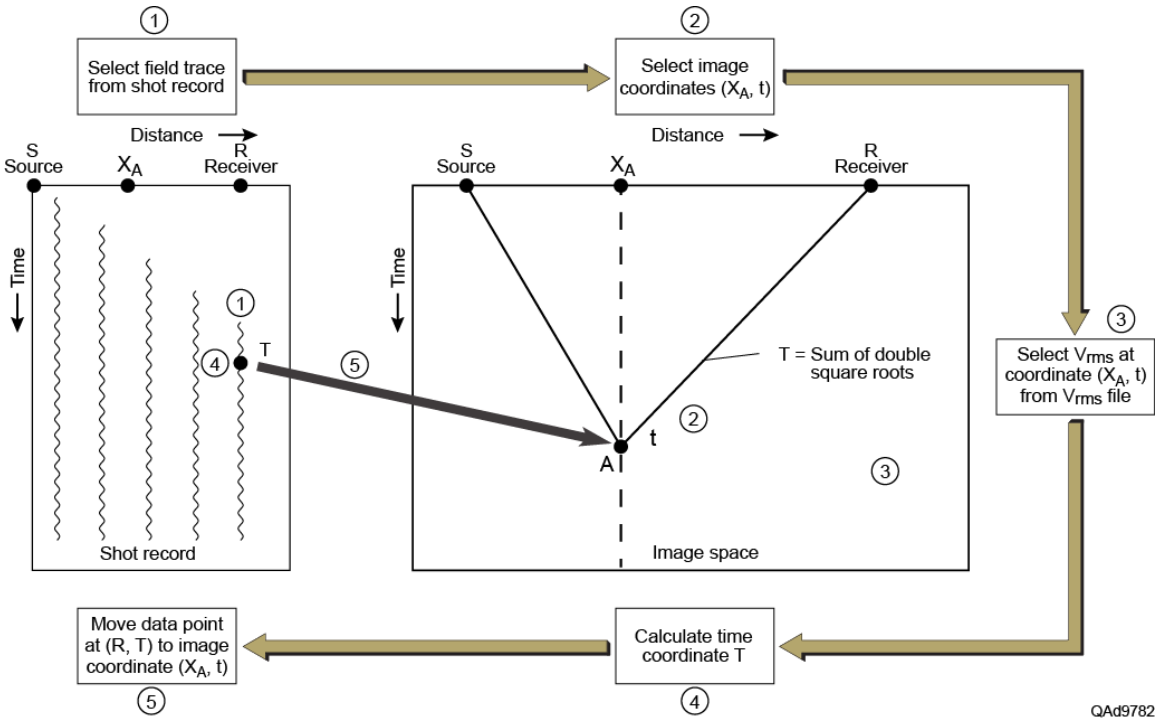

Figure 8.10. Simplifying prestack time migration to a 5-step calculation procedure.

Conclusions

Three seismic data volumes were generated by Geokinetics and provided to our research team. One volume, the P-P volume, was a CMP-based image. The other two volumes, a P-SV_1 volume and a P-SV_2 volume, were CCP-based images. All three volumes were generated using prestack time migration as the imaging algorithm. The P-SV_1 and P-SV_2 converted-SV images were rotated to natural-coordinate axes so that the P-SV_1 data were polarized in an azimuth of 80-degrees, which is the orientation of natural coordinate axis N1, and the P-SV_2 data were polarized in an azimuth of 170-degrees, the orientation of natural coordinate axis N2.

Chapter 9

Interpretation of Multicomponent Seismic Data

Introduction

The 3D multicomponent seismic data used in this study were acquired as multi-client lease data by industry partners Geophysical Pursuit and Geokinetics. Geokinetics processed the data to produce three time-migrated data volumes—a conventional P-wave volume, a fast-S converted-shear (P-SV_1) volume, and a slow-S converted-shear (P-SV_2) volume. Each data volume consisted of 30,448 data traces. Data traces were 4 seconds long. Image bin dimensions were 110-ft × 110-ft (33.5-m × 33.5-m). The seismic images spanned an area of approximately 23.8 km^2 (9.3 mi^2).

Important geologic calibration data were recorded in a well positioned at the center of the seismic image space spanned by the 3D data volumes. Vertical seismic profile (VSP) data acquired in this calibration well were invaluable for depth registering P and S seismic data. Additional calibration data acquired in this central-image well were a full suite of modern logs that provided rock and fluid properties needed for modeling P and S reflectivities. A log of particular value was the dipole-sonic log, which measured P, fast-S, and slow-S velocities, indicated fast-S and slow-S polarization azimuths, and estimated S-wave anisotropy. These dipole-sonic log data were used to generate P-wave and S-wave synthetic seismograms that aided depth registration of P and S data and identified key geologic targets in seismic images. As a result of having high-quality geologic calibration data, we achieved excellent time-to-depth correlations of geology with P-P, P-SV_1, and P-SV_2 images and developed confidence in the rock and fluid properties interpreted from seismic data.

Seismic Data Quality

Analysis of P-P, P-SV_1, and P-SV_2 data volumes showed S-wave data volumes were more distorted by migration irregularities along the edges of image space than was the P-wave volume. These S-wave migration artifacts produced greater structural dips, as well as more reflection smearing, than were present in the P-wave volume (Figs. 9.1a, 9.1b, 9.1c). All three data volumes had small blank-out areas inside the image space where landowners would not grant permission for their subsurface to be leased. To protect these no-permit areas, data across these no-lease properties were deleted from each data volume. To ensure these data gaps created no migration artifacts, data were deleted after, not before, wavefield migration.

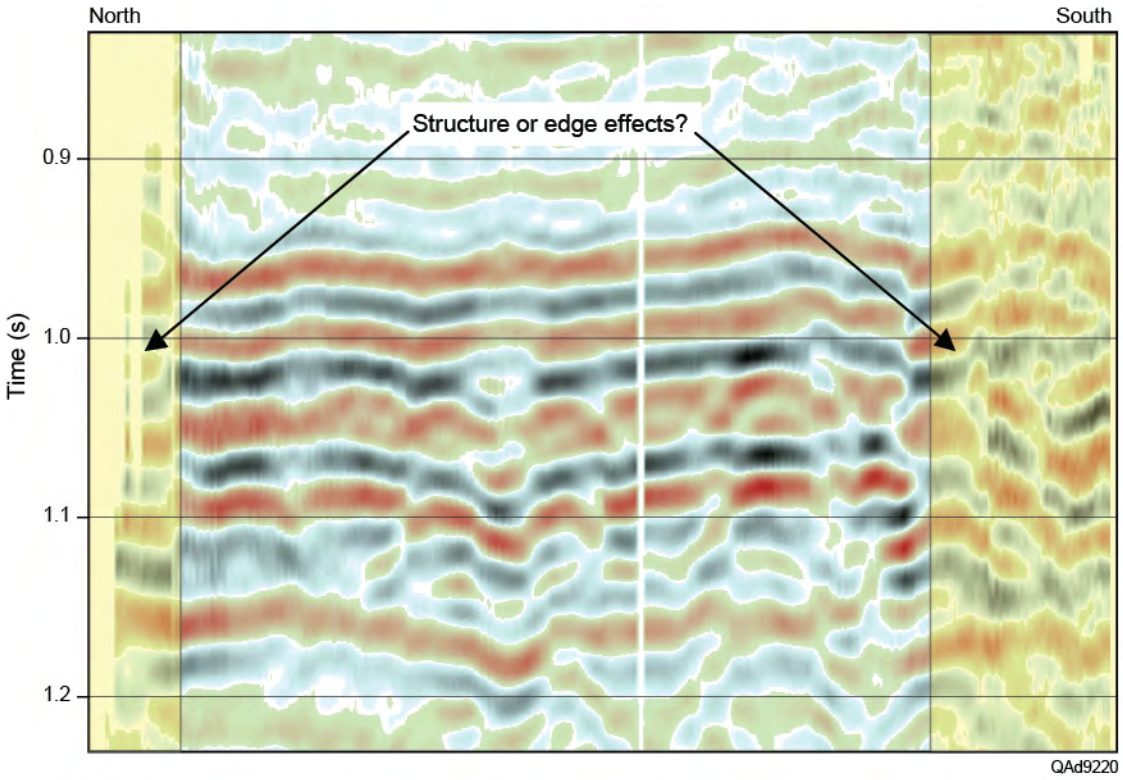

Figure 9.1a. Profile showing migration artifacts (shaded areas) along the edges of P-P image space.

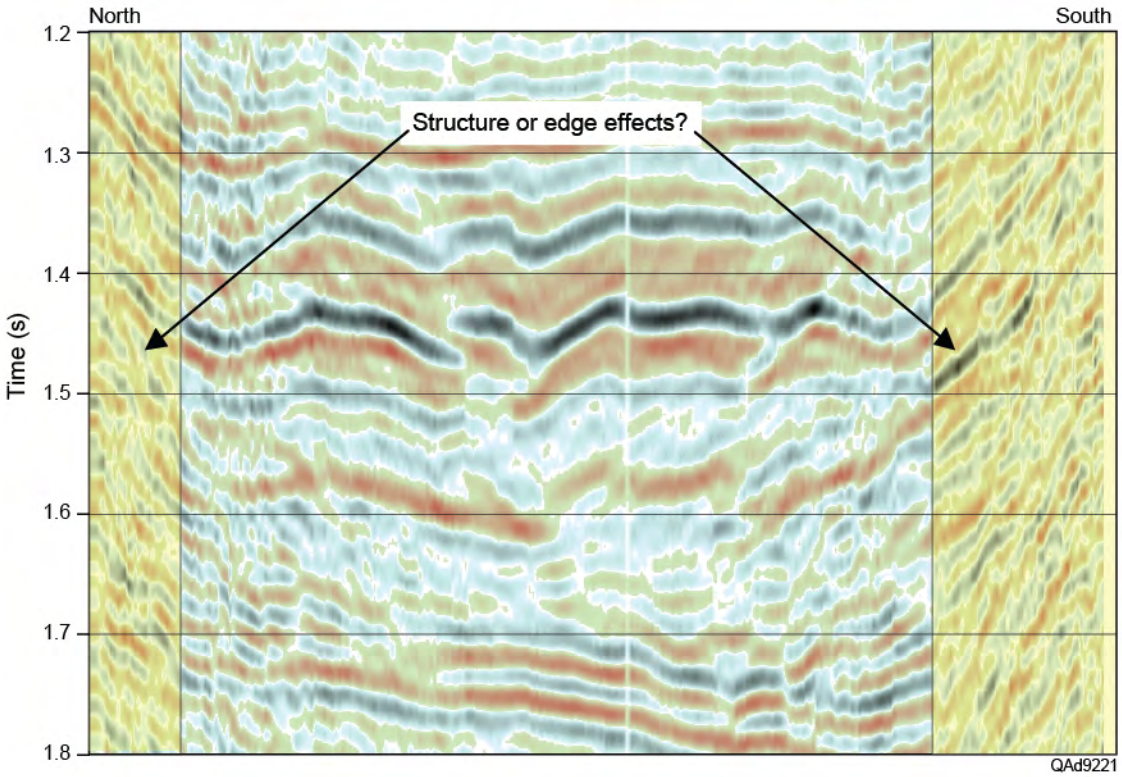

Figure 9.1b. Same profile as 9.1a showing migration artifacts (shaded areas) along the edges of P-S_1 (fast-S) mage space. Note the increase in reflection dip inside the shaded areas.

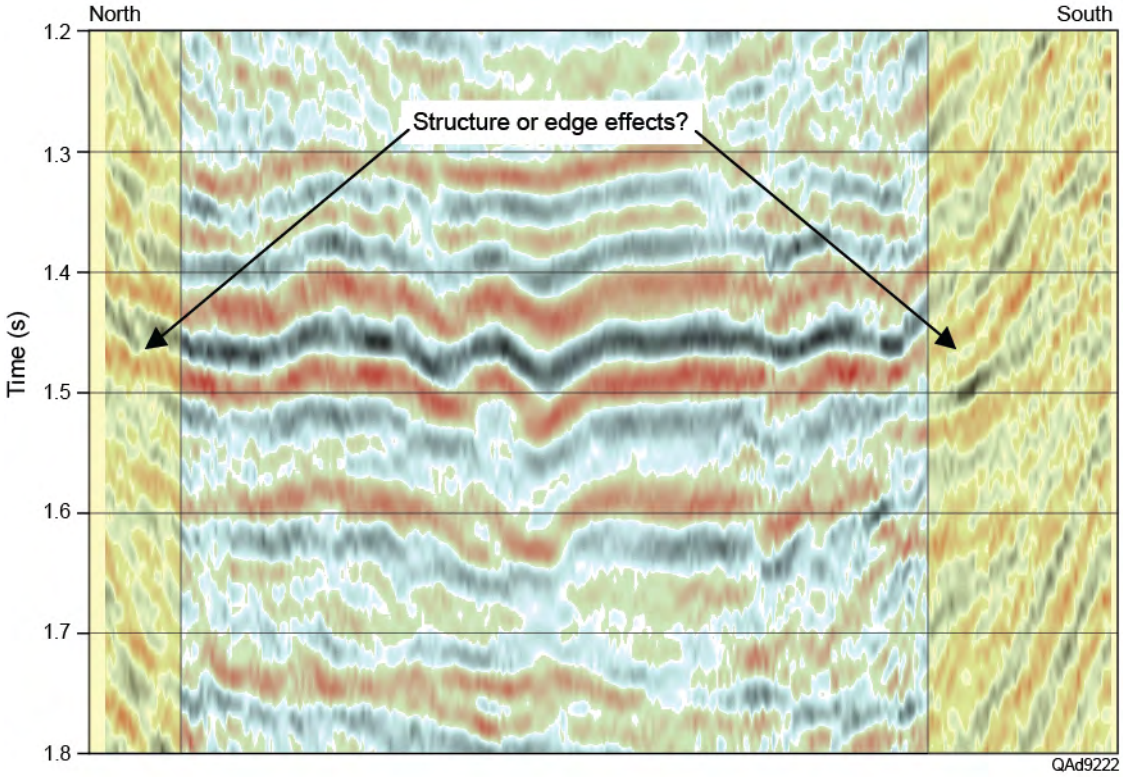

Figure 9.1c. Same profile as 9.1a showing migration artifacts (shaded areas) along the edges of P-S_2 (slow-S) mage space. Note the increase in reflection dip inside the shaded areas.

Seed Horizons

A geologic horizon interpreted along a seismic reflection event marks a chronostratigraphic surface. When a reflection event has good signal-to-noise character, there is increased confidence in the accuracy and validity of its associated interpreted horizon. These high-confidence horizons form the basis of a chronostratigraphic section that can be defined vertically and laterally throughout 3D seismic image space. These high-quality, high-confidence, interpreted chronostratigraphic surfaces are called *seed horizons*.

Seed horizons are interpreted along inline and crossline profiles separated by intervals Δx and Δy, respectively, where the magnitudes of Δx and Δy are selected by an interpreter based on her/his confidence that a seed horizon will not jump to an incorrect reflection event when switching interpretation analysis from profile to profile. In our interpretation of post-stack data volumes, Δx and Δy were usually every fifth profile in both the inline and crossline directions. A few profiles that cut across image space at arbitrary azimuths relative to inline and crossline directions were also interpreted to ensure the accuracy of our seed horizons.

P-wave and S-wave horizons were mapped simultaneously to ensure geology was depth registered in P and S image space and to establish optimal stratigraphic correlation between P and S data volumes. Mapping stratigraphic horizons at the edges of S-wave data volumes was difficult because of the migration inaccuracies illustrated on Figures 9.1b and 9.1c.Interpretation of a seed S-wave horizon along inline and crossline profiles was terminated where the time structure of that horizon deviated significantly from its depth-equivalent P-wave horizon time structure.

Seed horizons spanning targeted stratigraphic intervals were interpolated between interpreted profiles to create a continuous horizon surface across seismic image space. These continuous surfaces were used to guide calculations of depth-equivalent P and S seismic attributes. Interpolated horizons were mathematically extended across the full extent of the inline range and crossline range using a best-fit algorithm. Along the edges of seismic image space, interpolated horizons extending beyond the end points of seed horizons are considered to be only estimates of the correct time structure. Consequently, seismic attributes generated near the edges of 3C3D image space are less reliable than attributes calculated where reliable seed horizons were interpreted.

Frequency Spectra Analysis

Visual inspection of time-migrated volumes of Bradford County 3C3D seismic data indicated S-wave data produced better vertical resolution of geologic targets across our study area than did P-wave data. The profiles exhibited on Figures 9.1a through 9.1c demonstrate these differences in vertical resolution. Additional comparisons of P-wave and S-wave resolution of Marcellus-related geology will be shown throughout this chapter. Spectral analyses of time-domain P and S data volumes confirmed the frequency content of each 3D image was reasonably broad band. The P-wave data volume had a rather flat frequency spectrum between 10 and 40 Hz, with energy content then steadily reducing to -40 dB at 80 Hz (Fig. 9.2). Both S modes (P-SV_1 and P-SV_2) had spectra that were approximately flat from 8 to 35 Hertz, with reduced, but significant, energy content extending to almost 55 Hz (Figs. 9.3 and 9.4). The spectra shown on Figures 9.2 to 9.4 were calculated for trace lengths that extended from the Earth surface to slightly below what was interpreted to be seismic basement in each image space.

These spectral analyses introduce the concept that, for this particular geology, converted-SV data are superior to traditional P-P data for detecting and interpreting small-scale geological features. The real proof of whether one wave mode is superior to another wave mode for imaging thinner strata and smaller fault throws requires data comparisons be made in the depth domain rather in the time domain. These depth (spatial wavelength) comparisons are presented in a following section.

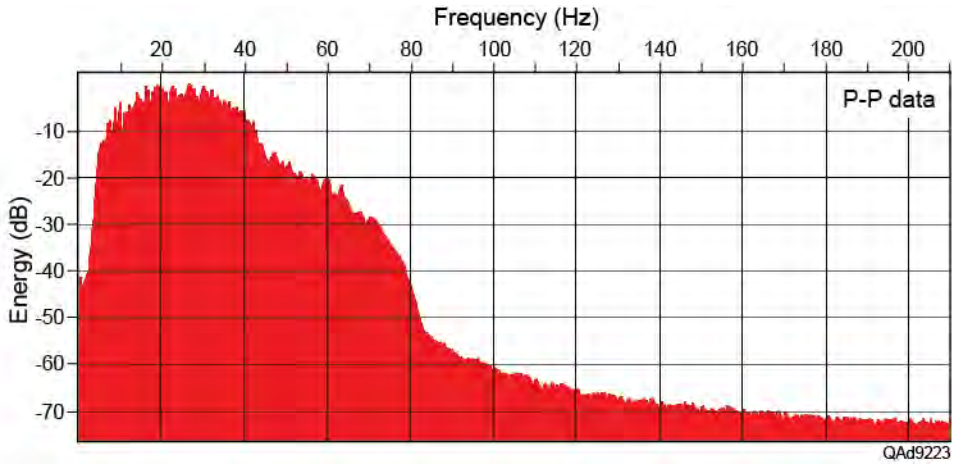

Figure 9.2. Frequency spectrum of P-P data.

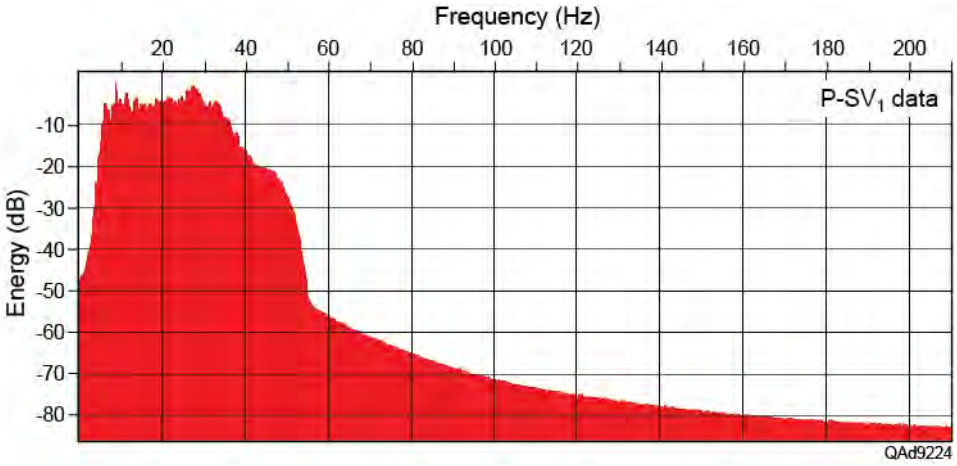

Figure 9.3. Frequency spectrum of P-SV_1 (fast-S) data.

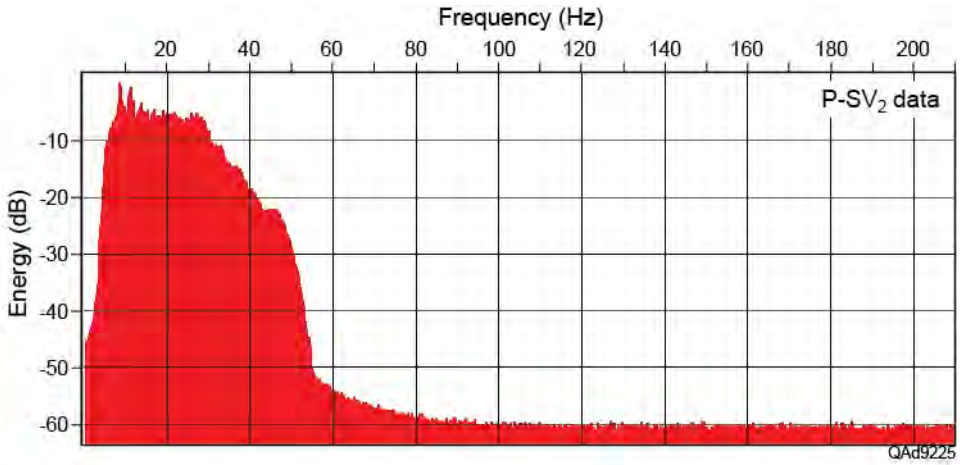

Figure 9.4. Frequency spectrum of P-SV_2 (slow-S) data.

Time to Depth Calibration

Before seismic interpretation is initiated, it is essential to determine which reflection events correlate with key geologic horizons. When interpreting multicomponent seismic data, time-to-depth calibrations must be established for P-wave data and for each S-wave mode involved in an interpretation. Data acquired in our central-image calibration well allowed two approaches to be implemented to establish time-to-depth correlations for the 3C3D Bradford County seismic data. The first approach was to utilize synthetic seismograms; the second approach was to use VSP time-based and depth-based images. We utilized the simpler, and more common, option of synthetic seismograms constructed from logs that use VSP data to establish accurate transformations from log depth to seismic-image time.

Depth Calibration Using Synthetic Seismograms

Velocity logs recorded in the central-image calibration well provided depth profiles of both P-wave velocity (V_P) and S-wave velocity (V_S). P-P and P-SV_1 synthetic seismograms were calculated by combining these velocity logs with the density log from the calibration well. These synthetic seismograms were our principal approach to defining depth-equivalent P and S reflection events as 3D P and S data volumes were interpreted. The correlations of seismic data and synthetic seismograms are shown on Figure 9.5 for P-P data and on Figure 9.6 for P-SV_1 data. The VSP-based calibration of log depth to seismic time defined depth-equivalent P and S horizons with high confidence.

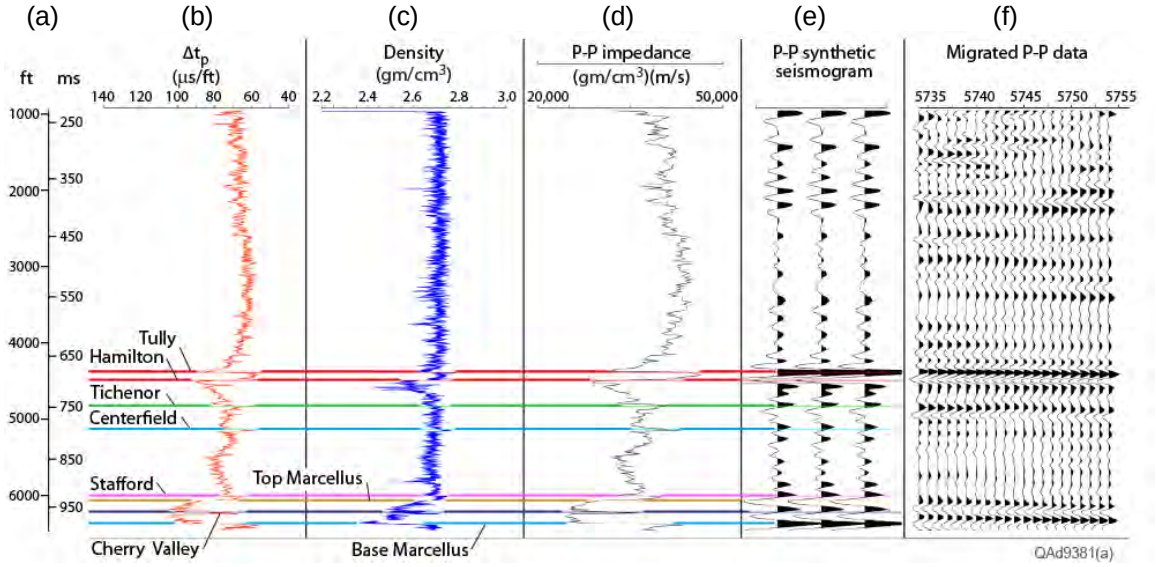

Figure 9.5. (a) Depth and P-P image time defined by VSP data. (b) P-wave sonic log. (c) Density log. (d) P-wave impedance. (e) P-P synthetic seismogram. (f) P-P seismic data local to the calibration well.

Additional confirmations of the accuracies of correlations between depth-based geology and time-based P and S images are shown on Figures 9.7 through 9.9 where the gamma-ray log recorded in the calibration well is displayed atop time-migrated P-P data (Fig. 9.7), P-SV_1 data (Fig. 9.8), and P-SV_2 data (Fig. 9.9). In each display, the depth-based gamma-ray curve is adjusted to the respective seismic image time using VSP time-depth information measured from VSP data acquired in the calibration well. Each significant change in gamma-ray magnitude correlates with a specific reflection event that allows depth-equivalent P and S horizons to be defined.

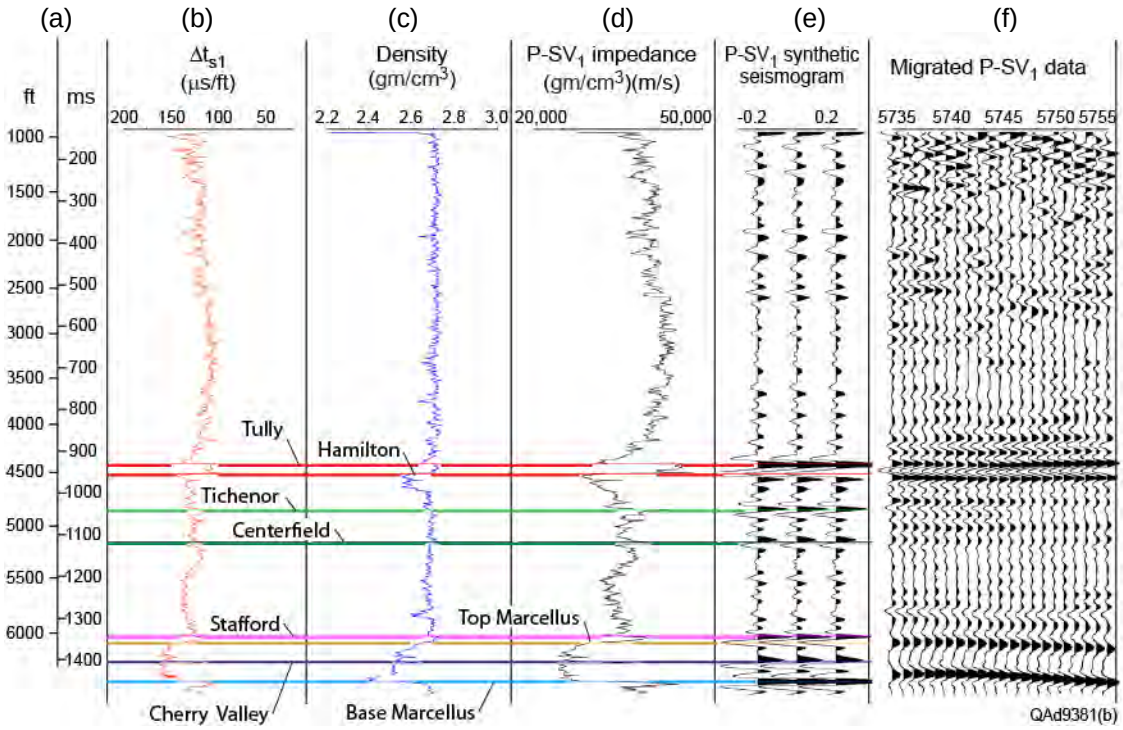

Figure 9.6. (a) Depth and P-SV_1 image time defined by VSP data. (b) S-wave sonic log. (c) Density log. (d) P-SV_1 impedance. (e) P-SV_1 synthetic seismogram. (f) P-SV_1 seismic data local to the calibration well.

The calibration well was drilled only to the Onondaga, immediately below the Marcellus, because the well was to be completed as a horizontal well in the Marcellus. Thus log-based and VSP-based calibration of P and S seismic data terminated at the top of the Onondaga Sandstone. The position of the deeper Oriskany unit shown on Figures 9.7, 9.8, and 9.9 is speculative. The position of the Oriskany was determined by extrapolating log-based time-to-depth curves and assuming the Oriskany was 450 to 500 ft (137 to 152 m) below the Onondaga. As a result, the seismic reflection feature labeled “Oriskany” on each image is reasonable but may not be precise.

One objective of this project was to evaluate the Utica Shale, which is even deeper than the Oriskany (Figure 3.5). No time-to-depth calibration local to our study site extended to the Utica. Thus defining seismic windows that span the Utica interval involves considerable speculation.

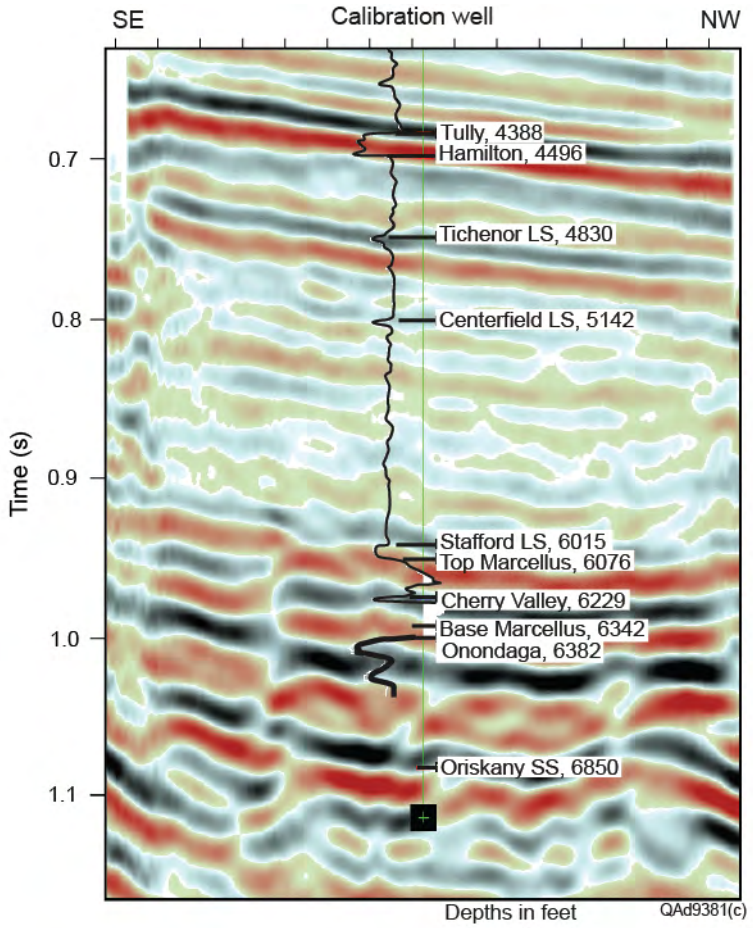

Figure 9.7. Time-migrated P-P data with gamma-ray log from the calibration well adjusted to VSP-defined P-P image time.

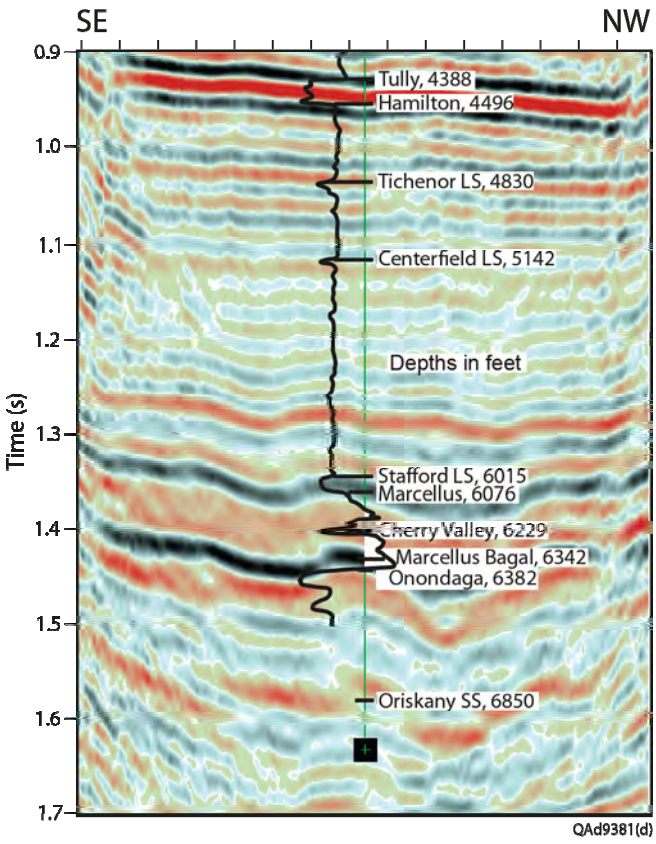

Figure 9.8. Time-migrated P-SV_1 data with gamma-ray log from the calibration well adjusted to VSP-defined P-SV_1 image time.

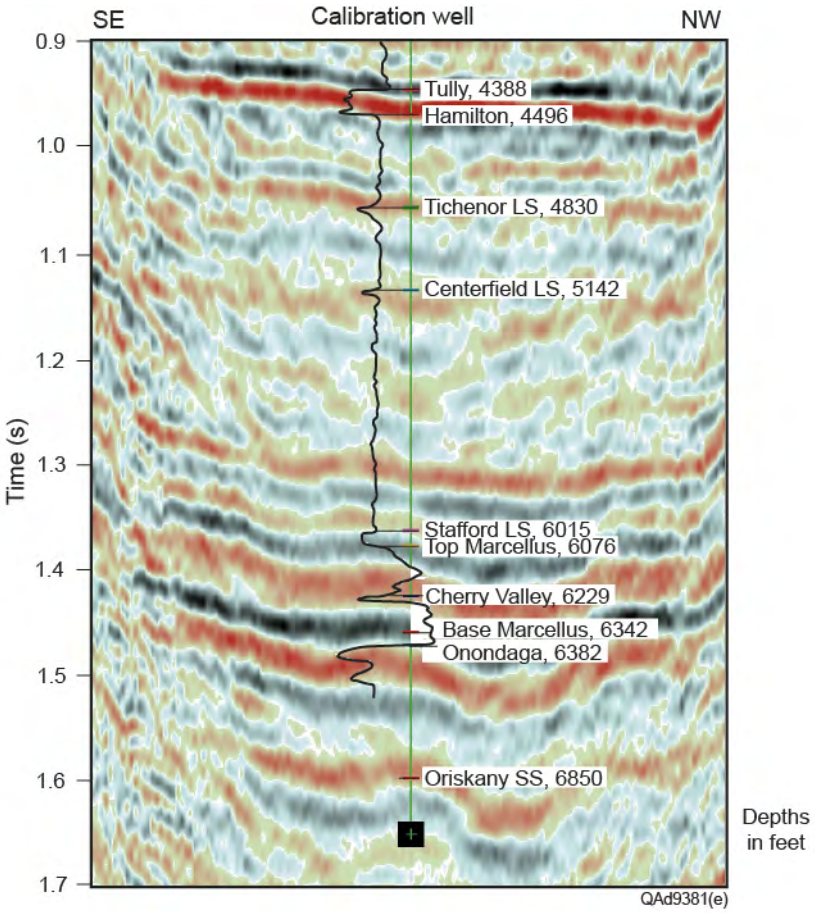

Figure 9.9. Time-migrated P-SV_2 data with gamma-ray log from the calibration well adjusted to VSP-defined P-SV_2 image time.

Depth-Converted P and S Data

A simple procedure was implemented to convert the Bradford County time-migrated P and S image volumes to depth (spatial wavelength) volumes. For each time-based volume, a single velocity function was calculated to convert image-time to depth across the entire 3D image space. Only one P-P time-to-depth conversion function was applied to the P-wave migrated-time volume. A spatially invariant V_P/V_S velocity ratio was then assumed and used to adjust this P-P time/depth relationship to create a P-SV time-to-depth conversion function. This single P-SV depth conversion was applied to both the P-SV_1 and P-SV_2 migrated-time data volumes.

Precise depth conversion requires several velocity functions, spaced at appropriate intervals across X-Y image space, be applied to a time-based seismic data volume. Because we used only a single time-to-depth conversion function across the entire image space of each data volume, our depth-converted data are only approximately correct. However, these approximate-depth volumes

are sufficiently accurate to allow important observations to be made about the relative vertical resolution of P and S seismic data.

Vertical slices through the P-P and P-SV_1 depth-converted data volumes are displayed on Figure 9.10. The vertical distances between the interpreted Tully and Marcellus horizons are labeled on each profile. By counting the number of peaks and troughs across a depth interval, these depth-domain profiles show P-SV_1 shear data have considerably better resolution than do P-P data. On average, P-SV_1 data have a dominant spatial wavelength of 200 ft over the depth range of 4,000 to 9,000 ft (5,000 ft divided by 25 wavelength cycles). In contrast, P-P data have a longer dominant wavelength of 250 to 280 ft depending on where the number of reflection cycles is counted across this 5,000-ft span. These depth resolution comparisons provide considerable confidence in the value of S-wave data for evaluating smaller geologic features associated with shale-gas plays.

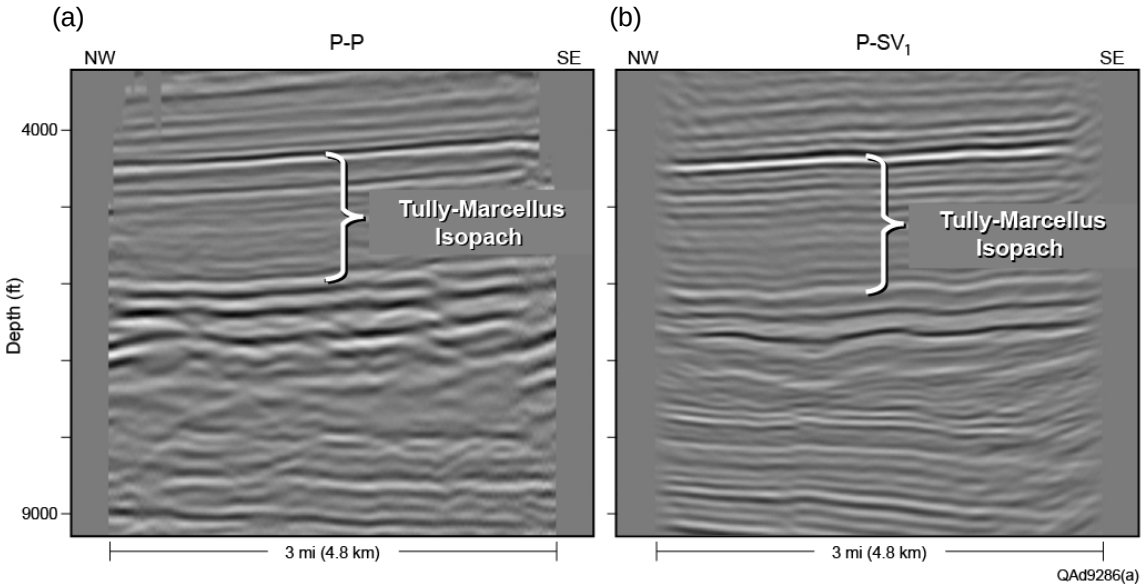

Figure 9.10. Equivalent profiles through depth-converted (a) P-P volume and (b) P-SV_1 volume.

Spectral analyses of depth-converted data volumes enforce these wiggle-trace comparisons of P-P and P-SV_1 spatial wavelengths. Spectral comparisons of depth-based P and S data are displayed as Figure 9.11. These spectra show depth-converted P-P data (Fig. 9.11a) are dominated by wavelengths of 100 to 800 ft; whereas depth-converted P-SV_1 data (Fig. 9.11b) are dominated by wavelengths of 40 to 400 ft.

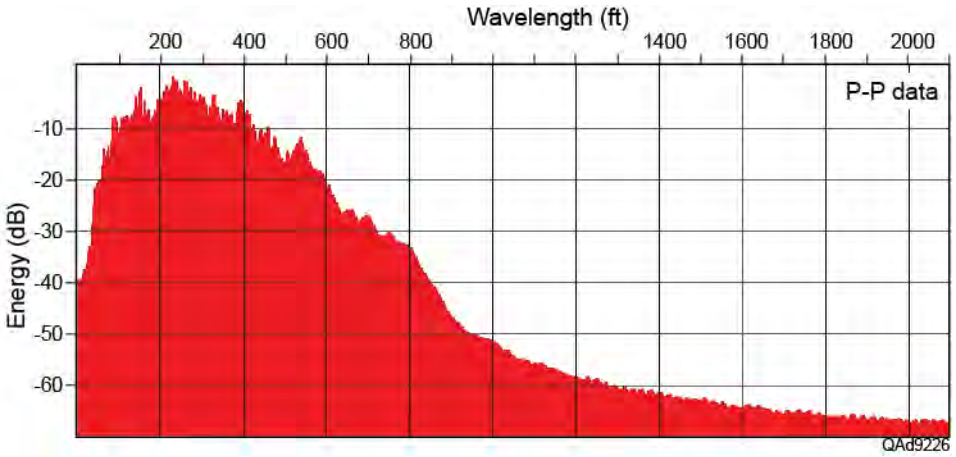

Figure 9.11a. Spatial-wavelength spectrum of depth-converted P-P data.

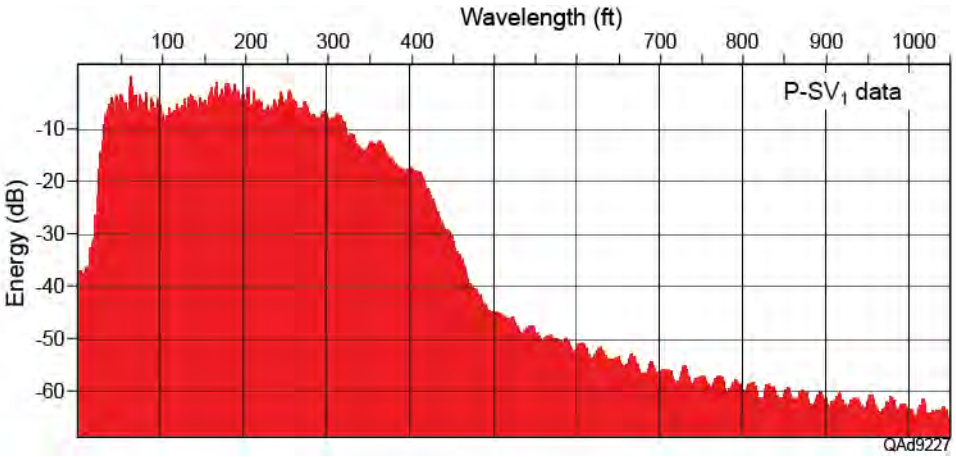

Figure 9.11b Spatial-wavelength spectrum of depth-converted P-SV_1 data.

Interpreting Depth-Equivalent P and S Horizons

The greatest problem confronting interpreters of P and S seismic data is to determine which S reflection is depth equivalent to a targeted P reflection event. The importance of accurate depth correlation between P-wave and S-wave data cannot be overemphasized. Until depth-equivalent P and S horizons are established, P and S seismic attributes cannot be compared across targeted stratigraphic depth intervals to determine attribute combinations that optimize the detection of specific rock and fluid properties.

A common approach to determining depth-equivalent events in 3D P and S data volumes is to work in section views, using procedures similar to those followed when interpreting 2D seismic profiles. This vertical-section approach to interpreting 3D P and S seismic data is satisfactory if adequate precautions are taken to ensure miscorrelations of key stratal surfaces do not occur. We think our

time-depth registration of P-P and P-SV data is accurate because our definitions of depth-equivalent P and S horizons were established using P and S traveltimes observed in VSP data acquired in the central-image calibration well (Fig. 4.1 of Chapter 4). P-P and P-SV traveltimes to key depth-based stratigraphic horizons penetrated by this VSP calibration well were marked at the well X-Y coordinates in each time-based data volume to define the P-P and P-SV reflection event associated with that horizon. Each horizon was then extended from this well-control point across all of P-P and P-SV image space.

Away from the VSP calibration well, inline and cross-line sections of P-P and P-SV data were compared to define characteristic features that should be expected on both data sets and which would increase confidence that depth-equivalent horizons were being followed as interpretation proceeded farther from the VSP calibration well. Geometric features such as stratigraphic terminations and lap-outs, if observed in both P and S image space, were important for deciding how to constrain the interpretation to depth-equivalent P and S horizons. However, as will be emphasized later, P-SV seismic sequences often differ from P-P seismic sequences so this interpretation guideline must be used with discretion.

An attempt was made to use fault surfaces for P-to-S depth correlation. If faults cut across reflections at significant angles away from vertical, it is often possible to match depth-equivalent breaks in P and S reflections. In such cases, interpreted P and S horizons can often be verified as being depth equivalent by comparing fault maps of these interpreted horizons. In contrast, if faults are near-vertical, it is difficult to decide how much vertical shift should be applied to an S profile to make a P-SV horizon depth-equivalent to a targeted P horizon. For near-vertical faults, fault maps of P and P-SV horizons show minor changes in X-Y coordinate location over large vertical intervals of P and S data windows. This focus on fault interpretation is a valuable approach to depth registration of P and S images, but it was not productive for our study area because no significant faults were present inside our seismic image space.

Devonian Sandstone Water-Storage Interval

Previous studies indicate transgressive Devonian sandstones are often found in the stratigraphic interval immediately below the Tully Limestone (Bruner and Smosna, 1994; Diecchio, 1985; Kostel and Carter, 2009a, 2009b; Milici and Swezey, 2006). Because porous, brine-filled sandstones are good candidates for water-storage reservoirs, we did a detailed interpretation of the interval between the interpreted tops of the Tully Limestone and Tichenor Limestone to determine how P and S seismic data react to these particular sandstone targets.

Time windows chosen for spectral analysis of the Tully-to-Tichenor interval for P-P, P-SV_1, and P-SV_2 data are shown on Figures 9.12a, b, and c,

respectively. The Tully unit is characterized by a strong reflection peak (black) immediately followed by a high-amplitude wavelet trough (red) in all three data volumes and is easily mapped across the image area. In contrast, the Tichenor Limestone appears as a modest-amplitude reflection in the P-P data volume, and has an even lower amplitude response in both the P-SV_1 data (Fig. 9.12b) and the P-SV_2 volumes (Fig. 9.12c). Despite these weaker expressions of the Tichenor unit, depth-equivalent Tichenor horizons were interpreted across the image space in all three data volumes. Visual inspection of these side-by-side data windows leads to an important research finding – *P-SV data provide better resolution of stratigraphy across our study area than do P-P data*. An important implication is that this same advantage of S-wave data may occur across many shale-gas prospects.

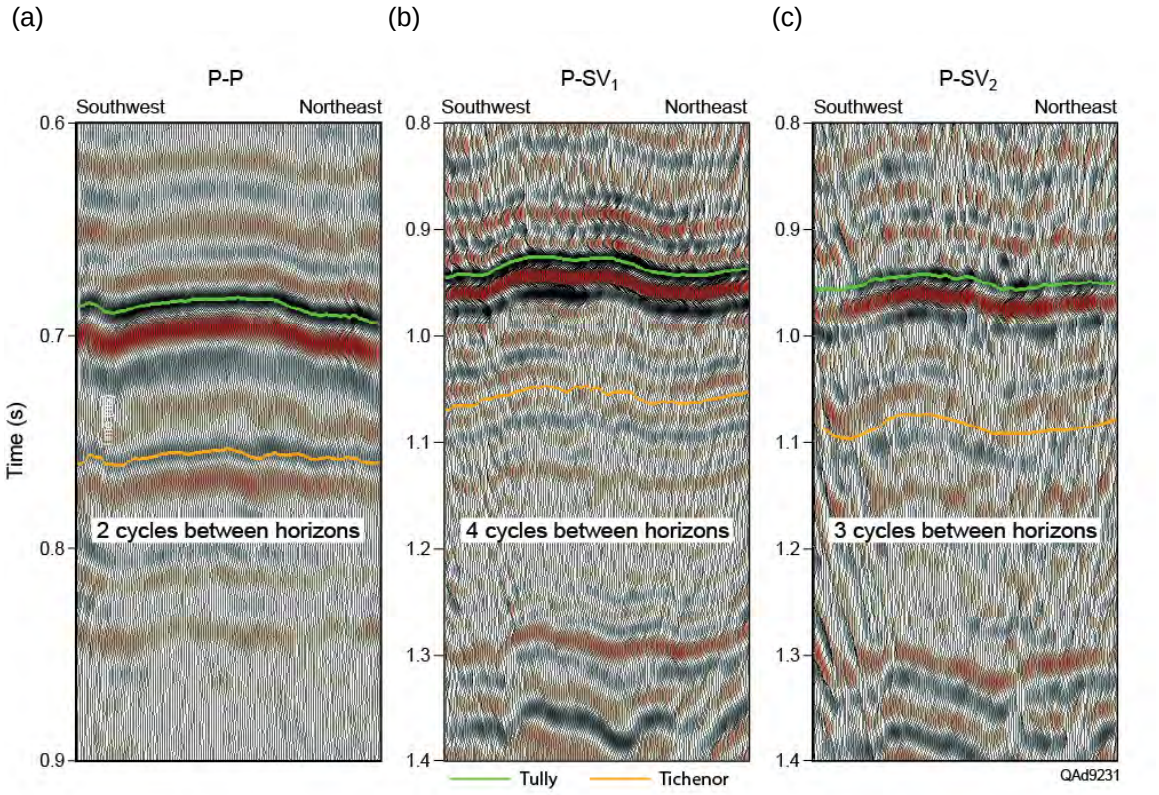

Figure 9.12. Profiles comparing Tully (green horizon) to Tichenor (orange horizon) intervals in (a) P-P, (b) P-SV_1, and (c) P-SV_2 image space.

P-P data show a marked decrease in the number of reflection cycles across the transgressive sandstone interval relative to the number of reflection cycles appearing in P-SV_1 and P-SV_2 images, another example of the improved spatial resolution of P-SV data compared to P-P data. P-SV_1 data provide the greatest stratigraphic detail after the three wave-mode volumes are time warped to equivalent time scales. Frequency analyses of the data after time warping are displayed on Figures 9.13a through 9.13c. These spectra show P-P data have good frequency content up to 50 Hz and then exhibit a sustained decline in

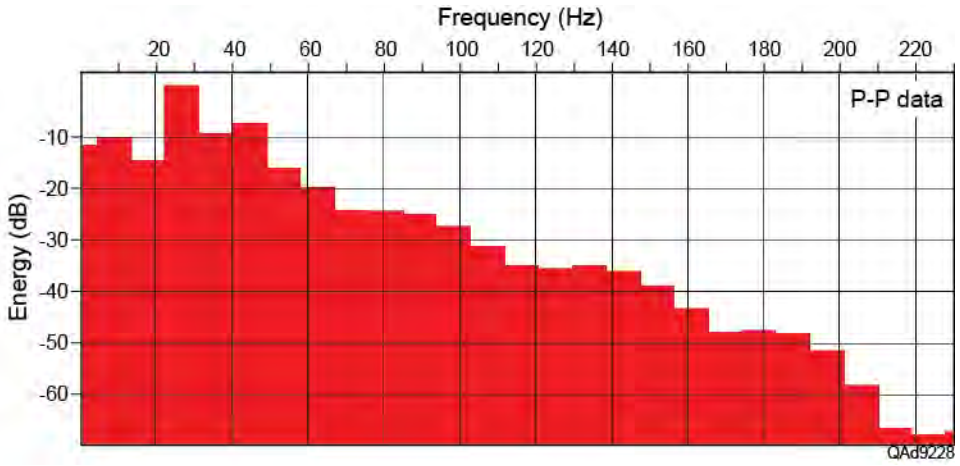

Figure 9.13a. P-P frequency spectrum for the Tully-to-Tichenor interval.

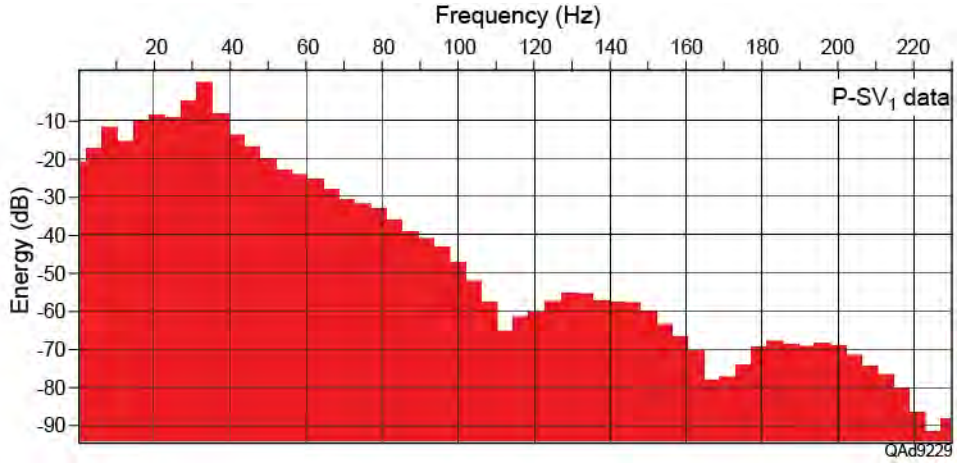

Figure 9.13b. P-SV_1 frequency spectrum for the Tully-to-Tichenor interval.

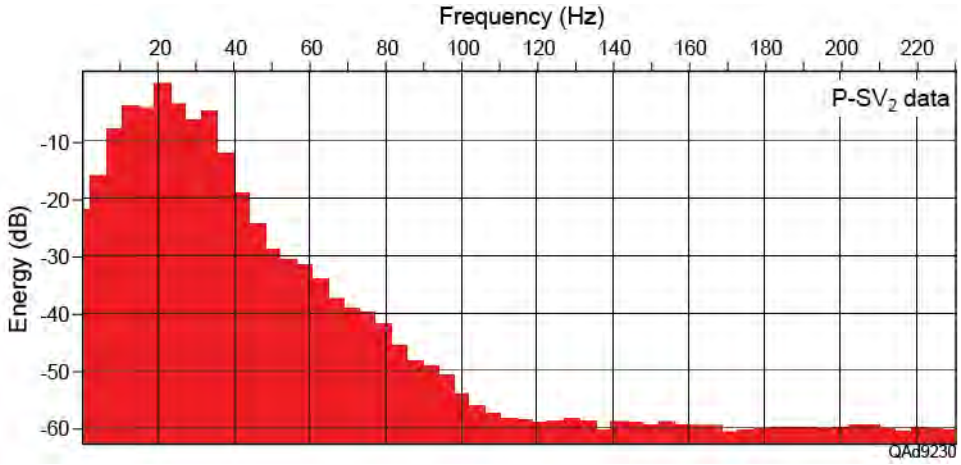

Figure 9.13c. P-SV_2 frequency spectrum for the Tully-to-Tichenor interval.

energy content of approximately 5 dB for each 20-Hz increase in frequency. P-SV_1 data have good energy content up to 40 Hz and then lose energy content almost twice as fast as do P-P data (~5 db per 10-Hz interval). P-SV_2 data have good energy content up to 35 Hz and then decay in energy even faster than do P-SV_1 data.

Amplitude Attributes across Devonian Water-Storage Interval

Many attributes can be calculated from seismic data. In our elastic wavefield seismic stratigraphy interpretation across this prospect, we gave heavy weight to amplitude-based P and S attributes, with these attributes determined using depth-equivalent stratal surfaces. Amplitude horizon slices were extracted from P and S data volumes at 2-ms intervals. For the geology imaged by these Bradford County 3C3D seismic data, we found amplitude attributes failed to identify unique reflection patterns in P-P and P-S data that could be used for depth-correlation purposes, but they were valuable for evaluating subsurface structural trends and particularly valuable for detecting erosion-like features within the Tully-to-Tichenor interval.

Root-mean-square (rms) P-P reflection amplitudes across the Tully-to-Tichenor interval are shown in map view on Figure 9.14. Several small black areas occur across the color map. These black areas are no-lease properties where subsurface geological information cannot be shown, thus seismic information across these properties are deleted from the data volumes. Similar blank-out areas will be shown on numerous maps that follow. Basically, P-P reflection amplitudes show only minor variations across the image area of approximately 9 mi^2 (23 km^2). Amplitude variations appearing near the edges of image space are not given significant geological importance because of the edge-related migration artifacts discussed in association with Figures 9.1a through 9.1c.

An important research finding was that P-SV_1 data imaged a southwest to northeast trending feature within the Tully-to-Tichenor interval (Fig. 9.15) that appears similar to an eroded channel. However, the feature has no meandering character, and its linear geometry suggests there may be a genetic relationship to structure. This feature was not revealed by either P-P data (Fig. 9.14) or P-SV_2 data (Fig. 9.16). These amplitude-attribute comparisons are an example of the increased geological information provided by elastic wavefield seismic stratigraphy (joint interpretation of P and S data) compared to the amount of information provided by traditional seismic stratigraphy (which uses only single-component P-wave data). The erosion-like feature has a significant size, being approximately 0.25 mi (0.4 km) wide and extending across the full 3 mi (4.8 km) dimension of the image space.

The detection of this depositional feature has significant implications in evaluating water-storage reservoirs. There is not sufficient subsurface information to define the type of lithological fill within this particular geobody. Thus the feature can be a lateral barrier to fluid flow, or it could enhance fluid flow, depending on the nature of its internal lithology, porosity, and permeability. In either case, it is essential that anyone who considers Devonian sandstones within this stratigraphic interval as possible water-storage reservoirs be aware of this reservoir heterogeneity. The key point of this interpretation is that multicomponent seismic data provide a picture of reservoir compartmentalization that is not available if shale-gas operators utilize only single-component P-wave seismic data.

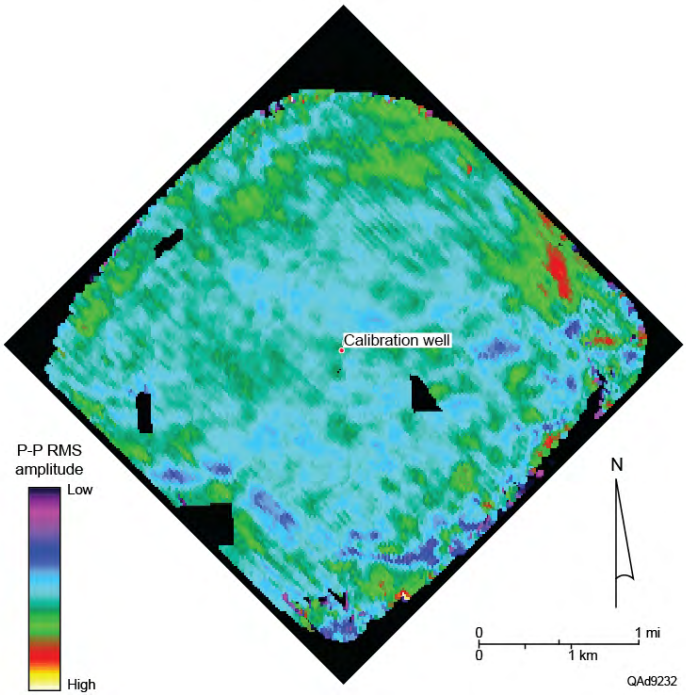

Figure 9.14. P-P rms amplitudes across the Tully-to-Tichenor interval. The black areas within the image space are no-lease properties where subsurface seismic properties cannot be shown. Amplitude anomalies near the edges of image space are not assigned significant importance because of migration artifacts that occur along the outer edges of 3D image space.

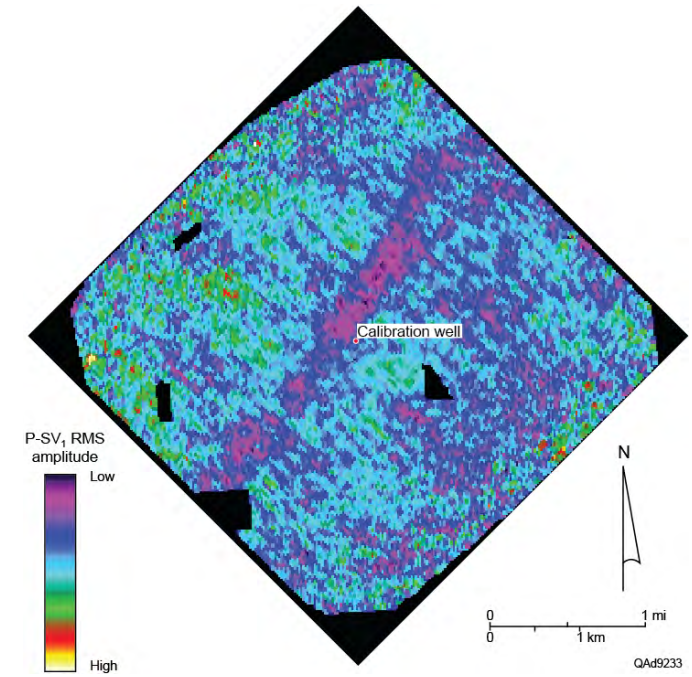

Figure 9.15. P-SV_1 rms amplitudes across the Tully-to-Tichenor interval showing an interpreted incised channel in purple (low-magnitude amplitudes). The black areas within the image space are no-lease properties where subsurface seismic properties cannot be shown. The southwest-to-northeast trending low-amplitude feature is given major interpretation importance because the amplitude effects extend across the central image space where migration artifacts have minimal effects on amplitude behavior.

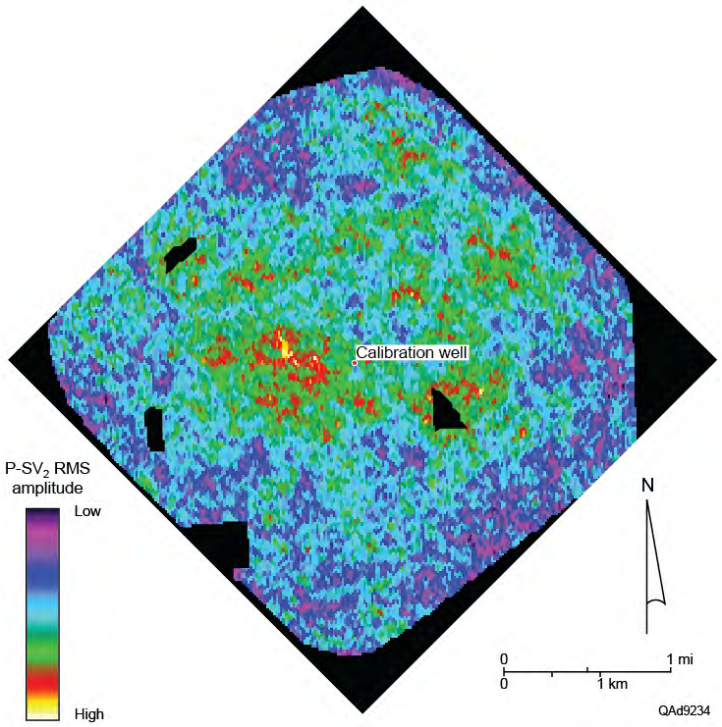

Figure 9.16. P-SV_2 rms amplitudes across Tully-to-Tichenor interval. The incised channel seen by the fast-S mode (Fig. 9.10) is not evident in this slow-S image. The black areas within the image space are no-lease properties where subsurface seismic properties cannot be shown.

P-SV_1 and P-P profiles across this stratigraphic feature are shown on Figure 9.17. A mounding geometry is associated with the feature on both profiles, but reflector dimming occurs within and below this mounding only on the P-SV_1 image. This reflector dimming creates the reduced rms amplitude values that appear as the purple low-amplitude corridor extending across the map on Figure 9.15.

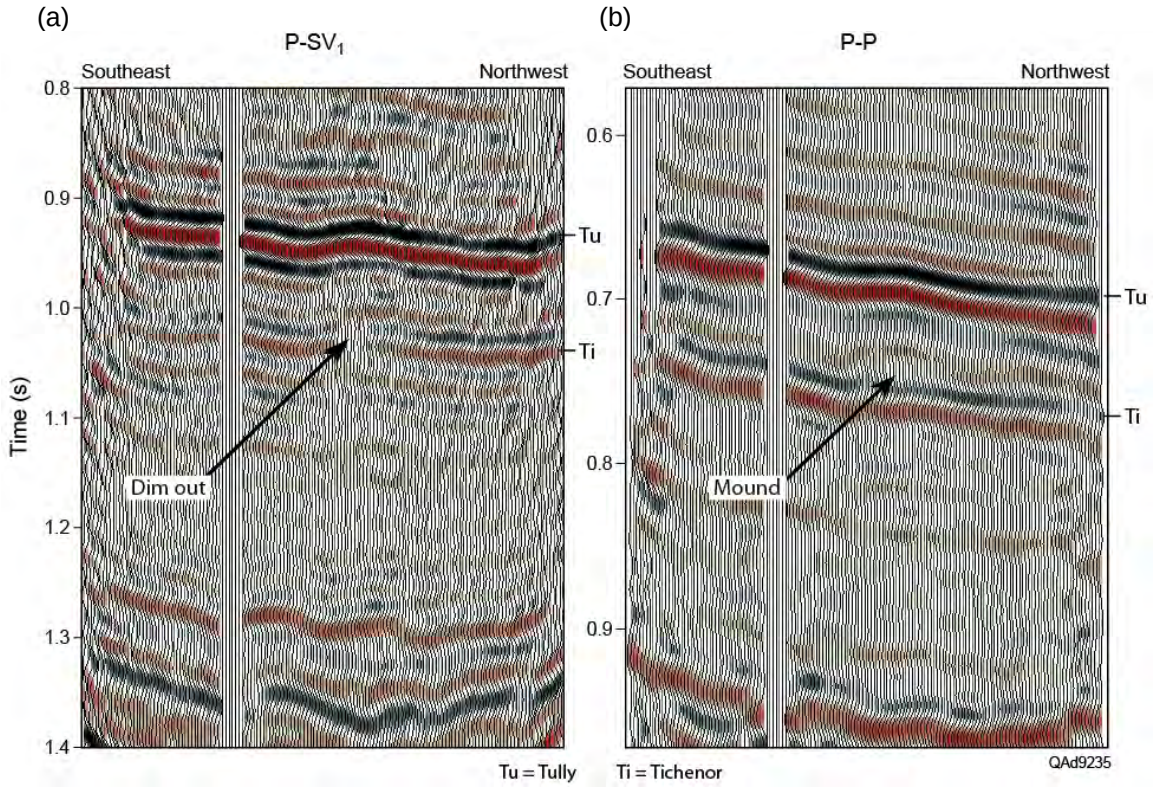

Figure 9.17. (a) P-SV_1 profile showing mounding (red trough) immediately above dim-out of peak (black) and trough (red). (b) P-P image along same profile shows mounding but no reflection dim-out.

Tully Structure

Because the sandstone-prone interval immediately below the Tully can contain units that could be storage reservoirs for hydrofrac flow-back waters, it was essential to verify if faults breached the Tully to create conduits that would allow injected water to migrate upward into shallow aquifers. A structural interpretation of the Tully was done to determine if evidence of breaching faults was present. No faults were found that disrupted the Tully Limestone in any of the three seismic data volumes. This time-based interpretation showed that across the 9.3 mi^2 (23.8 km^2) area of seismic image space, the Tully Limestone is structurally high in the southeast portion of the image space and dips northwest in a rather gentle, gradual manner. Structural maps of the Tully horizon

interpreted from P-P, P-SV_1, and P-SV_2 data volumes are shown on Figures 9.18, 9.19, and 9.20, respectively. A gentle structural ridge appears on each time-based structural map. The ridge-like feature is much smaller in P-P image space and has a different azimuth orientation than it does in either P-SV image space. An arrow is placed on each map to indicate the trend of this structural ridge.

It must be emphasized that these maps were constructed from time-based seismic data, and thus differences between P and S time-based structure are expected. Time-based P and S structural maps will have similar geometry only if V_P and V_S velocities vary in synchronization across X-Y seismic image space. Because azimuth-dependent rock properties cause V_S velocity to vary with azimuth more than does V_P velocity, P and S velocities rarely vary in synchronization at all seismic image coordinates. In a rigorous seismic interpretation, P and S data should be converted to depth, using reliable seismic-based P and S velocities, so depth-based, not time-based, structure maps can be generated. We did not construct depth-based structural maps because there was no need to do so to achieve the basic research objectives of this study, or to determine if breaching faults eliminate the Tully Limestone as an effective seal for Devonian water-storage reservoirs.

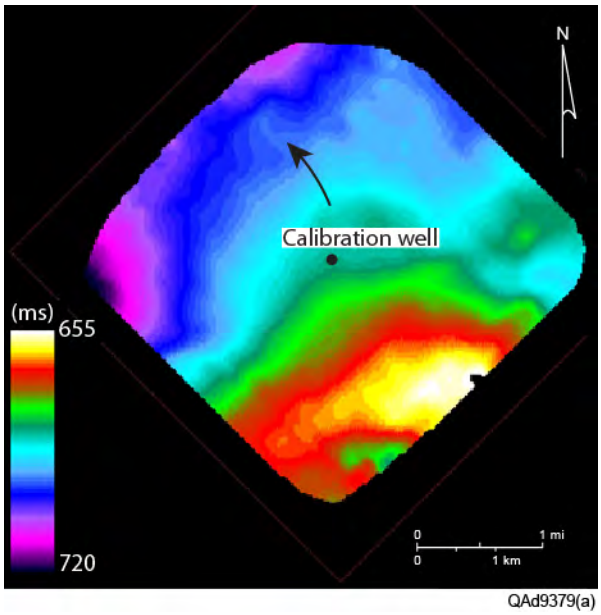

Figure 9.18. P-P time structure map of the Tully Limestone. The arrow emphasizes a modest ridge-like structure. The structure across this 24 km^2 area may look different when converted to depth.

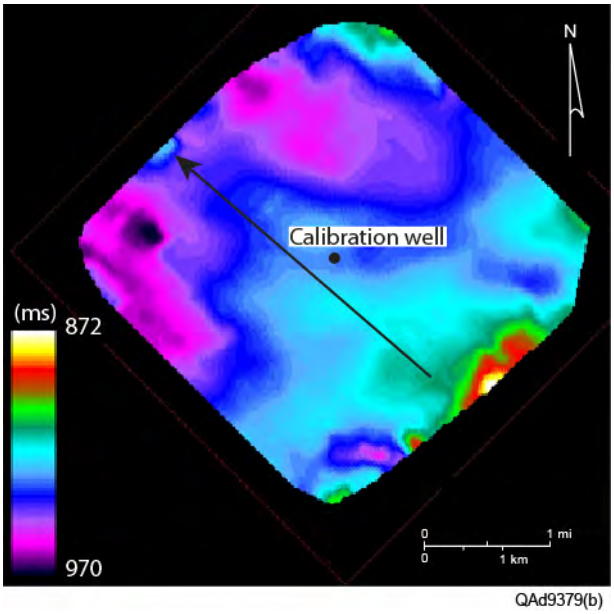

Figure 9.19. P-SV_1 time structure map of the Tully Limestone. The arrow emphasizes a structural ridge, which may have a different size and shape in a depth-based map.

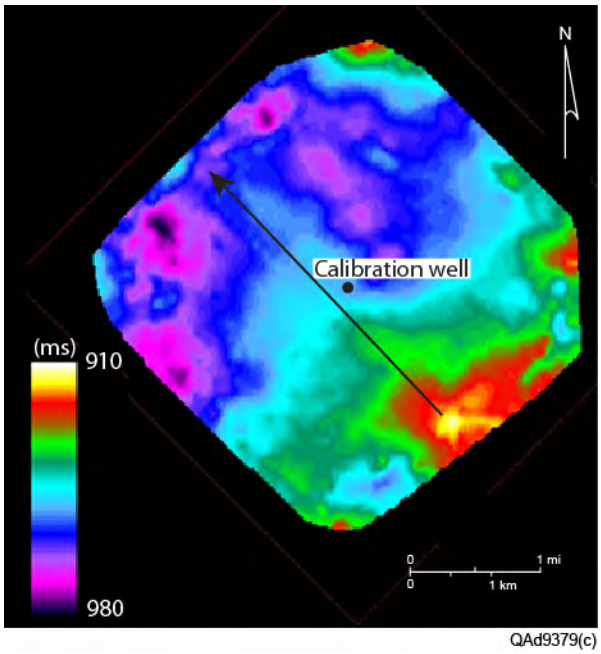

Figure 9.20. P-SV_2 time structure map of the Tully Limestone. The arrow emphasizes a structural ridge, which may have an altered shape in a depth-based map.

Tully to Tichenor Stratal Surfaces

A fundamental premise of seismic stratigraphy is that a seismic reflection event follows a **chronographic surface**, which is a depositional surface where geologic time does not change. Stated another way, a seismic reflection event defines a bedding surface, or **stratal surface**, which is a surface where geologic time is constant. All seismic stratigraphy studies are based on the principle that geologic time is constant along a horizon that follows a fixed seismic reflection phase. A corollary to this principle is that a seismic horizon that is conformable to a seismic reflection is also a surface along which geologic time is constant.

If the top and base of an interval is bounded by reflection events that are conformable to each other, it is rather simple to interpolate an arbitrary number of conformable horizons that span the interval between these two reflections. Seismic attributes calculated on each successive internal conformable surface describe stratigraphy within the interval at fixed increments of geologic time. A different strategy, developed by Zeng (2001, 2006), must be implemented if reflection events at the top and base of an interval are not conformable. In this approach, an interval having a time-varying thickness is divided into an arbitrary number of uniformly spaced sub-intervals as shown on Figure 9.21.

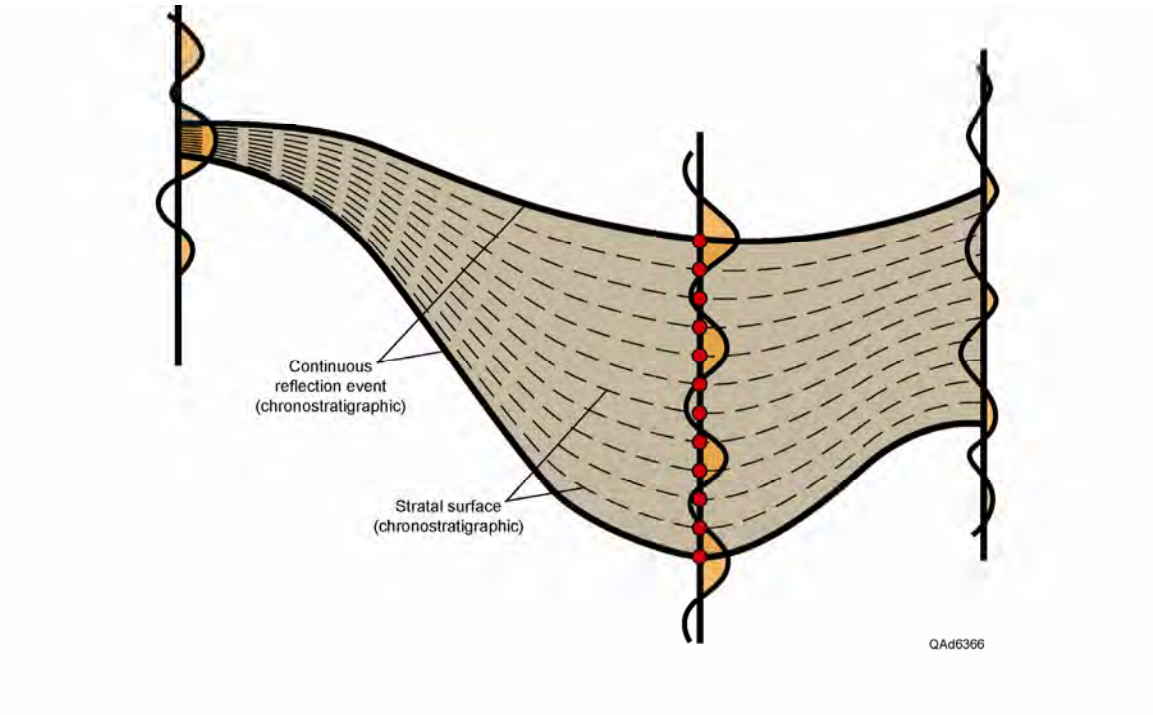

Figure 9.21. Stratal slices along a seismic profile where there are significant variations in the interval thickness between two chronostratigraphic reflections.

At any two coordinates along this profile, the vertical spacing between adjacent interpolated surfaces differs in seismic time but is constant in geologic

time. The result is a series of surfaces that define depositional features within the interval at fixed increments of geologic time. The creation of the interpolated surfaces between Reflections A and B on Figure 9.21 is called **stratal slicing**. In this example, the interval between Reflection A and Reflection B is divided into 11 sub-intervals. If the time interval at some point on the profile is 11 ms, each sub-interval is 1 ms thick at that image coordinate. If the interval from A to B is 110 ms thick at a second point on the profile, each sub-interval is 10 ms thick at this second image coordinate. Even though the magnitude of seismic image time spanned by each sub-interval differs at these two points, the geologic time across each sub-interval is MY/11 at both points, where MY is the geologic time difference between Reflection A and Reflection B. Because of the interpolation technique used to create these sub-intervals, the creation of stratal slices is also called **proportional slicing**.

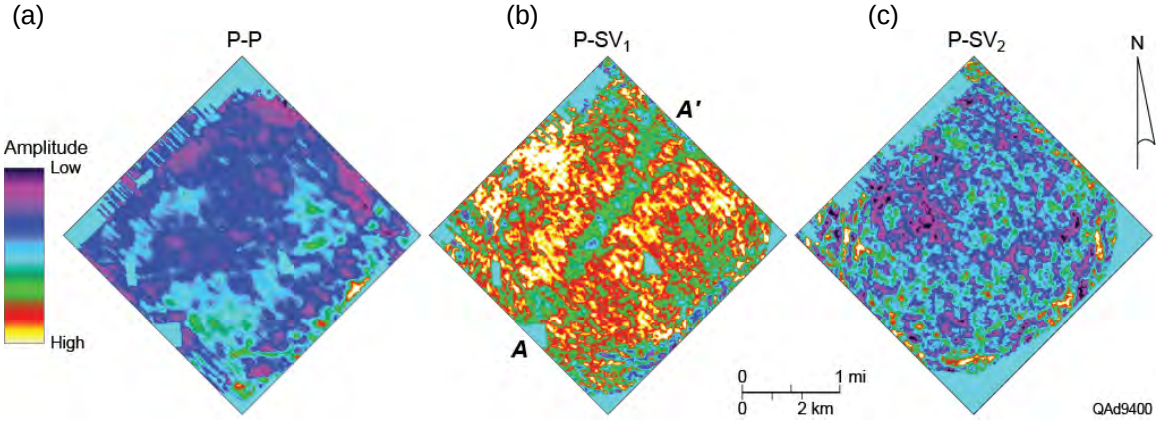

Figure 9.22. Stratal slice results showing depth-equivalent surfaces within the Tully-to-Tichenor interval. (a) P-P stratal slice. (b) P-SV_1 stratal slice. The channel-like image labeled **A-A′** is a key reservoir compartmentalization feature not revealed in the other data volumes. (c) P-SV_2 stratal slice. The attributes displayed on each surface are reflection amplitude values scaled as shown by the color bar.

This stratal time slicing technique was applied to the Tully-to-Tichenor interval to expand knowledge of the internal architecture of rock units that might be used for injecting hydrofrac flow-back water. All three data volumes (P-P, P-SV_1, and P-SV_2) were analyzed. Interpreted Tully and Tichenor horizons defined on Figures 9.7 to 9.9 were used as bounding seismic reflections to guide the stratal slicing. Example stratal slices from the volumes are exhibited on Figure 9.22. The heterogeneous feature internal to this interval revealed by amplitude analysis of P-SV_1 data (Fig. 9.15) is more prominent in this stratal-slice analysis (Fig. 9.22b). For example, stratal slicing shows a clear bifurcation of the feature at the northeast edge of the image space. This stratal-slice interpretation adds credence to the assumption that the channel-like feature contributes to reservoir compartmentalization. The interpretation also verifies the following important concept of elastic wavefield seismic stratigraphy—*one or more key depositional features not seen by one wave mode may be seen by another wave mode*. In this instance, S-wave data see a feature that P-wave data do not see. In other instances, P-wave data will see features that S-wave data do not see.

Reflection Cycles across Devonian Water-Storage Interval

A second example demonstrates an instance where P-P data are more useful than P-SV_1 data for understanding the stratigraphy of the Tully-to-Tichenor interval. In this case, the number of reflection troughs within the Tully-to-Tichenor interval was counted in P-P and P-SV_1 data sets. Although P-P data had fewer reflection troughs across the interval than did P-SV_1 data, the number of P-P troughs changed in some portions of the image space (Fig. 9.23), which indicates alterations in bedding thickness or bedding geometry. In contrast, the number of P-SV_1 reflection troughs stayed constant across the image space (Fig. 9.24). P-P and P-SV_1 profiles following trends AB labeled on Figures 9.23 and 9.24 are exhibited on Figure 9.25 to illustrate the behavior of P-P and P-SV_1 reflectivity within the Tully-to-Tichenor interval.

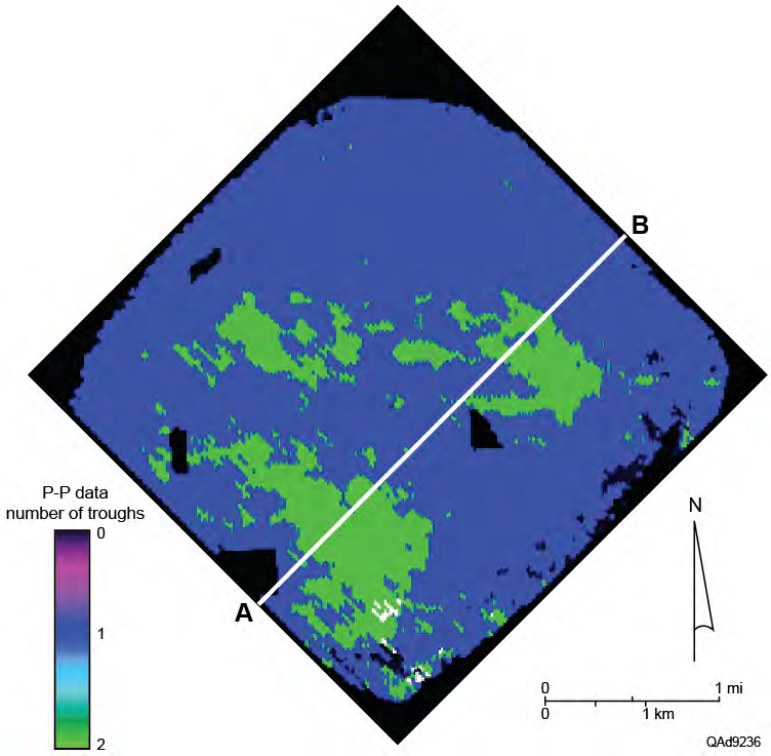

Figure 9.23. Number of P-P reflection troughs across the Tully-to-Tichenor interval. In some areas, the number of troughs increases from 1 to 2.

Although it has been emphasized that the spatial resolution of P-P data across our study area is less than the spatial resolution of P-SV_1 data, image coordinates where changes in the number of P-P reflection troughs occur must be considered as locations where there is a change in the internal compartmentalization of the Tully-to-Tichenor interval even if P-SV_1 data show little variation at the same coordinates. Thus maps of numerical counts of

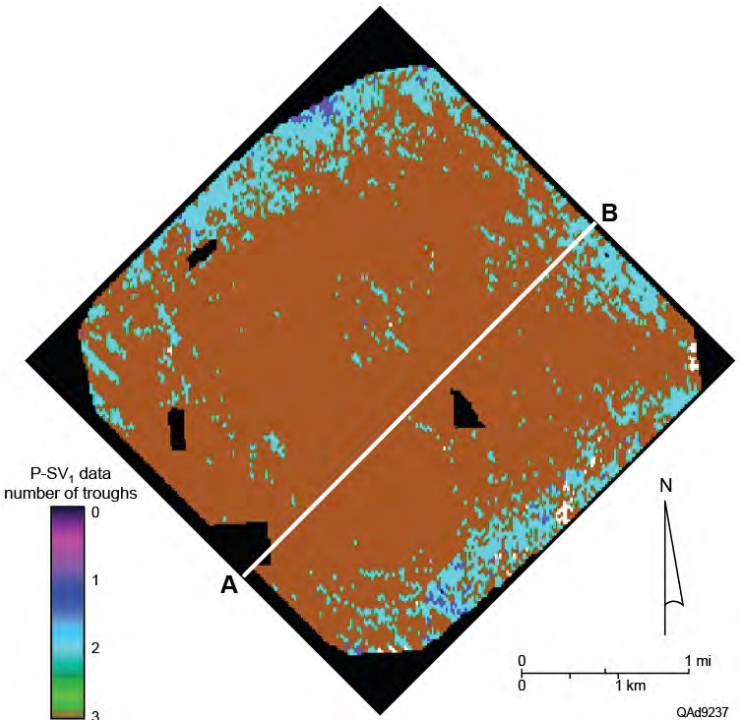

Figure 9.24. Number of P-SV_1 reflection troughs across the Tully-to-Tichenor interval. The number of troughs stays constant at 3 across the valid portion of image space. The reduced number of troughs near the edges of image space is ignored because of the migration artifacts that occur in these regions.

(a)

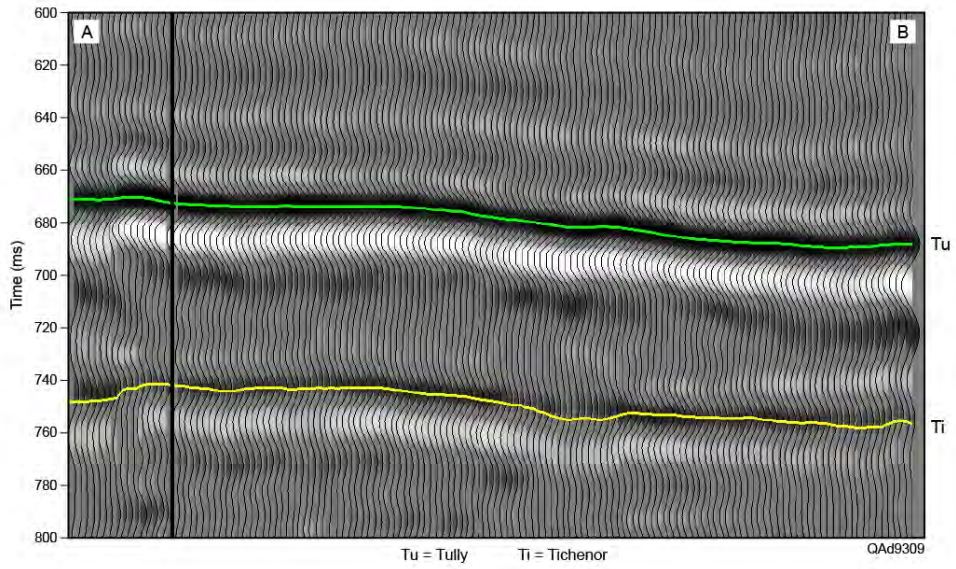

(b)

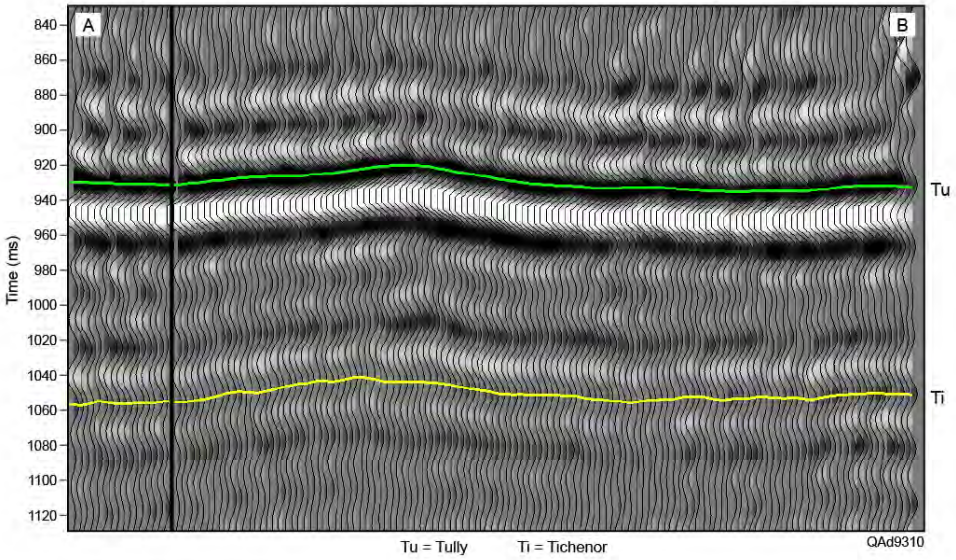

Figure 9.25. (a) P-P profile AB. (b) P-SV_1 profile AB.

reflection troughs (or peaks) across a stratigraphic interval are valuable in elastic wavefield seismic stratigraphy applications. It should also be emphasized that a constant number of reflection peaks and troughs across a target interval does not necessarily imply the internal layering of that interval is unchanging. Inspection of the P-P and P-SV_1 profiles on Figure 9.25 shows the amplitudes of peaks and troughs between the Tully and Tichenor horizons vary significantly at different image coordinates as reflection events are followed across the profile. Such

amplitude variations are often caused by alterations in thick stacks of interfingering thin-bed layers. All seismic attributes must be combined to reach optimal stratigraphic interpretation, particularly when stacked thin beds are involved.

Marcellus Shale Interval

The Marcellus Shale is divided into two distinct units—the Upper Marcellus and the Lower Marcellus. The boundary between these two units is the Cherry Valley Limestone. To characterize the Marcellus interval, it was essential to accurately interpret depth-equivalent P-P and P-SV horizons that correlate with the Top of Marcellus, Cherry Valley Limestone, and Base of Marcellus. Examples of these depth-equivalent surfaces are illustrated on Figure 9.26.

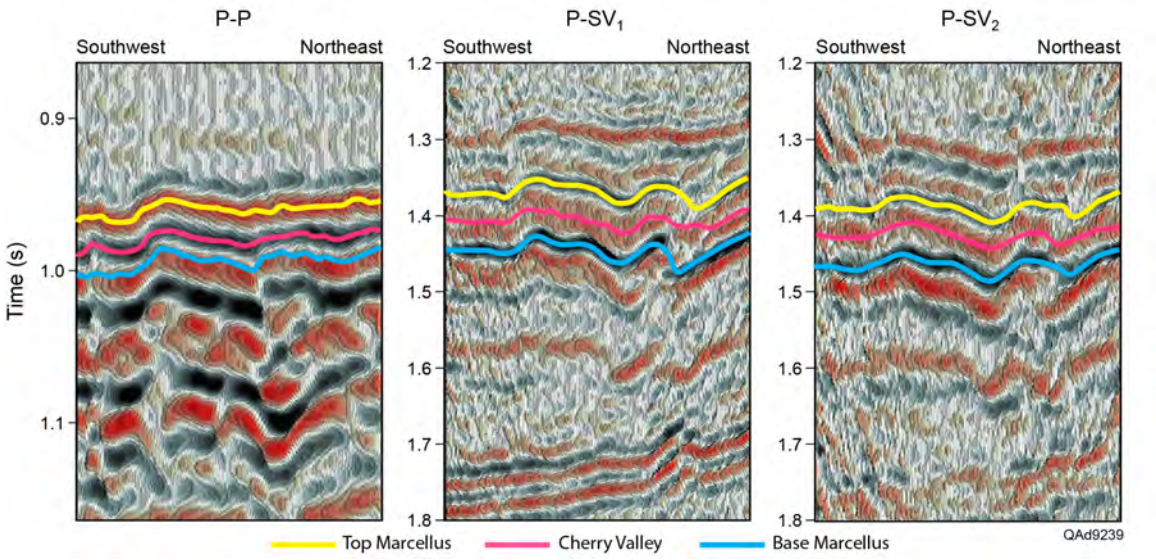

Figure 9.26. Profiles showing P-P, P-SV_1, and P-SV_2 images of the Marcellus interval.

Visual inspection of the profiles displayed on Figure 9.26 implies both P-SV modes have a better vertical resolution across the Marcellus interval than do P-P data. The improvement in spatial resolution provided by S-wave modes is another important research finding that encourages the use of multicomponent seismic technology in shale-gas studies rather than relying on only single-component P-P seismic data.

The profiles exhibited on Figure 9.26 show the top and base of the Marcellus interval are associated with bold reflection events in all three data volumes. However, mapping the Cherry Valley horizon posed problems. The Cherry Valley Limestone was not imaged as an individual reflection trough or peak in any seismic data volume, making any attempt to create a Cherry Valley horizon arbitrary. Automatic picking algorithms failed to track any consistent seismic feature related to the Cherry Valley Limestone, making it necessary to

find a seismic attribute that might help discriminate the Cherry Valley unit from its surrounding Marcellus Shale units. After a series of trials, it was determined instantaneous phase was the best attribute to use to define the Upper Marcellus-Cherry Valley interface. An example profile from the P-SV_2 data volume is shown on Figures 9.27 and 9.28 to illustrate the advantage of using instantaneous frequency to map the Cherry Valley Limestone interface. Manual interaction was required to extend the Cherry Valley interface across some areas of image space.

Frequency spectra calculated in seismic windows dominated by the Marcellus interval are displayed on Figure 9.29. These spectra confirm the frequency content of P-SV_1 data across the Marcellus Shale interval spans a broader range (10-40 Hz) than do P-P data (15-30 Hz). This frequency comparison indicates P-SV_1 data should lead to improved resolution of prospect features. P-SV_2 data are characterized by a narrower frequency band dominated by lower frequencies (10-20 Hz). The lack of higher frequencies in P-SV_2 data indicates the P-SV_2 data volume will be the least valuable of the three post-stack volumes for analyzing the Marcellus interval. However, P-SV_2 data were never ignored in our interpretation. In particular, P-SV_2 data were essential for calculating azimuthal anisotropy behavior exhibited by fast-S and slow-S modes. Such anisotropy is critical for quantifying fractures and horizontal stress fields related to the Marcellus Shale.

The improved resolution of Marcellus geology provided by P-SV data compared to P-P data is more striking when wavelength spectra are considered. P-P wavelengths (λ_P) are defined as $\lambda_P = V_P/f$, where f = frequency, and P-SV wavelengths (λ_S) are defined as $\lambda_S = V_S/f$. Thus,

$$\lambda_S = \lambda_P (V_S/V_P). \quad (9.1)$$

Because the V_P/V_S velocity ratio within the Marcellus is approximately 1.6, this wavelength relationship simplifies to,

$$\lambda_S = 0.62\lambda_P. \quad (9.2)$$

P-SV wavelengths are thus significantly shorter than P-P wavelengths within the Marcellus Shale interval.

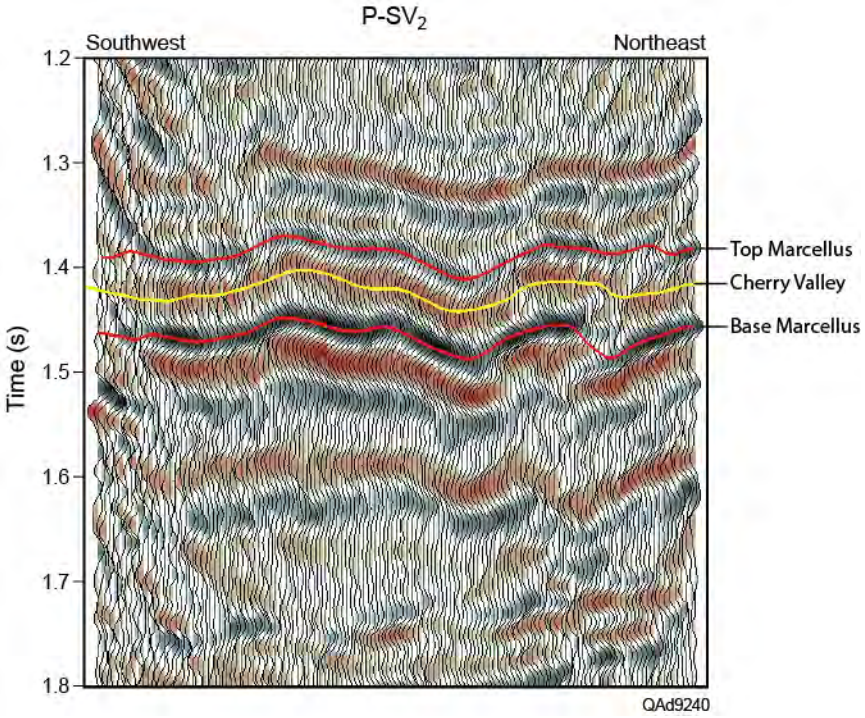

Figure 9.27. Variable-area wiggle-trace profile through P-SV_2 data volume with interpreted horizons across the Marcellus Shale interval.

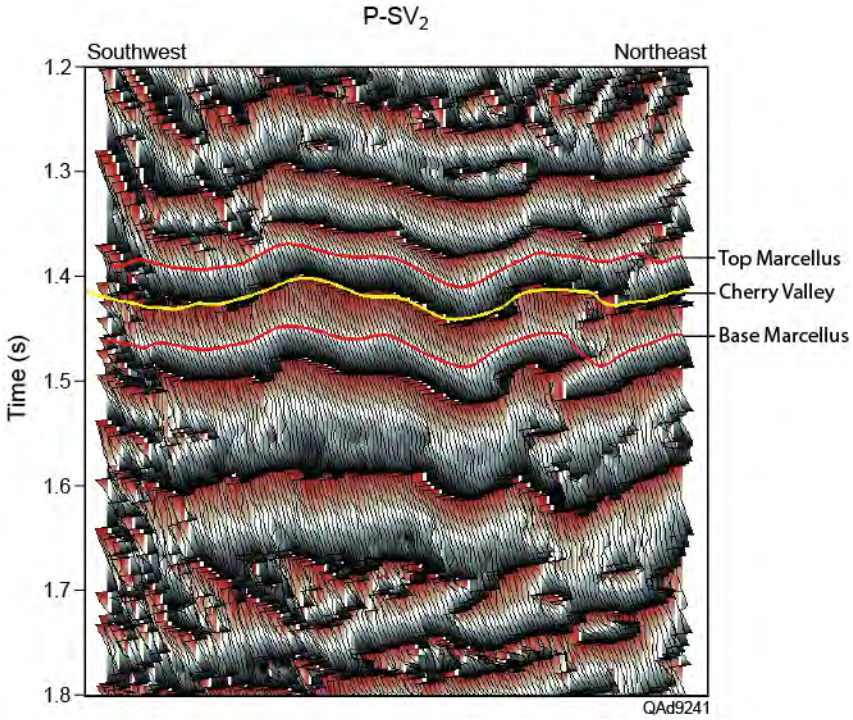

Figure 9.28. Instantaneous phase display along the profile of Figure 9.27. On this profile, the Cherry Valley correlates with a distinctive zero crossing in instantaneous phase. On other profile, manual interaction was required to define the interface.

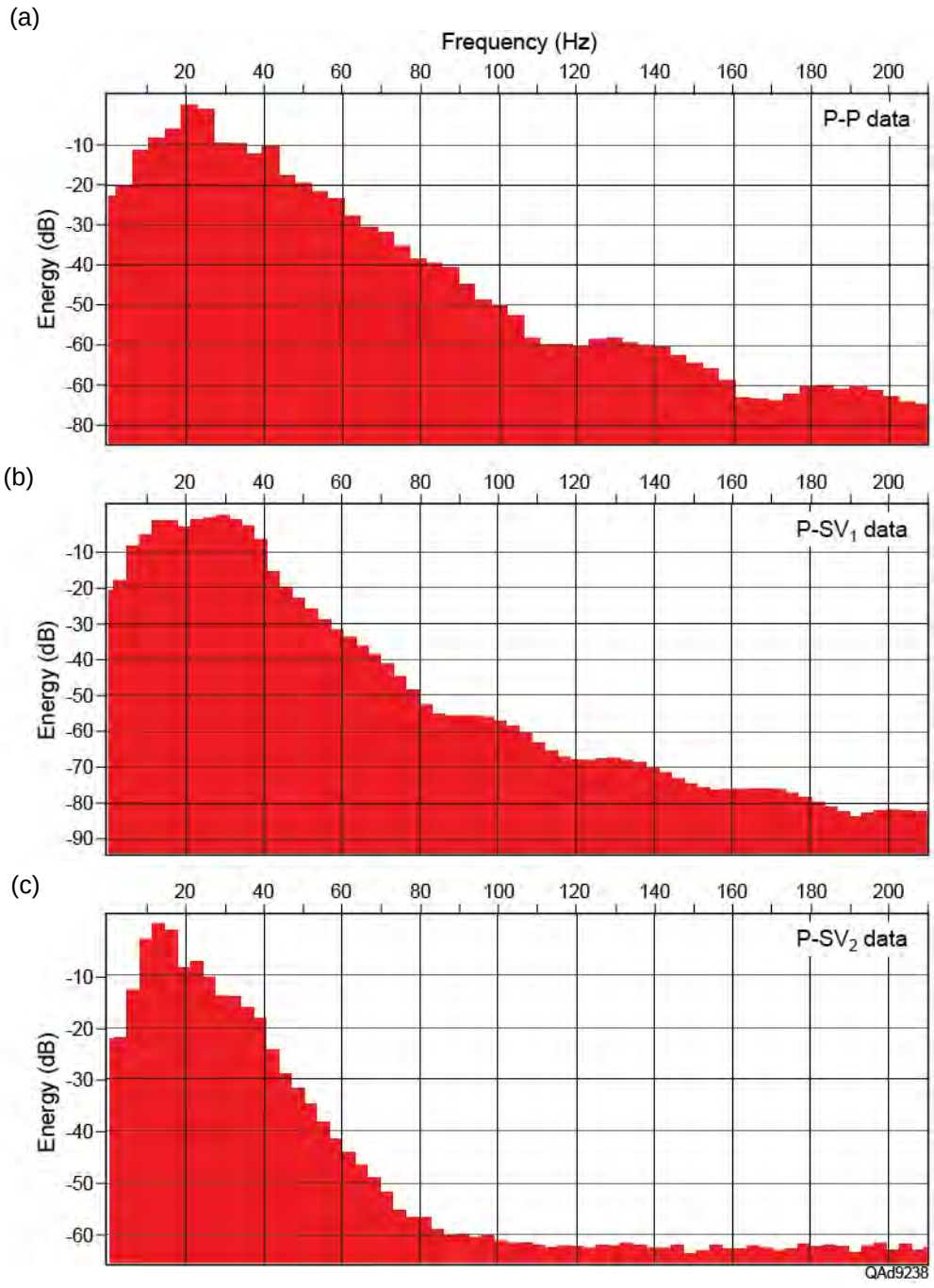

Figure 9.29. (a) P-P frequency spectrum across the Marcellus interval (900–1100 ms). (b) P-SV_1 frequency spectrum across the Marcellus interval (1300–1600 ms). (c) P-SV_2 frequency spectrum across the Marcellus interval (1300–1600 ms).

Marcellus Structural Interpretation

Structural complexity increases within the Marcellus interval. Both P-P and P-SV data showethe Marcellus has a strong structural-fold fabric, with fold axes trending east-to-west. These linear folds were mapped and correlated in both P-P and P-SV data volumes to better understand local effects of tectonic stress on the Marcellus. Although the natural fracture pattern within the Marcellus Shale is below the resolution of these post-stack seismic data, these structure maps provide a partial understanding of probable Marcellus fracture patterns. Understanding stress fields is useful for determining where natural fractures should be localized and for predicting how embedded fractures may behave when reactivated during hydraulic fracture treatments, or when pore pressure is altered because of fluid injections.

Similar fold patterns occur in both the Upper and Lower Marcellus units, but folds within the Lower Marcellus have slightly larger vertical relief than do their equivalents in the Upper Marcellus. These differences in fold height imply stresses acting on the Lower Marcellus may have been greater than stresses that generated folds in the Upper Marcellus. Folds are evident on P-P data (Fig. 9.30) but are more pronounced in P-SV_1 data (Fig. 9.31) and P-SV_2 data (Fig. 9.32). Because of the limited size of our 3D3C seismic survey (9 mi^2 [23 km^2] of image space), we cannot demonstrate that the structural complexities associated with the Marcellus Shale are associated with any specific regional orogenic event (for example, Taconian or Acadian), or if they are caused by more recent neotectonic joint systems formed during regional uplifting.

Conventional interpretation of compressional stresses implies maximum horizontal stress is oriented perpendicular to the long axis of the folds shown on Figures 9.30 to 9.32. The local azimuth of minimum horizontal stress σ_2 is thus approximately east-west. The local azimuth of maximum horizontal stress σ_1 is approximately north-south. As a result, structural deformation across this seismic image space was north-south, which produced the series of east-west structural ripples shown on Figures 9.30 to 9.32.

(a)

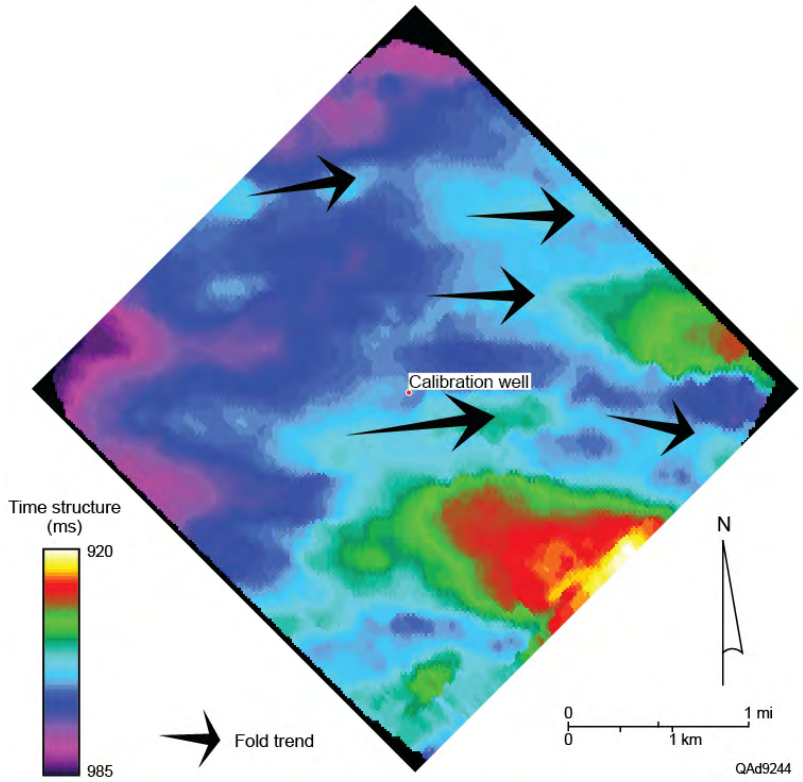

(b)

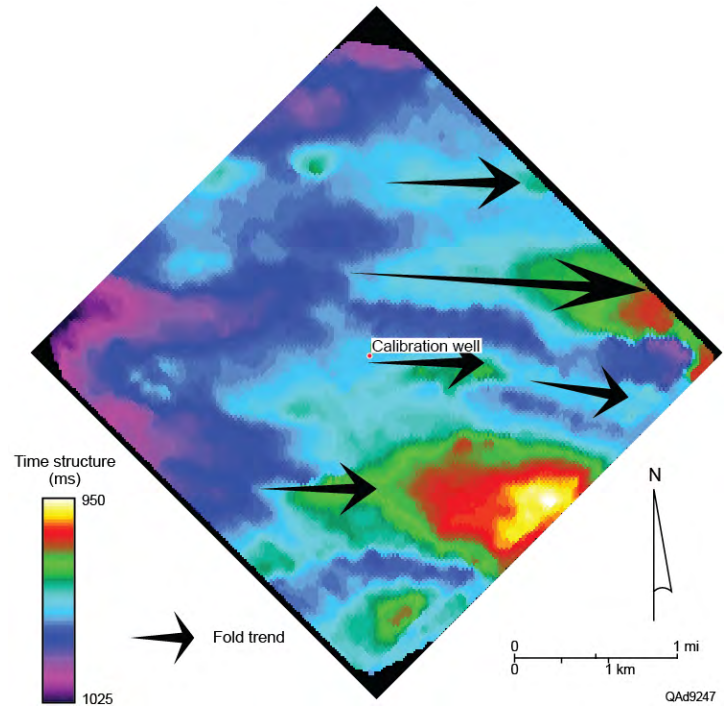

Figure 9.30. (a) Upper Marcellus Shale P-P time structure. (b) Lower Marcellus Shale P-P time structure. The arrows show linear fold axes and azimuths of minimum horizontal stress.

(a)

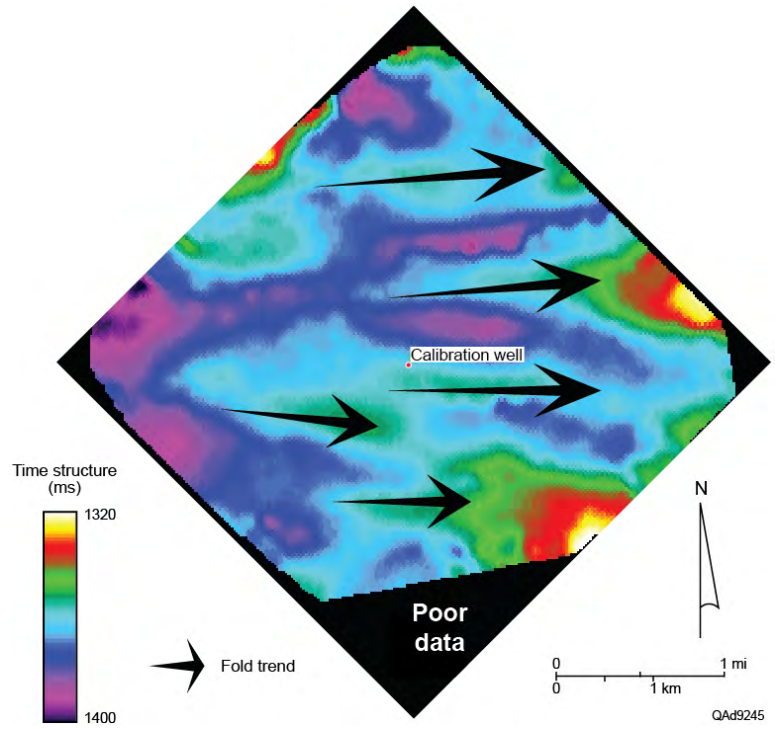

(b)

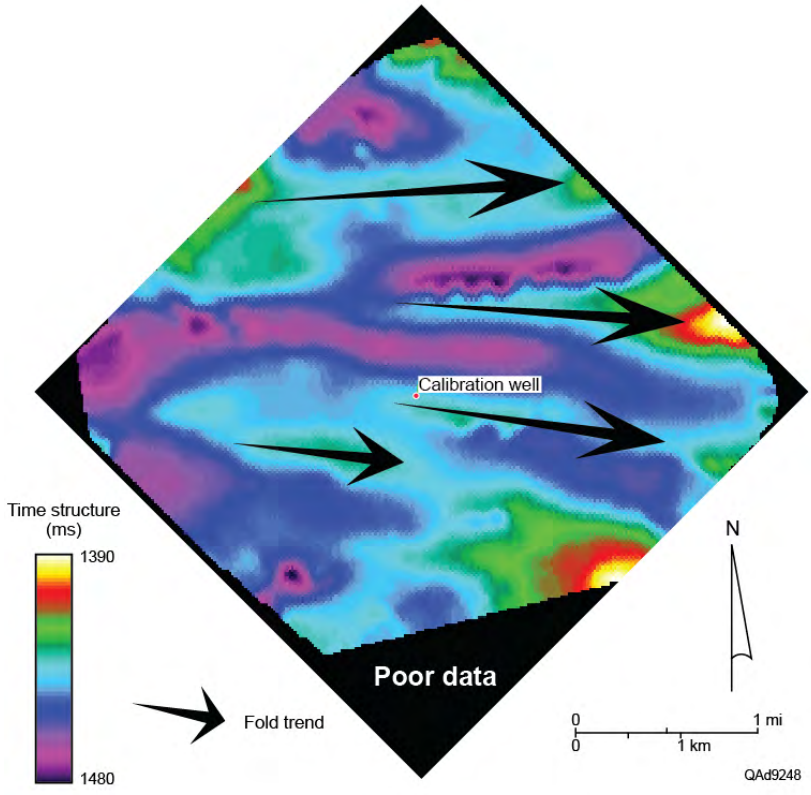

Figure 9.31. (a) Upper Marcellus Shale P-SV_1 time structure. (b) Lower Marcellus Shale P-SV_1 time structure. The arrows show linear fold axes and azimuths of minimum horizontal stress.

(a)

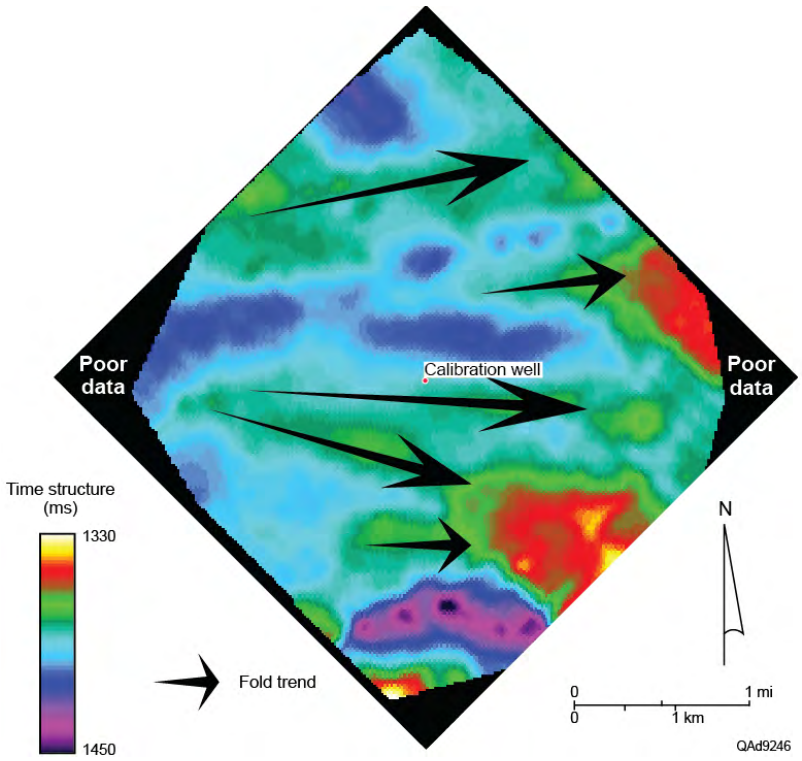

(b)

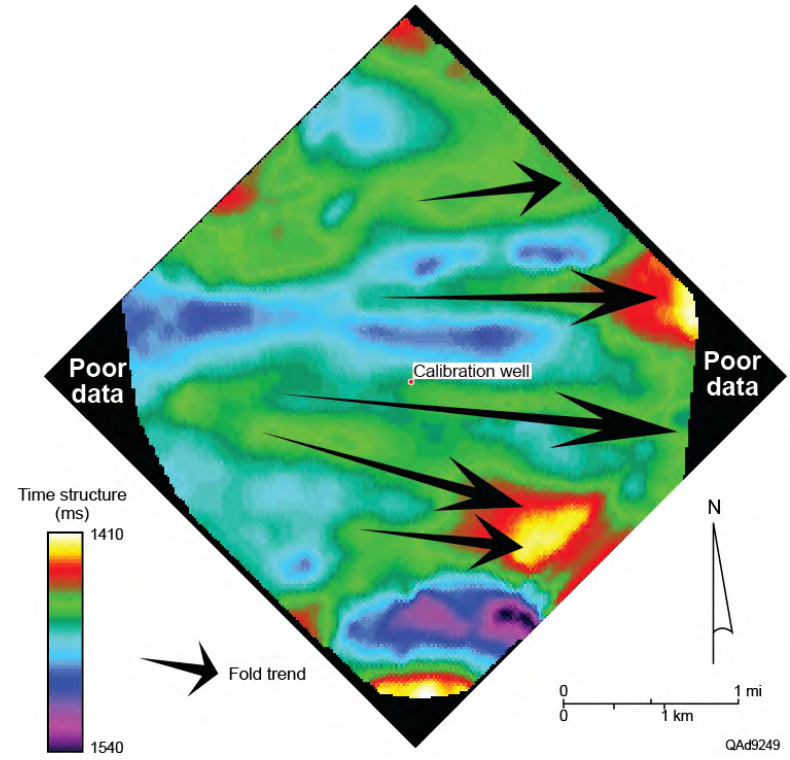

Figure 9.32. (a) Upper Marcellus Shale P-SV_2 time structure. (b) Lower Marcellus Shale P-SV_2 time structure. The arrows show linear fold axes and azimuths of minimum horizontal stress.

The relationship between natural fracture orientations and present-day stress are important factors in well planning for hydraulic fracturing. The orientation of natural fractures was evaluated in the central calibration well where a shear wave anisotropy log was acquired. Rose diagrams of interpreted fracture orientations generated by Halliburton, the logging contractor, show fracture orientations in the Upper Marcellus (Fig. 9.33a) and Lower Marcellus (Fig. 9.33b) range from slightly south of east-west to approximately 45-degrees north of east-west. The orientations of extensional fractures and shear fractures drawn on the rose diagrams are our interpretations of the fracture patterns, not Halliburton's interpretation. If this fracture interpretation is implemented, maximum horizontal stress σ_1 would align with extensional fractures, making σ_1 have an orientation approximately 100-degrees from north, which contradicts the fold-based stress interpretation shown as Figures 9.30 through 9.32. A significant fact implied by these rose diagrams is that most fractures within the Marcellus interval are oriented parallel to fold axes within the Marcellus interval. Fracture set A labeled on each display is our interpretation of possible shear fractures, which typically are oriented approximately 30-degrees away from extensional fractures. We conclude the seismic-based interpretations that maximum horizontal stress is north-south (Figs. 9.30 – 9.32) is correct for this prospect area rather than this local, log-based indication that maximum horizontal stress is east-west.

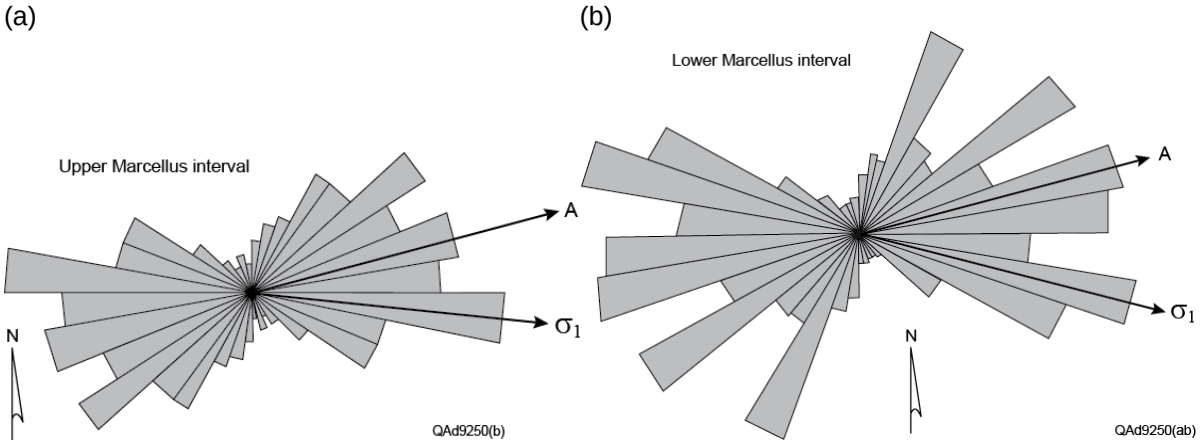

Figure 9.33. Rose diagrams calculated from borehole image logs acquired in the central-image calibration well for (a) Upper Marcellus and (b) Lower Marcellus. σ_1 defines the "interpreted" direction of maximum horizontal stress implied by these rose diagrams. In this interpretation, fractures along trend σ_1 should be extensional fractures. Shear fractures should then be oriented in a direction that is usually in a direction approximately 30-degrees away from σ_1, such as the fractures sets labeled A.

Marcellus Seismic Amplitude Attributes

Numerous horizon-constrained seismic attributes were generated during our interpretation of the Upper Marcellus and Lower Marcellus intervals. The objective of this amplitude-attribute analysis was to determine if any amplitude calculations derived from post-stack data volumes would provide additional evidence of faulting, fracturing, or jointing within the Marcellus Shale interval.

We found no amplitude attribute that provided structural, faulting, or fracturing information about the Marcellus that differed from information shown by structural maps (Figs. 9.30 to 9.32). Amplitude attribute maps for the Lower Marcellus showed narrow trends of increased P-P and P-SV_1 reflectivities (Figs. 9.34b and 9.35b) that tracked the structural folds on corresponding structural-fold maps for these two seismic modes (Figs. 9.30b and 9.31b). We have no technical explanation why there is a good correlation between intra-Marcellus folds and P-P and P-SV_1 reflectivity within the Lower Marcellus and a poor correlation between these two properties for the Upper Marcellus. We document only our empirical observation of good-vs-poor correlations for these two seismic attributes for each of the Marcellus units. No reflectivity pattern emerged from our interpretation of P-SV_2 data that had any structural or stratigraphic significance across the Marcellus interval (Fig. 9.36).

(a)

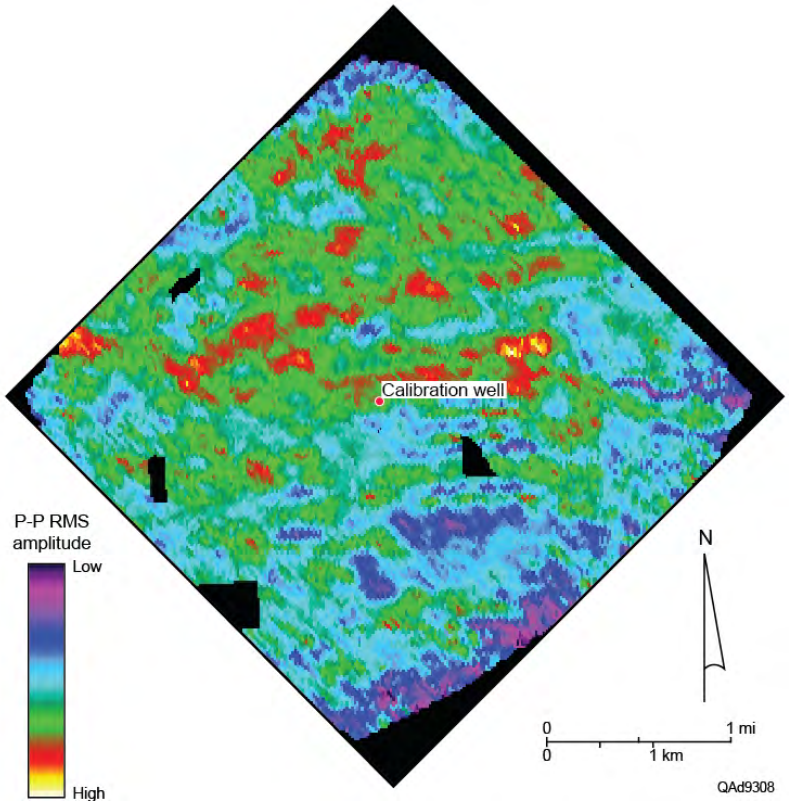

(b)

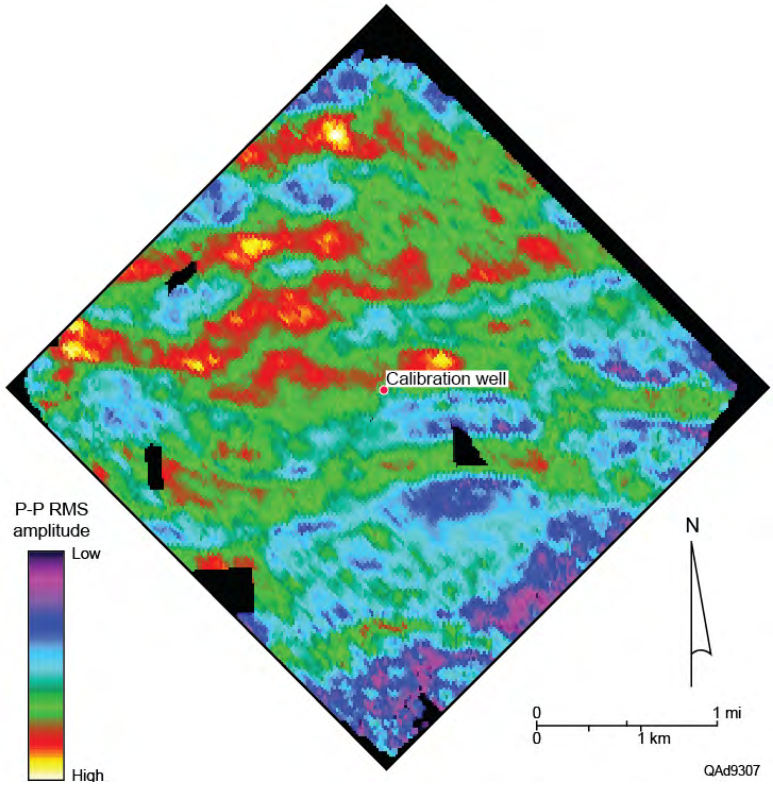

Figure 9.34. P-P rms amplitudes across (a) Upper Marcellus and (b) Lower Marcellus.

(a)

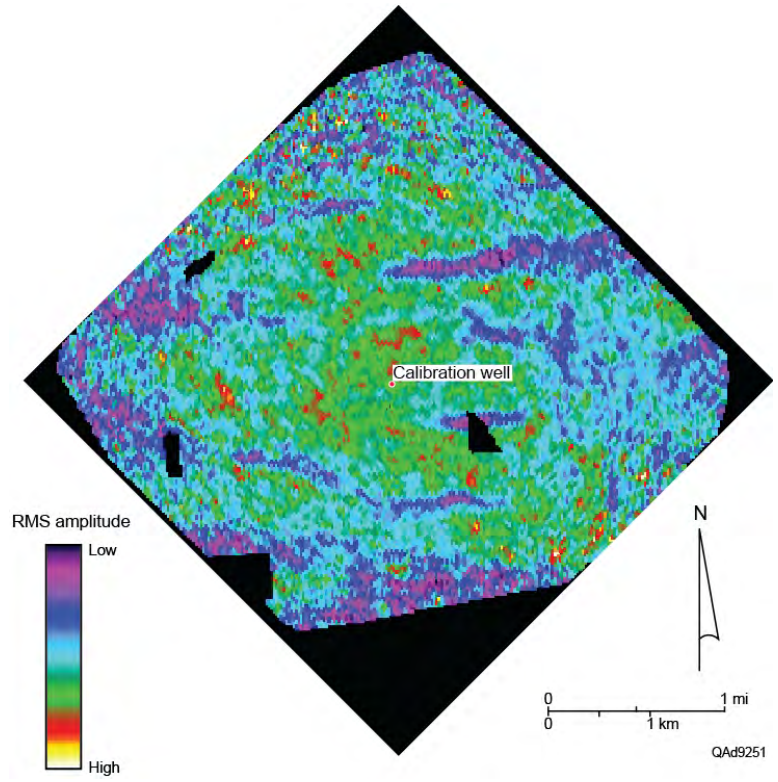

(b)

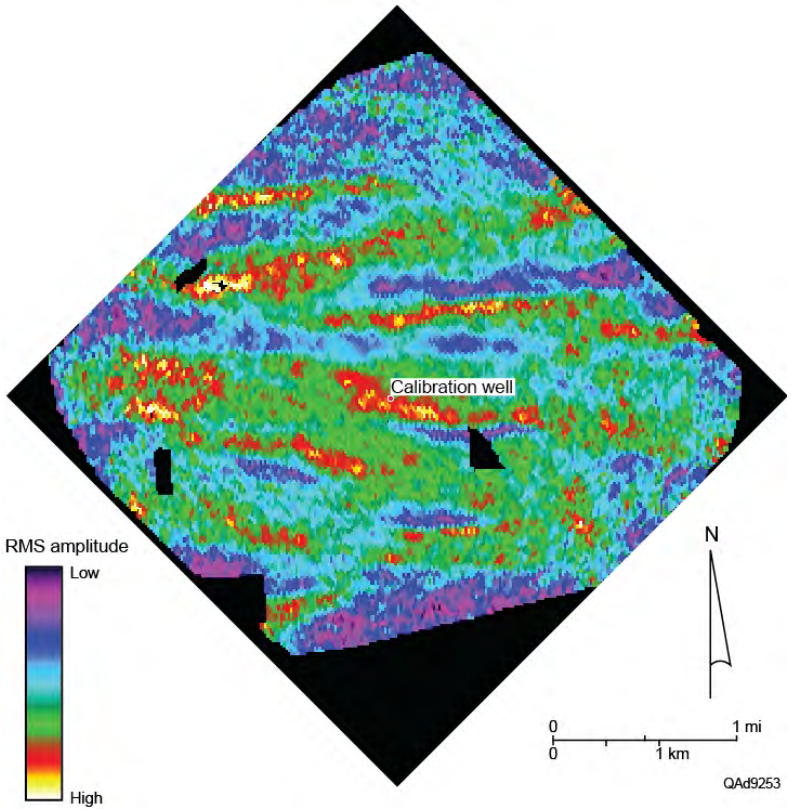

Figure 9.35. P-SV_1 rms amplitudes across (a) Upper Marcellus and (b) Lower Marcellus.

(a)

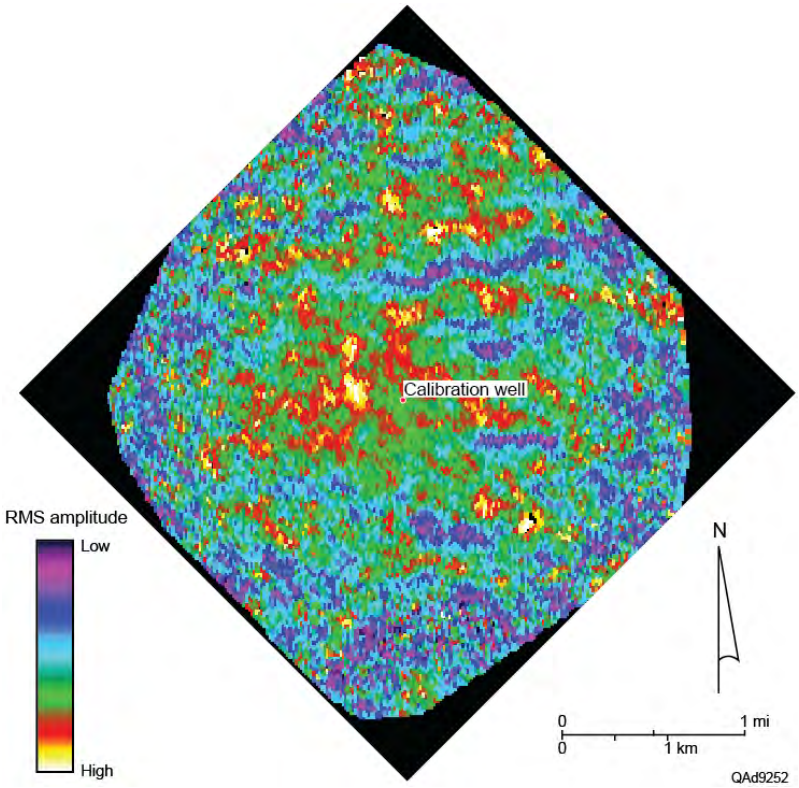

(b)

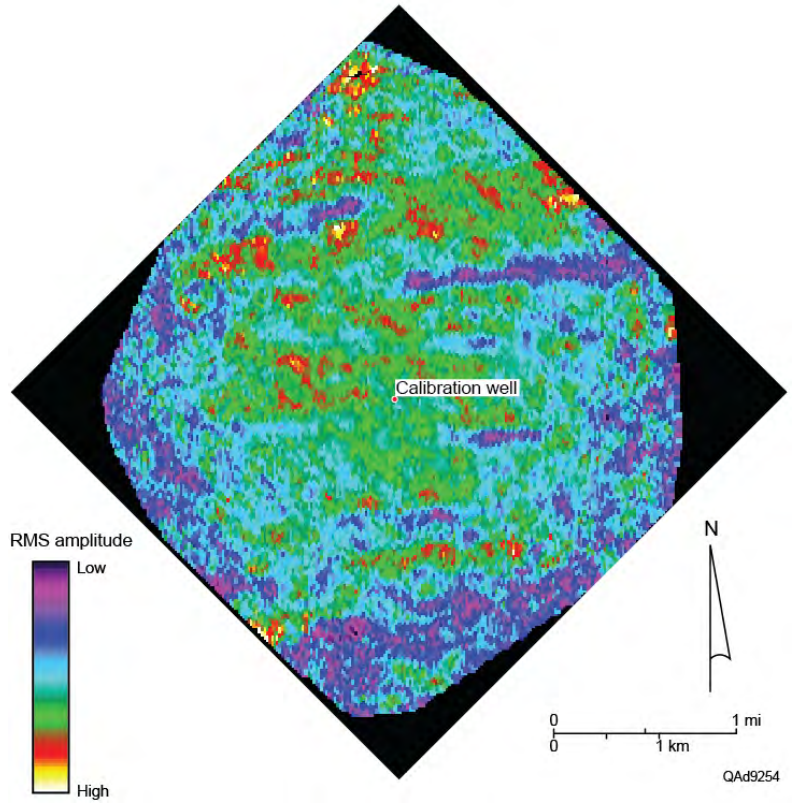

Figure 9.36. P-SV_2 rms amplitudes across (a) Upper Marcellus and (b) Lower Marcellus.

Marcellus Stratal Slices

The stratal slicing concept described by Figure 9.21 was applied to the Marcellus Shale interval to determine if a stratal-slice approach could find stratigraphic features not exhibited by other interpretations. Depth-equivalent stratal slices from each of the three data volumes are displayed on Figure 9.37. Each stratal slice shows amplitude anomalies that trend in the same direction as the structural folds exhibited on the maps displayed on Figure 9.30 to 9.32. This stratal slicing effort added confidence to the structural fold picture previously developed (Figs. 9.30–9.32) and provided no evidence that would make an interpreter suspect there was internal compartmentalization within the Marcellus. At the depth level chosen for this comparison, both S-mode volumes show stronger amplitudes than does the P-P mode. These example stratal slices are representative of those created across the full Marcellus interval in that amplitude anomalies trended along structural folds, and no subtle stratigraphic pinch-outs or other features were found.

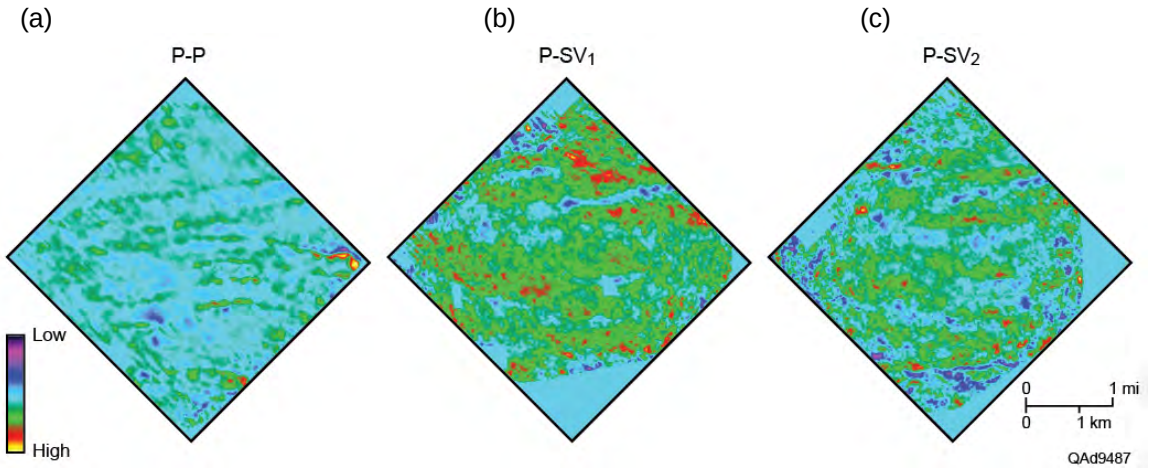

Figure 9.37. Comparisons of depth-equivalent stratal slices within the Upper Marcellus Shale. (a) P-P stratal slice. (b) P-SV_1 stratal slice. (c) P-SV_2 stratal slice. The attribute displayed on the slices is reflection amplitude.

Marcellus S-Wave Anisotropy

Vertical fractures, when consistently oriented across an interval, cause that interval to be an azimuthally anisotropic seismic propagation medium. Because the mechanical strength of such a medium is stronger parallel to fractures than it is perpendicular to fractures, a seismic mode exhibits a faster propagation velocity parallel to fractures than it does perpendicular to fractures.

This difference in propagation velocities is more pronounced for S waves than it is for P waves. For this reason, azimuthal anisotropy is often referred to as S-wave anisotropy. The quantity S_{ANI} will be used to indicate seismic-based S-wave anisotropy is defined as,

$$(9.3) \quad S_{ANI} = (V_1 - V_2) / V_2,$$

where V_1 is fast-S velocity and V_2 is slow-S velocity. If fast-S and slow-S images of a targeted anisotropic interval are available, seismic-based interval values of V_1 and V_2 can be approximated as,

$$(9.4) \quad V_1 = D / \Delta T_1 \text{ and } V_2 = D / \Delta T_2,$$

where D is the thickness of the interval, ΔT_1 is the time thickness of the interval on a fast-S image, and ΔT_2 is the time thickness of the interval on a slow-S image. Substituting Equation 9.4 into Equation 9.3 leads to a simple calculation that transforms fast-S and slow-S post-stack seismic data into estimates of seismic-based S-wave anisotropy:

$$(9.5) \quad S_{ANI} = (\Delta T_2 / \Delta T_1) - 1.$$

We calculated this quantity, S_{ANI}, across the Upper Marcellus and Lower Marcellus intervals. Maps of these seismic-based estimates of S-wave anisotropy are displayed on Figure 9.38.

Anisotropy measurements taken at the calibration well are: Upper Marcellus 1.7% and the Lower Marcellus 1.6%, respectively. At the location of the calibration well, the Upper Marcellus has an east-to-west trending anisotropy zone of approximately 2.5-percent immediately north of the well location. The Lower Marcellus shows a northwest-to-southeast trending anisotropy zone of approximately 2-percent that passes immediately south of the calibration well. The areas highlighted with green-red-to-yellow colors have slightly higher S-wave anisotropy and may define localized increases in fracture intensity.

(a)

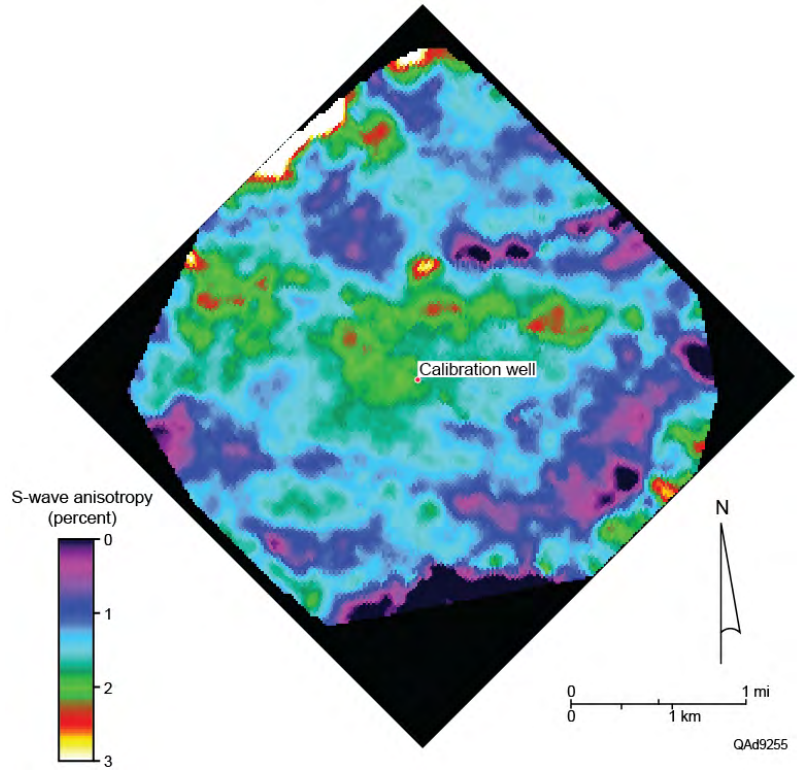

(b)

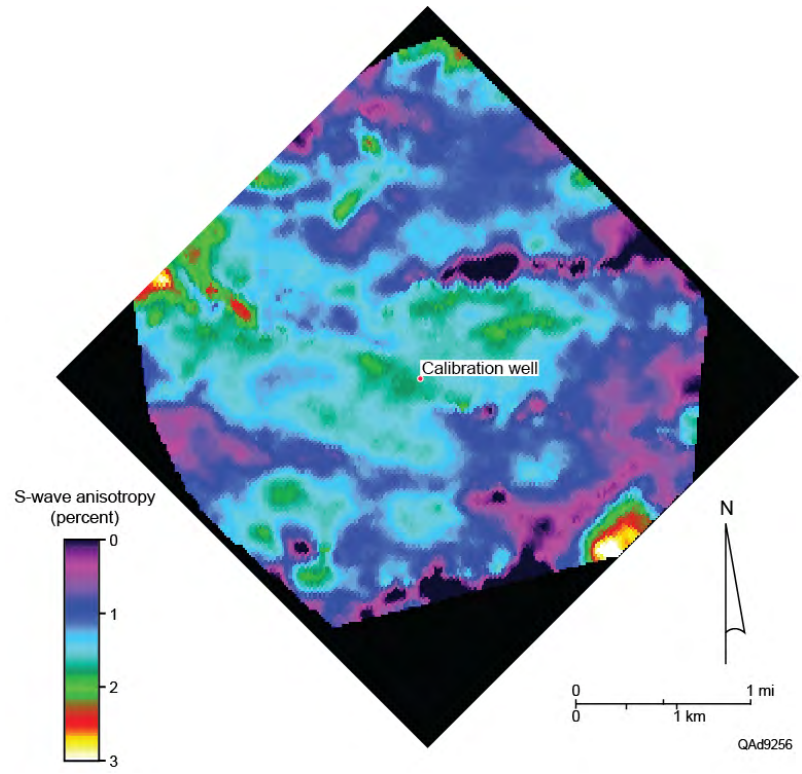

Figure 9.38. S-wave anisotropy calculated for (a) Upper Marcellus and (b) Lower Marcellus.

The S-anisotropy values shown on Figure 9.38 are sensitive to subtle variations in the position of the Cherry Valley interface that separates Upper and Lower Marcellus. Because the Cherry Valley Limestone could not be interpreted with automatic horizon-picking algorithms, manual intervention by an interpreter was required to define the position of this thin intra-Marcellus limestone. This interpreter action may introduce some ambiguity in the position of the boundary separating Upper and Lower Marcellus. Thus S-wave anisotropy was calculated across the total Marcellus interval to compare against results determined for the upper and lower units of the Marcellus. This total-Marcellus anisotropy is displayed as Figure 9.39 and shows anisotropy varies from 0.75 to 1.7 percent. For all practical purposes, S-wave anisotropy within the Marcellus Shale is too small to use traveltime differences in fast-S and slow-S modes to infer fracture density.

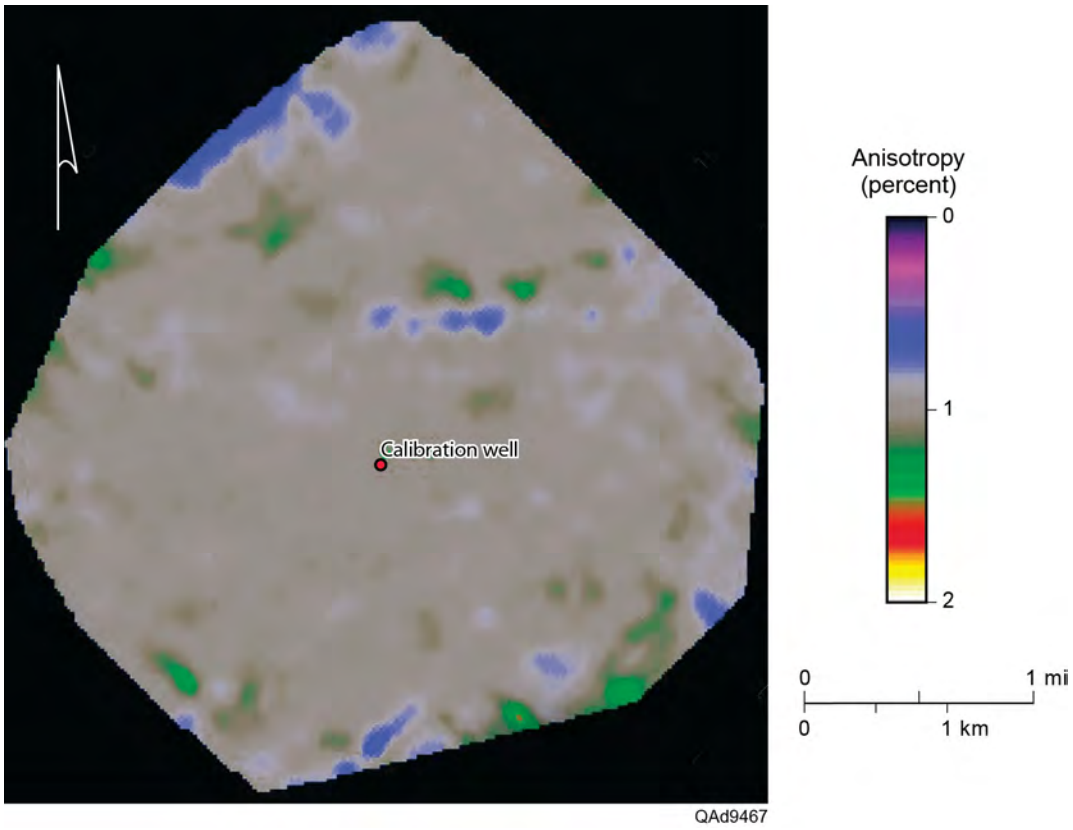

Figure 9.39. S-wave anisotropy across the total Marcellus interval.

Curvature

Curvature is a recent seismic attribute developed to aid interpreters. Two types of curvature can be calculated: (1) structural curvature, and (2) amplitude curvature. Amplitude curvature is a calculation that reacts to lateral variations in reflection amplitude strength along an interpreted horizon. Structural curvature is a calculation that describes lateral variations in the time (or depth) coordinate of a horizon. Here, the emphasis is on structural curvature, not amplitude curvature.

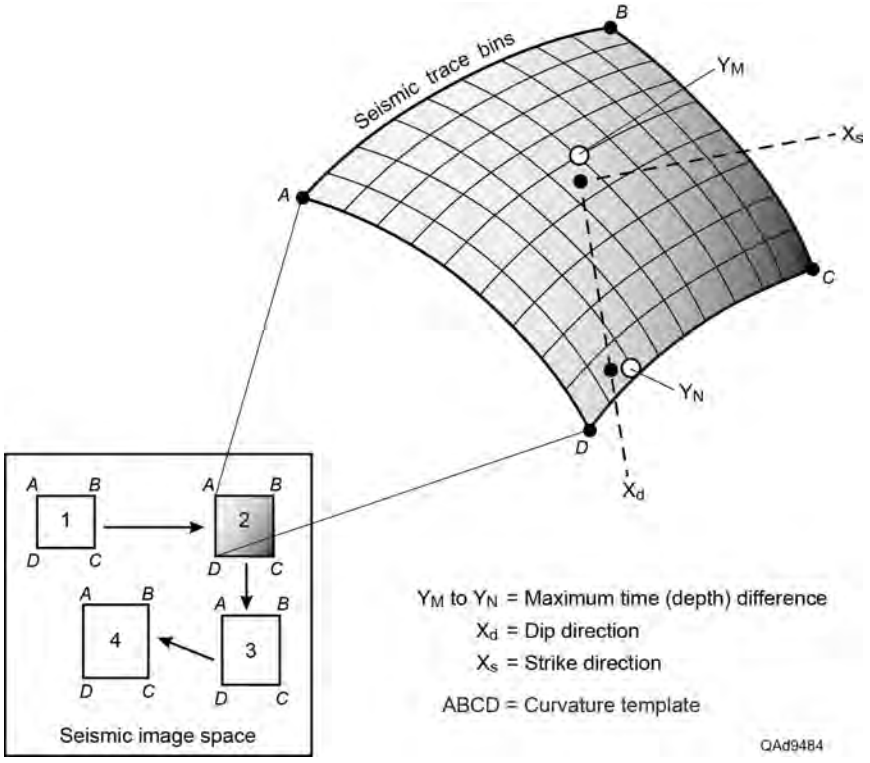

Figure 9.40. Procedure used to calculate local dip and strike directions. In this example, local dip and strike related to data point Y_M are calculated using a 9 × 9 analysis template ABCD. This template moves over the interpreted seismic horizon so that analysis point Y_M is positioned at every data point on the surface. The movement of the template to four different analysis points is shown at the lower left.

Structural Curvature

Structural curvature is calculated using time-based or depth-based seismic data that define geometrical configurations of subsurface structure. First and second time derivatives (time-based seismic data), or first and second depth derivatives (depth-based seismic data), can be calculated throughout a 3D volume of interest and then classified in a number of ways, such as most-positive curvature, most-negative curvature, minimum curvature, maximum curvature, mean curvature, Gaussian curvature, dip curvature, strike curvature, shape

index, or azimuth curvature. The list of curvature attributes that can be calculated continues to grow as more people apply curvature concepts to seismic data interpretation. Any structural curvature attribute can be filtered to emphasize long-wavelength curvature or short-wavelength curvature, depending on what an interpreter wishes to see in an interpretation.

We found **dip curvature** and **strike curvature** to be valuable seismic attributes for the Marcellus interval. The manner in which these two curvatures is determined is illustrated on Figure 9.40. Surface ABCD represents a portion of a seismic interpreted horizon that exhibits structural curvature. This small square of image bins is the area over which curvature is calculated. The size of this analysis area is arbitrary and can be defined by a seismic interpreter. In the example drawn on Figure 9.40, the dimensions of the analysis template are (9 bins) X (9 bins), which is a typical template size. Change in structure is measured in all azimuth directions from the central image bin Y_M of template ABCD. The azimuth in which the largest time (depth) difference is measured is defined as the local dip, which on Figure 9.40 is dashed line X_d passing from point Y_M to point Y_N. Local strike is defined as the azimuth normal to the calculated local-dip azimuth. This analysis template moves over the complete interpreted horizon so local dip and strike are calculated at every image bin on the interpreted horizon as shown in the lower left of the figure.

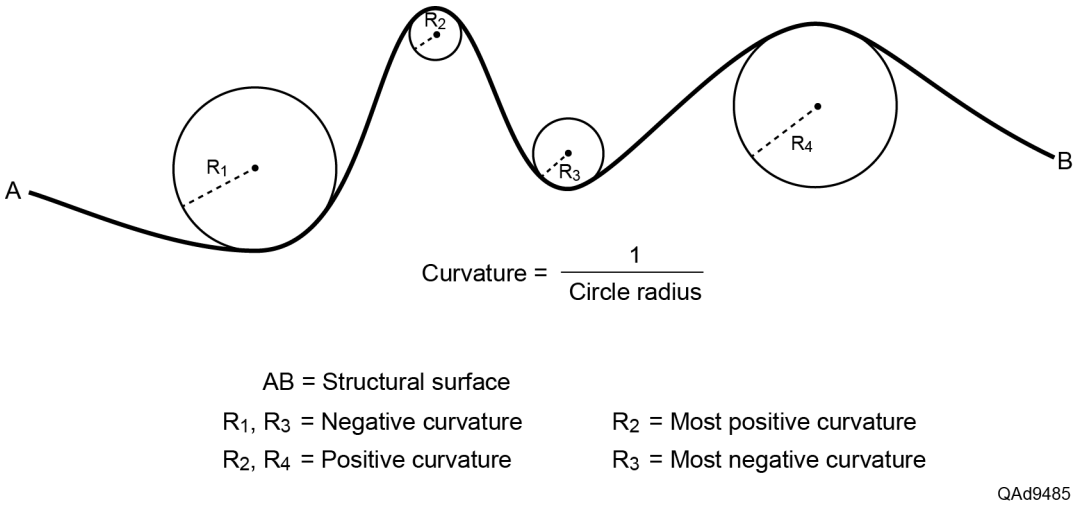

Figure 9.41. Estimating structural curvature by fitting circles to an interpreted structural horizon at each local point on the surface. This illustration is a 2D view along a selected profile traversing an interpreted surface.

After dip and strike directions are determined as continuous XY-coordinate functions across an interpreted horizon, dip and strike curvature are calculated by fitting circles to the structural surface as shown on Figure 9.41. When a circle of radius R is found such that its circumference makes maximum contact with local curvature of the structural surface, the inverse of the circle radius (1/R) is

defined as an indicator of structural curvature. On Figure 9.41, there are illustrations of positive curvature, negative curvature, most-positive curvature, and most-negative curvature.

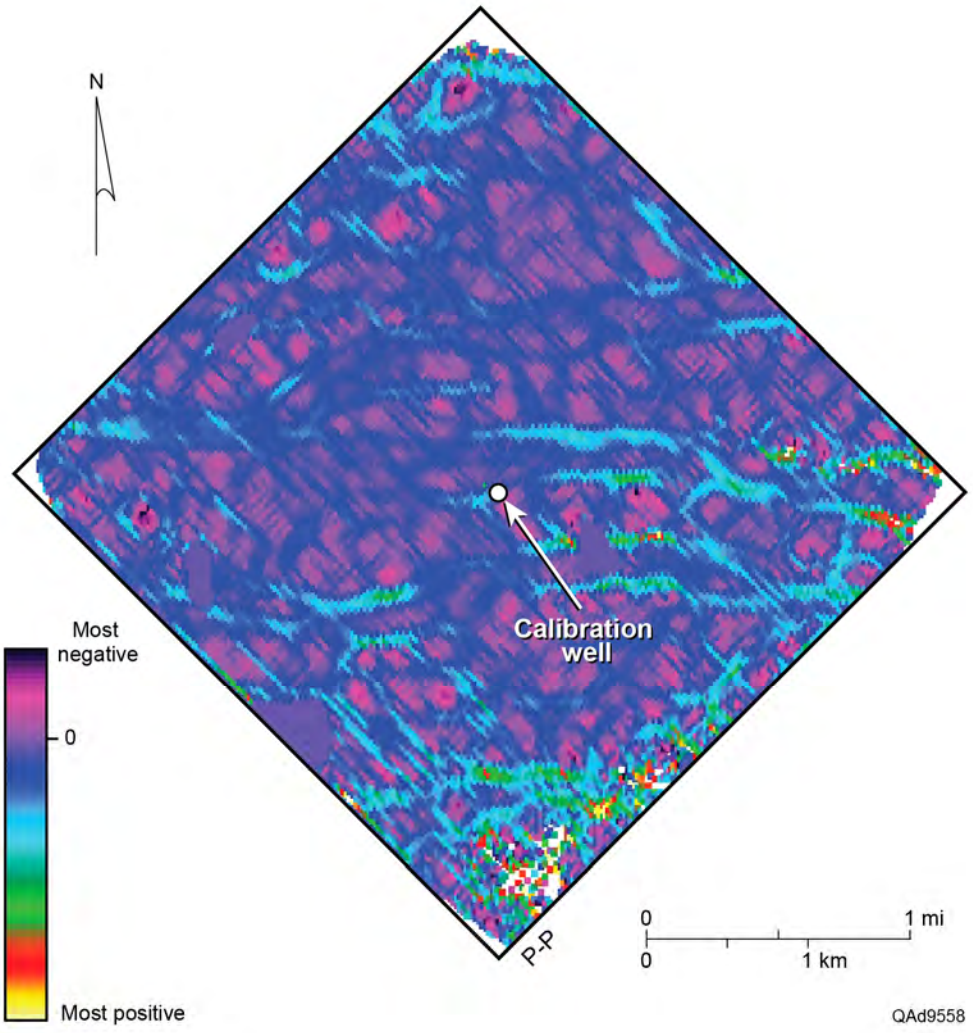

Figure 9.42. P-P dip curvature for the Upper Marcellus.

Marcellus Curvature

A structural curvature analysis was done for the Marcellus interval to identify trends of maximum curvature, which in turn, may correspond to trends of increased fracture intensity. Curvature was calculated in both dip and strike directions, as those attributes are defined on Figure 9.40. Results are displayed as Figure 9.42 for P-P data, Figure 9.43 for P-SV_1 data, and Figure 9.44 for P-SV_2 data. In each seismic image space, structural curvature calculated in the dip direction provided a map that exhibited less data-acquisition footprint effects than did curvature calculated in the strike direction. Thus the displays on

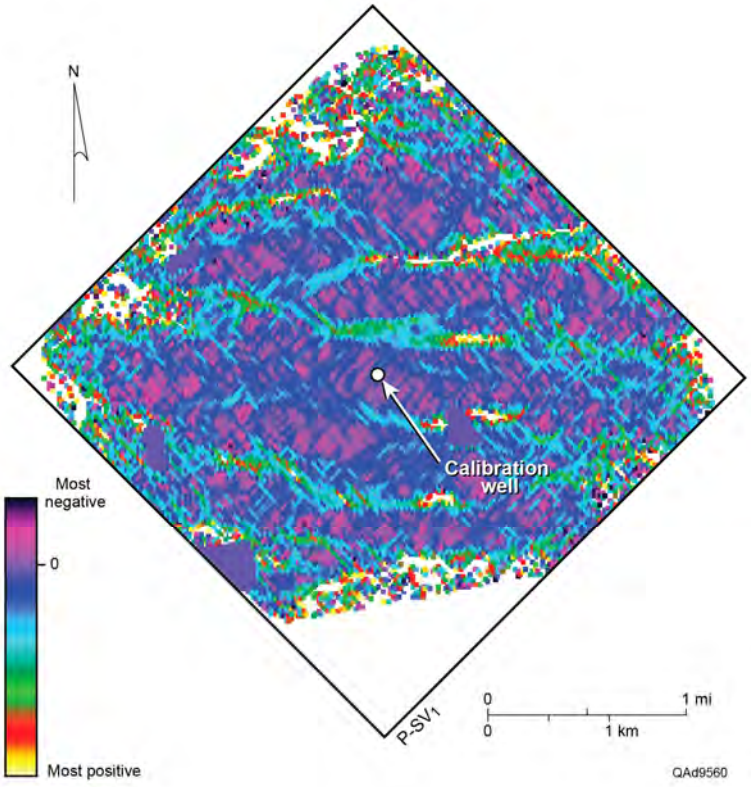

Figure 9.43. P-SV_1 dip curvature for the Upper Marcellus

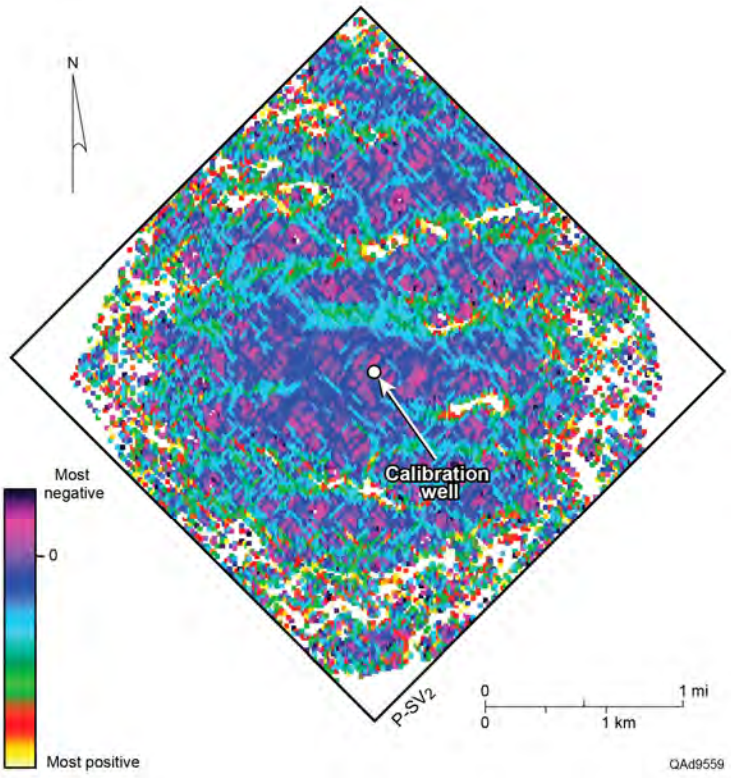

Figure 9.44. P-SV_2 dip curvature for the Upper Marcellus.

Figures 9.42–44 are restricted to curvature measured in the dip direction. These structural curvature results confirm the validity of the structural folds within the Marcellus displayed on Figures 9.30 through 9.32. The trends of maximum curvature (either most-positive or most-negative) are tentatively viewed as trends of enhanced fracture density.

Utica Shale Interval

Maps published by the Marcellus Center for Outreach and Research (MCOR) operated by Penn State University indicate the depth of the Utica Shale across our study area is approximately 12,000 ft (3660 m), and that the average thickness of the Utica interval should be 200 to 250 ft (60 to 75 m). These maps are displayed as Figures 9.45 and 9.46, respectively. Because we had no well control that extended to the local depth of the Utica Shale at our study site, we had to estimate the two-way time where the Utica Shale would be in P-P and P-SV seismic image spaces. We assumed a value of the V_P/V_S ratio between the base of the Marcellus Shale and the top of the Utica Shale to guide our interpretation of which P-SV reflection event corresponded with the top of the Utica Shale in the P-P image domain. We used the relationship:

$$\frac{V_P}{V_S} = 2\left[\frac{\Delta t_S}{\Delta t_P}\right] - 1,$$

to relate the V_P/V_S velocity ratio across the Marcellus-to-Utica interval to the ratio of the P-SV and P-P isochron thicknesses of the interval. In this equation, Δt_S is the isochron thickness of the Marcellus-to-Utica interval measured with P-SV data and Δt_P is the isochron thickness measured with P-P data.

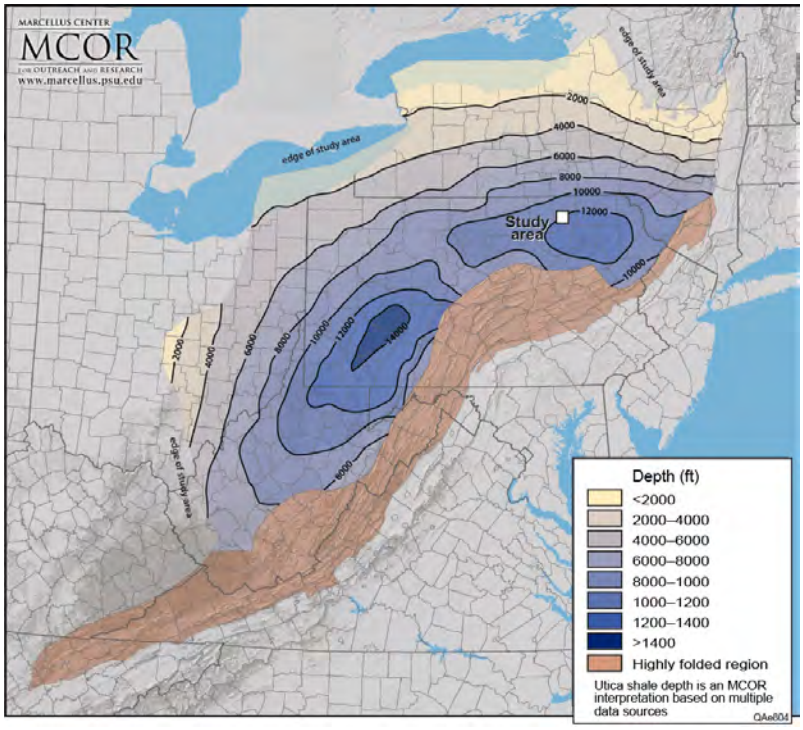

Figure 9.45. Utica Shale depth map (MCOR website, www.marcellus.psu.edu).

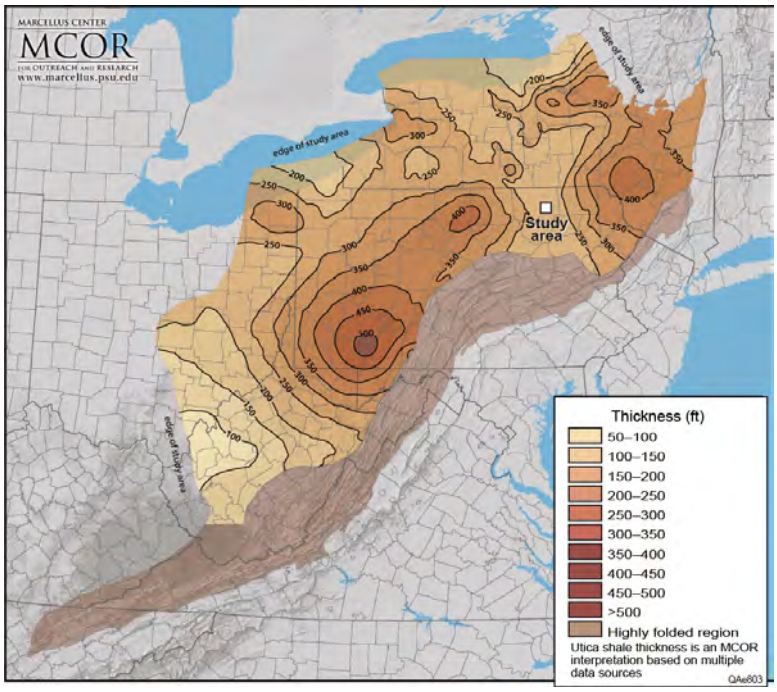

Figure 9.46. Utica Shale thickness map (MCOR website, www.marcellus.psu.edu).

We could not define the exact position of the Utica Shale in P-P image space because no deep P-wave calibration data were available. Thus we chose a prominent P-P reflection that we will refer to as a “near Utica” event (Figs. 9.47a, b) as the top of the Utica Shale interval. This particular reflection was selected Top Utica because it was the best quality reflection event that was twice as deep in P-P image time as was the Top Marcellus (1.8 sec for the “near Utica” and 0.9 sec for the Top Marcellus). This logic was used because the Utica Shale is approximately twice as deep as the Marcellus Shale in measured depth, with the depth of the Utica Shale being 12,000 ft [3660 m] versus a depth of 6075 ft [1830 m] for the Marcellus. Embedded in this logic is the assumption that the average velocity across the Marcellus-to-Utica interval is approximately the same as the average velocity to the depth of the Marcellus. The Top Marcellus is well constrained in P-P image space because of the high-quality synthetic seismogram that was used to identify the appropriate reflection (Fig. 9.5) for the Marcellus Shale.

We used a V_P/V_S ratio of 1.6 to determine which reflector in the P-SV_1 image domain corresponded with the robust P-P reflector we identified as “near Utica” because a V_P/V_S ratio of 1.6 was measured over most of the interval down to the Marcellus from log data acquired in the central-image calibration well. We assumed this same V_P/V_S value could be extended deeper to the estimated top of the Utica Shale unit. This assumption resulted in the selection of the P-SV_1 event identified on Figure 9.48b as the P-SV_1 “near Utica” reflection and to the choice of the P-SV_2 event identified on Figure 9.49b as the P-SV_2 “near Utica” reflection. As a confirmation of our logic, we used a V_P/V_S ratio of 2.0 across the Marcellus-to-Utica interval, but could not find any consistent P-SV_1 or P-SV_2 reflector (which would have to be approximately 150 ms deeper than the event shown on Figure 9.47b) that could be consistently mapped throughout the P-SV_1 and P-SV_2 data volumes.

(a) (b)

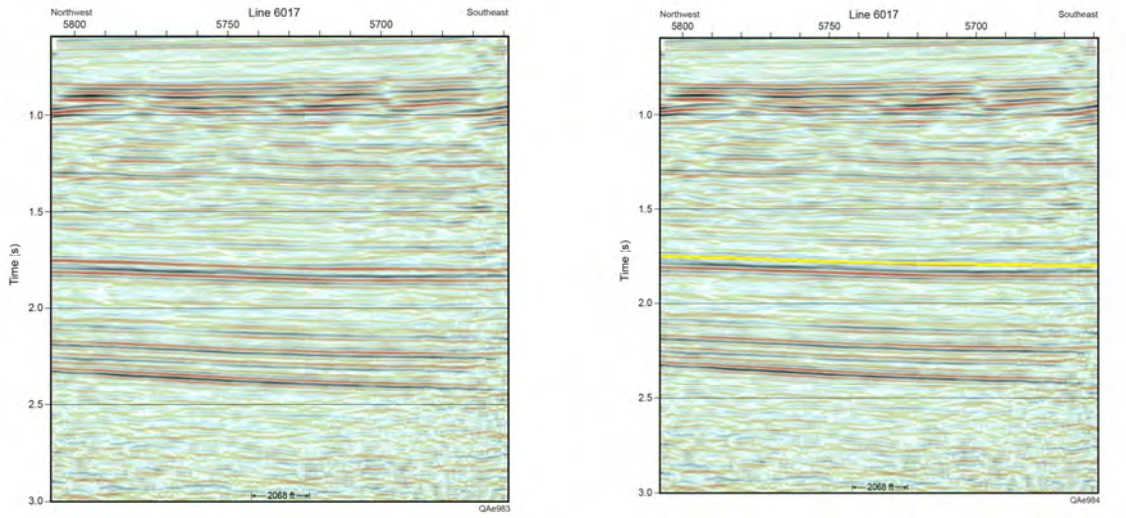

Figure 9.47. (a) Uninterpreted northwest to southeast P-P seismic profile passing through the center of P-P image space. (b) Interpreted northwest to southeast P-P seismic profile passing through the center of P-P image space. The selected P-P “near Utica” reflection is shown as the yellow horizon.

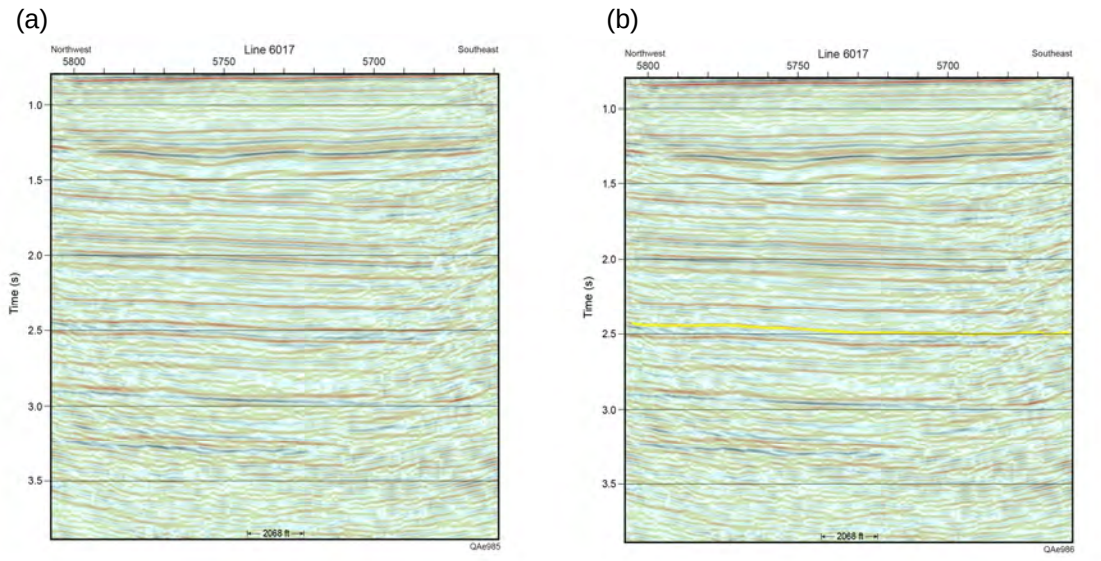

Figure 9.48. (a) Uninterpreted northwest to southeast P-SV_1 seismic profile passing through the center of P-SV_1 image space. (b) Interpreted northwest to southeast P-SV_1 seismic profile passing through the center of P-SV_1 image space. The event selected as the “near Utica” reflection is marked in yellow.

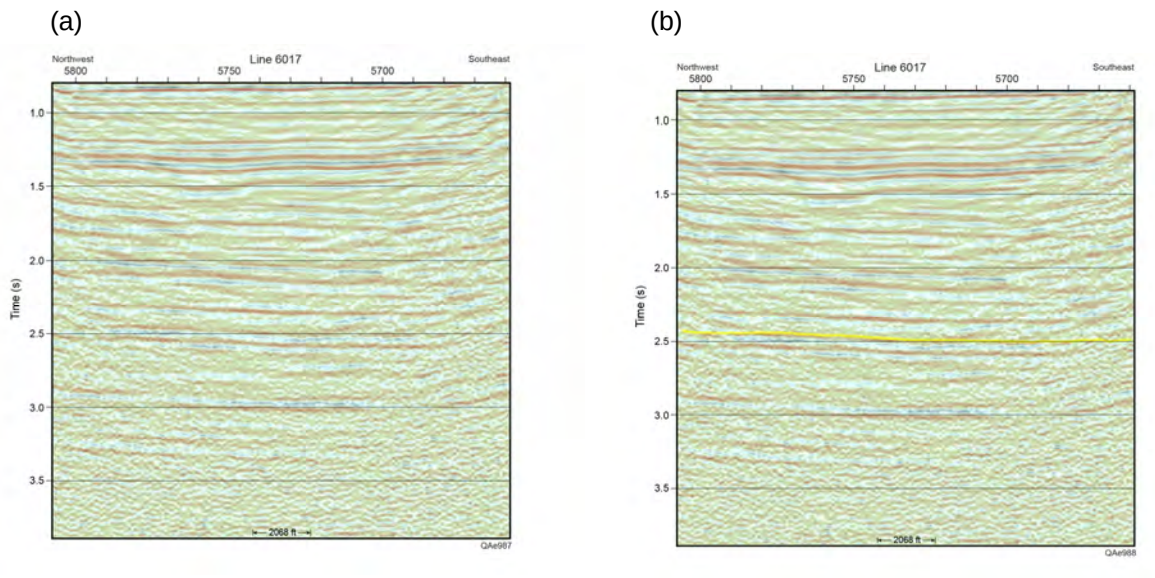

Figure 9.49. (a) Uninterpreted northwest to southeast P-SV_2 seismic profile passing through the center of P-SV_2 image space. (b) Interpreted northwest to southeast P-SV_2 seismic profile passing through the center of P-SV_2 image space. The event selected as the “near Utica” reflection is marked in yellow.

Spectral Analysis

The frequency content of reflection data across the Utica interval (Figs. 9.50 to 9.52) is not as broadband as the frequency content across the shallower Tully and Marcellus intervals (Figs 9.13 and 9.24). At the depth of the Utica Shale, P-P data have dominant energy in the frequency interval from 10 to 40 Hz, and P-P reflection strength then steadily decreases at a rate of approximately 0.2 dB/Hz. Across the Utica interval, both P-SV_1 and P-SV_2 data have dominant energy between 8 and 30 Hz, and reflection strength then decreases at a rate of 0.4 dB/Hz until the noise floor is reached at 160 Hz. The fundamental principle that the resolution of P-SV data is better than the resolution of P-P data still

exists for the deeper Utica Shale interval as has been emphasized for shallower Tully and Marcellus intervals (Figs. 9.12 and 9.26).

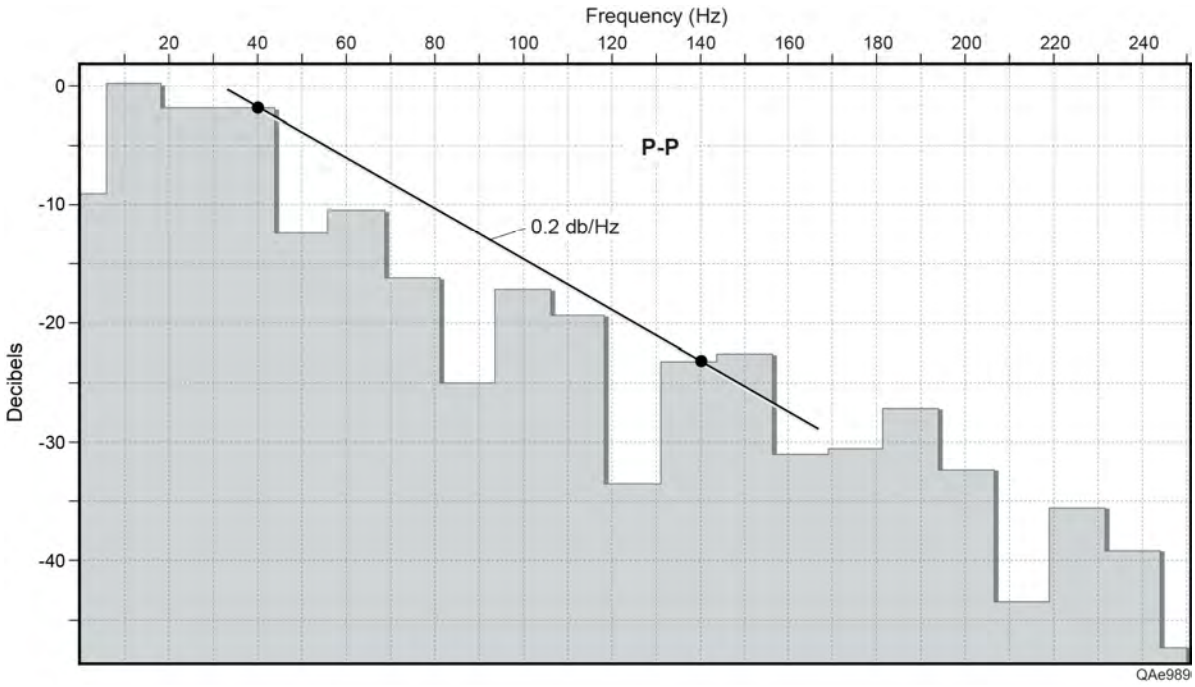

Figure 9.50. P-P frequency across the “near Utica” interval.

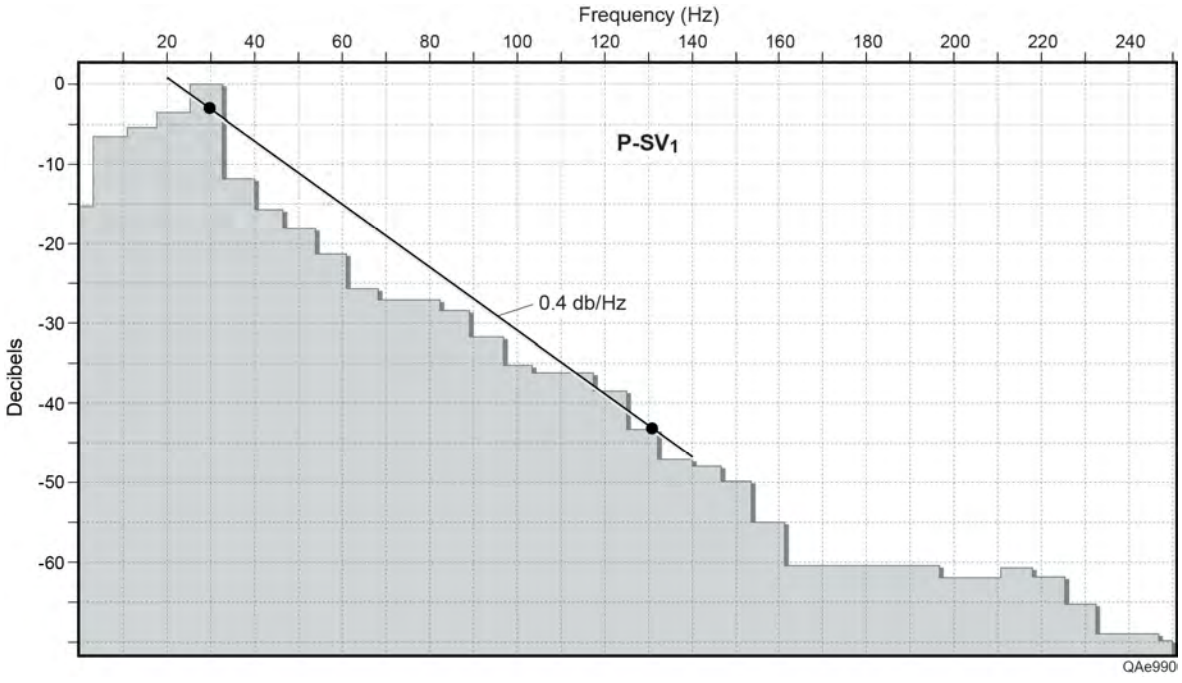

Figure 9.51. P-SV_1 frequency across the “near Utica” interval.

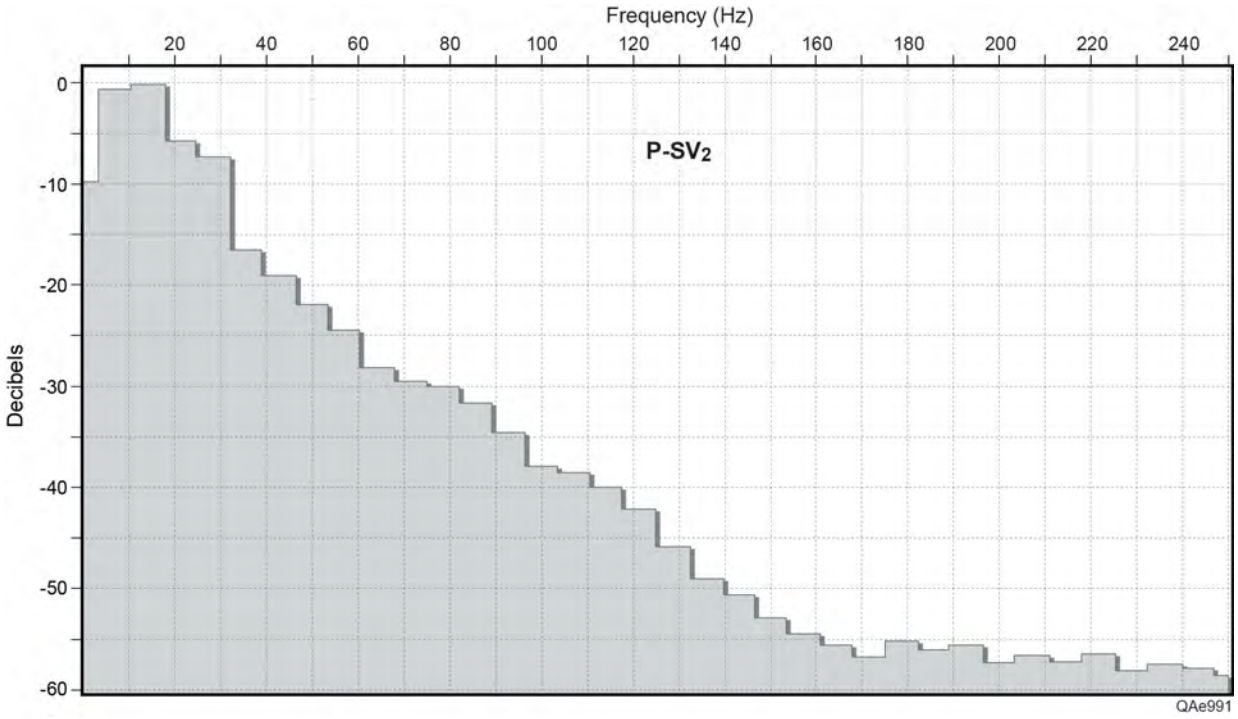

Figure 9.52. P-SV_2 frequency across the “near Utica” interval.

We are not confident that the P-P and P-SV horizons depicted as “near Utica” are in fact related to the actual Utica interval. These interpreted events should be viewed only as first-order approximations of the Utica interval. However, time structure maps generated from these interpreted horizons can probably be used to make generalizations about the structural trends of the Utica Shale across our study area even if the Utica is a short distance above or below our interpreted horizon. Structural maps of each “near Utica” horizon are displayed as Figures 9.53 and 9.54. Both P-P data and P-SV_1 data indicate there are no faults cutting through the Utica Shale and that the structural dip of the Utica is due south.

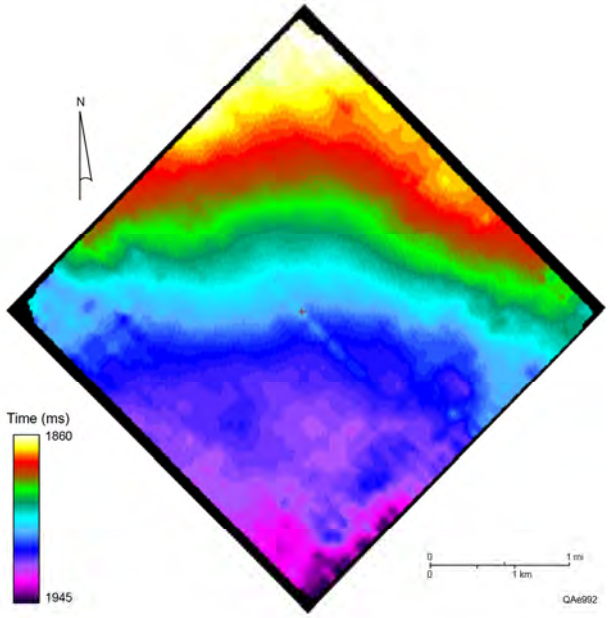

Figure 9.53. P-P time structure map of the “near Utica” horizon.

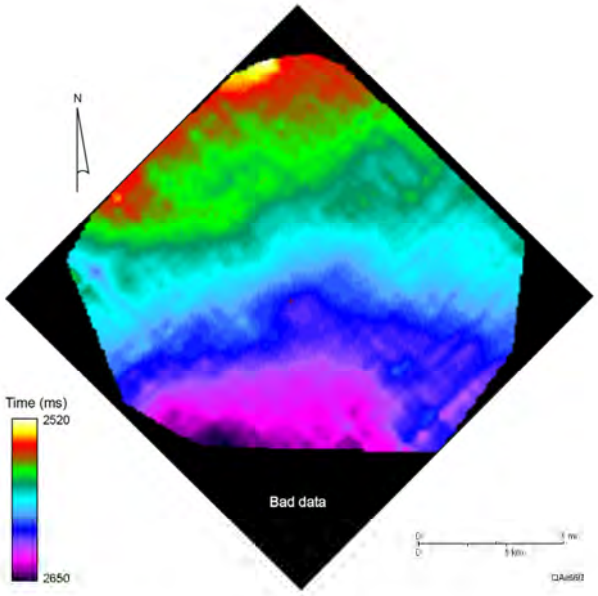

Figure 9.54. P-SV_1 time structure map of the “near Utica” horizon.

A detailed seismic attribute analysis of the Utica Shale interval was not done because we were not confident that the interpreted horizons were accurately positioned on the Utica unit. Also, given the great depth (12,000 ft [3660 m]) of the Utica Shale, the relatively thin interval (200 to 250 ft [60 to 75 m]) of the shale section, and the reduced frequency bandwidth of the seismic data that images the Utica, it is doubtful that seismic attributes would provide reliable rock and fluid properties or dependable fracture information.

As a substitute for a detailed seismic attribute analysis, a limited attribute analysis was done that focused on only RMS amplitude behavior. In this analysis, amplitude maps were constructed and analyzed for clues to geological conditions related to the Utica Shale interval. Figure 9.55 shows P-P RMS reflection amplitudes calculated over a 30-ms time window starting at the top of the “near Utica” horizon. P-SV_1 and P-SV_2 RMS reflection amplitudes calculated over a 60-ms time window starting at the top of the “near Utica” P-SV_1 and P-SV_2 horizons are shown as Figures 9.56 and 9.57, respectively. Each attribute map shows random distributions of amplitudes across seismic image space with no distinguishable stratigraphic trends or structural features. These results indicate that neither P-P data nor converted-SV data (whether P-SV_1 or P-SV_2 data) provide significant fracture or azimuthal anisotropy information for the Utica Shale, and that neither P-P data nor converted-SV data (whether P-SV_1 or P-SV_2 data) have an advantage for reservoir characterization at the depth of the Utica Shale.

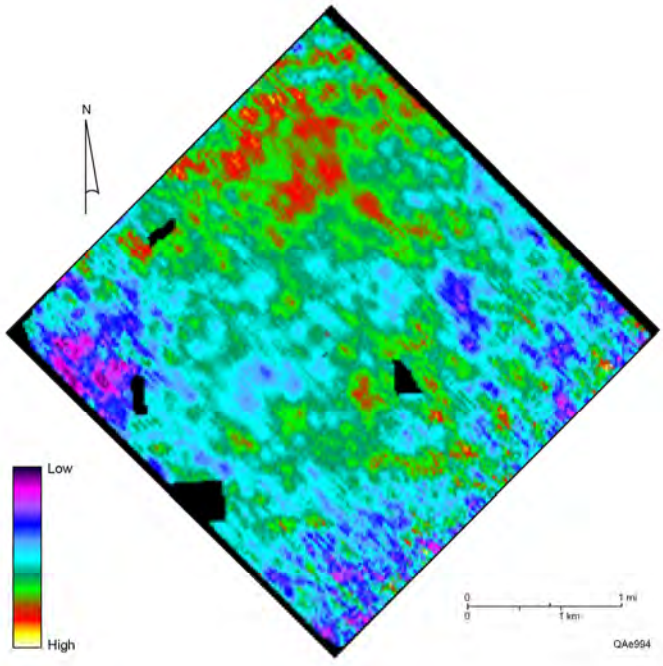

Figure 9.55. P-P RMS amplitude map across the “near Utica” interval.

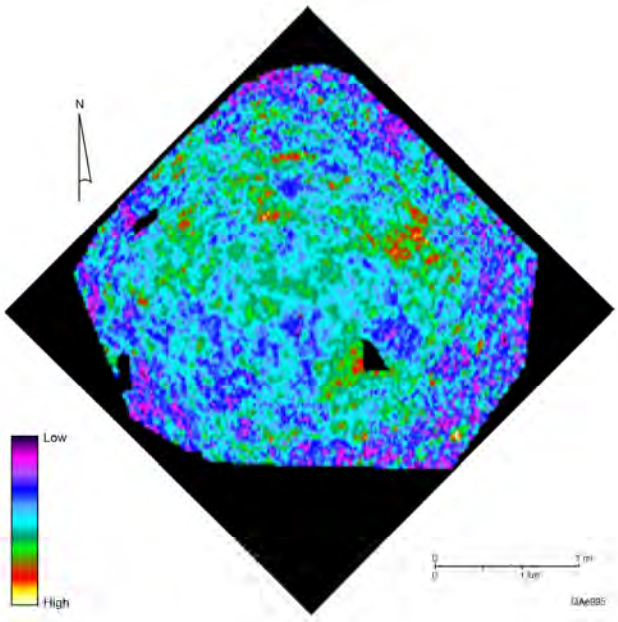

Figure 9.56. P-SV_1 RMS amplitude map across the “near Utica” interval.

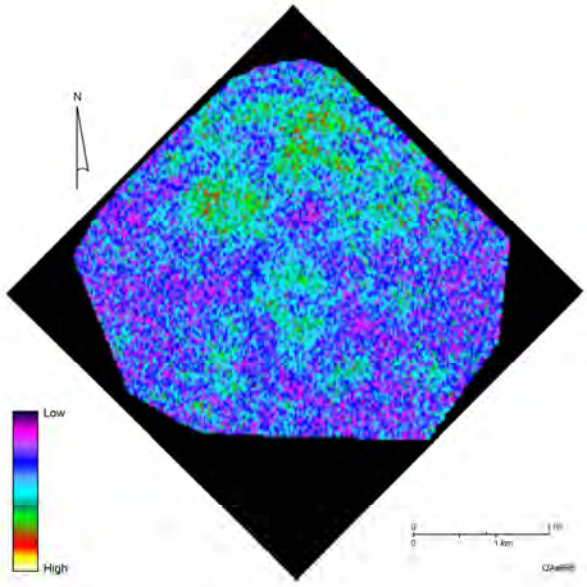

Figure 9.57. P-SV_2 RMS amplitude map across the “near Utica” interval.

Conclusions

The objectives of our study were to study: (1) porous, brine-filled units that could serve as storage reservoirs for flow-back water produced during hydrofracture operations, (2) the Marcellus Shale, and (3) the Utica Shale. Objective 1 was achieved by investigating an interval where porous sandstone should be present, this being the Tully-to-Tichenor interval. Objective 2 was accomplished by performing an intense study of the Marcellus Shale. Objective 3 was achieved by doing a modest evaluation of the seismic data windows where our best guess positioned the Utica Shale in P-P and P-SV image spaces across our study area. The Utica Shale is approximately 5000 ft (1525 m) below the deepest available well log data local to our seismic data grid, and the position of the Marcellus in each seismic image space can only be approximated. The great depth of the Utica Shale, coupled with the absence of any depth-to-time calibration data extending below the Onondaga, did not allow the Utica Shale to be determined with confidence in any seismic data volume.

The 3C3D seismic data used in this study provided the most dramatic contrast between P-wave and S-wave imaging of geologic targets that our research teams has observed in the 12 years our laboratory has been engaged in multicomponent seismic interpretation. The impressive aspect of these data was that both the P-SV_1 (fast-S) mode and P-SV_2 (slow-S) mode provided better spatial resolution of key geologic targets than did P-P (compressional) data. The latter data (P-P) are the principal seismic data used to evaluate shale-gas prospects. The increase in P-SV_1 resolution over P-P resolution was particularly significant, with P-SV_1 wavelengths being approximately 40-percent shorter than P-P wavelengths. Research findings discussed in this chapter should be considered by all shale-gas operators in the Appalachian Basin so they can take advantage of the increased resolution of converted-shear modes relative to P-wave data. Results equivalent to ours should occur wherever the overburden above the Marcellus is similar to overburden properties where our data were acquired.

In addition to S-wave data providing better resolution of geologic targets, we found S-wave images described reservoir heterogeneities that P-P data could not see. Specifically, a channel-like feature was imaged in the Tully-to-Tichenor interval by P-SV_1 data, and no indication of the feature existed in P-P data. This finding is important because this interval contains attractive sandstones that can be utilized as reservoirs for injecting flow-back waters produced during hydrofrac operations. If units are considered for water-storage purposes, it is essential to know all heterogeneities internal to the unit to understand reservoir compartmentalization. We conclude it is essential that multicomponent seismic data be used whenever an Appalachian Basin operator is searching for potential water-injection reservoirs.

All three data volumes (P-P, P-SV_1, and P-SV_2) showed linear folds existed in the Marcellus Shale. These fold trends were not observed in the stiff rocks above and below the Marcellus. The approximate east-west orientation of these folds agreed with the orientation of Marcellus fractures interpreted in borehole image logs acquired in the central-image calibration well. The consistent fold orientations across seismic image space imply Marcellus fracture properties should be reasonably consistent across the image area.

Isopach thicknesses of P-SV_2 and P-SV_1 images across the Marcellus were combined to estimate S-wave anisotropy within the Marcellus. This anisotropy attribute is important because it is a qualitative indicator of fracture intensity. Seismic-based anisotropy values were small, of the order of 1 to 2 percent, which were the same values calculated from fast-S and slow-S modes measured with a dipole sonic log acquired in the central-image well. This seismic result is both encouraging and discouraging. It is encouraging because seismic-based estimates of anisotropy agree with values defined by calibration logs. The result is discouraging because it incorrectly implies few fractures are present in the Marcellus.

As we began this study, we had hopes that good-quality S-wave data would allow fracture intensity within the Marcellus to be estimated with acceptable reliability. This logic was driven by our experience with using S-wave data to infer fracture attributes in rock units where there was a single dominating fracture set. As we began to understand the Marcellus had orthogonal joint sets, we began to question how S-wave data would differ when orthogonal joints were widely spaced versus when the joints were closely spaced. The rock physics theory described in Chapter 5 explains how conventional thinking about the use of S-wave anisotropy has to be modified when S-wave propagate in an orthorhombic medium such as a unit with internal orthogonal joints. That theory predicts there is effectively no fast-S and slow-S direction when orthogonal joints are present. Regardless of which azimuth an S-wave particle-displacement direction is oriented, the medium behaves as a slow-S medium. There is in effect no fast-S mode.

In this type of medium, the best indicator of orthogonal-joint intensity appears to be the magnitude of V_S velocity across the Marcellus. Where joint intensity increases, V_S interval velocity should decrease. Where joint intensity decreases, V_S interval velocity should increase. We thus abandon the use of S-wave anisotropy for predicting joint intensity in the Marcellus and propose a new attribute—V_{S2} interval velocity—for mapping increases and decreases in joint intensity.

Impact to Producers

Chapter 10

Impact on Shale-Gas Producers

Introduction

We conclude the research findings developed in this study can have considerable impact on the direction multicomponent seismic technology proceeds in shale-gas exploitation. This view is summarized and documented in this closing chapter. Important principles emphasized by our research findings are:

- Simple, lower-cost, and widely used vertical-force seismic sources produce full-elastic wavefields, and

- Elastic wavefield seismic stratigraphy provides more information about geological systems than does traditional single-component P-wave seismic stratigraphy.

Impact of Research Findings

The research findings developed in this study impact shale-gas seismic technology in two important areas: (1) seismic data acquisition, and (2) geologic interpretation of seismic data.

Seismic Data Acquisition

When a decision is reached to acquire multicomponent seismic data across an onshore shale-gas area, traditional approaches are to:

- Option 1: Use a commonly available vertical-force type of source (vertical vibrator, shot-hole explosive, or vertical impact) together with appropriate arrays of surface-positioned 3C sensors and record two wave modes – a P-P compressional wave mode and a P-SV converted shear mode.

- Option 2 : Use both a vertical-force source and a horizontal-force source (either a combination of vertical impact and inclined-impact sources, or a combination of vertical vibrators and horizontal vibrators) together with appropriate surface arrays of 3C sensors and record a full-elastic wavefield. To most geophysicists, this option means acquiring P-P, SH-SH, SV-SV, and P-SV wave modes.

Option 2 is more expensive than Option 1 because of the necessity to use two types of sources to generate the required P and S wave modes. For this reason, most multicomponenent data acquisition involves Option 1. As a result, seismic interpreters are penalized by not having access to S-S wave modes created when S-waves are generated directly at each source station by horizontal-force sources.

The research accomplished in this study adds to evidence produced by our research team in previous studies that demonstrates radial and transverse S-wave modes propagate directly from the point where a vertical-force source applies its force vector to the Earth. We are now convinced the wave modes listed in Option 2 can be acquired using only vertical-force seismic sources. Vertical-force sources are widespread, reasonably low cost, and all exploration-focused geophysicists are familiar with them. Perhaps more importantly, vertical-force sources can be used in a wider range of environments than can horizontal-force sources, which allows shale-gas multicomponent seismic technology to be practiced in any environment where standard P-wave seismic data are utilized. For example, horizontal-force sources (horizontal vibrators or inclined impacts) cannot be deployed across swamps, marshes, dense timber, or rugged topography, but shot-hole explosives can. Thus not only do our research findings establish the concept that full-elastic seismic wavefields can be acquired with simpler, lower-cost sources than what have been traditionally used to acquire such data, but our findings also allow full-elastic wavefield data to be acquired across prospect areas where traditional horizontal-force sources cannot be used.

This research finding – that full-elastic wavefield data can be acquired with vertical-force sources - can have significant impact on the practice of the shale-gas seismic data-acquisition community and on the use of multicomponent seismic data in shale-gas exploitation.

Geological Interpretation of Seismic Data

Our research findings add to the evidence amassed by the Exploration Geophysics Laboratory at the Bureau of Economic Geology that elastic wavefield seismic stratigraphy is superior to common, single-component, P-wave seismic stratigraphy for extracting geological information from seismic data (Hardage, et al. 2006; Hardage, 2010b). Specifically, research documented in this project shows:

1. S-wave data often reveal depositional features that cannot be seen with P-P data (Fig.9.15).

2. Across some stratigraphic intervals, S-wave data have better vertical resolution of stratigraphic layering than do P-P data (Figs. 9.10, 9.12, and 9.26).

These two applications alone should convince seismic interpreters that there is great value in doing joint interpretations of P and S data. By combining P and S interpretations into an “elastic wavefield” seismic stratigraphy analysis, more information is created to define rock properties, fluid properties, depositional facies patterns, depositional sequence patterns, fracture orientation and intensity, and subtle faults across a prospect area.

A research finding that offers great potential is our evidence presented in Chapter 6 that shows previously unused seismic modes can be extracted from vertical-force wavefields and applied in geological interpretations. Specifically, these new seismic modes are the SR-SR (radial shear), ST-ST (transverse shear), and perhaps the SV-P (converted P) modes. The value of these previously unused wave modes is that each mode has a different reflectivity behavior at geologic interfaces than does its companion wave modes. As a result, any one of these shear modes can potentially reveal a rock property or fluid property that is difficult to see with its companion wave modes.

Applications to Shale-Gas Exploitation

Applications of our research findings to the shale-gas community can be quite important. We demonstrate that by applying multicomponent seismic technology to the evaluation of Marcellus Shale prospects, the following benefits occur:

1. Eroded incised channels are revealed in stratigraphic intervals where potential water-storage reservoirs could be located (Fig. 9.15 and 9.22). Such depositional features can compartmentalize a reservoir and affect fluid movement within a reservoir system. The presence of an incised channel can be a positive effect or a negative effect, depending on whether the channel enhances or inhibits fluid flow. The important point is that it is essential to detect such depositional features, and across our study area, these incised channels could be detected with S-wave data but not with P-P seismic data.

2. S-waves are much more responsive to the presence of fractures than are P-waves. Specifically, the polarization azimuth of the fast-S mode indicates fracture orientation. In addition, we show that fast-S and slow-S seismic data can be combined to estimate S-wave anisotropy and that this seismic-based estimate has the same magnitude as S-wave anisotropy predicted by dipole-sonic log data. These S-wave anisotropy data are directly proportional to fracture intensity and provide a valuable fracture attribute that cannot be calculated from P-wave seismic data.

3. There is an increased resolution of shale-gas stratigraphy provided by P-SV seismic data relative to the resolution provided by P-P data. Across our study area, P-SV data provided approximately a 40-percent improvement in resolution of think stratigraphic layering.

Conclusions

Research findings developed and documented in this study are significant. Several of our findings involving seismic modes emanating from vertical-force source stations address fundamental principles that will affect how future seismic data-acquisition will be done across shale-gas prospects. Other findings add to the mounting evidence that elastic wavefield seismic stratigraphy should be practiced in reservoir characterization studies rather than traditional single-component P-wave seismic stratigraphy. Both of these impact areas are significant for evaluating shale-gas prospects and have applications any study where it is essential to understand reservoir compartmentalization and to detect fluid-flow barriers.

Technology Transfer Efforts

Technology Transfer

Technology transfer activities were a major part of the deliverables required for this study. Our principal technology transfer efforts included the following:

1. Workshop presented at the University of Pittsburgh. The people who will best benefit from the technology developed and demonstrated in this study are operators across the Appalachian Basin. To ensure our research findings were distributed to Appalachian Basin operators, a technology transfer workshop was held at the University of Pittsburgh in July 2012, near the end of the 3-year study. We had excellent cooperation from Dr. William Harbert at the University of Pittsburgh who assisted in circulating announcements advertising the workshop and in arranging physical facilities for the workshop program. Material distributed at the workshop closely approximated the material incorporated into this final project report, both in content and in format. Attendance at the workshop was 67.

2. Peer-reviewed papers. Three peer-reviewed papers have been submitted for publication. One paper was a case-history written to influence seismic data interpreters. This paper will appear in an early issue of a new journal titled *INTERPRETATION* that the Society of Exploration Geophysicists will launch in the second quarter of 2013. The second paper compared direct-S modes produced by vertical-force sources and horizontal-force sources to show the important principle that vertical-force sources produce direct-S modes equivalent to those produced by horizontal-force sources. This second paper has been accepted for publications in *Journal of Seismic Exploration*, and is scheduled for an early 2013 issue. The lead author on each of these two papers is Engin Alkan, PhD candidate. The third paper was written by lead author Michael DeAngelo, a member of the research team that did this study, and has been accepted for publication in *Journal of Seismic Exploration*. This paper is likewise expected to be published in early 2013.

3. PhD thesis. One PhD thesis was based on the multicomponent seismic data used in this study. The PhD candidate, Engin Alkan, completed his thesis defense at The University of Texas at Austin in November 2012. The thesis title is *Exploring Hydrocarbon-Bearing Shale Formations with Multicomponent Seismic Technology and Direct-Shear Mode Analysis as a New Tool*. This thesis can be accessed through the Jackson School of Geosciences (JSG) at UT Austin as soon as the document is entered into the JSG PhD thesis library.

4. Final project report. The final project report is a major technology transfer deliverable. The report can be accessed by contacting the funding agency, the Research Partnership to Secure Energy for America (RPSEA), through their Web site (www.rpsea.org).

5. Oral presentation of research findings. The principal research findings amassed during this study were distributed as oral presentations at three annual meetings of the sponsors of the Exploration Geophysics Laboratory (Years 2010, 2011,and 2012) and at geophysical society meetings in Houston and Dallas.

6. Distribution of research findings via EGL Web sites. The final report is available via the following link to research projects completed by the Exploration Geophysics Laboratory (EGL): (http://www.beg.utexas.edu/egl/)

Conclusions

Conclusions

S-Waves and Orthogonal Joint Systems

The Marcellus Shale is an interesting seismic propagation medium in that it is an orthorhombic rock having two sets of orthogonal joints. This study showed the presence of orthogonal joint systems may be overlooked in seismic data because orthogonal joint sets cause azimuth variations in P and S reflection amplitudes and velocities to be small. This lack of S-wave azimuth sensitivity to orthogonal joints is in contrast to the high azimuth sensitivity that S waves exhibit when there is a single set of aligned fractures.

Our rock physics modeling showed that when orthogonal joint sets are involved, an interpreter must abandon the classic approach of utilizing azimuth-dependent P-SV_1 and P-SV_2 reflectivity and velocity behaviors to define fracture attributes and must implement new procedures for characterizing joint systems such as those embedded in the Marcellus Shale. To estimate fracture densities of orthogonal joints within the Marcellus Shale, it is necessary to create maps showing spatial variations in S-wave interval velocity across the Marcellus Shale. Fracture density of Marcellus joint sets increases when this S-wave interval velocity decreases, and fracture density decreases when S-wave interval velocity increases.

A second seismic interpretation technique that can indicate trends of increased joint fracturing is to create P and S time-based or depth-based structure maps that define the structural curvature across the Upper and Lower Marcellus. Fracture density appears to increase as structural curvature increases. Thus identifying trends of maximum-curvature in P-wave and S-wave image space can be helpful for defining trends of attractive fracture density.

Vertical-Force Seismic Sources

Field test data show that compressional (P), radial shear (SV), and transverse shear (SH) modes are produced directly at the point where a vertical-force applies its force vector to the Earth. This observation is a fundamental principle that can have profound effects on the use of multicomponent seismic technology by shale-gas operators because vertical-force sources (vertical vibrators, vertical impacts, and shot-hole explosives) are widespread and can operate in a wide range of surface environments (swamps, marshes, dense timber, extreme topography). By using vertical-force sources to generate direct-S waves, shale-gas operators can utilize full elastic wavefields in prospect evaluation without the constraints of relying on horizontal-force sources (primarily horizontal vibrators) to generate S waves directly at a source station.

P-Wave and S-Wave Resolution

An important aspect of the multicomponent seismic data used in this study was our documentation that P-SV_1 (fast-S) and P-SV_2 (slow-S) modes provided better spatial resolution of key geologic targets than did P-P (compressional) data. Spatial resolution is controlled by the wavelength spectrum of an illuminating wavelet, with shorter wavelengths providing better resolution of geologic targets. The increase in P-SV_1 resolution over P-P resolution was particularly significant across our study area, with P-SV_1 wavelengths being one-half to two-thirds of the magnitudes of P-P wavelengths. Unfortunately, P-P seismic data are the principal seismic data used to evaluate shale-gas prospects. Perhaps the most important finding of this study is that shale-gas operators across the Appalachian Basin can achieve better resolution of Marcellus geology by utilizing converted-shear seismic data rather than by relying totally on conventional P-wave seismic data.

Elastic Wavefield Seismic Stratigraphy

Conventional seismic stratigraphy utilizes P-wave seismic data to analyze reservoir systems. In contrast, elastic wavefield seismic straigraphy utilizes both P-wave and S-wave seismic data in reservoir characterization. In this study, we found S-wave images described intra-reservoir heterogeneities that P-P data could not see. Specifically, a channel-like feature was imaged in the sand-prone Tully-to-Tichenor interval by P-SV_1 data, and no indication of this intra-reservoir feature existed in P-P data. This finding is important because this Devonian interval contains attractive sandstones that can be utilized as reservoirs for storing flow-back waters produced during hydrofrac operations. If rock units are considered for water-storage purposes, it is essential to know all heterogeneities internal to the unit to understand reservoir compartmentalization. An important conclusion reached in this study is that it is essential that multicomponent seismic data be used whenever an Appalachian Basin operator is searching for reservoir units where hydrofrac flow-back water can be stored.

Marcellus Folds and Maximum Horizontal Stress

All three seismic data volumes (P-P, P-SV_1, and P-SV_2) showed linear folds extending across the Marcellus Shale. These fold trends were not observed in the stiffer rocks above and below the Marcellus. The approximate east-west orientation of these folds agreed with the orientation of Marcellus fractures interpreted in borehole image logs acquired in the local calibration well. The consistent fold orientations across the seismic image space we studied imply maximum horizontal stress vectors are oriented approximately east-west in this local region of the Appalachian Basin.

Recommendations

Recommendations

Two fundamental recommendations can be stated based on the analyses done in this study:

1. Shale-gas operators across the Appalachian Basin should place increased emphasis on the use of multicomponent seismic technology. This study illustrates the significant increase in stratigraphic resolution that P-SV data provide compared to the resolution of P-P seismic data. Rather than continue to rely on only P-wave seismic data to evaluate shale-gas systems across the Appalachian Basin, operators need to integrate S-wave data into their interpretation database. In addition to increasing the resolving power of seismic data, the use of S-wave data allows intra-reservoir heterogeneities to be seen that are missed by P-wave data. These two contributions of S-wave data – increased resolution of geologic targets and improved reservoir characterization – are powerful justifications for expanding the use of multicomponent seismic technology across the Appalachian Basin.

2. Shale-gas operators should begin to utilize the S-wave modes that are produced directly at the point where a vertical-force seismic source applies its force vector to the Earth. These direct-S modes allow SV-SV and SH-SH images to be made in addition to converted-SV (P-SV) modes. An attraction of using these direct-S modes is that SV-SV and SH-SH images can be made using the same common-midpoint (CMP) data-processing strategies that are used to construct conventional P-P seismic images. CMP data-processing techniques are more widespread and more battle-tested than are algorithms used to construct converted-mode images such as P-SV images, thus high-confidence SV-SV and SH-SH images should be produced by any reputable seismic data processor. Additional advantages of using direct-S waves produced by vertical-force sources are: (1) vertical-force sources are widely available as vertical vibrators, vertical impacts, and shot-hole explosives, and (2) such sources can be used in any environment where conventional P-wave seismic data are acquired. Thus environments where horizontal-force sources (horizontal vibrators) cannot operate (such as swamps, marshes, dense timber, or extreme topography) can be evaluated with vertical-force source S waves.

Acknowledgments

The seismic equipment tests done at the Devine Test Site could not have been done without the assistance of many sponsors of the Exploration Geophysics Laboratory. Mitcham Industries provided the MaxiWave system used for the vertical receiver array as well as surface 3C geophones and DSU3 solid state MEMS sensors, a recording truck, and field technicians. Halliburton provided wireline services and engineers. Dawson Geophysical provided vibrators, vibrator support personnel, and transportation for other sources. Sercel provided a 428 recorder, supporting engineers, and EUnite cable-free boxes. Seismic Source and i-Seis combined to provide Sigma cable-free boxes, a Universal Encorder, and engineering staff. Austin Powder provided explosives and a licensed shooter. United Services Alliance and Vecta Technology provided their accelerated-weight (nitrogen spring) impact source and source operators. OyoGeospace provided a variety of special geophones, GSR cable-free boxes, and field personnel.

Neither could this study have been done without Geophysical Pursuit and Geokinetics providing access to their 3C3D seismic data in Bradford County, Pennsylvania. Proper analysis of these multicomponent seismic data was possible because Chesapeake Energy allowed access to log data acquired in a well they drilled at the center of this 3C3D seismic grid, and because Chesapeake and their partners, Anadarko Exploration, Statoil, and Southwestern Energy, provided access to critical vertical seismic profile data acquired in this central-image well.

Our interpretations of the P-P and P-SV seismic data volumes were done with Landmark software. The seismic profiles, attribute maps, and synthetic seismogram calibrations displayed throughout this report are Landmark products. We at the Bureau of Economic Geology are indebted to Landmark for providing software licenses that allow students and academic research staff to do these types of investigations.

References

Aki, K., and P.G. Richards, 1980, Quantitative seismology – theory and methods: W.H. Freeman and Co.

Alford, R.M., 1986, Shear data in the presence of azimuthal anisotropy: SEG Expanded Abstracts, 56th Annual Meeting, p. 476-479.

Alford, R.M., 1989, Multisource multireceiver method and system for geophysical exploration: U.S. patent 4,803,666.

Alkan, E., 2007, Multi-dimensional land seismic data acquisition techniques and random survey design: Master of Science Thesis in Geological Sciences, The University of Texas at Austin.

Alkan, E., and B. Hardage, 2007, Was that survey crew sober?: AAPG Explorer, v. 28, no. 10, p. 40-41.

Batzle, M., and Z. Wang, 1992, Seismic properties of pore fluids: Geophysics, v. 57, p. 1396-1408.

Boswell, R. 1996. Play Uds; Upper Devonian black shales, *in* Roen, J.B., and Walker, B.J., 1996, Atlas of major Appalachian gas plays: West Virginia Geological and Economic Survey Publication, v. 25, p. 93-99.

Bruner, K., and D. Smosna, 1994, Porosity development in Devonian lithic sandstones of the Appalachian foreland basin: Northeastern Geology, v.16, p. 202-214.

Bruner, K., and D. Smosna, 2008. A trip through the Paleozoic of the Central Appalachian basin with emphasis on the Oriskany Sandstone, Middle Devonian shales, and Tuscarora Sandstone: Dominion Exploration and Production, INC

Castagna, J.P., M.L. Batzle, and T.K. Kan, 1993, Rock physics – the link between rock properties and AVO response, in J.P. Castagna and M.M. Backus (eds), Offset-dependent reflectivity – theory and practice of AVO analysis, Chapter 2: SEG Investigations in Geophysics Series No. 8, p. 135-171.

Castle, J.W., and A.P. Byrnes, 2005, Petrophysics of Lower Silurian sandstones and integration with the tectonostratigraphic framework, Appalachian Basin, United States: AAPG Bulletin, v. 89, p. 41-60.

DCNR (Pennsylvania Department of Conservation and Natural Resources), 2009a, Geologic carbon sequestration opportunities in Pennsylvania: Revision 1.1, 150 pages. http://www.dcnr.state.pa.us/info/carbon/reports-research.aspx.

DCNR (Pennsylvania Department of Conservation and Natural Resources), 2009b, Assessment of risk, legal issues, and insurance for geologic carbon sequestration in Pennsylvania: 401 pages. http://www.dcnr.state.pa.us/info/carbon/reports-research.aspx.

Diecchio, R.J., 1985, Regional controls of gas accumulation in Oriskany sandstone, Central Appalachian basin: AAPG Bulletin, v. 69, p. 722-732.

Durham, L.S., 2011, With Marcellus it's all about the fractures: Amer. Assoc. Petrol. Geol. Explorer, v. 32, no. 10, p. 24-30.

Engelder, T., G. G. Lash, and S. Uzcategui, 2009, Joints sets that enhance production from Middle and Upper Devonian gas shales of the Appalachian Basin: American Association of Petroleum Geologists Bulletin, 93, 857–889.

Engelder, T., 2011, Outcrops of the Marcellus Formation: Pennsylvania State University, http://geosc.psu.edu/~engelder/marcellus/marcellus.html.

Evans, M.A., 1994. Joints and décollement zones in Middle Devonian shales; evidence for multiple deformation events in the central Appalachian Plateau: Geological Society of America Bulletin, v.106, p. 447-460.

Ettensohn, F.R., 1994, Tectonic controls on formation and cyclicity of major Appalachian unconformities and associated stratigraphic sequences: SEPM Concepts in Sedimentology and Paleontology #4, Tectonic and Eustatic Controls on Sedimentary Cycles, p. 217-242.

Hardage, B.A., M.M. Backus, M.V. DeAngelo, S. Fomel, K. Fouad, R.J. Graebner, P.E. Murray, R. Remington, and D. Sava, 2006, Elastic wavefield stratigraphy – an emerging seismic technology: Final Report, U.S. DOE Contract DE-PS26-02NT15375.

Hardage, B.A., 2009, Horizontal wave testing: AAPG Explorer, v. 30, no. 12, p. 26–27.

Hardage, B.A. 2010a, Vertical wave testing: AAPG Explorer, v. 31, no. 1, p. 32–33.

Hardage, B.A., 2010b, Elastic-wavefield seismic stratigraphy and reservoir characterization, *in* D.H. Johnston, ed., Methods and applications in reservoir geophysics, Chapter 6: The road ahead: SEG Investigations in Geophysics Series No. 15, p. 513-530.

Hardage, B.A., M.V. DeAngelo, P.E. Murray, and D. Sava, 2011, Multicomponent seismic technology: Geophysical References Series, No. 18, Society of Exploration Geophysicists, Tulsa, OK, 318 pages.

Harper, J.A., 1990. Leidy gas field, Clinton and Potter Counties, Pennsylvania, in Beaumont, E. and Foster, N.H., compilers Structural Traps I, Tectonic Fold Traps: AAPG Treatise of Petroleum Geology, Atlas of oil and gas Fields, p. 157-190.

Harper, J.A., and D.G. Patchen, 1996, Play Dos (Devonian updip stratigraphic pinchout), the Lower Devonian Oriskany Sandstone structural play, in Roen, J.B. and Walker, B.J. (eds), The atlas of major Appalachian gas plays: West Virginia Geologic and Ec onomic Survey Publication, v. 25, p. 118-125.

Harper, J.A, 2005. An overview of carbon sequestration in Pennsylvania: wpweb2.tepper.cmu.edu/ceic/SeminarPDFs/Harper_CO2_Sequestration_4_28_05.pdf:

Harper, J.A., 2008, The Marcellus Shale – an old "new" gas reservoir in Pennsylvania: Pennsylvania Geology, Pennsylvania Bureau of Topographic and Economic Survey, v. 38, no. 1, p. 2-13..

Harper J.A., and J. Kostelnik, 2010. The Marcellus Shale Play in Pennsylvania: Pennsylvania Department of Conservation and Natural Resources. http://www.marcellus.psu.edu/resources/publications.php Accessed October 15,

Harper, J.A., 2011, An introduction to carbon sequestration – what's being done in Pennsylvania: http://www.pbi.org/resources/rxtras/6364_ELF/Harper.pdf.

Hudson, J.A., 1981, Wave speeds and attenuation of elastic waves in materials containing cracks: Geophys. Jour. Royal Astrom. Soc., v. 64, p. 133-150.

Hudson, J.A., 1990, Overall elastic properties of isotropic materials with arbitrary distribution of circular cracks: Geophys. J. Int., v. 102, p.465-469.

Hudson, J.A., 1994,Overall properties of anisotropic materials containing cracks: Geophys. J. Int., v. 116, p. 279-282

Jilek, P., 2002, Converted PS-wave reflection coefficients in weakly anisotropic media: Pure and Applied Geophys., v. 159, p. 1527-1562.

Kostelnik, J., and K.M. Carter, 2009a, The Oriskany Sandstone updip permeability pinchout: A receipe for gas production in northwestern Pennsylvania: Pennsylvania Geology, v. 39, no.4. p. 19-34.

Kostelnik, J., and K.M. Carter, 2009b, Unraveling the stratigraphy of the Oriskany Sandstone: A necessity in assessing its site-specific carbon sequestration potential: Environmental Geosciences, v. 16, no.4, p. 187-200.

Lash, G.C., 2007, Influence of basin dynamics on Upper Devonian Black Shale deposition, western New York state and northwest Pennsylvania: AAPG Search and Discovery Article #30050 (2007).

Laughrey, C.D., D.A. Billman, and M.R. Canich, 2004, Petroleum geology and geochemistry of the Council Run gas field, north central Pennsylvania: AAPG Bulletin, v. 88, p. 213-239.

Levin, F., 1979, Seismic velocities in transversely isotropic media I: Geophysics, v. 44, p. 918-936.

Levin, F., 1980, Seismic velocities in transversely isotropic media II: Geophysics, v. 45, p. 3-17.

Miall, A.D., and R.C. Blakely, 2009, The Phanerozoic tectonic and sedimentary evolution of North America in Miall, A.D. (ed) Sedimentary Basins of the World, Vol. 5, Chapter 1, p.1-28.

Milici, R.C., and C.S. Swezey, 2006. Assessment of Appalachian Basin oil and gas resources: Devonian shale- Middle and Upper Paleozoic total petroleum system: USGS Open File Report 2996-1237, 70p.

Miller, G., and H. Pursey, 1954, The field and radiation impedance of mechanical radiators on the free surface of a semi-infinite isotropic solid: Proc. Royal Soc. London, Series A, v. 223, p. 521-541.

National Energy Technology Laboratory (NETL), 2009. Modern shale gas development in the United States: A primer: http://www.netl.doe.gov/technologies/oil-gas/publications/EPreports/Shale_Gas_Primer_2009.pdf

NETL. 2010. Impact of the Marcellus shale gas play on current and future CCS activities.32 p http://www.alleghenyconference.org/PDFs/PELMisc/PSUStudyMarcellusShale072409.pdf (Accessed December 6, 2010).

Nuttall, B.C, J.A. Drahovzal, C.F. Eble, and R.M. Bustin, 2005. Analysis of the Devonian Black Shale in Kentucky for Potential Carbon Dioxide Sequestration and Enhanced Natural Gas Production: Final Report: DOE Grant DE-FC26-02NT41442, 120 p.

Nyahay, R., J. Leone, L.B. Smith, J.P. Martin, and D.J. Jarvie, 2007, Update on regional assessment of gas potential in the Devonian Marcellus and Ordovician Utica shales of New York: AAPG Search and Discovery Article 10136 (posted October 1, 2007 after presentation at the 2007 AAPG Eastern Section Meeting September 16-17, 2007, Lexington, KY).

Opritza, S.T., 1996, Lower Devonian Oriskany sandstone updip permeability pinch-out, in J.B. Roen and B.J. Walker, eds., The atlas of major Appalachian gas plays: West Virginia Geological and Economic Survey Publication, 25, p. 126-129.

Patchen, D.G., and J.A. Harper, 1996, The Lower Devonian sandstone combination traps play, in J.B. Roen and B.J. Walker, eds., The atlas of major Appalachian gas plays: West Virginia Geological and Economic Survey Publication, 25, p. 118-125.

Pennsylvania Geological Survey, 1995.Fourth Series *Bedrock Geology of the Freeburg 7.5 minute Quadrangle, Snyder County, Pennsylvania* (Map): Open-File Reports Cartography by United States Geological Survey. ORF 95-04. http://www.dcnr.state.pa.us/topogeo/pub/openfile/pdfs/of95_04_freeburg.pdf.

Rickard, L.V., 1984. Correlation of the subsurface Lower and Middle Devonian of the Lake Erie region: Bulletin of the Geological Society of America, v. 95, p.814–828.

Robertson, J.D., and D. Corrigan, 1983, Radiation patterns of a shear-wave vibrator in near-surface shale: Geophysics, v. 48, p. 19–26.

Roen, J.B., and B.J. Walker, 1996, The atlas of major Appalachian gas plays: West Virginia Geologic and Economic Survey Publication, V. 25, 201 pages.

Rowan, E.L. J.E. Repetski, and R.T. Ryder, 2008, [Abstract] Evidence for paleo-fluid flow westward from the Appalachian basin: AAPG Eastern Section Meeting, Pittsburgh.

Ruger, A., 1998, Variation of P-wave reflectivity with offset and zimuth in anisotropic media: Geophysics, v. 63, p. 935-947.

Sager, M. 2007. Petrologic study of the Murrysville sandstone in southwestern Pennsylvania. Unpublished Masters Thesis West Virginia University 1451665, 99 pages.

Schmoker, J.W., 1981. Determination of organic matter content of Appalachian Devonian shales from gamma-ray logs: AAPG Bulletin, v. 65, p. 1285-1298.

Skeen, J.C., 2010, Basin analysis and aqueous chemistry of fluids in the Oriskany Sandstone, Appalachian Basin, USA: Thesis submitted to Eberly College of Arts and Sciences, West Virginia University, 109 pages.

Smith, L.B., and J. Leone, 2010. Integrated Characterization of Utica and Marcellus Black Shale Gas Plays, New York State: Search and Discovery Article #50289 (2010).

Smith, L.B., 2011. Geology of the black shales of New York: Marcellus Shale Lecture Series, Department of Geology, University of Buffalo: http://www.glyfac.buffalo.edu/mib/course/marcellus/ (accessed October 8, 2011).

Smosna, R., and M.L. Sager, 2008, [Abstract] The making of a high-porosity, high-permeability reservoir - the Murrysville Sandstone of Pennsylvania: AAPG Eastern Section Meeting, Pittsburgh.

Sondergeld, C.H., and C. S. Rai, 1992, Laboratory observations of shear-wave Propagation in anisotropic media: The Leading Edge, v. 11, p. 38-43.

Thomsen, L., 1986, Weak elastic anisotropy: Geophysics, v. 51, p. 1954-1966.

Tsvankin, I.,1997, Refelection moveout and parameter estimation for horizontal transverse isotropy: Geophysics, v. 62, p. 614-629.

Tsvankin, I., 2001, Seismic signatures and analysis of reflection coefficients in anisotropic media: Elsevier Science.

USGS Report 2006-1237 Table 2. Generalized stratigraphic nomenclature for the Devonian Shale- Middle and Upper Paleozoic: http://pubs.usgs.gov/of/2006/1237/pdf%20tables/table2.pdf

U.S. Department of Energy, 2008, 2008 carbon sequestration atlas of the United States and Canada, Second edition, 140 pages.

Vavricuk, V., and I. Psencik, 1998, PP-wave reflection coefficients in weakly anisotropic elastic media: Geophysics, v. 63, p. 2129-2141.

White, J. E., 1983, Underground sound—applications of seismic waves: Elsevier Science Publishers.

Wood, L., 2004a, Removal of noise from seismic data using improved Radon transforms: U.S. Patent 6,691,039 B1.

Wood, L., 2004b, Removal of noise from seismic data using improved tau-p filters: U.S. Patent 6,721,662 B1.

Wrightstone, G., 2009, Marcellus shale, geologic controls on production: AAPG Search and Discovery Article #10206.

Zeng, H., 2001, From seismic stratigraphy to seismic sedimentology – a sensible transition: Gulf Coast Assoc Geol. Soc. Trans. v. 51, p. 412-420.

Zeng, H., 2006, Stratal slicing makes seismic imaging of depositional systems easier: AAPG Explorer, v. 27, no. 6, p. 26-27.

Acronyms, Abbreviations, and Glossary

3C3D: 3-component and 3-dimensional.

a: Crack radius

α: aspect ratio of cracks (ratio of short and long axes of a crack)

ANISO: magnitude of S-wave velocity anisotropy. Calculation procedure is defined by Equation 4.1.

anisotropy: a rock property that causes the magnitude of wave mode velocity, particularly the velocity of an S mode, to vary with direction of propagation. A more explicit term **azimuthal anisotropy** is used when wave-mode velocity varies with azimuth. Azimuthal anisotropy is important for detecting and quantifying fractured intervals.

asymptotic bin: a CCP stacking bin for a converted-mode (e.g. a P-SV mode) positioned at X-Y coordinates that do not vary as imaging depth increases. For shallow interfaces, the X-Y coordinates of a CCP vary rapidly with depth. Asymptotic bins appear in the deeper portion of seismic image space.

AVAZ: amplitude versus angle and azimuth

C: elastic stiffness tensor

$\mathbf{C_{ij}^{0}}$: components of isotropic elastic-stiffness tensor

$\mathbf{C_{ij}^{1}}$, $\mathbf{C_{ij}^{2}}$: first-order and second-order corrections of elastic-stiffness tensor

CCP: common-conversion point. A point in the subsurface where a downgoing wave mode propagating with velocity V1 converts to an upgoing wave mode that propagates with a different velocity V2. See **CMP**. For a **P-SV** mode, a CCP coordinate for a given source-receiver pair is closer to the receiver station than to the source station. For an **SV-P** mode, the CCP is closer to the source station.

chronostratigraphic surface: a rock surface representing a fixed geologic time. Seismic reflections are assumed to follow chronostratigraphic surfaces. See **stratal surface**.

CMP: common midpoint. A point in the subsurface where a downgoing wave mode propagating with velocity V1 converts to an upgoing wave mode that propagates with the same velocity V1. In an Earth having flat horizontal layers, this reflection point is half way between a source and a receiver, hence the term “midpoint”. See **CCP**.

crossline: the direction perpendicular to receiver lines. See **inline**.

e: fracture density

FD: fracture density

FK: a data space defined in terms of frequency versus wavenumber. A forward FK transform converts seismic data from the time-space domain to the frequency-wavenumber domain. An inverse FK transform converts data from the frequency-wavenumber data domain to the time-space domain. In FK data space, seismic modes are defined in terms of their frequency content and their propagation velocity. Wave mode propagation velocity V is given by V = F/K, the slope of a wave mode's energy trend in FK data space.

$\gamma^{(S)}$: vertical shear-wave splitting parameter

GR: gamma-ray log

horizontal transverse isotropy: a seismic propagation medium in which rock properties are isotropic in a direction perpendicular to a horizontal axis of symmetry. Such a medium describes a system of parallel, vertical fractures in a thick uniform layer. See **HTI** and **vertical transverse isotropy**.

HTI: horizontal transverse isotropy.

inline: the direction in which a receiver line is deployed. See **crossline**.

Love wave: a surface wave that propagates across the Earth-air interface with a particle-displacement vector that is: (1) parallel to the Earth surface, and (2) perpendicular to the direction the wave is moving. This particle displacement is an **SH** displacement, and this type of surface wave can be produced only by an **SH** source. Wave motion is confined to the Earth surface. A Love wave does not propagate into the Earth as a body wave. See **Rayleigh wave**.

MEMS: micro-electronic mechanical system. A solid state accelerometer concept used to acquire 3C seismic data.

MRCSP: Midwest Regional Carbon Sequestration Partnership.

N1: natural coordinate axis 1.

N2: natural coordinate axis 2.

natural coordinate axes: a data coordinate system within the Earth with its axes oriented in the directions of the natural anisotropy axes existing in the Earth's

rock system. As S waves propagate in the Earth, their polarization directions adjust to be aligned with natural coordinate axes **N1** and **N2**.

N/V: number of cracks per unit volume

offset: the horizontal, straight-line distance between a seismic source and a seismic sensor.

orthorhombic: a seismic propagation medium consisting of thin-bed layering and (1) one set of parallel fractures normal to bedding, or (2) two sets of orthogonal fractures normal to bedding. An orthorhombic medium has three symmetry planes – one plane parallel to bedding, one plane normal to bedding and parallel to fractures, and the third normal to bedding and perpendicular to fractures.

Φ: porosity

P-P: conventional P-wave seismic data; P-wave down and P-wave up.

proportional slicing: the process of dividing a seismic interval into a series of surfaces that each follow a fixed geologic time. See **stratal slicing**.

P-SV: converted-shear data; P-wave down and SV-wave up. See **SV-P**.

P-wave: compressional wave

radial: the straight line direction from a source station to a receiver station. See **transverse**.

radial-shear: a shear displacement in the vertical plane passing through a source station and a receiver station. Also called **radial-S**, **SR**, or **SV**. See **transverse-shear**.

random geometry: a seismic data-acquisition geometry in which the distances and azimuths between receiver stations and source stations differ in a random manner across a data-acquisition grid. See **regular geometry**.

Rayleigh wave: A wave that travels along the Earth-air interface and produces both vertical and inline-radial displacement as it propagates. The resulting particle displacement motion is elliptical with the ellipse tilted toward the source point where the wave originated. This type of surface wave is produced by vertical-displacement sources. Wave motion is confined to the Earth surface, and a Rayleigh wave does not propagate into the Earth as a body wave. See **Love wave**.

regular geometry: a seismic data-acquisition geometry in which source and receiver lines occur at consistent spacings and source-station and receiver-station positions along these lines occur at consistent intervals. See **random geometry**.

S_1: fast S mode. In a fractured medium, an S_1 mode is polarized parallel to aligned fracture planes. In a stress field, S_1 is polarized parallel to maximum horizontal stress.

S_2: slow S mode. In a fractured medium, an S_2 mode is polarized perpendicular to aligned fracture planes. In a stress field, S_2 is polarized perpendicular to maximum horizontal stress.

sagital plane: a plane passing through a source station, a receiver station, and a reflection point produced by a wave mode propagating between that source and receiver.

seed horizon: a high-quality, high confidence chronostratigraphic surface interpreted across a 3D seismic volume

S-S: S-wave seismic data involving a downgoing S mode and the same upgoing S mode, where S can be **SH**, **SR**, **SV**, or **ST**.

S-wave: shear wave.

SH: shear mode having a horizontal displacement vector. See **ST** and **transverse-shear**.

SR: shear mode having a radial displacement vector. See **SV** and **radial-shear**.

ST: shear mode having a transverse displacement vector. See **SH** and **transverse-shear**.

stratal slicing: the process of creating a seismic horizon that follows a fixed geologic time. See **proportional slicing**.

stratal surface: a surface that follows a fixed geologic time. See **chronostratigraphic surface**.

SV: shear mode having a vertical displacement vector. See **SR** and **radial-shear**.

SV-P: converted P mode. SV-wave down and P-wave up. See **P-SV**.

transverse: the direction perpendicular to the vertical plane passing between a source station and a receiver station. See **radial**.

transverse-shear: shear displacement perpendicular to the vertical plane passing through a source station and a receiver station. Also called **transverse-S**, **ST**, or **SH**.

vertical transverse isotropy: a seismic propagation medium in which rock properties are isotropic in a direction perpendicular to a vertical axis of symmetry. Such a medium describes a system of stacked thin beds. See **VTI** and **horizontal transverse isotropy**.

VSP: vertical seismic profile.

VSX: an accelerated-weight seismic source patented by Vecta Technology and manufactured by United Service Alliance.

VTI: vertical transverse isotropy.

Appendix A

Wave Mode Reflectivity in Orthorhombic Media

Orthorhombic media describe most fractured reservoirs; however, the difficulties of dealing with the nine elastic constants required to characterize such media have caused orthorhombic assumptions to not be used in many seismic analyses of fractured targets. The nine independent elastic stiffness coefficients ($\mathbf{c_{ij}}$) of an orthorhombic medium can be written in matrix form as

$$C = \begin{pmatrix} c_{11} & c_{12} & c_{13} & 0 & 0 & 0 \\ c_{12} & c_{22} & c_{23} & 0 & 0 & 0 \\ c_{13} & c_{23} & c_{33} & 0 & 0 & 0 \\ 0 & 0 & 0 & c_{44} & 0 & 0 \\ 0 & 0 & 0 & 0 & c_{55} & 0 \\ 0 & 0 & 0 & 0 & 0 & c_{66} \end{pmatrix}. \quad \text{(A.1)}$$

Figure 5.10 of Chapter 5 presents a schematic representation of an orthorhombic medium having three orthogonal symmetry planes. Two symmetry planes are vertical, and one is horizontal. If there are two vertical, orthogonal sets of joints as there are in the Marcellus Shale (Fig. 5.11), it is assumed fracture set 1 (parallel to symmetry plane 1) has the higher fracture density, and fracture set 2 (parallel to symmetry plane 2) has a fracture density smaller than, or equal to, fracture set 2. Additional assumptions are coordinate axis **x1** (Fig. 5.10) is orthogonal to symmetry plane 1, and coordinate axis **x2** is orthogonal to symmetry plane 2. As a result, an S-wave mode with its particle-displacement vector polarized along **x1** represents the slow S-mode (S_2-wave), and an S-wave mode polarized in the **x2** direction is the fast S-mode (S_1-wave). The vertical axis orthogonal to symmetry plane 3 (Fig. 5.10) is denoted as coordinate axis **x3**.

The polarization of shear waves with respect to vertical incidence varies with azimuth. If the elastic-stiffness matrix (Eq. A.1) has the inequality $c_{44}>c_{55}$ (or in other words, fracture set 1 has higher fracture density than fracture set 2), a vertically traveling fast-S mode S_1 is polarized in the x2 direction. This S_1 mode represents a transverse SH wave for any phase direction in the [x1 x3] plane (symmetry plane 2, Figure 5.10). As we move the arrival direction of the S_1-wave around the x3 axis (vertical axis) to the [x2 x3] plane (symmetry plane no.1), its polarization changes from transverse (cross-plane), to in-plane (in other words, the mode changes from from SH in symmetry plane 2 to SV in symmetry plane 1). Thus, an S_1 wave propagating in the [x1 x3] plane (symmetry plane 2) is equivalent to an SH-wave in VTI media, while in the [x2 x3] plane (symmetry

plane 1), it is equivalent to an SV-wave. Likewise, the polarization of the S_2-wave changes from SV in the [x1 x3] plane to SH in the [x2 x3] plane.

Thomsen-Type Anisotropic Parameters in Orthorhombic Media

Tsvankin (1997) introduced a standard set of anisotropic parameters for orthorhombic media based on the nine coefficients of the elastic stiffness matrix (Eq. A.1). This parameter set contains vertical velocities V_{P0} and V_{S0} and seven dimensionless Thomsen-type anisotropic coefficients:

(A.2) $V_{P0} = \sqrt{\frac{c_{33}}{\rho}}$ P-wave vertical velocity. ρ is the density of the rock;

(A.3) $V_{S0} = \sqrt{\frac{c_{55}}{\rho}}$ S-wave vertical velocity polarized in x1 direction (S_2-mode);

(A.4) $\varepsilon^{(1)} = \frac{c_{22} - c_{33}}{2c_{33}}$ VTI ε parameter in [x2, x3] symmetry plane 1;

(A.5) $\gamma^{(1)} = \frac{c_{66} - c_{55}}{2c_{55}}$ VTI γ parameter in [x2, x3] symmetry plane 1;

(A.6) $\delta^{(1)} = \frac{\left(c_{23} + c_{44}\right)^2 - \left(c_{33} - c_{44}\right)^2}{2c_{33}\left(c_{33} - c_{44}\right)}$ VTI δ parameter in [x2, x3] symmetry plane 1

(A.7) $\varepsilon^{(2)} = \frac{c_{11} - c_{33}}{2c_{33}}$ VTI ε parameter in [x1, x3] symmetry plane 2;

(A.8) $\gamma^{(2)} = \frac{c_{66} - c_{44}}{2c_{44}}$ VTI γ parameter in [x1, x3] symmetry plane 2;

(A.9) $\delta^{(2)} = \frac{\left(c_{13} + c_{55}\right)^2 - \left(c_{33} - c_{55}\right)^2}{2c_{33}\left(c_{33} - c_{55}\right)}$ VTI δ parameter in [x1, x3] symmetry plane 2;

(A.10) $\delta^{(3)} = \frac{\left(c_{12} + c_{66}\right)^2 - \left(c_{11} - c_{66}\right)^2}{2c_{11}\left(c_{11} - c_{66}\right)}$ VTI δ parameter in [x1, x2] symmetry plane 3;

Another important parameter is the shear wave splitting at normal incidence given by:

(A.11) $\gamma^{(s)} = \frac{c_{44} - c_{55}}{2c_{55}}$.

Parameters $\varepsilon^{(1)}$ and $\varepsilon^{(2)}$ can be used to approximate fractional differences between vertical and horizontal P-wave velocities in planes [x1, x3] and [x2, x3] to create a measure of P-wave anisotropy between these two planes. Similarly, coefficients $\gamma^{(1)}$ and $\gamma^{(2)}$ can be used to estimate S-wave anisotropy for the same planes.

Vertical S-wave velocity polarized in the x2 direction (the fast S_1-mode) is given as:

(A.12) $$V_{S1} = \sqrt{\frac{c_{44}}{\rho}} .$$

Phase Velocities in Symmetry Planes

Analyzing wave-mode propagation in symmetry planes provides important insights into wave propagation physics in orthorhombic media. Only S-waves propagating in symmetry planes can be described as SV and SH modes. As wave propagation moves away from symmetry planes, S modes change, and designations S_1 and S_2 are more appropriate for S-waves propagating outside of symmetry planes.

Tsvankin (2001) gives the following expressions for P and SV phase velocities in the [x1, x3] symmetry plane. In this notation, angle θ is measured with respect to vertical axis x3:

(A.13) $$\frac{V_P{}^2(\theta)}{V_{P0}^2} = 1 + \varepsilon^{(2)} \sin^2\theta - \frac{f}{2} + \frac{f}{2}\sqrt{\left(1 + \frac{2\varepsilon^{(2)}\sin^2\theta}{f}\right)^2 - \frac{2\left(\varepsilon^{(2)} - \delta^{(2)}\right)\sin^2 2\theta}{f}}$$

(A.14) $$\frac{V_{SV}{}^2(\theta)}{V_{P0}^2} = 1 + \varepsilon^{(2)} \sin^2\theta - \frac{f}{2} - \frac{f}{2}\sqrt{\left(1 + \frac{2\varepsilon^{(2)}\sin^2\theta}{f}\right)^2 - \frac{2\left(\varepsilon^{(2)} - \delta^{(2)}\right)\sin^2 2\theta}{f}} ,$$

Quantity *f* is defined as $f = 1 - \left(\frac{V_{S0}}{V_{P0}}\right)^2$.

V_{P0} and V_{S0} are the vertical velocities defined as Equations A.2 and A.3, and θ is the angle between the vertical axis and the direction of propagation (the incidence angle). P and SV phase velocities in the [x1, x2] symmetry plane are given by Equations A.13 and A.14, with the exception that $\varepsilon^{(1)}$ and $\delta^{(1)}$ are used instead of $\varepsilon^{(2)}$ and $\delta^{(2)}$.

SH phase velocity in the vertical [x1, x3] plane is given by:

(A.15) $$V_{SH[x1\,x3]} = V_{S0}\sqrt{\frac{1+2\gamma^{(1)}}{1+2\gamma^{(2)}}}\sqrt{1+2\gamma^{(2)}\sin^2\theta}.$$

In vertical plane [x2, x3], SH phase velocity is:

(A.16) $$V_{SH[x2\,x3]} = V_{S0}\sqrt{1+2\gamma^{(1)}\sin^2\theta}.$$

In this context, the term “SH-wave” refers to two different shear modes in the vertical symmetry planes.

Reflectivity as a Function of Incidence Angle and Azimuth

From a mathematical perspective, wave-mode reflectivities in orthorhombic media are more complex than reflectivity equations in isotropic or transversely isotropic media. However, orthorhombic-medium equations simplify for waves propagating in the symmetry planes of an orthorhombic medium. For example, Ruger (1998) defines approximate P-wave reflection coefficients in orthorhombic symmetry planes as:

(A.17) $$R^{[x1\,x3]}(\theta) = \frac{1}{2}\frac{\Delta Z}{\overline{Z}} + \frac{1}{2}\left[\frac{\Delta V_{P0}}{\overline{V}_{P0}} - \left(\frac{2\overline{V}_{S0}}{\overline{V}_{P0}}\right)^2\frac{\Delta G^{(2)}}{\overline{G}^{(2)}} + \Delta\delta^{(2)}\right]\sin^2\theta + \frac{1}{2}\left(\frac{\Delta V_{P0}}{\overline{V}_{P0}} + \Delta\varepsilon^{(2)}\right)\sin^2\theta\tan^2\theta,$$

(A.18) $$R^{[x2\,x3]}(\theta) = \frac{1}{2}\frac{\Delta Z}{\overline{Z}} + \frac{1}{2}\left[\frac{\Delta V_{P0}}{\overline{V}_{P0}} - \left(\frac{2\overline{V}_{S1}}{\overline{V}_{P0}}\right)^2\frac{\Delta G^{(1)}}{\overline{G}^{(1)}} + \Delta\delta^{(1)}\right]\sin^2\theta + \frac{1}{2}\left(\frac{\Delta V_{P0}}{\overline{V}_{P0}} + \Delta\varepsilon^{(1)}\right)\sin^2\theta\tan^2\theta$$

.

In these equations, $R^{[x1\ x3]}$ and $R^{[x2\ x3]}$ are P-P reflectivity in the [x1, x3] and [x2, x3] symmetry planes, respectively, with the following notations:

(A.19) $$V_{P0} = \sqrt{\frac{c_{33}}{\rho}}, \qquad V_{S1} = \sqrt{\frac{c_{44}}{\rho}}, \qquad V_{S0} = \sqrt{\frac{c_{55}}{\rho}}, \qquad G^{(1)} = \rho\left(V_{S1}\right)^2, \qquad G^{(2)} = \rho\left(V_{S0}\right)^2.$$

Z represents P impedance at normal incidence, and ΔZ is the difference between P impedance in the lower and upper half spaces. V_{P0} is the vertical P wave velocity. $\overline{V}_{S1}$ is the average vertical S velocity of the two half spaces for an S wave polarized perpendicular to axis x1 (fast polarization). $\overline{V}_{S0}$ is the average vertical S velocity of the two half spaces when an S wave is polarized perpendicular to axis x2 (slow polarization). $G^{(1)}$ and $G^{(2)}$ are given by the product of rock density and the square of V_{S1} and V_{S0}, respectively. $\overline{G}^{(1)}$ and $\overline{G}^{(2)}$ represent the average value of $G^{(1)}$ and $G^{(2)}$ in the two half spaces, while $\Delta G^{(1)}$ and $\Delta G^{(2)}$ are the differences between $G^{(1)}$ and $G^{(2)}$ in the lower and upper

half spaces. All of the other anisotropic parameters $\varepsilon^{(1)}$, $\delta^{(1)}$, $\varepsilon^{(2)}$, $\delta^{(2)}$, are the Thomsen-type anisotropic coefficients described by Tsvankin (1997). θ is again the angle of incidence.

Vavrycuk and Psencik (1998) used first-order perturbation theory to derive P-P reflection coefficients for an interface between two weakly anisotropic media. Jilek (2002) used the same first-order perturbation theory and derived reflection coefficients for converted P-SV waves in weakly anisotropic media. In this report we use Vavrycuk and Psencik theory, as well as Jilek's approach, to compute reflectivities of P-P and P-SV modes as a function of incidence angle and azimuth for orthorhombic media.